Catalytic De-halogenation of Halogen-containing Solid Wastes by Nanostructures of Transition Metals and Their Oxide Configurations

Oday H. Ahmed, BSc, MSc

This thesis is presented for the degree of

Doctor of Philosophy

MURDOCH UNIVERSITY

U N I V E R S I T Y

PERTH, WESTERN AUSTRALIA

College of Science, Health, Engineering & Education, Murdoch

University, Western Australia

2020

Declaration

I declare that:

a) The thesis is my own account of my research, except where other sources are acknowledged.

b) The extent to which the work of others has been used is clearly stated in each chapter and certified by my supervisors.

c) The thesis contains as its main content, work that has not been previously submitted for a degree at any other university

....

Oday H. Ahmed

October 2019

Supervisory Statement

We, the undersigned, attest that Higher Research Degree candidate, **Oday H. Ahmed**, has devised, synthesised and carried out the computational quantum-mechanical calculations, analysed data, and has written all papers included in this thesis. **Associate Professor Zhong-Tao Jiang** and **Associate Professor Mohammednoor Altarawneh** provided the necessary advice, project direction and assisted with the editing of the papers, consistent with normal supervisors-candidate relations.

....

A/Prof Zhong-Tao Jiang   A/Prof Mohammednoor Altarawneh

October 2019   October 2019

Dedication

This thesis is dedicated to my father Mr. Hameed Ahmed:

You are gone but your belief in me has made this journey possible.

You would have been the most proud of what I have done.

Forever in my heart and thoughts.

I love you endlessly.

Acknowledgements

I would like to express my deepest appreciation to all those who made it possible for me to complete my research and the thesis.

I give special gratitude I give to A/Prof Zhong-Tao Jiang and A/Prof Mohammednoor Altarawneh, supervisors of my PhD project and thesis. I sincerely thank the principal and coordinating supervisor, A/Prof Zhong-Tao Jiang, for providing friendly, instructive and supportive environment during my PhD candidature period at Murdoch University. To my co-supervisor, A/Prof Mohammednoor Altarawneh, I would like to think him for his professional guidance, patience, enthusiasm, encouragement, and valuable support throughout my candidature. I am forever grateful.

I would also like to extend my gratitude to the team members of the Surface Analysis and Materials Engineering Research Group at Murdoch University. Many thanks to Dr Hatem Taha, Dr Niveen W Assaf, Dr Ibukun Oluwoye, Dr Khalil Ibrahim, Dr Hantarto Widjaja and Dr. Waleed Nassar for friendship, support, sharing your knowledge and experience with me throughout my PhD years.

This PhD study would not have been possible without the financial support of the Higher Committee for Education Development in Iraq (HCED) scholarship, it is gratefully acknowledged.

To my family, special thanks go to my Mother. Thank you for all the sacrifices that you have made for me and your prayers for me during my difficult times. I cannot express how grateful

Abstract

This thesis presents a series of scientific investigations examining the potential dual role for nanostructure of several 3d transition metals and their oxides in the catalytic de-halogenation of halogen laden materials as well as their mediating formation of toxic halogenated aromatics through accurate density functional theory (DFT) calculations. These investigations have been instrumental to (i) understand, on a precise atomic scale, mechanisms operating in fixation of halogens on transitional metal and their oxides, (ii) design of a large-scale catalytic upgrading unit that operates to extract the valuable metals loads from electric arc furnace dust (EAFD) and (iii) provide important fingerprints for environmental burdens associated with thermal recycling of e-waste and subsequent generation of notorious dioxins compounds and phenoxy-type environmental persistent free radicals (EPFRs). Herein, we have carefully benchmarked the accuracy of systematically obtained results versus experimental values pertinent to investigated systems, namely, lattice parameters, density of states and surface relaxations.

The initial part of the dissertation focuses on the reaction mechanisms of major products from thermal decomposition of polyvinyl chloride (PVC) and brominated flame retardants (BFRs) with nanostructures (clusters and surfaces) of hematite (α-Fe$_2$O$_3$), zincite (ZnO) and magnetite (Fe$_3$O$_4$). The detailed kinetic analysis indicates that dissociative adsorption of hydrogen halides molecules, the major halogen fragments from thermal degradation of halogen laden materials, over those metal oxide structures affords oxyhalides structures via modest activation barriers. Transformation of oxyhalides into metal halides occurs through two subsequent steps, further dissociative adsorption of hydrogen halides over the same structures followed by the release of H$_2$O molecule. In the course of the interaction of halogenated alkanes and alkenes with the selected metal oxide structures, the opening channel in the dissociative addition route requires lower activation barriers in reference to the direct HCl/Br elimination pathways.

However, sizable activation barriers are encountered in the subsequent β C-H bond elimination step. The obtained accessible reaction barriers for reactions of halogenated alkanes and alkenes with the title metal oxides demonstrate that the latter serve as active catalysts in producing clean olefins streams from halogenated alkanes.

Finally, we examined the dissociative adsorption of a phenolic molecules on Cu and Fe surfaces and their partially oxidized configurations to elucidate the specific underpinning mechanism of the title reaction and the kinetics feasibility to germane to generate phenolate-type EFPRs. Our simulated results show that dissociative adsorption of the phenol molecule is kinetically and thermodynamically preferred over the partially oxidized configuration in reference to neat surfaces. Computed charge transfer and density of state (DOS) indicates accumulation of spin density on the phenolic's O following fission of the O-H bond. Obtained results shall be instrumental in efforts that aim to recycle the non-metallic fraction in e-waste.

Table of Contents

Chapter 3   55

Chapter 4   80

List of Publications

<u>Journal Articles</u>

I. **O. H. Ahmed**, M. Altarawneh, Z.-T. Jiang, M. Al-Harahsheh, B.Z. Dlugogorski, Reactions of products from thermal degradation of PVC with nanoclusters of α-Fe$_2$O$_3$ (hematite), *Chem. Eng. J.*, 323 (**2017**) 396-405.

II. **O. H. Ahmed**, M. Altarawneh, M. Al-Harahsheh, Z.-T. Jiang, B.Z. Dlugogorski, Recycling of zincite (ZnO) via uptake of hydrogen halides, *Phys. Chem. Chem. Phys.*, 20 (**2018**) 1221-1230.

III. **O. H. Ahmed**, M. Altarawneh, M. Al-Harahsheh, Z.-T. Jiang, B.Z. Dlugogorski, Catalytic de-halogenation of alkyl halides by copper surfaces, *J. Environ. Chem. Eng.*, 6 (**2018**) 7214-7224.

IV. **O. H. Ahmed**, M. Altarawneh, M. Al-Harahsheh, Z.-T. Jiang, B.Z. Dlugogorski, Catalytic de-chlorination of products from PVC degradation by magnetite (Fe$_3$O$_4$), *Appl. Surf. Sci.*, 480 (**2019**) 792-801.

V. **O. H. Ahmed**, M. Altarawneh, M. Al-Harahsheh, Z.-T. Jiang, B.Z. Dlugogorski, Formation of phenoxy-type environmental persistent free radicals (EPFRs) from dissociative adsorption of phenol on Cu/Fe and their partial oxides, *Chemosphere*, 240 (**2020**) 124921.

VI. M. Altarawneh, **O. H. Ahmed**, Z.-T. Jiang, B.Z. Dlugogorski, Thermal recycling of brominated flame retardants with Fe$_2$O$_3$, *J. Phys. Chem. A,* 120 (**2016**) 6039-6047.
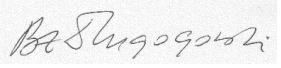
Conferences

   I.   **O. H. Ahmed**, M. Altarawneh, Z.-T. Jiang, Influence of iron oxide on the pyrolysis of poly (vinyl chloride)(PVC), Australian Institute of Physics (AIP) Postgraduate Conference, 13 October **2016**, University of Western Australia, WA, Australia.

  II.   **O. H. Ahmed**, M. Altarawneh, Z.-T. Jiang, B.Z. Dlugogorski, Reaction of Alkyl Halides with the Copper (100) Surface, Australian Symposium on Computational Chemistry, 1-2 December **2016**, University of Western Australia, WA, Australia.

 III.   **O. H. Ahmed**, M. Altarawneh, Z.-T. Jiang, B.Z. Dlugogorski, Thermal degradation of poly (vinyl chloride) (PVC) over magnetite (111) surface. Inaugural Murdoch University Annual Research Symposium, 8 November **2017**, Murdoch University, WA, Australia.

 IV.   **O. H. Ahmed**, M. Altarawneh, B.Z. Dlugogorski, Z.-T. Jiang, The catalytic de-hydrogenation of phenol molecular by metallic Cu(100), Fe(100) and their oxides surfaces. Australian Institute of Physics (AIP) Postgraduate Conference, 15 November **2018**, University of Western Australia, WA, Australia.

  V.   **O. H. Ahmed**, M. Altarawneh, Z.-T. Jiang, B.Z. Dlugogorski, Catalytic effectiveness of franklinite (110) surface toward recycling of the halogenated waste steam*,* Physical Chemistry Australia Conference, 11-14 February **2019**, University of Western Australia. WA, Australia.

 VI.   **O. H. Ahmed**, M. Altarawneh, Z.-T. Jiang, B.Z. Dlugogorski, Co-pyrolysis of brominated flame retardants with polymeric materials (polyethylene). 10th International Conference on Materials for Advanced Technologies, 23- 28 June **2019**, Marina Bay Sands, Singapore.

VII.   **O. H. Ahmed**, M. Altarawneh, Z.-T. Jiang, Catalytic de-halogenation of halogen-containing solid wastes by transition metal oxides, Australian Institute of Physics (AIP) Postgraduate Conference, 14 November **2019**, University of Western Australia, WA, Australia.

Statement of Contribution

This thesis has been developed in the format of thesis by publication. Chapters four, five, six, seven and eight within this thesis have been published in scientific journals. These chapters represent collaborative works.

O. H. Ahmed, M. Altarawneh, Z.-T. Jiang, M. Al-Harahsheh, B.Z. Dlugogorski, Reactions of products from thermal degradation of PVC with nanoclusters of α-Fe$_2$O$_3$ (hematite), *Chem. Eng. J.*, 323 (**2017**) 396-405.

Author's Name	Contribution	Overall Percentage (%)	Signature
O. H. Ahmed	Computational modelling, data collection and analysis, writing the manuscript and revision	70	
M. Altarawneh	Discussions, manuscript preparation and revision		
Z.-T. Jiang	Discussions and manuscript preparation	30	
M. Al-Harahsheh	Manuscript preparation		
B.Z. Dlugogorski	Manuscript preparation		

O. H. Ahmed, M. Altarawneh, M. Al-Harahsheh, Z.-T. Jiang, B.Z. Dlugogorski, Recycling of zincite (ZnO) via uptake of hydrogen halides, *Phys. Chem. Chem. Phys.*, 20 (**2018**) 1221-1230.

Author's Name	Contribution	Overall Percentage (%)	Signature
O. H. Ahmed	Computational modelling, data collection and analysis, writing the manuscript and revision	70	
M. Altarawneh	Discussions, manuscript preparation and revision		
M. Al-Harahsheh	Manuscript preparation	30	
Z.-T. Jiang	Discussions and manuscript preparation		
B.Z. Dlugogorski	Manuscript preparation		

O. H. Ahmed, M. Altarawneh, M. Al-Harahsheh, Z.-T. Jiang, B.Z. Dlugogorski, Catalytic dechlorination of products from PVC degradation by magnetite (Fe_3O_4), *Appl. Surf. Sci.*, 480 (**2019**) 792-801.

Author's Name	Contribution	Overall Percentage (%)	Signature
O. H. Ahmed	Computational modelling, data collection and analysis, writing the manuscript and revision	70	
M. Altarawneh	Discussions, manuscript preparation and revision	30	
M. Al-Harahsheh	Manuscript preparation		
Z.-T. Jiang	Discussions and manuscript preparation		
B.Z. Dlugogorski	Manuscript preparation		

O. H. Ahmed, M. Altarawneh, M. Al-Harahsheh, Z.-T. Jiang, B.Z. Dlugogorski, Catalytic dehalogenation of alkyl halides by copper surfaces, *J. Environ. Chem. Eng.*, 6 (**2018**) 7214-7224.

Author's Name	Contribution	Overall Percentage (%)	Signature
O. H. Ahmed	Computational modelling, data collection and analysis, writing the manuscript and revision	70	
M. Altarawneh	Discussions, manuscript preparation and revision	30	
M. Al-Harahsheh	Manuscript preparation		
Z.-T. Jiang	Discussions and manuscript preparation		
B.Z. Dlugogorski	Manuscript preparation		

O. H. Ahmed, M. Altarawneh, M. Al-Harahsheh, Z.-T. Jiang, B.Z. Dlugogorski, Formation of phenoxy-type environmental persistent free radicals (EPFRs) from dissociative adsorption of phenol on Cu/Fe and their partial oxides, *Chemosphere*, 240 (**2020**) 124921.

Author's Name	Contribution	Overall Percentage (%)	Signature
O. H. Ahmed	Computational modelling, data collection and analysis, writing the manuscript and revision	70	
M. Altarawneh	Discussions, manuscript preparation and revision		
M. Al-Harahsheh	Manuscript preparation	30	
Z.-T. Jiang	Discussions and manuscript preparation		
B.Z. Dlugogorski	Manuscript preparation		

Glossary of Abbreviations and Technical Terms

AED   Atomic emission detector

AES   Anger electron spectroscopy

BDE   Bond dissociation energy

BFRs   Brominated flame retardants

BO   Born−Oppenheimer

BSSE   Basis set superposition error

CI-NEB   Climbing image-nudged elastic band

DDE   Decabromo diphenyl ethane

DFT   Density functional theory

DNP   Double-polarised numeric basis set

DOS   Density of state

DRIFT   Diffuse reflectance infrared fourier transform spectroscopy

DSC   Deferential Scanning Calorimetry

EAFD   Electric arc furnace dust

EPA   Environmental protection authority

EPFRs   Environmental persistent free radicals

EPR   Electron paramagnetic resonance

ER   Eley–Rideal

EU	European Union
FR	Flame retardant
FS	Final state
GC/MS	Gas chromatography–mass spectrometry
GGA	Generalized Gradient Approximation
HBCD	Hexabromocyclododecane
HCB	Hexachlorobenzene
HF	Hartree-Fock
HR-AES	High-resolution Auger electrons spectroscopy
HREELS	High-resolution electron energy loss
ICP	Inductively coupled plasma
IR	Infrared spectroscopy
IS	Initial state
LDA	Local density approximation
LEED	Low-energy electron diffraction
LH	Langmuir-Hinshelwood mechanism
LST/QST	Linear synchronous and Quadratic synchronous transit approaches
NBFRs	Novel brominated flame retardants
o-SQ	o-semiquinone

PAW	projector augmented wave
PBBs	Polybrominated biphenyls
PBDD/Fs	Polybrominated dibenzo-*p*-dioxins and dibenzofurans
PBDEs	Polybrominated diphenyl ethers
PBE	Perdew-Burke-Ernzerhof functional
PCDD/Fs	Polychlorinated dibenzo-*p*-dioxin and dibenzofurans
PDOS	Projected density of states
PE	Polyethylene
PEFR	Persistent free environmental radical
PES	Potential energy surfaces
PET	Polyethylene terephthalate
PP	Polypropylene
PS	Polystyrene
PVC	Polyvinyl chloride
PW	Perdew-Wang
PXDD/Fs	Mixed polychlorinated/brominated dibenzo-*p*-dioxins and dibenzofurans
RMM-DIIS	Residual minimization with direct inversion of the iterative subspace
SEM	Scanning electron microscopy
SFM	Scanning force microscopy

TBBPA	Tetrabromobisphenol A
TGA	Thermogravimetric analysis
TG-MS	Thermogravimetric–mass spectrometry
TISE	Time-independent Schrödinger equation
TPR	Temperature-programmed reaction
TS	Transition state
TST	Transition state theory
VASP	Vienna Ab initio simulation package
XANES	X-ray absorption
XPS	X-ray photoelectron spectroscopy
XRD	X-ray powder diffraction

List of Figures

List of Tables

Chapter 1

Introduction and Overview

1.1. General Overture

Halogenated flame retardants (HFRs) are a wide group of commercial chemicals (particularly, chlorinated and brominated flame retardants) that are applied to many consumer products to improve their fire resistance [1, 2]. Chlorinated and brominated flame retardants are just like a pair of twins, albeit with different characteristics, that are utilized in a wide range of indoor and outdoor objects such as furniture, plastics, and electronic and electrical equipment [1]. The association of increasing consumption of HFRs with the accumulation of high volumes of halogenated organic waste imposes serious environmental and public health concerns despite their high energy content [3-5]. Disposal of this waste through thermal processes such as incineration and thermal pyrolysis is a truly daunting task as it often includes high-temperature processes inside well-enclosed combustion chambers [6]. In addition, the formation of harmful halogenated organic pollutants, most notably polychlorinated dibenzo-p-dioxins and furan (PCDD/Fs) and their brominated counterparts, produced during thermal-based recycling processes, has the potential for harmful environmental and health consequences [7, 8].

Integration of pyrolysis with catalytic upgrading has emerged as a viable alternative strategy for the commonly utilized high-temperature combustion based on two compelling grounds: (i) to minimize environmental pollution and (ii) to maximize resource recovery [9]. Nevertheless, commonly used catalysts in these methods such as sodium hydroxide, treated red mud and zeolites usually results in the formation of considerable quantities of coke and afford a rather lower selectivity in the generation of the valuable single aromatic compounds [10, 11], which is a major drawback of the available thermal/catalytic recycling technique. Hence, there is a need to examine the performance of other economical — yet efficient — catalysts on a large scale. Co-pyrolysis of halogenated organic waste with electric arc furnace dust (EAFD) now represents a focal abatement strategy of the title two categories of waste materials on an

industrial scale. Experimental results from different groups have demonstrated an effective performance of EAFD in generating halogen-free hydrocarbon feedstock from thermal recycling of halogenated plastics wastes, due to its high content of metallic oxides [12, 13].

Quantum mechanical simulations and computational modelling by using accurate density functional theory (DFT) calculations have had an unparalleled influence in providing an insightful understanding of challenging problems pertinent to the chemistry of materials and their chemical reactivity. The research being reported in this present thesis employed DFT calculations to thoroughly investigate the modelling structures of transition metals and their oxides in their dual role of the catalytic de-halogenation of halogen-containing solid wastes and their mediating generation of notorious dioxins compounds and phenoxy-type environmental persistent free radicals (EPFRs).

1.2. Thesis Objectives

The purpose of this thesis is to present the findings of research to design more efficient catalysts and to optimize currently deployed procedures. The thesis will provide atomic-base insight into the detailed reaction pathways and to identify the key elementary steps that dictate the reaction rates. The dissertation fulfils the following objectives:

1. Mapping out reaction corridors leading to halogenation of metal oxides (namely Fe_2O_3, ZnO and Fe_3O_4), an important chemical phenomenon in the chemical recycling of the metal oxides content in the EAFD.

2. Identifying and investigating the elementary steps that govern the degradation of multiple halogenated hydrocarbons over a copper surface. This, in turn, will provide an atomic-based insight into mechanistic and thermo-kinetic aspects that might not be easily acquired by explicating the experimental measurements alone.

3. Investigating reaction mechanisms and energy barriers for the formation of phenoxy-type EPFRs over surfaces of pure Cu(100) and Fe(100) and their oxygen-covered configurations. The prime focus is to contrast the catalytic capacity of the aforementioned reactions of the title reaction with analogue values reported in the literature for transition metal oxides.

1.3. Thesis Structure

Figure 1.1 presents the structure of the thesis which is arranged as follows.

Chapter 2 reviews the relevant available literature on: 1) the formation mechanism of EAFD with a principal focus on its chemical structure, 2) the thermal decomposition of halogenated flame retardants, and 3) the most commonly used methods to treat and recycle those wastes. The chapter:

    (a) Briefly summarises the industrial synthesis of EAFD

    (b) Presents the main mechanisms for dust formation

    (c) Reports the chemical structure of EAFD and identifies its main mineral phases

    (d) Summarizes the chemical structure of polyvinyl chloride (PVC) and brominated flame retardants (BFRs)

    (e) Summarizes previous studies relevant to the treatment of two hazardous wastes (EAFD and halogenated flame retardants, mainly PVC and BFRs plastic wastes)

(f) Presents the most effective technique for processing those two types of waste to obtain the highly valuable resources of all elements, taking into account the environmental impact of the toxic components that are anticipated to form.

Chapter 3 summarizes the theoretical background of the computational techniques employed within the scope of this study as well as concepts behind the deployed quantum chemical processes along with a brief summary of the basic concepts of *ab initio* atomistic thermodynamics and density function theory (DFT) approaches. This chapter also presents a brief description on the computer software utilized within the scope of this study.

Chapter 4 reports a theoretical investigation into the reaction of HCl and selected chlorinated hydrocarbons, with α-Fe$_2$O$_3$ as a model compound for metal oxides in EAFD. Throughout the discussion the difference in activation energies among the two halogenated systems is pointed out. This chapter maps reaction networks operating during the interaction of a cluster model of dehydrated α-Fe$_2$O$_3$ with both HCl and major products from the degradation of PVC. Findings can help to understand, on a precise molecular basis, the mechanisms of chlorine fixation on transitional metal oxides in the form of metal chlorides. Such knowledge finds direct application in the pursuit to design effective and viable recycling technologies for halogenated waste steam.

Chapter 5 provides a systematic theoretical thermal-kinetic study to investigate chemical interplay between HCl/HBr and zincite surfaces, as a representative model for structures of zinc oxides in EAFD by using different sets of functionals, unit cell size and energy cut-off. Geometric and electronic properties of bulk and surfaces ZnO are introduced. The chapter compares computed conversion of ZnO into zinc chlorides and bromides into ZnO versus data

extracted from a weight loss curve for the ZnO + HCl system. It is hoped that thermo-kinetic and mechanistic aspects pertinent to HCl/HBr uptake by ZnO surfaces can assist in the design of a large-scale catalytic upgrading unit that operates to extract the valuable zinc loads from EAFD.

Chapter 6 reports a comprehensive computational study of the initial reactions between $(Fe_3O_4)(111)$ surface and selected chlorinated hydrocarbons. The geometric, structure and electronic properties of the bulk and the clean (Fe_3O_4) (111) surface are first discussed. That is followed by a comparison of the catalytic effect of both Fe_{oct2} and Fe_{tet1} terminated magnetite (111) surface toward dissociative adsorption of HCl molecule. Finally, we provide a significant insight into the possible interaction pathways of the selected chlorinated hydrocarbons over magnetite (111) surface. Results reported in this chapter shall be instrumental in efforts aiming to optimize a unit operation for the concurrent treatment of the title two categories of waste materials; i.e., EAFD and PVC.

Chapter 7 introduces a comprehensive density functional (DFT) study into the mechanistic steps and kinetic factors dictating fission of Br/Cl-C bond in a selected group of halogenated compounds. The first part of this chapter benchmarks calculated parameters for bulk and copper surface with analogous experimental and other calculated values. This is followed by a survey of energy requirements for the fission of Cl/Br-C bonds in the title compounds (2-chloropropane, chloromethane, chloroethyne, chloropropene, chlorobenzene, and their brominated counterparts). Finally, we present Arrhenius parameters for the bond scission reactions. It is hoped that findings from the study in this chapter can provide an insight into chemical phenomena operating in the recycling the polymeric fraction of e-waste and other severely halogenated fuels.

Chapter 8 investigates reaction mechanisms and energy barriers for the formation of phenoxy-type EPFRs over surfaces of pure Cu(100) and Fe(100) and their oxygen-covered configurations. The prime focus is to contrast the catalytic capacity of the aforementioned reactions of the title reaction with analogue values reported in the literature for transition metal oxides. Kinetics parameters are provided for all investigated reactions. It is hoped that results of the study reported in this chapter will be useful in the continuous pursuit to understand the transformation chemistry of phenol $\rightarrow$ phenoxy-type EPFRs.

Chapter 9 makes concluding remarks and presents recommendations for future research.

Catalytic De-halogenation of Halogen-containing Solid Wastes by Nanostructures of Transition Metals and Their Oxide Configurations

Chapter 1

Introduction and Overview
➤ General Overture   ➤ Thesis Objectives   ➤ Thesis Structure

Chapter 2

Literature Review
➤ Electric Arc Furnace Dust   ➤ Polyvinyl Chloride   ➤ Brominated Flame Retardants

Chapter 3

Theoretical Background
➤ Transition State Theory   ➤ Density Function Theory   ➤ VASP, DMol³, Phonopy

Objective 1   **Objective 2**   **Objective 3**

Chapter 4

Reactions of products from thermal degradation of PVC with nanoclusters of α-Fe₂O₃ (hematite)
➤ Investigates the reaction of a cluster model of α-Fe₂O₃ with a wide range of chlorinated alkanes, alkenes and aromatics.

Chapter 5

Recycling of zincite (ZnO) via uptake of hydrogen halides
➤ Examines geometric and electronic properties of bulk and surfaces ZnO
➤ Explores reaction pathways of HCl/Br over a ZnO surfaces

Chapter 6

Catalytic De-chlorination of Products from PVC degradation by Magnetite (Fe₃O₄)
➤ Discusses the geometric and structure properties of the bulk and the clean (Fe₃O₄) surface.
➤ Interaction pathways of the selected chlorinated hydrocarbons over magnetite

Chapter 7

Catalytic De-halogenation of Alkyl Halides by Copper Surfaces
➤ Surveys energy requirements for the fission of Cl/Br-C bonds of alkyl halides
➤ Presents Arrhenius parameters for their bond scission reactions

Chapter 8

Formation of Phenoxy-type Environmental Persistent Free Radicals (EPFRs) from Dissociative Adsorption of Phenol on Cu/Fe and their Partial Oxides
➤Investigates reaction mechanisms and energy barriers for the formation of phenoxy-type EPFRs

Chapter 9

Conclusions and Recommendations
➤ Main concluding remarks of the thesis   ➤ Outlooks and recommendations for the future direction

Figure 1.1. Thesis structure.

Chapter 2

Literature Review

2.1. Introduction

Chlorinated and brominated flame retardants or so-called halogenated flame retardants (HFRs) include a diverse group of anthropogenic chemicals (namely, organochlorine and organobromine compounds) that have been widely employed to slow or prevent the ignition. The purpose of deploying these materials is to improve the fire resistance features of treated objects in order to meet flame retardant criteria as defined by fire safety codes [2, 3, 14-17]. HFRs show considerable potential for delaying combustion by releasing halogen atoms that capture hydroxyl radicals from the gradually established ignition medium. HFRs are extensively deployed in myriad industrial and commercial applications such as textiles, mattresses, furniture, plastic, baby products and electronic and electrical equipment [2, 18-20]. However, because of their persistence and their widespread utilization, brominated and chlorinated flame retardants are distributed all over the world and can be found even in remote areas where they had never been employed [3, 21]. This, in turn, has accumulated a massive amount of halogenated organic compound wastes in the environment. Incomplete combustion of these halogenated organic wastes often results in the formation of notably large fractions of hazardous halogenated hydrocarbons compounds including polychlorinated dibenzo-p-dioxins and furan (PCDD/Fs) and their brominated counterparts (PBDD/Fs) [7, 8, 22-24]. PCDD/Fs along with their brominated counterparts migrate into the environment from nearly all thermal processes such as heated materials, uncontrolled fires, waste recycling processes and municipal waste incinerators, etc [25, 26]. As a result, the continuing release of halogenated organic wastes poses a significant concern, not only on the environment but also on public health [27, 28].

Landfill and open burning processes are largely considered to be the most common — as well as widely used — processes to deal with the incremental volume of halogenated organic waste

[29, 30]. A great deal of research has been undertaken to explore sustainable and more efficient recycling technology [6, 11, 31, 32] to overcome drawbacks of landfill and open burning, such as loss of high chemical value and high energy density of the organic matter in halogenated wastes, a reduction of landfill capacity, high equipment costs and release of hazardous compounds. Recently, energy recovery processes such as catalytic pyrolysis are receiving more attention as a mainstream approach for the environmentally safe and economically effective disposal of the polymeric constitutes of halogenated organic wastes [33-35]. The presence of appreciable concentrations of metallic content in halogen-containing objects (as in e-waste) was shown to be effective in capturing emitted hydrogen halides during pertinent thermal operations [35-37].

Of all the investigated catalysts, transition metals oxides are potentially effective catalysts for capturing emitted hydrogen halides and reducing the generation of halogenated hydrocarbons from thermolysis of polymeric materials laden with halogenated compounds [38, 39]. Iron and zinc oxides, which are the main constituents of electric arc furnace (EAF) dust [12, 13, 40], have shown a remarkable halogen fixation ability toward hydrogen halides in a complex process that releases water and corresponding metal halides [41].

2.2. Electric Arc Furnace Dust (EAFD)

Steel-making industrial technology, employed by most integrated mills, comprises an electric melting apparatus that uses an electric-arc furnace (EAF) as the principal equipment for melting steel scrap. A variety of gaseous and liquid effluents, and solid wastes, are emitted during various processing steps in the EAF operation. The major contaminants that enter the atmosphere are nitrogen oxides, carbon (II) oxide, organic compounds and solid particles [40, 42-45]. Among those solid wastes, EAFD, which is complicated of recycling in the steel-making plant, is a potentially hazardous metallurgical waste by-product to both human health and environment [43, 46]. In general, both blast furnaces (which produce approximately 70% of steel production worldwide) and EAFs are the main sources for dust formation during steel scrap recycling, steel making carbon and steel making methods. To date, four main industrial processes for the production of crude steel have been patented: elastic blast furnace/basic oxygen furnace, direct reduction, smelting reduction and direct melting of scrap by EAF; the latter has increased in importance over the last two decades [42, 47]. During the last two decades, the global output of crude steel via electric arc furnace technology has substantially increased from ~30% to ~40% with a projected increase of another 10% by 2030 [48]. In 1980, 1990 and 1998 the electric arc furnace method accounted for 23%, 28% and 34% of total global production [42]. Consequently, increasing steel generation through electric arc furnace technology increases the amount of dust. In each tonne of crude steel manufactured, around 15–20 kilograms of dust are collected, creating 4.3–5.7 metric tonnes of hazardous EAFD that requires disposal on a yearly basis worldwide [49, 50].

Formation of EAF dust is a relatively complex process and comprises five main stages, stages as shown in Scheme 2.1 [44, 51].

Furnace charging
- Steel scrap and the additive materials (i.e., coal, lime, etc.) are placed into specific charging containers that are emptied into the furnace.

Melting
- An electric arc is generated among the steel scrap and the graphite electrodes which requires the charge melting and the creation of a steel bath covered by a slag layer, which can be removed by a number of volatile solute elements such as cadmium and lead volatile together with zinc.

Refining
- Phosphorus is separated from the steel bath via interfacial interactions between both the liquid metal and the slag, while injection of oxygen enhances the decarburization reaction with dissolved carbon and bubbles of carbon monoxide are generated. This, in turn, serves to eliminate other dissolved gases.

Slag foaming
- The slag layer transfers the bubbles of carbon monoxide into foam, which can be promoted by adding coal powder.

Casting
- In this step, the liquid steel is cast after control the temperature of the bath and the composition.

Scheme 2.1. Five main steps for formation of EAF dust [44, 51].

In the EAF process, five mechanisms are suggested for the formation of the dust precursor [44, 52-54]. Figure 2.1. displays the schematic representation of the dust formation mechanisms in a typical EAF process.

- Volatilization mechanism, particularly obvious at the hot areas in the arc spot (a) and the oxygen injection spot (a1), but also occur in the CO bubbles.

- Mechanical emission of metal drops as the result of electric-arc blow (b) and of the oxygen injection (b2) on the steel bath.

- Projection of small metal drops by blowing out CO bubbles (c) which are formed through the decarburization of the steel bath.

- Bursting of metal drops (d) as a result of the contact with an oxidizing gaseous phase within the surface.

- Direct fly-off of solid particles (e) through the introduction of powder materials into the furnace (i.e., coal for slag foaming, turned back dust, additions, slag making additions, etc.).
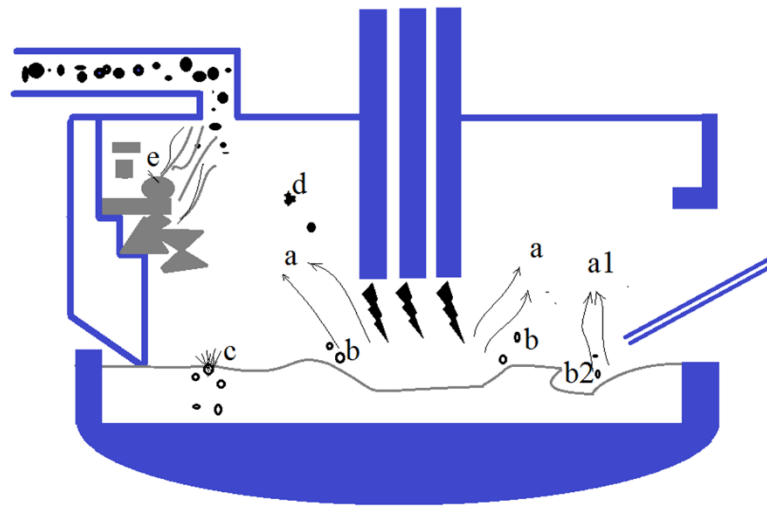
Figure 2.1. Schematic representation of the mechanisms of dust formation in EAF [55].

Among these mechanisms, volatilization and the bursting of the CO bubbles represent the principal mechanisms of dust precursor emission. According to previous experimental quantifications of each mechanism made by numerous authors [52, 56, 57], it is obvious that volatilization mechanism accounted for about 27% of the dust, while 60% of the dust is produced by the bursting of CO bubbles mechanism. The latter formed the dust in an Fe/ air system which is similar to the bursting of CO bubbles mechanism in an H_2O/system [57]. Figure 2.2 displays the percentage of materials produced in the final EAF dust.
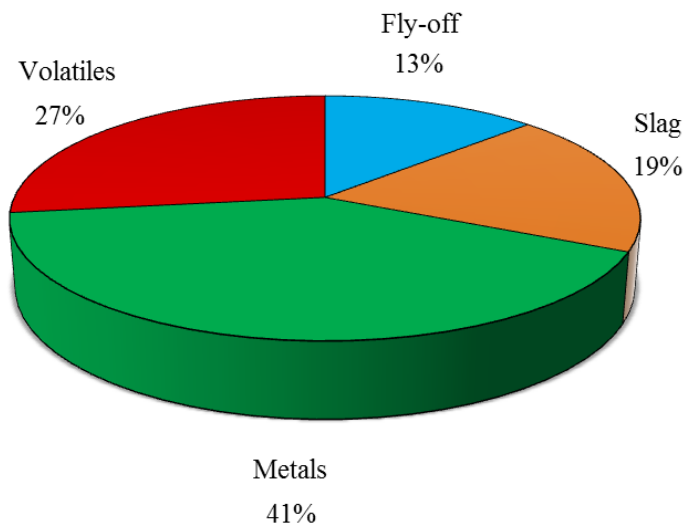
Figure 2.2. Part of volatilization, direct fly-off, metals and slag projections in final EAF dust [54].

Metal contents in EAFD are found either in the form of free oxide or as composite structures of iron oxides conjugated with metals of the spinel type: MFe_2O_4 (M= Zn, Fe, Mn, Ni or Cd) [58-60]. The principal elements of EAFD are zinc and iron followed by calcium, in the form of simple or mixed oxides. This is confirmed by Pickles [61] who found that the calcium represents the third highest metallic component in EAF dust after zinc and iron [61]. These latter two compounds notably lead to franklinite ($ZnFe_2O_4$), zincite (ZnO), hematite (Fe_2O_3), magnetite (Fe_3O_4), wustite (FeO) and may also be present in small concentrations of hydrated zinc chloride. Dust also comprises a small but significant amount of nickel, magnesium, cadmium, manganese, copper, lead and chromium in the form of oxides in addition to halides such as potassium chloride (KCl) and sodium chloride (NaCl) [12, 51, 62, 63]. Table 2.2 lists the content of other components in EAF dust. Although the majority of element species are oxide forms, there are also sulphates, silicates and small amounts of chlorides, fluorides and sulphides [61]. Several laboratory-scale experiments on EAF dust samples using X-ray diffraction, scanning electron microscopy and mass spectrometry found the principal

constituent is franklinite followed by magnetite, which are a strong presence of zinc and iron oxides [64, 65].

However, in recent years the amount of chlorine in the dust has increased because of rising chlore-containing impurities in steel scrap such as paints, rubbers and polymers [40]. Chlorine is known to be involved in the generation of alkaline metal chlorides via thermal degradation of these contaminants by the high temperature of the electric arc furnace steelmaking, and chlorine can form hazardous Cl-compounds either in simple gaseous forms such as Cl_2 and HCl or in a form of notorious pollutants and so-called persistent free environmental radicals (PEFR) [66-69]. Polychlorinated dibenzo-*p*-dioxins (PCDDs), polychlorinated dibenzofurans (PCDFs) and hexachlorobenzene (HCB) represent the most highly hazardous compounds that are emitted during this process [67, 70, 71]. These hazardous Cl-compounds are mainly produced in the process of the electric arc furnace steelmaking via *de novo* synthesis reaction after incineration. It has also been revealed that some existing metal chlorides in the dust can work as catalysts for the synthesis in a low temperature of 573 K [72-74]. To conclude, as chlorine represents the third abundant component in EAF dust after zinc and iron its behaviour is particularly significant and deserves further analysis.

2.3. Physical Characterization of EAFD

The physical properties of EAF dust can be determined based on both the steel species and the smelting technology conditions [75]. Basic physical properties of EAF dusts include: (i) dimensions of particles, (ii) absolute dust density and (iii) grain composition [76]. Determination of the particle size of EAF dust is a fundamental for both the chosen removal equipment and estimating the hazardous of the human organism exposure [76]. EAF dust particles cover a wide range of sizes vary from 0.1 μm to more than 200 μm [54, 77]. Thus,

EAF dust is finer particles and can be easily airborne which indicates the difficulty in separating its contents or its treating by utilizing the traditional physical processes [76]. Absolute dust density can be defined as the absolute density of its particles being identical in terms of crystal structure and chemical composition of the individual components [76]. The density of EAF dust ranges from 1.1 g/cm^3 to more than 2.5 g/cm^3, and its specific surface area is about 4m^2/g [78]. This means that numerous voids exist inside the dust and they in turn occupy great volumes for transportation and storage [75]. While the grain composition of EAF dust represents one of the most important physical properties being a quantitative distribution of its particles regarding their size. This characteristic can be determined by means of a multi-sieve elutriator by appropriately selecting the set of sieves identical to the range of particle dimensions [76]. After sieved the dust samples, the remains on each sieve are scaled and then a respective percentage share is calculated regarding the initial sample weight. Table 2.1 displays some physical properties of EAF dust.

Table 2.1. Some physical properties of EAF dust.

Physical property	Determination value	References
Mean Particle Diameter	10 μm	[40]
	75 μm	[76]
	20 μm	[79]
	3.27 μm	[80]
Density	2.5 g/cm^3	[40]
	3.91 g/cm^3	[78]
	4.93 g/cm^3	[81]
Specific Surface Area	4.01 m^2/g	[82]
Specific Gravity	0.8–5.5	[80, 83]

Table 2-2. Chemical structure wt% of EAFD obtained from various investigations.

Iron	Zinc	Aluminium	Copper	Nickel	Palladium	Cadmium	References
39.20	23.51	0.3	0.34	0.04	4.57	0.01	[84]
37.08	12.20	0.41	0.17	-	1.72	0.01	[85]
35.88	0.77	0.34	-	5.26	0.28	-	[86]
32.0	24.80	1.03	0.02	-	1.84	0.03	[87]
27.23	17.05	-	-	0.0	1.28	0.9	[88]
24.60	19.40	-	0.42	-	4.5	0.1	[89]
22.01	4.11	0.21	-	2.2	0.36	-	[90]

2.4. Chemical Structure of EAFD

EAFD forms as a result of volatile metals that cross into the vapour phase as the producing temperature of the furnace in which they are oxidized is cooled in the extractive air flow. EAF dust can also be defined as a complex form of chocolate-brown particles or as a form of fine powder accompanied by fume gas [91, 92], the latter frequently comprised of various compounds of heavy metallic oxides and some chlorides as well [93]. In general, EAF dust structure depends on both the quality of steel scrap and other process input substances, with the structure becoming quite complex in various scrap types that contain a range of components [94]. In addition to factory-specific parameters, dust production mechanisms interfere in the metal speciation as well. The produced volume of EAF dust is approximately 1–2% (mass fraction) of the scrap charged in a typical smelting furnaces mill [95]. As this production can lead to a considerable amount depending on the mill size, the quantity might also play a

significant role in dust processing [96, 97]. Consequently, EAFD is truly the end outcome of a sequence of chemical and physical phenomena in which the materials give rise to the EAFD pass. The phenomena, which occur over various environments along the gas path, define the physical aspect and mineral and chemical composition of the newly produced dust [40]. The significant point of identifying the chemical composition of the dust lies in the control or reduction of the respective issues that might be encountered through processing these substances or can help to expect the results. Once the dust is collected in the baghouse, it is of importance to analyse it for its chemical forms and mineralogical structures.

Mineralogical structure and grain morphology of EAF dust is investigated by various laboratory techniques such as the combination of high-resolution Auger electrons spectroscopy (HR AES), X-ray photoelectron spectroscopy (XPS) and scanning electron microscopy (SEM) coupled with energy dispersive X-ray [67, 93, 98, 99]. Based on those techniques, the sizes of EAF dust particles can be characterized as three morphological kinds [42, 44]. The first morphological type is in the form of sphere-like particles whose sizes are less than 20 μm. The second type involves lime and coal particles which can be in the form of an irregular spheroid of the medium size in the range of (20–500 μm). The last type is likely generated by low-temperature agglomeration, which is fragile and breaks up easily. Their sizes vary between 20 and 1000 μm [44, 79].

The produced dust is opulent in metallic oxides that can be used as secondary feedstock in the generation of valuable metals such as zinc, iron, lead and precious other metals [50, 100]. The average concentrations of both zinc and iron in dust vary in the range of 2–46% and 10–45% with an average production amount of 0.86–1.14 and 1.33–1.77 metric tonnes per year, respectively [12, 55, 101]. In fact, EAF dust bearing zinc and iron metals present various forms

of oxide compounds that can be extracted from franklinite ($ZnFe_2O_4$) [40, 102]. Zinc can exist in two main phases: zinc oxide (ZnO) and zinc ferrite ($ZnFe_2O_4$). Approximately 50–80% of the zinc from EAF dust is in the form of ZnO, the remainder associated with iron oxide, resulting in the form of $ZnFe_2O_4$ [103]. In addition to franklinite, iron can mostly present in the form of magnetite, Fe_3O_4. This dust also contains other metals such as lead (4–9%), manganese (1–1.5%), silicon (1–1.5%), copper (0.1–0.5%) and cadmium (0.1–0.3%) [89, 104, 105]. Table 2.3 and Figure 2.3 present mineral phases for elements encountered in the EAF dust and their crystalline structures, respectively.

Table 2-3. Some identified mineral phases for different elements encountered in the EAFD.

Element	Identified mineral phases	References
Zinc	ZnO, $ZnFe_2O_4$, $ZnCl_2$	[67, 106]
Iron	Fe_2O_3, Fe_3O_4, $ZnFe_2O_4$, $MgFe_2O_4$, Fe-Ni, Fe-Cr alloy	[106, 107]
Aluminium	$Al_2O.SiO_2$, Al_2O_3, $Al_2O.2SiO_2.2H_2O$	[42]
Nickel	Ni-Fe alloy, Ni-Cr-Fe,	[108]
Sulfide	FeS, S, Ni_7S_6;NiS_2,	[42]
Cadmium	CaF_2, $Ca(OH)_2$, $3CaO.2SiO_2$, CaO, $CaCO_3$	[106, 107]
Magnesium	MgO, $MgFe_2O_4$, Mg_3O_4, Mg_2SiO_4	[106, 109]
Lead	$PbCl_2$, PbO, $PbO.PbSO_4$, $PbSO_3$/$PbSO_4$	[42, 110]

In view of the above, the products contain high purity and crude zinc oxides, pig iron, and other more stable deposits. When zinc and iron is extracted from EAF dust and returned to the economic cycle, there will be a saving in the energy required for the production of these metals from their natural ores and greater protection of natural resources [92, 105]. Therefore, EAF

dust is of high economic importance as a secondary source of Zn and Fe in the steel making

processes and when using an economical method to separate the EAF dust metals mixture.
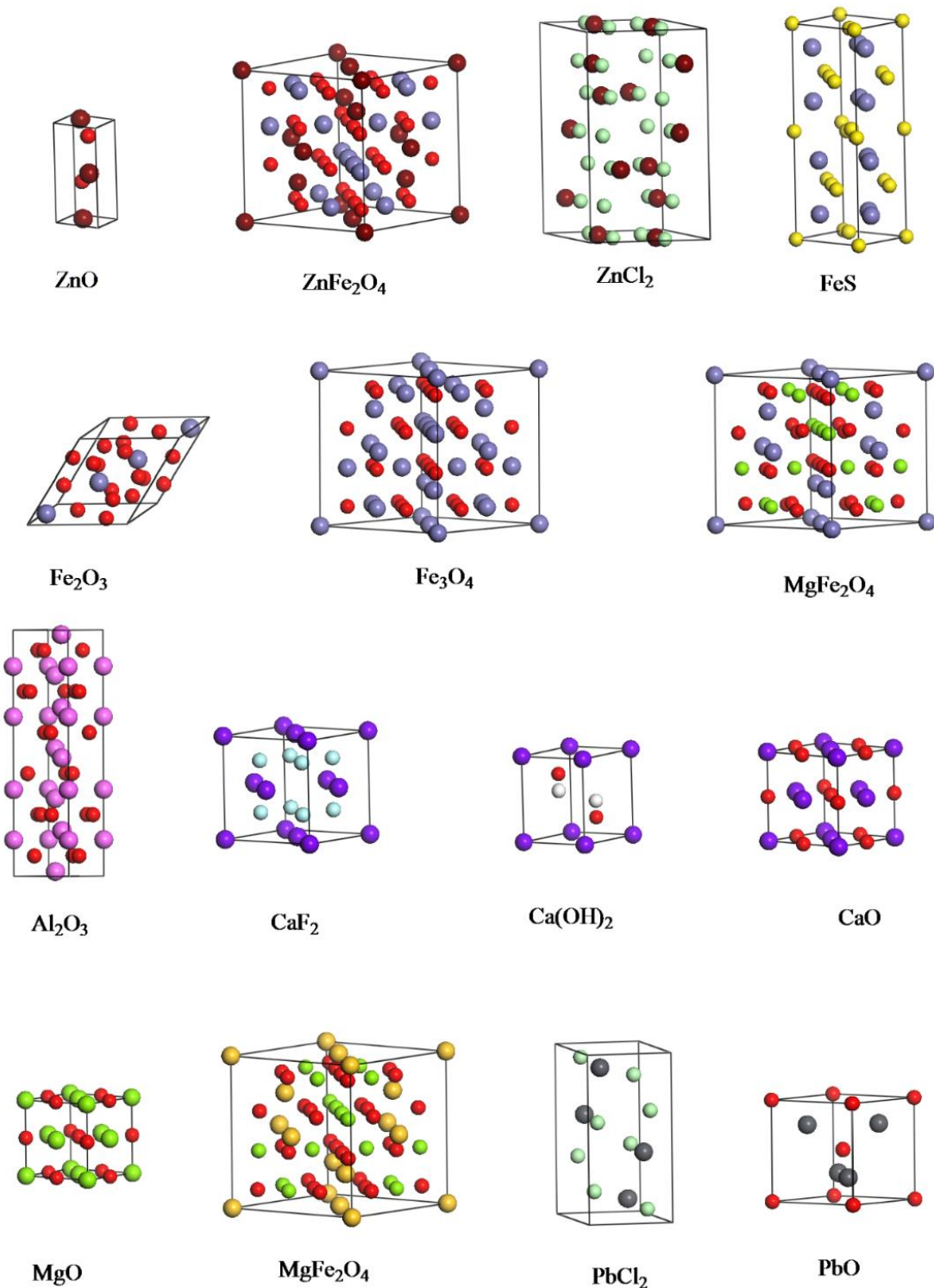
Figure 2.3. The typical crystalline structures of the mineral phases for various elements in the EAFD.

.

2.5. Polyvinyl Chloride (PVC)

Polyvinyl chloride (PVC) represents one of the most commonly employed polymers in piping systems, thermoplastics and many other household and industrial applications [111-113]. Among the thermoplastic industries, it ranks third in the volume of worldwide production, following polyethylene and polypropylene [114, 115]. The polar nature of PVC because of the Cl atom in its repeat unit allows it to be a compound that can be added to a wide range of rigid and flexible products, more than any other polymer [116, 117]. This is the major factor responsible for the versatile application of PVC [118, 119]. Moreover, because of its virtues of acid and alkali resistance, mechanical strength, chemical performance stabilization and cost-effectiveness, PVC has become a universal polymer utilized into wide ranges of short and long-life products such as wrapping materials, shopping and garbage bags, packaging films, clothing, toys, fluid containers, cable insulation, window frames, floors coverings, roofing sheets, etc. [119-122]. The demand for this polymer has grown steadily over the last few decades with all global major markets registering a positive increase in demand and production, specifically in the Eurozone. The predicted world market demand for PVC in 2015 was more than 43 Mt/Y in contrast to the recorded production of 36 Mt/Y in 2011, of which close to 5.5 Mt was consumed in Europe alone [114, 123]. This trend is expected to increase by 3.2% annually in the future [6, 124]. According to the United Nations Environmental Program, 22–43% of the thermoplastics utilized globally is wasted. Figure 2.4 shows the regional distribution of global PVC production.
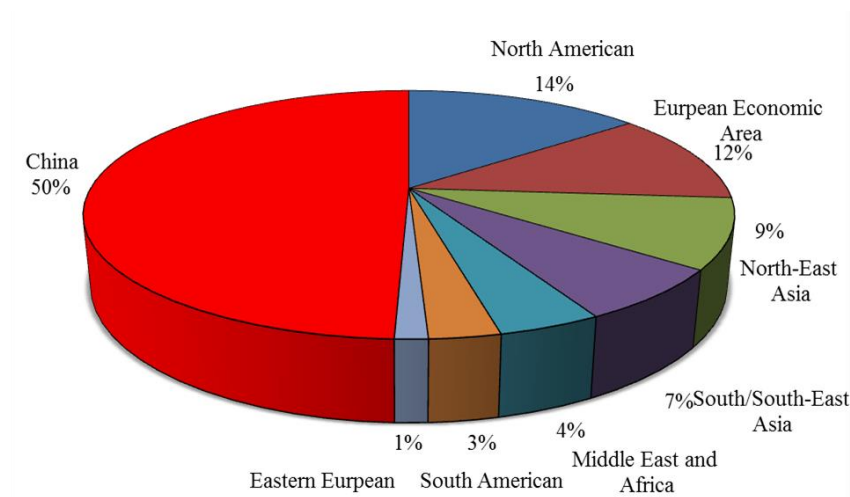
Figure 2.4. World distribution of PVC plastic production in 2016 [6].

.

Due to their relatively long life-cycles, there is a long term time-lag between the consumption and accumulation of PVC waste (~50 years), a gigantic and undesirable volume of waste accumulates at the end of their life cycles globally [118, 122, 125]. The matter of finding an effective and safe disposal method for this waste has increasing gained importance in public discussion. Landfill and open burning methods have been the most common and widely used processes to deal with the profusion of PVC-containing waste in past decades, but these methods are now considered undesirable and do not comply with regulations enacted by the Environmental Protection Authority (EPA) [112, 126-128]. For example, the European Union (EU) has established a series of regulations and legislations to reduce the amount of landfilled or incinerated wastes [129]. Incomplete combustion of PVC products leads to the generation of notorious polychlorinated dibenzo-*p*-dioxins and furan (PCDD/Fs), which has triggered a great deal of research to pioneer alternative methods to deal with the ever increasing amount of PVC wastes [130].

In the past two decades the formation mechanism of PCDD/Fs during combustion processes has been closely examined in laboratory studies under different conditions of combustion [131-

133]. PCDD/Fs are formed through homogeneous and heterogeneous pathways [134]. The homogeneous pathway involves the interaction of structurally related precursors in the gas phase at temperatures between 400 K and 800 K [135, 136]. The heterogeneous route involves two pathways. The first is the so-called de novo synthesis during the burning of a carbonaceous matrix with simultaneous chlorination and oxidation in a temperature range of 200–400 K in the presence of oxygen. The second route occurs in the same temperature range as the first but through catalytic-assisted coupling of precursors [131, 137]. Toxicological profiles of these compounds depend principally on the number and position of chlorine atoms on the two benzene rings [132, 136]. Figure 2.5 depicts the chemical structures of PCDD/Fs compounds.

Polychlorinated dibenzodioxins (PCDDs)

Polychlorinated dibenzofuran (PCDFs)
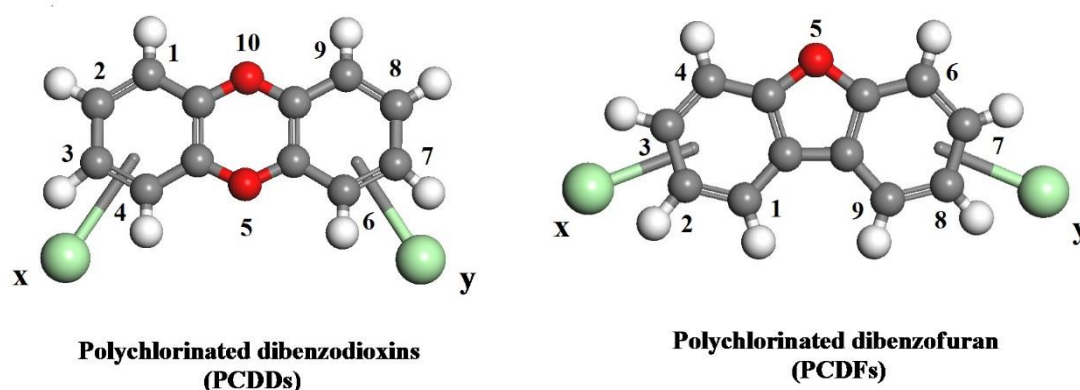
Figure 2.5. General structure formula of polychlorinated dibenzo-*p*-dioxins (PCDDs) and dibenzofurans (PCDFs). The position of chlorine atoms and the possible number results in 75 different isomers in PCDD congeners and 135 in PCDF congeners (x = 1-4 while y = 0-4) [138].

.

The consensus in the literature is that recycling of the PVC is the most environmentally friendly and economic alternative to recover energy [139-141]. Numerous studies have discussed examples to evaluate the feasibility of recycling process. They found the properties of the PVC profile are not affected when virgin PVC polymer is replaced by recycled polymer [142-144]. The studies concluded that recycled PVC waste can be successfully reused in a variety of

products including pipes, bottles, pipe fittings and other forms, retaining excellent features for performance and appearance. On the other hand, Al-Salem et al. [145] and Wu et al. [146] strongly recommended that contaminant waste plastics not be redeployed in food packaging applications owing to serious health issues. Because it is suitable for all recycling methods, PVC waste is currently among the highest recycled waste in developed countries, particularly in the United States and European countries.

In recent years three main methods have emerged for recycling and treating PVC-plastic waste: energy-recovery (incineration and pyrolysis), mechanical and chemical techniques [145, 147-149]. Energy-recovery can treat PVC waste that comprises a large volume of impurities and combustible solids [139, 141]. This method involves taking advantage of the high energy value of PVC wastes by incineration, but problems occur with poor or incomplete burning of PVC waste, such as health and environmental damage because of the release of large amounts of hydrogen chloride and other toxic products, including dioxins and acid gases [9, 150, 151].

Mechanical recycling or so-called "material recycling" is a technically relatively simple recycling method by reinserting clean PVC waste in a new product with nearly the same performance level as the original product [112, 118]. This method entails separation, grinding and feeding of ground product into conversion machines, with no change in inherent properties of the PVC-material. Mechanical recycling processes can be preferable and attractive when there is a sufficient stream of single homogenous waste separated at source [152, 153]. For example, approximately 1.4 Mt of pre- and post-consumer PVC waste was recycled in 2010 through the mechanical process [118]. On the other hand, this method of treatment remains economically unacceptable because of costly corrosion problems associated with hydrochloric acid and chlorine emission from PVC-waste. In addition to these economic constraints, the

lack of homogeneity in PVC wastes presents a major problem for mechanical recycling of used plastics as well [9, 145, 154].

The third method is chemical or feedstock treatment, which has become an economically feasible and environmentally friendly technology for PVC plastics recycling. This method, which includes various techniques such as pyrolysis, hydrothermal processing and catalytic pyrolysis, involves the conversion of PVC polymer into shorter-chains (low molecular weights) based on the idea of cracking polymer waste into the primary chemicals. The obtained products generally appear in the form of liquid or gas with a high purity grade, which can be purified and reused in polymerization or petrochemical processes to provide either the same or a related polymer. This process can be suitable to deal with mixed plastics waste from various sources and is considered as a significant end-of-life cycle for PVC treatment.

Table 2-4. Main differences between the three main methods of PVC waste recycling [122].

Recycling methods	Pollution formation	Costs	Recycled product	Feature of the recycled product
Landfill	Very high	Low cost	No recycled materials	-
Open burning	Very high	Low cost	Energy	Generally, energetically not efficient
Mechanical process	Low	Middle cost	PVC	Depends on the feedstock materials and methods variable of recycling
Chemical process	Usually low	High cost	Diverse row materials	Depends on the feedstock materials and methods variable of recycling

2.6. Brominated Flame Retardants (BFRs)

Flame retardants (FRs) are frequently utilized in many combustible materials in order to retard ignition and to achieve fire safety requirements [17, 155, 156]. The principal criteria for the running of any compound as a flame retardant are compatibility with the polymer and stability during the lifetime of the product. As a result, there are more than 175 types of FRs for commercial use such as phosphorus compounds (e.g., phosphine oxides, organophosphates and red phosphorus), inorganic salts (e.g., aluminium hydroxide, antimony trioxide, and borate), nitrogen-based compounds (e.g., melamine derivatives and melamine) and halogenated organic compounds (e.g., chlorinated paraffin and alicyclic compounds, and brominated aromatic compounds) [157-159]. With lower decomposing temperature and higher trapping efficiency, organobromine compounds have become more popular and frequently applied as a flame retardant in comparison with other FRs types. At least 75 FRs are brominated flame retardants (BFRs), each of which has specific features and toxicological performance [17, 160]. BFRs can be defined as a wide group of bromine-containing organic compounds which are incorporated into polymeric materials of consumer products such as electrical and electronic equipment, construction materials, furniture, textiles and upholstery, vehicles and various commercial plastic products to enhance their fire resistance [17, 21, 161, 162]. Based on their wide usages and mode of incorporation into the polymers, BFRs can be categorized into three subgroups: brominated monomer, additive and reactive components [17, 163]. A brominated monomer is applied in the generation of brominated polymers, which are then introduced into the feed blend prior to polymerization or mixed with non-halogenated polymers. Additive BFRs are incorporated into the mass of materials or polymers and reactive BFRs are blended covalently to the chemical structure of the polymers. Therefore, additive BFRs do not chemically bond strongly to the matrix in which they are more likely to release or leach from the substrate through their lifespans [163, 164].

BFRs are used to prevent/delay the inset of ignition in treated materials through emitting Br atoms, which are effective in capturing the hydroxyl radicals, primarily produced from the progressively established burning environment [17, 155]. This, therefore, eliminates the capability of the flame to propagate. The global market demand for these chemicals has increased steadily with all major markets recording positive growth in production and demand. For example, in 2000 approximately 310,000 metric tonnes of BFRs were demanded worldwide [17], growing to over 690,000 tonnes in 2008, which represents a growth of over 100% over less than one decade [3].

Polybrominated diphenyl ethers (PBDEs) and polybrominated biphenyls (PBBs) have been among the most widely used chemicals and attracted great interest as BFRs during the past decade [155, 165]. However, those two types of BFRs were voluntarily withdrawn or banned globally because of their adverse effects not only on the environment but also on the health of living organisms and human beings [166]. Bans for producing and utilizing PBDEs and PBBs have resulted in all major markets moving toward the use of alternative BFRs (specifically, hexabromocyclododecane (HBCD) and tetrabromobisphenol A (TBBPA)). The latter represents the most extensively employed BFRs as it has been deemed a substitute for certain polybrominated diphenyl ethers, with a global market production more than 170,000 metric tonnes in 2004, which is approximately 60% of BFRs production [156, 163]. Figure 2.6 illustrates the chemical structures of the four brominated flame retardants. With the current high growth rate in both production and concomitant expanding inventory, significant volumes of TBBPA can be released into the environment in the foreseeable future [156]. In Figure 2.7, the main products formed by the degradation of TBBA are illustrated.
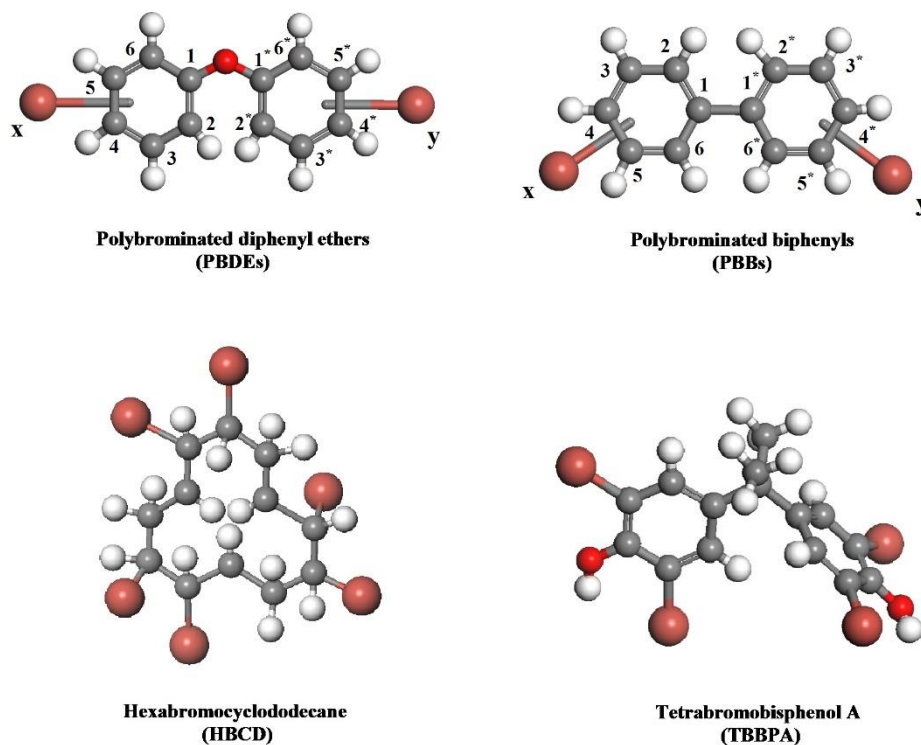
Figure 2.6. Chemical structure of the four brominated flame retardants (PBDEs, PBBs, HBCD, TBBPA) [166].
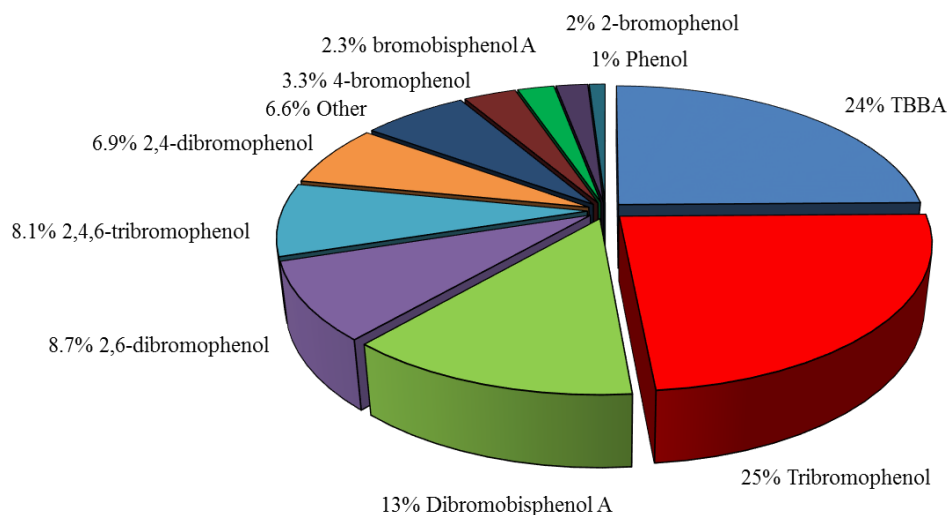
Figure 2.7. Weight % yields of main products formed through the degradation of TBBA at a constant heating rate of 10 °C/min [167].

BFRs are globally distributed through the environment in a variety of ways, such as car interiors, workplaces, emissions during manufacture, waste disposal, volatilization or dust

formation through the utilization of treated products in homes, and during recycling of BFR-containing objects [168-171]. Consequently, they have been found in biota such as birds, fish and mammals (including humans), and the environment such as water, air, lakes and soil [163, 172-174].

This pervasive environmental distribution of BFRs has been a subject of concern that stems from reported adverse effects created by some BFRs on the environment and human health [162, 175, 176]. BFRs are the main source of bromine in Br-containing dioxins and furans and can act as potent precursors for the generation of PBDD/Fs and PXDD/Fs [177-179]. The toxic emissions could be formed throughout the entire lifecycle of BFRs products: production, pyrolysis, recycling and uncontrolled fire and combustion. PBDD/Fs and PXDD/Fs refer to a group of 75 PBDDs and 135 PBDFs the same species as for their chlorinated analogous [177]. PBDD/Fs have physical-chemical characteristics similar to those of PCDD/Fs, although they might be low volatile and bind more particulates [160, 179]. Moreover, the analogous chemical features of chlorine and bromine propose that the generation mechanism of both PBDD/Fs and PCDD/Fs might undergo comparable paths [179]. Bromine is not as ubiquitous as chlorine in fires and combustion, yet it follows related sets of reactions as chlorine and therefore has the potential to form a group of compounds similar to PCDD/Fs [180]. Therefore, PBDD/Fs can be formed either via de novo synthesis or from coupling of structurally-related precursors, as the same pathways as for PCDD/Fs [181, 182]. Figure 2.8 depicts the chemical structures of PBDD/Fs compounds. The coupling of structurally-related precursors represent the most relevant path for the generation of PBDD/Fs, resulting from the presence of Br in brominated aromatic compounds (e.g., PBBs, PBDEs, bromophenols) serving as direct precursors for the formation of PBDD/Fs [183, 184]. However, these precursors can be decomposed and give the preference to the de novo synthesis in the formation of new PBDD/Fs under efficient

combustion conditions, as is the case of PCDD/Fs in municipal waste incinerators [185]. Du et al. [186] reported that the release of PBDD/Fs from stack gas created by different combustion and metallurgic industrial thermal methods are because of both reactions of precursors and also de novo formation, mainly BFRs as polybrominated diphenyl ethers (PBDEs) present in wastes from commercial products, which can be used as alternative fuels in such processes. In contrast are the findings of Ortuño et al. [187] and Vehlow et al. [188] who examined the formation of PBDD/Fs in laboratory experiments. They revealed the de novo pathway of PBDD/Fs is highly predominate under well-controlled combustion conditions. Other investigations have revealed that the presence of the catalytic metals such as iron, zinc, copper and metal oxides has a significant effect on the decomposition of BFRs, resulting in by-products such as bromophenols, and then continue, by means of dimerization or condensation of the bromophenols to generate PBDDs [189-191].
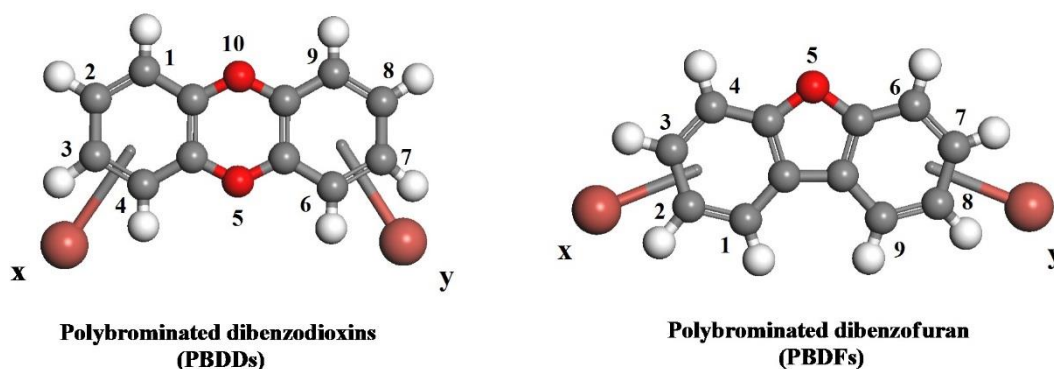
Figure 2.8. General structure formula of polybrominated dibenzo-*p*-dioxins (PBDDs) and dibenzofurans (PBDFs) (x + y = 1 − 8) [192].

Because of the structural similarities between PBBD/Fs and BFRs (e.g., PBDEs, PBBs HBCDs and TBBPA, etc.), PBBD/Fs can be formed even under mild thermal stress through precursor pathways, which are of higher relevance for the formation of PBDD/Fs during thermal processes. Experimental investigations suggested that thermal degradation of pure BFRs and

material laden BFRs usually include (i) release of HBr and the formation of brominated bisphenols (ii) fission of the isopropylidene bridges and the liberation of brominated phenols and (iii) generation of growing molecular weight components [193]. Those suggestions well correspond with Marongiu et al.'s study [194] who used a semi-detailed kinetic model to examine the thermal degradation of TBBPA as the most commonly used BFRs materials. They revealed that the decomposition of TBBPA occurred in a temperature range of 473–773 K, liberating gaseous mixtures of HBr molecule and various harmful bromo-organic compounds such as the precursors of PBDD/Fs and brominated phenols [194]. Moreover, Barontini et al. [195] investigated the primary thermal degradation pathways of tetrabromobisphenol A (TBBA) in a laboratory-scale fixed bed reactor in both constant isothermal (483–K) and heating rate (283 K/min, 276–K) modes. They reported that HBr, brominated phenols, brominated bisphenol A species and char were the principal products formed in the decomposition method. They also found that scission reactions to phenols and radical de-bromination reactions represented the most important thermal degradation mechanisms of TBBA.

The profusion of BFRs-based materials that produce enormous undesirable amounts of wastes have accumulated all over the globe, making effective and safe disposal of these brominated materials a truly daunting task. As mentioned previously, among the used recycling methods, chemical recycling represents a promising technology that would transform plastics into their basic chemical building blocks.

2.7. Chemical Recycling of Plastic Waste

Chemical recycling of plastic waste, also known as tertiary recycling, can be defined as a most effective technique to obtain the entire resources of all the elements and to eliminate the toxic components contained in the polymeric wastes [196]. This technique is employed to break

down or convert the waste polymers chain into their basic chemical building blocks (original monomers) or into valuable chemicals via many chemical processes [144, 197]. The quality of the product formed from this recycling method depends on two main factors, namely the chemical composition of the polymeric material and the operating conditions of reactors applied such as pressure, temperature and residence time [198]. Obtained products can be utilized again as feedstock in numerous industrial processes for the production of petrochemical products. The chemical recycling technique includes three main approaches: hydrocracking degradation, gasification process and pyrolysis process [197, 199, 200].

2.8. Pyrolysis Process of Plastic Waste

Pyrolysis process has received renewed attention for recycling plastic waste that is currently not recycled, but are incinerated and/or landfilled and that are a challenge to depolymerize, owing to the several operational and environmental advantages [201, 202]. It has been reported that the pyrolysis process has more merits compared to other recycling processes, such as good selectivity to higher added value products and very low energy consumption (only 10% of the energy content of plastic waste is consumed during the pyrolysis process) [203, 204]. Moreover, the emission of toxic gases is much lower than that of the incineration process. In general, the pyrolysis process is defined as a thermal process that enables a variety of hydrocarbons in an oxygen-free atmosphere, and works to preserve valuable resources and protect the environment by limiting the volume of non-degradable plastic wastes [205, 206]. The long-chain organic components of the plastic waste are degraded by the single impact of high temperatures (573–1173 K), forming liquid oil and gaseous products, whilst the inorganic elements such as fillers and metals remain unaltered and free of any organic matter, which makes their separation easily recovered and reused [204, 207]. The choice of this method by many researchers stemmed from its capacity to produce a high volume of liquid oil up to 80

wt% at a moderate temperature (i.e., 773 K) [208]. The high amount of liquid oil produced can be utilized in various applications such as turbines, furnaces, diesel engines and boilers without the requirements of treatment and upgrading [209]. Unlike other recycling methods, pyrolysis is considered as a green method and does not cause water contamination. Also, the gaseous by-product of pyrolysis has a substantial thermal value that can be reemployed to compensate for the overall energy demand of the pyrolysis plan [210].

Although it has been suggested that pyrolysis is a promising method for treating halogenated plastic waste, it forms hydrocarbons (oil) with a high content of chlorine and bromine [211, 212]. Moreover, pyrolysis of chlorine/bromine-containing plastics produces acid gas (hydrogen chloride/bromide) which generate toxic and corrosive conditions that affect processing equipment [212]. A fundamental challenge of the pyrolysis process is the complexity of interactions that take place, especially when mixed plastics wastes are treated. In this context, various polymer wastes give rise to totally different products based on their dominant decomposition route. The obtained products can be affected by any type of impurities and could lose a large part of their value [11].

The pyrolysis process can be improved by means of dehalogenation methods which prevent the formation of halogenated compounds when plastic wastes are pyrolysed. De-halogenation methods can be divided into three convenient groups: stepwise pyrolysis, co-pyrolysis with adsorbents and catalytic pyrolysis [204]. Stepwise pyrolysis process occurs at a low-temperature to remove chlorine from the original sample as HCl which is pyrolysed as in a conventional run [213]. However, introducing the adsorbents to the sample will decrease the HCl emission because the resultant HCl is fixed by means of physical and/or chemical adsorption and is consequently retained in the solid fraction [214, 215]. In the co-pyrolysis

process with adsorbents, the emission of HCl can be reduced, since the evolved HCl is fixed by physicochemical adsorption and retained in the solid fraction. Several green materials have been used as HCl adsorbents such as alkaline adsorbents (e.g., $CaCO_3$, CaO, $NaHCO_3$) and biomass constituents [204, 216]. By comparing stepwise pyrolysis with the conventional pyrolysis process, it has been suggested that stepwise pyrolysis can be an effective technique for the dechlorination of pyrolysis liquids producing a low quantity of aromatic compounds and heavy hydrocarbons [213]. For example, introducing $CaCO_3$ as adsorption leads to the retention of a significant amount of chlorine in the solid fraction, but more chlorine is observed in the liquids, which includes a higher volume of aromatics [217]. The chlorine content of the liquid produced can be reduced to one third by using a low-temperature de-hydrochlorination step; the effectiveness of this process cannot be improved by introducing $CaCO_3$ adsorbent [217]. By using TG-FT-IR, Zhu et al. [218] studied the pyrolysis behaviour of PVC with a heating rate of 30 C/min. They found that the pyrolysis of PVC might be divided into two main steps. The first step occurs in a temperature range of 553–673 K and involves de-hydrochlorination with the formation of some conjugated double bonds that break through the second decomposition step. The second step involves the formation of some hydrocarbons in a temperature range of 673–833 K. The authors also observed that the mass transition ratio of 65% and the temperature maximum rate of 593 K were in the first decomposition step of PVC. Figure 2.9 illustrates the main two steps of PVC pyrolysis.
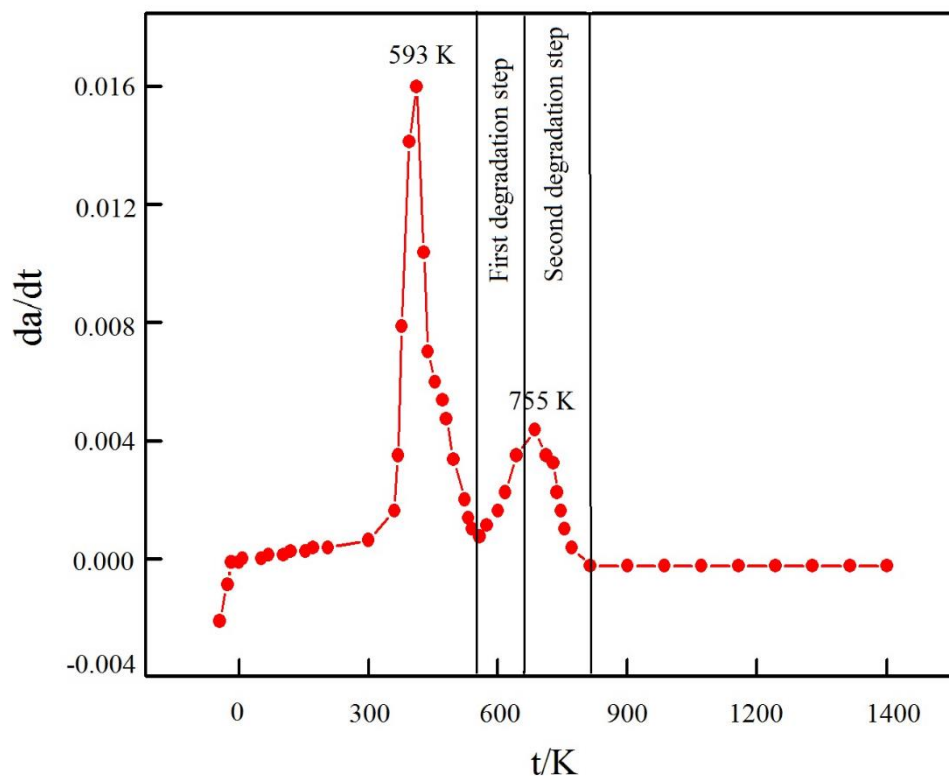
Figure 2.9. TG-DTG curve of degradation steps of PVC pyrolysis [218].

On the other hand, the pyrolysis behaviour of bromine-containing plastics primarily depends on the form of chlorine. In this context, in the absence of any fire retardant synergists (e.g., Sb_2O_3), the emission of HBr will not occur at a different temperature range from the degradation of the polymer matrix as in chlorinated plastics [219]. On the contrary, when the plastic has synergists Sb_2O_3, the degradation undergoes into two different regions. Sb_2O_3 starts the degradation by reacting with the HBr that evolved from the FR at the low-temperature level, which is the reason why Sb_2O_3 can be applied as a FR synergist [219]. For example, Bhaskar et al. [220] and Mitan et al. [221] investigated the pyrolysis of polyethylene/polypropylene/polystyrene mixed plastics with high impact polystyrene containing decabromo diphenyl ethane (DDE) as flame retardants with or without Sb_2O_3 as a synergist by using the two-stage method. They found the first stage occurs at 603 K for 2 hours and the second stage took place at 703 K continuing until the end of the pyrolysis reaction.

Their results showed that under the controlled temperature pyrolysis conditions, the generated oil from the first stage had higher brominated compounds than in the second stage in all samples and the presence of antimony could further enhance the rate of bromine release through generating SbBr$_3$ at low pyrolysis temperatures. Therefore, oil products that include relatively less bromine content can be obtained in the second stage. However, processing brominated plastics containing antimony by the two-stage pyrolysis technique does not convert the toxic organic bromines into inorganic bromine, but just concentrate them in the first stage oils [221].

The limitations with the two pyrolysis routes are that the entire processes are temperature-dependent (high operating temperatures), and the obtained liquid oil may contain impurities and residues in addition to halogenated compounds, which hinder its further reuse in commercial applications. Therefore, catalytic pyrolysis could provide a solution to these difficulties by allowing control of the product distribution and decreasing the reaction temperature [217, 219].

2.9. Catalytic Pyrolysis Process

Catalytic pyrolysis has become more important in terms of resource conservation and environmental protection. Catalytic pyrolysis is potentially an effective and appealing technique for processing plastic wastes to produce high-value products [11, 222]. The use of a catalyst during the treatment of plastic wastes will make the reaction conditions less stringent and reduce energy consumption throughout the entire process, thereby affecting the total operating cost [217]. The catalytic pyrolysis process has numerous advantages compared to other treatment processes as follows.

- Reducing the interaction temperature rate and shortening residence times. This significant reduction in the decomposition temperature and reaction time in the presence of the catalyst will increase the conversion rates for a wide range of plastic wastes with less energy consumption [223, 224].

- Inhibiting the generation of undesired products such as chlorinated and brominated hydrocarbon compounds. This represents an interesting feature especially in the presence of material-laden PVC and BFRs [9, 225].

- The selectivity of products is enhanced under catalytic conditions. For example, the presence of catalyst in the pyrolysis process of polyolefins, aromatic hydrocarbons and branched will increase the quality of the potential obtained fuels [9, 225].

Table 2.5. presents the main differences between thermal pyrolysis and catalytic pyrolysis processes using various types of catalyst. It can be concluded that the latter process shows not only high potential for producing liquid oil but also for reducing decomposition temperature.

Table 2-5. The main differences between thermal pyrolysis and catalytic pyrolysis

Type of catalyst			Red mud	Red mud	ZSM-5	ZSM-5	Y-zeolite	Natural zeolite
Type of plastic			PE, PS, PP, PVC, PET	PE, PS, PP, PVC, PET	PE, PS, PP, PVC, PET	PE, PS, PP, PVC, PET	Municipal plastic waste	Municipal plastic waste
Operating temperature			713K	773K	713K	773K	723K	723K
Amount of catalyst			10%	10%	10%	10%	50%	50%
Main pyrolysis product %	Thermal pyrolysis	Gases	17.7	34.0	17.7	34.0	28.0	28
		Liquid	79.3	65.2	79.3	65.2	58.0	58
		Char	3.0	0.8	3.0	0.8	14.0	14
	Catalytic pyrolysis	Gases	21.6	41.3	40.4	58.4	52.0	34
		Liquid	76.2	57.0	56.9	39.8	14.0	50
		Char	2.2	1.7	3.2	1.8	12.0	16
References			[214]	[214]	[214]	[214]	[37]	[37]

In general, catalytic pyrolysis is either homogeneous or heterogeneous [198, 226]. The homogeneous process involves a single phase (usually a liquid solution), while in the heterogeneous process the catalyst is solid. Aluminium chloride ($AlCl_3$) catalysts are a common homogeneous catalyst in plastic solid waste pyrolysis [227]. In this process (liquid phase), the catalyst comes in direct contact with the molten polymer phase to assist with converting the partially degraded oligomers. On the other hand, the heterogeneous ones represent the most common kind of catalysts utilized in pyrolysis of plastic solid waste. This

is in turn based on the fact that the fluid product can be simply separated from the solid catalyst and then can be easily reformed and reused. Most general examples of such operations are nano-crystalline zeolites applied ones [228], conventional acid solid, mesostructured catalyst, metal supported on carbon and basic oxides [229]. Moreover, heterogeneous catalysts have been reported to resist stringent reaction conditions up to 35 MPa and 1573 K and can generally be simply separated from the gas and liquid reactants and products [230].

The literature regarding catalytic pyrolysis of plastics reveals that extensive investigation has been made into catalytic efficiency and mechanisms in various catalytic systems. A range of catalyst materials have been investigated for their potential in upgrading the quality and de-halogenation from the pyrolysis of materials laden with both PVC and BFRs. Among those catalysts, natural zeolite [37, 217, 231-233], FCC catalysts [234-237], red mud [217], minerals [238] and metallic oxides [239, 240] have attracted greatest attention. In particular, metal oxides such as Fe_2O_3, ZnO, Fe_3O_4, Al_2O_3 and PbO have shown good results for capturing emitted hydrogen halides (HCl and HBr) and reducing the generation of halogenated hydrocarbons from thermolysis of polymeric materials laden with halogenated compounds. In this context, metal oxides interrupt the aromatic hydrocarbon formation and this process can occur without changing the type of chemical species found in the final products. Benzene is one of the main liquid products and it can be produced in various amounts based on the type of metal oxides [241]. For example, Blazsó and Jakab [242] found that introducing metal oxide catalysts, especially Fe_2O_3 and ZnO, can delay the formation of benzene by approximately 30%, less than for pure PVC. Even though metal oxides display significant catalyst reaction steps through heterogeneous formation of PCDD/Fs and PBDD/Fs, they readily react with hydrogen halides (HCl and HBr) in a process that eliminates the halogen content from the reaction medium. The consumed halides transform the metal oxides into metal halides.

2.10. Fixation of Cl Content in PVC by Introducing Metal Oxides

Considerable interest in investigating the performance of metals and their oxides on the thermal degradation of PVC polymer arises based on their great potential to act as chlorine fixers or absorbers [243, 244]. In this context, combined treatment or so-called "co-pyrolysis" of both electric arc furnace dust (EAF) dust and PVC has emerged as a promising approach for an environmentally synchronous recycling methodology for both resources (i.e., metallic oxides in EAF dust and the chlorine content in PVC polymer [38, 101, 245]. As we mentioned in an earlier section (i.e., section 2.3) the produced dust of the EAF process essentially contains a considerable amount of zinc and iron in the form of simple or mixed oxides, followed by a small but significant amount of calcium and lead oxides. XRD patterns reported by Al-Harahsheh found that EAF dust contains mainly of zincite, franklinite, hematite and magnetite [101]. The consensus of opinions in the literature has shown that the introduction of metallic oxides through thermal decomposition of PVC polymer acts as a dechlorinating agent and can inhibit the formation of chlorinated hydrocarbons [59, 241]. Consequently, the metallic oxides will convert to their respective chlorides (volatile metallic chlorides) which are easily volatile at low temperature or dissolvable in water [59]. A study carried out by Al-Harahsheh et al. [59] showed that the presence of EAF dust through the thermal degradation of PVC polymer enhances the mass loss of PVC polymer in the initial step from 37% to almost 80% and significantly decreases the activation energy values of the de-hydrochlorination system. They also found that the activation energies of H-Cl bond cleavage by the metallic oxides will be in the range 33.7%–41.8 kcal mole^{-1}. This step is associated with the generation of metallic chlorides (mainly, $FeCl_3$, $PbCl_2$, $ZnCl_2$ and $FeCl_2$) and water vapour. Additional evidence of the interaction of metallic oxides with the thermally evolved HCl was reported by Karayildirim et al. [246]. The authors reported that the pyrolysis of PVC polymer in the presence of red mud can produce iron chloride. The relationship of this product with iron oxide stems from

the fact that the major reactive component in the used red mud is iron oxide, which represents approximately 37% of the other oxides. The authors concluded that iron oxide present in the red mud worked as an HCl fixator. Introducing metallic oxides during thermal degradation of pure PVC polymer considerably changes its structure and reduces the onset degradation temperature to a lower value [247, 248]. TGA profiles indicate the weight loss curve of the decomposition of pure PVC exhibited two main peaks corresponding to elimination of HCl gaseous at around 470 K and fission of the carbon bonds in the PVC backbone above 633 K. In this regard, Zhang et al. [249] examined the reaction mechanism of PVC polymer with ZnO based on thermogravimetric–mass spectrometry (TG-MS). They showed that the PVC polymer interacts directly with ZnO at a temperature of 473 K, which is lower than that of thermal degradation of the pure PVC polymer (i.e., >523 K). The authors also observed that dehydrochlorination of PVC polymer in the presence of ZnO proceeds without the formation of volatile organic compounds and the only volatile product was water. Table 2.6 summarises studies that report co-pyrolysis of PVC with metal oxides.

Table 2-6. The catalytic effect of metal oxides on the pyrolysis of materials laden with chlorinated compounds.

Type of catalyst used	Analysis technique/operating conditions	Composition	Catalyst effect	References
ZnO	TG-MS (353–1223 K) Heating rate 40 K/min Particle size 1.48µm	• 0.3 ZnO -0.6 PVC • 0.3 ZnO -1.0 PVC	• Prevent the formation of HCl and the volatile organic compounds such as benzene. • Reduce the chlorination temperature of Zn from 523–473 K. • 73% and 84% of ZnO has been chlorinated for 0.3 ZnO -0.6 PVC and 0.3 ZnO-1.0 PVC, respectively.	[249]
Fe_2O_3	TG-MS (353–1223 K) Heating rate 40K/min Particle size 8.45µm	• 0.25 Fe_2O_3-0.6 PVC • 0.25 Fe_2O_3-1.0 PVC	• Dehydrochlorination of PVC takes place at a lower temperature range of 513–673 K.	[249]
ZnO	GC/MS (673–1073 K) Particle size 1.9 µm Quartz reactor tube	• 1:2 ZnO/PVC	• Introducing ZnO significantly suppresses the formation of liquid products and enhances the char formation. • Reduction of chlorobenzene formation. • $ZnCl_2$ evaporation started above 673 K	[241]

	τ=10 and 30 min			
Fe_2O_3	GC/MS (673–1073 K) Particle size 9.9 µm Quartz reactor tube τ=10 and 30 min	• 1:2 Fe_2O_3/PVC	• Addition of iron oxide enhances the formation of gaseous products, CO and CO_2 and promotes the formation of chlorobenzene. • Formation of $FeCl_2$ enhances the char formation.	[241]
La_2O_3	GC/MS (673–1073 K) Particle size 15 µm Quartz reactor tube τ=10 and 30 min	• 1:2 La_2O_3/PVC	• Adding of La_2O_3 converts Cl from PVC to oxychloride with the performance of more than 75% at 673 K and 95% at 1073 K.	[241]
ZnO	TG-MS (353–1223 K) Model batch-type reactor Particle size 0.3µm	• 0.3 ZnO -0.6 PVC • 0.3 ZnO -1.0 PVC	• CI in PVC is converted into chlorinate Zn at 473–893 K. • Evolution of HCl is negligible compared with the case of pure PVC decomposition at a similar temperature range.	[250]

ZnO	XRD (1023–1273 K)		• The activation energy of ZnO chlorination is 14 kcal mole^{-1} and this relatively lower than the value of dissociation of the unstable compound in the gas phase.	[251]
Fe$_2$O$_3$-ZnFe$_2$O$_4$-ZnO-PbO mixture	XRD (1346 K)	• 36.8% Fe$_2$O$_3$-12.4% ZnFe$_2$O$_4$-4.3% ZnO and PbO.	• Zinc oxide and lead oxide were converted to ZnCl$_2$ and PbCl$_2$, and removed from oxide mixture, while iron oxide remained as oxide in the chlorinated residue. • Oxygen and chlorine partial pressure have affected the chlorination rate of ZnO, while that of lead oxide was scarcely affected.	[100]
Fe$_2$O$_3$	TGA, X-ray, XRD (473–1273 K) Quartz reactor tube	• 1:1 Fe$_2$O$_3$/PVC	• The chlorination test of hematite showed that the PVC can be used as a chlorinating agent. The reaction gives metal chlorides.	[252]
Metal oxides mixture	TGA, SEM, X-ray Particle size under 10 µm	• 9:1 metal oxides/PVC	• Chlorination of iron oxides occurs at 573 K in form of FeCl$_3$ • ZnCl$_2$ volatilizes at a lower temperature than the other metal chlorides.	[253]

ZnO	TGA, XRD, FT-IR (453–673 K) Heating rate 10K/min	• 0.75 ZnO-1.0 PVC • 0.3 ZnO-1.0 PVC	• Presence of ZnO reduces the required temperature for de-hydrochlorination of PVC • De-hydrochlorination of PVC producing only H_2O and $ZnCl_2$ at around 473 K without HCl formation	[254]
Fe_2O_3	Py-GC/MS (303–973 K) Quartz reactor tube	• 1:20 Fe_2O_3/PVC	• Fe_2O_3 reduced the onset temperature of dehydrochlorination by attracting chlorine (weakening the C–Cl bonds in PVC) • The presence of Fe_2O_3 hinders benzene formation as far as it is forming chlorides with HCl.	[255]
SA/Fe_3O_4	GC-MS, GC-AED (633–703 K) Glass reactor tube	• 2:8:1:2 PE/PVC/SA/Fe_3O_4 • 2:8:1:2 PE/PVC/SA/Fe_3O_4 • 2:8:1:2 PE/PVC/SA/Fe_3O_4	• Fe_3O_4 decrease the chlorine content to a very low • The chlorine removed from the products of decomposition of PVC mixed plastics are fixed as of ferrous chloride	[256]

2.11. Fixation of Br Content in TBBA by Introducing Metal Oxides

Catalytic dechlorination and debromination processes by introducing metal oxides share very similar operational trends with those entailing chlorinated compounds. Thus, combined treatment of EAFD and bromine-containing objects (i.e., TBBA) has also attracted recent researchers' attention in regard to extracting the valuable metals containing in EAFD and reducing the formation of toxic polybrominated dibenzop-dioxins/furans (PBDD/Fs). Several experimental studies have shown that the main products from thermal degradation of TBBA are released as gaseous products in the form of HBr, mixtures of harmful compounds, such as brominated benzenes and phenols in addition to a vast range of brominated aromatics [194, 257, 258]. Approximately half of the initial bromine in the origin TBBA was observed to transform into gaseous HBr just above 673 K with considerably fewer amounts if compared to the degradation of pure TBBA [166, 259]. Many metal oxides, such as La_2O_3, CuO, Fe_2O_3, CaO, and ZnO, have been used as bromine fixation or absorbing agents. Fe_2O_3 and ZnO were found to have a significant impact on bromine fixation through generating of metal bromide or oxybromide [240, 260, 261].

As a result of various scanning calorimetry run and several laboratory-scale experiments, Grabda et al. [261, 262] investigated operational conditions that dictate bromination of zinc oxide through thermal decomposition of TBBA. Their electron probe microanalyzer and thermal scanning utilizing X-ray diffractometer indicated that about 70% of the total TBBA's Br content is released in a temperature range of 563–613 K. They found that bromination of ZnO revealed high sensitivity in regard to the mixing TBBA:ZnO ratios. For example at TBBA:ZnO mixing ratios of 3.34:1 and 5.17:1, the bromination efficiency attained values of 41–61% and ~80%; respectively. It was shown that the bromination efficiency of ZnO is strongly correlated with the HBr amount co-existing with particles of ZnO.

Along the same line of enquiry, Oleszek et al. [263] used DSC, TG, and TG–MS techniques to investigate the reactions between PdO and Fe_2O_3 and HBr from thermal degradation of TBBP A under inert and oxidizing atmospheres. They found that during the thermal scanning of pure TBBPA two endothermic phenomena were displayed. The first related to the melting of TBBPA at a temperature range of 451–454 K, while the second was associated with progressive decomposition of TBBPA from 533 K to a maximum of 581 K. DSC-TGA analysis showed that introducing metal oxides changes the degradation behaviour of TBBPA where the mixtures (TBBPA + metal oxides) displayed two various phenomena. The endothermic phenomenon coincided with the melting peak of pure TBBPA, which showed that it had started melting in the mixture and the exothermic event that revealed the presence of newly formed bromides ($PbBr_2$, $FeBr_2$). This indicated that the exothermic phenomenon was accompanied by the bromination reaction that occurs due to TBBPA degradation and bromine evolution. Table 2.7 summarises studies that report co-pyrolysis of materials laden with brominated compounds

Table 2-7. The catalytic effect of metal oxides on the pyrolysis of materials laden with brominated compounds.

Type of catalyst used	Analysis technique/operating conditions	Composition	Catalyst effect	References
ZnO	TG-MS and X-ray (493–1573K) Under various atmospheres Heating rate 10 °C/min	• 1:3.34 ZnO/TBBPA	• Simultaneous TG-MS measurements show that the existence of ZnO strongly impacts the TBBPA degradation pathway and causes enhancement of char formation. • In an oxidizing atmosphere, approximately 70% of Zn is brominated. 43% of that is in the form of $ZnBr_2$ and vaporizes in a temperature range of 633–753 K. The other 27% in form of $ZnBr_2$ and possibly ZnOBr vaporizes gradually together with successive degradation of surrounding organic char.	[264]
Fe_2O_3	DSC, TG, and TG–MS (296–1573K) Under inert and oxidizing atmospheres Heating rate 10 °C/min	• 1:3.41Fe_2O_3/TBBPA	• Simultaneous TG–MS measurements indicated that the addition of iron oxide enhances char formation through strongly accelerated the degradation of TBBPA	[263]

PbO	DSC, TG, and TG–MS (296–1573 K) Under inert and oxidizing atmospheres	• 1:1.22 PbO /TBBPA	• HBr acted as an excellent brominating agent for PbO and separated 79% of Pb as a volatile bromide from the solid up to 853 K.	[263]
ZnO	TGA, GC/MS and X-ray (373–1073 K) Particle size 1-10µm Heating rate 10 °C/min Quartz reactor tube τ=10 min	• 2:1 ZnO /TBBA	• ZnO showed the superior ability of the bromine abstraction by the enhancement of the benzene generation at 673 K.	[240]
La_2O_3	TGA, GC/MS and X-ray (373–1073 K) Particle size 1-10µm Heating rate 10 °C/min Quartz reactor tube τ=10 min	• 2:1 La_2O_3/TBBA	• Introducing La_2O_3 is particularly effective for the reduction of HBr emission. • La_2O_3 suppresses the formation of hydrogen bromide and brominated organic compounds. Especially significant suppression of ~90% is achieved compared with the result of pure TBBA.	[240]

Sb$_2$O$_3$	DSC, GC/MS and X-ray (413–923 K) Under inert and oxidative atmospheres Quartz reactor tube Heating rate 10 °C/min	• 1:2.81 Sb$_2$O$_3$/TBBPA	• Thermal treatment of TBBPA in the presence of Sb$_2$O$_3$ showed that the released HBr at temperatures up to 713 K may react with the oxide and form SbBr3 which evaporates immediately and can be trapped in the condensate phase. • More than 60% of the maximum amount of Sb converted into SbBr$_3$.	[265]
ZnO	DSC, GC/MS and X-ray (413–923 K) Particle size 2.6µm Quartz reactor tube Heating rate 1 °C/min	• 1:3.34 ZnO/TBBPA • 1:5.17 ZnO/TBBPA	• Bromination of ZnO occurred at 545 K and above 563 K with an effectiveness of up to 81% based on the experimental conditions. • The produced ZnBr$_2$ started to volatilize at 613 K and yield 45% at 923 K.	[266]
ZnO	C/ICP, GC/MS and X-ray (503–583 K) Particle size 2.6µm	• 1:3.34 ZnO/TBBPA	• The bromination rate is highly dependent on heating time and it increases with time until the bromine source is depleted. • The maximum bromination yield ranges from 64–70%.	[262]

	Quartz reactor tube			
ZnO	GC/MS, X-ray and ICP (1173 K) Quartz reactor tube	• 2:1 ZnO /TBBA	• The addition of ZnO significantly suppresses the formation of hydrogen bromide and brominated organic compounds. • More than 80% of HBr yield is reduced by the addition of zinc oxide and for the brominated organic compounds, essentially no formation of bromophenols was observed by the addition of a high amount of ZnO.	[260]
ZnO	TGA, DSC and ICP (1073 K) Quartz reactor tube Heating rate 10 °C/min	• 1:2.74 ZnO /PCB	• Addition of zinc oxide led to the fixation of bromine as stable zinc bromide. • The formation and the evaporation of $ZnBr_2$ can be as a result of the promotion of the degradation of PCB.	[267]

It must be mentioned that the newly formed bromides (i.e., $ZnBr_2$) are boiled around 923 K, which is lower than the boiling point of $ZnCl_2$ (996 K) that are produced in chlorination-evaporation of zinc using PVC. This suggests that the energy consumption of the bromination process could be lower than that of the chlorination process. Table 2.8 displays a simple comparison between the bromination-evaporation process with TBBA and chlorination-evaporation process with PVC.

Table 2-8. Differences between the bromination and chlorination evaporation processes [59, 261, 268].

Factors	Operating Temperature	Mass ratio	Boiling point of main degradation outcome	Energy consumption	Main degradation product
Bromination evaporation with TBBA	1173 K	3.34:1	996 K	Low	$ZnBr_2$
Chlorinated evaporation with PVC	1173 K	2.33:1	923 K	High	$ZnCl_2$

2.12. Research gaps in current knowledge

Having surveyed the literature reporting research related to combined treatment of both EAFD and plastic materials bearing organo-halogen compounds, several gaps in present knowledge can be identified.

- The literature presents no theoretical accounts that treat both categories of the titled pollutants simultaneously.

- Despite numerous investigations into the mixing of PVC and BFRs with metal oxides over the last few years, the literature presents no mechanistic or kinetics information at the molecular level interaction mechanisms of hydrogen halides and other halogenated C_1-C_6 cuts over transitional metal oxides. Chapters 4, 5 and 6 in this thesis present the elemental processes governing these interactions at a precise atomic scale.

- While there are various previous theoretical and experimental studies that have addressed the interaction of halogenated short unbranched hydrocarbons with copper surface from different views, a detail mechanistic understanding of its role in surface-mediating rupture of carbon-halogen bond has remained poorly understood. The elementary steps that govern the degradation of multiple halogenated hydrocarbons over a copper surface are shown in Chapter 7.

- Notwithstanding the numerous experimental studies and computational calculations, several mechanistic aspects dictating the formation of notorious dioxins compounds and phenoxy-type environmental persistent free radicals (EPFRs) remain unexplained on an atomic-based insight, most notably regarding the operating reaction barriers prevailing over pure metallic surfaces and their partially oxide states. This has been conducted, in detail, in Chapter 8.

Chapter 3

Theoretical Background

3.1. Schrödinger Equation

The properties of matter on a precise molecular basis are explained using the quantum mechanics laws. From that nanoscale point of view, a molecular system entity consists of a number of light, negatively charged atomic electrons and heavier, positively charged nuclei. As a consequence, these atomic electrons and nuclei can be treated as electromagnetically reacting point charges [269, 270]. Therefore, non-relativistic Hamiltonian for the molecular system will have the form:

$$\hat{H} = -\sum_i \frac{\hbar^2}{2m_e} \nabla_{r_i}^2 - \sum_j \frac{\hbar^2}{2M_j} \nabla_{R_j}^2 - \sum_{i,j} \frac{Z_j e^2}{4\pi\epsilon_0 |R_j - r_i|} + \sum_{i \neq j} \frac{e^2}{4\pi\epsilon_0 |r_i - r_j|}$$

$$+ \sum_{i \neq j} \frac{Z_i Z_j e^2}{4\pi\epsilon_0 |R_i - R_j|} \tag{3.1}$$

Or we can write Eq. 3.1 in a more compact form as in Eq. 3.2:

$$\hat{H} = \hat{T}_e(r) + \hat{T}_N(R) + \hat{V}_{eN}(r,R) + \hat{V}_{ee}(r) + \hat{V}_{NN}(R) \tag{3.2}$$

where $\hbar$ is the Plank's constant, ∇^2 is the Laplacian operator and e signifies the charge on the electron. i refers to the electrons while j runs over nuclei. The first and second terms describe the kinetic energy of the electrons and nuclei, correspondingly. The third, fourth and the last terms of Eq 3.1 correspond to the Coulomb interaction between electrons and nuclei, among electrons and among nuclei, respectively. In atomic units Eq 3.1 may be written as in Eq. 3.3:

$$\hat{H} = -\sum_i \frac{1}{2} \nabla_{r_i}^2 - \sum_j \frac{1}{2M_j} \nabla_{R_j}^2 - \sum_{i,j} \frac{Z_j}{|R_j - r_i|} + \sum_{i \neq j} \frac{1}{|r_i - r_j|} + \sum_{i \neq j} \frac{Z_i Z_j}{|R_i - R_j|} \tag{3.3}$$

When considering that the work is in Cartesian coordinates, the Laplacian operator of Eq. 3.1 is equivalent to partial differential with respect to *x, y* and *z* coordinates and is expressed as Eq. 3.4:

$$\nabla = \frac{\partial}{\partial x}i + \frac{\partial}{\partial y}j + \frac{\partial}{\partial z}k \qquad\qquad 3.4$$

The corresponding time-independent Schrödinger equation (TISE) for this system can be described by the following form (Eq. 3.5):

$$\hat{H}\psi(r,R) = E\psi(r,R) \qquad\qquad 3.5$$

where ψ signifies the total wave function of the system and E represents the total energy of the system. Note that the wave function postulates the probabilistic details of an electron's behaviour and depends on the position of a molecular system's particle. ψ should be normalised, continuous, single valued and antisymmetric regarding the interchange of electrons [271, 272]. Solving Eq 3.4 is analytically possible only for a few select systems, for instance the H atom. However, because of the high degree of complexity of the correlated motions of particles in the many-bodied system including both electrons and nuclei of the wave-function, it is impossible to carry out the above equation in practice. Therefore, several approximation computational methods have to be imposed in order to obtain an entire description of such a system.

3.2. The Born−Oppenheimer Approximation

The Born−Oppenheimer approximation (BO) represents the most fundamental approximations in condensed matter chemical physics and physics to simplify the solution to the Schrödinger equation [270]. This approximation streamlines the solution through separating the electronic and nuclear movements of the considered systems [273, 274]. Based on the state that parts of a molecular system (i.e., nuclei) are have greater mass than the other system part (i.e., electrons) (strictly speaking, the mass of the proton is about 1836 times the mass of an electron), the Born−Oppenheimer approximation allows one to envision the nuclear moving on a single potential energy surface is accompanied with a single electronic quantum state [275]. The latter can be obtained by treating the TISE for a series of fixed nuclear geometries [276, 277]. In the molecular context, this means that due to the slow motion of the nuclei on the scale of velocities correlated to the electron it is justifiable to suppose that at any moment the electron will be in its ground state with regard to the instantaneous nuclear arrangement [269, 273]. Therefore, with the Born−Oppenheimer approximation, for fixed nuclear geometries, Eq. 3.1 can be written as:

$$\hat{H} = -\sum_i \frac{\hbar^2}{2m_e} \nabla_{r_i}^2 - \sum_{i,j} \frac{Z_j e^2}{4\pi\epsilon_0 |R_j - r_i|} + \sum_{i \neq j} \frac{e^2}{4\pi\epsilon_0 |r_i - r_j|} + \sum_{i \neq j} \frac{Z_i Z_j e^2}{4\pi\epsilon_0 |R_i - R_j|} \qquad 3.6$$

Or

$$\hat{H} = \hat{T}_e(r) + \hat{V}_{eN}(r, R) + \hat{V}_{ee}(r) + \hat{V}_{NN}(R) \qquad 3.7$$

It is important to mention here that the potential energy of nucleus−nucleus Coulomb interaction contributes to the total energy by augmenting it with a constant value. Therefore,

leaving the last term of Eq. 3.6 or 3.7 out will not affect the corresponding wave function. Consequently, we can re-write Eq. 3.6 or Eq. 3.7 as:

$$\hat{H}_e = -\sum_i \frac{\hbar^2}{2m_e} \nabla_{r_i}^2 - \sum_{i,j} \frac{Z_j e^2}{4\pi\epsilon_0 |R_j - r_i|} + \sum_{i \neq j} \frac{e^2}{4\pi\epsilon_0 |r_i - r_j|} \qquad 3.8$$

Or

$$\hat{H}_e = \hat{T}_e(r) + \hat{V}_{eN}(r, R) + \hat{V}_{ee}(r) \qquad 3.9$$

Eq. 3.8 is called the electronic Hamiltonian and the electronic time-independent Schrödinger equation is taken to be:

$$\hat{H}_e \psi(r, R) = E_e \psi(r, R) \qquad 3.10$$

Note that with the Born–Oppenheimer approximation, the total Hamiltonian can be written as:

$$\hat{H} = \hat{H}_e + \hat{T}_N(R) \qquad 3.11$$

3.3. Hartree-Fock Theory

Hartree-Fock (HF) theory represents one of the earliest wave-function approximation methods to be developed for solving the electronic Schrödinger equation resulting from the TISE into a more tractable form [272, 278]. The HF theory is based on the assumption that the electronic wave-function of the molecular system can be represented through a single Slater determinant [279]. That means each electron of the system can be considered to be moving in a mean field

of all the other electrons and the nuclei. It is important to mention here that the field of the electron's motion is called the self-consistent field and the wave functions of the individual electrons are called orbitals. The solution to the Schrödinger equation must be determined by iterating a trial solve to self-consistency because the average field where every electron moves depends on the orbitals of all of the other electrons in the system [279]. Therefore, with Hartree-Fock approximation, the Hamiltonian equation for the many-body system can be transferred into numerous equations for coupled single-particles and it can be read as:

$$\hat{H} = \sum_{i=1}^{N} h_i \qquad\qquad 3.12$$

where N represents the total number of the electrons and h_i is the one-electron Hamiltonian operator which describes the motion of electrons in the mean field of the nuclei. Note that the operator in Eq. 3.12 is separable when the terms of the Hamiltonian are only electron kinetic energy and nuclear attraction, and may be expressed as:

$$h_i = -\frac{1}{2}\nabla_i^2 \ - \sum_{j=1}^{L}\frac{Z_j}{r_{ij}} \qquad\qquad 3.13$$

where L is the total number of the nuclei. The two-electron Hamiltonian operator equation can be defined as:

$$Z_{i,k} = \frac{1}{r_{ik}} \qquad\qquad 3.14$$

The electronic Hamiltonian operator can be written more simply as:

$$\hat{H}_e = \sum_i h_i + \sum_{i<k}^{L} Z_{i,k} \qquad\qquad 3.15$$

When there is no electronic coupling (i.e., the electrons do not interact with each other), it will be useful to separate the many-body wave-function into a product of single-electronic wave-functions that can be depicted by an equation:

$$\psi(r_1, r_2, \ldots, r_N) = \varphi_1(r_1)\varphi_2(r_2) \ldots \varphi_N(r_N) \qquad\qquad 3.16$$

The above form is called a Hartree-Product equation. HF theory is impartially convenient for solving the concepts of self-consistency and many-body system. However, this crude approximation has some the disadvantage of unsuccessfully satisfying the anti-symmetry requirement for electronic wave functions (the Pauli Exclusion Principle). This principle assumes that the wave-function of the many-body system has to be anti-symmetric with regard to the interchange of any set of space-spin position [278]. Also, the obtained approximate energies of electrons are not accurate enough for most practical applications in chemistry. In general, the failure of the HF method to describe electron correlations accurately arises from the inadequacy of its average-field to address the interaction among electrons.

3.4. Density Function Theory

In the previous sections, we presented some approximations to solve the TISE for a many-body system based on the term of the wave-function theory (a $3N$-dimensional anti-symmetric wave-function for a system with N electrons). In this section, we will present the solution using another method (i.e., Density Function Theory). DFT has been considered as an unparalleled method for the simulation of interesting problems in quantum chemistry and computational

physics that illustrates the electronic states of materials and molecules in the concept of the three- dimensional electronic density of the system [280, 281]. Despite the common thought that DFT is a relatively new, its history approximates the Schrödinger equation and is about five decades old in its modern formulation [282, 283]. In practice, DFT is always applied in the form proposed by Kohn and Sham in 1965 [284]. The basic quantity of this theory is built around the assumption that the energy of an electronic system can be described in the concept of its electron probability density $\rho(r)$[285]. For an N electron system, the term $\rho(r)$ signifies the total electron density at a special point in space r and can read as:

$$N = \int \rho(r)dr \qquad\qquad 3.17$$

Equation 3.17 can be re-written for each nucleus A located at an electron density maximum r_A as:

$$\left.\frac{\partial \bar{\rho}(r_A)}{\partial r_A}\right|_{r_A=0} = -2Z_A\rho(r_A) \qquad\qquad 3.18$$

where $\bar{\rho}$ is the spherically averaged density, r_A represents the radial distance from the nucleus A and Z is the atomic number of the nucleus.

The advantage of the DFT approach over a more pure approximation based on the notion of wave-function can be best represented considering the following: the wave-function for an N electron system would have $3N$ coordinates per electron in addition to another one for each electron when the spin is included (i.e., $4N$ coordinates for each electron). The electron density is independent on the number of electrons that comprise the system, which is based only on $3N$

coordinates [286, 287]. Therefore, whilst the complexity of the wave-function rises with an increasing number of electrons for the system, the electron density is independent of the considered system size, and maintains the same number of variables.

3.4.1. The Thomas-Fermi Method

This approach which is also called the "statistical theory" was created independently by Llewellyn H. Thomas and E. Fermi in 1927 shortly after Schrödinger proposed the quantum-mechanical wave equation [282]. Thomas-Fermi method is a quantum mechanical approach for the electronic structure of a large molecule or atom comprising a large number of electrons (N) that approximately describe the ground state energy E(N) and the electronic density (ρ (r)) [288, 289]. In other words, this theory can be defined by the energy functional $\mathcal{E}(\rho)$ or the ground state energy of the system for a certain number of electrons, which have a particular charge, in the atom.

$$\mathcal{E}(\rho) = \frac{3}{5} \int_{\mathbb{R}^3} \rho(r)^{\frac{5}{3}} d(r) - \int_{\mathbb{R}^3} \frac{z}{|r|} \rho(r) d(r) + \frac{1}{2} \iint \frac{\rho(r)\rho(\acute{r})}{|r - \acute{r}|} \qquad 3.19$$

where the first term is the minimum electronic kinetic energy required to produce ρ (r), which is associated with a system of the non-interacting electrons in a homogeneous electron gas. The second term represents the attractive interaction between the electron and the nucleus. The last term signifies the repulsive energy among the electrons [289]. Even though the Thomas-Fermi method presents good estimates for the atoms, it fails to explain the electronic properties of complicated systems or those involving chemical interactions that did not predict molecule bonding [290]. That failure, in turn, can be due to the fact that the real orbital structure of electrons is not included. Furthermore, the kinetic energy functional provides a rough approximation to the accurate kinetic energy.

3.4.2. The Hohenberg-Kohn Theorem

Although the Thomas-Fermi theory was able to correlate the energy and other properties of the system with the electronic density, albeit with some limitations, formal evidence of this assumption was developed by P. Hohenberg and W. Kohn in 1964 [291]. Hohenberg-Kohn introduced two theorems that constitute the fundamentals of DFT as a practical computational method. These theorem state that the external potential is a function of the ground-state density. In another sense, the density, which is obvious in 3D space, is employed to define the complicated physics behind the interactions among electrons and, consequently, defines everything regarding the system[286].

First theorem: it states that there is a one-to-one mapping between the external potential $V_{ext}(r)$, of a many-electron system and the ground state density ρ (r) [292]. Thus, the ground state density uniquely determines the Hamiltonian and, consequently, all other properties of the system. It is clear that it is possible to obtain a unique ground state density for the system by providing the external potential [282].

Proof of the first theorem: to prove the first Hohenberg-Kohn theorem, the ground state of the system was assumed to be non-degenerate. This proof is based on a minimum energy principle and this theorem can be also valid for degenerate ground state systems. Suppose, however, there are two external potentials, $V_{ext}(r)$ and $\grave{V}_{ext}(r)$, that vary by more than a constant and lead to the exact ground state density of the system $\rho(r)$. These two potentials in turn would produce two different Hamiltonian, $\hat{H}$ and $\grave{\hat{H}}$ which would have different ground state wave-functions ψ and $\grave{\psi}$. The first Hohenberg-Kohn theorem can be given as:

$$\hat{H}\,\psi = E_0\psi \qquad\qquad\qquad 3.20$$

$$\hat{H}\grave{\psi} = \grave{E}_0\grave{\psi} \tag{3.21}$$

Now, using the variational principle:

$$E_0 = \left\langle \psi \left| \hat{H} \right| \psi \right\rangle < \left\langle \grave{\psi} \left| \hat{H} \right| \grave{\psi} \right\rangle$$

$$< \left\langle \grave{\psi} \left| \hat{H} - \grave{\hat{H}} + \grave{\hat{H}} \right| \grave{\psi} \right\rangle$$

$$< \left\langle \grave{\psi} \left| \hat{H} - \grave{\hat{H}} \right| \grave{\psi} \right\rangle + \left\langle \grave{\psi} \left| \hat{H} \right| \grave{\psi} \right\rangle$$

$$E_0 < \int \rho(\mathrm{r}) \left[V_{ext}(\mathrm{r}) - V\grave{}_{ext}(\mathrm{r}) \right] d\mathrm{r} + \grave{E}_0 \tag{3.22}$$

Similarly, the above calculation can be repeated but with primes and non-primes quantities.

$$\grave{E}_0 = \left\langle \grave{\psi} \left| \hat{H} \right| \grave{\psi} \right\rangle < \left\langle \psi \left| \hat{H} \right| \psi \right\rangle$$

$$< \left\langle \psi \left| \grave{\hat{H}} - \hat{H} + \hat{H} \right| \psi \right\rangle$$

$$< \left\langle \psi \left| \grave{\hat{H}} - \hat{H} \right| \psi \right\rangle + \left\langle \psi \left| \grave{\hat{H}} \right| \psi \right\rangle$$

$$\grave{E}_0 < - \int \rho(\mathrm{r}) \left[V_{ext}(\mathrm{r}) - V\grave{}_{ext}(\mathrm{r}) \right] d\mathrm{r} + E_0 \tag{3.23}$$

By adding Eq. 3.22 and Eq. 3.23 together, it will give a contraction:

$$E_0 + \grave{E}_0 < E_0 + \grave{E}_0 \tag{3.24}$$

Hence, using two different external potentials cannot have the same ground state density $\rho(\mathrm{r})$; that is, each external potential $V_{ext}(\mathrm{r})$ must provide a unique density. Based on this theorem the TISE can be written in terms of the electronic density rather than the wave-function.

$$\hat{H} = V_{ext} + \hat{H}_{int} \qquad\qquad 3.25$$

$$E = \langle \psi | \hat{H} | \psi \rangle = \int V_{ext}(\mathrm{r})\rho(\mathrm{r}) \, d\mathrm{r} + F_{HK}[\rho] \qquad\qquad 3.26$$

Note that energy is expressed in terms of the electron density. As mentioned above, the first theorem of Hohenberg-Kohn proves the existence of a functional correlation between the ground state densities and the external potentials of the many electron systems, but it does not mention anything about either the practical methods to gain the ground state electron densities or the analytic form of the universal functional $F_{HK}(\rho)$. The latter issue has been filled by the second theorem.

Second theorem: it states that the universal functional $F[\rho(\mathrm{r})]$ can be defined in terms of the density, and the exact ground state is the global minimum value of this functional. In other words, this global minimum value of energy functional is the exact ground state density of the system and the exact ground state energy minimizes this functional. Therefore, both the exact ground state density and energy are completely determined via the functional $E[\rho(\mathrm{r})]$.

Proof of the second theorem: since the first theorem allows a density to uniquely define its potential (i.e., Hamiltonian and wave-function), the wave-function can be utilized as a trial wave-function for the problem with a different external potential. This can be expressed as follows:

$$F[\rho(\mathrm{r})] = E_{int}[\rho(\mathrm{r})] + T[\rho(\mathrm{r})] \qquad\qquad 3.27$$

where $E_{int}[\rho(r)]$ is the interaction energy and $T[\rho(r)]$ signifies the kinetic energy. For any wave-function $\grave{\psi}$ the energy functional can be read, according to variational principle, as:

$$E[\grave{\psi}] = \langle \grave{\psi} | \hat{T} + \hat{T}_{int} + \hat{V}_{int} | \grave{\psi} \rangle \qquad 3.28$$

Following the first Hohenberg-Kohn theorem, $\grave{\psi}$ has to relate to a ground state with external potential and electronic density. Hence, $E[\grave{\psi}]$ will be a functional of $\grave{\rho}(r)$:

$$E[\grave{\psi}] = E[\grave{\rho}(r)]$$

$$= \int \grave{\rho}(r) V_{ext}^{\grave{}}(r)\, dr + F[\grave{\rho}(r)]$$

$$> E[\grave{\psi}_0]$$

$$= \int \rho_0(r) V_{ext}(r)\, dr + F[\rho_0(r)]$$

$$= F[\rho_0(r)] \qquad 3.29$$

Thus, one can find the exact ground state energy and density through minimizing the total energy functional system in terms of the variations of the density. Finally, even though the Hohenberg-Kohn theorems use electronic density as the basic variable, it is still difficult to compute any properties of a many-body system because the Hohenberg-Kohn universal functional is unknown (i.e., it does not have any information on the nuclei and its position). So, searching for approximations that are able to solve these difficulties remains one of the main purposes of DFT theory.

3.4.3. The Kohn-Sham Equations

In 1965, a significant stage toward applicability of DFT has been performed by W. Kohn and L. Sham who developed a formalism that is the basis for the present application of DFT in the computational chemistry area. This formalism is a practical approach to solving the Hohenberg-Kohn theorem and is based on the assumption of replacing the real many-body systems with a virtual system of non-interacting electrons, where the virtual system has an overall ground state density equal to the density of the real system. The main premise in the Kohn-Sham method is that the kinetic energy functional of the many-body system can be separated into two parts: the first being the kinetic energy of non-interacting electrons and can be calculated exactly, whilst the second part is a small correction term accounting for the interaction among electrons in the real system.

Based on the Kohn-Sham formalism, the ground state energy of a system containing N nuclei and n electrons can be written as:

$$E(\rho) = -\sum_{X=1}^{N} \int \frac{Z_X}{r_{Xi}}\, \rho(r_1) dr_1 - \frac{1}{2}\sum_{i=1}^{n} \int \grave{\psi}_i(r_1)\nabla_i^2\, \psi_i(r_1) dr_1 + \frac{1}{2}\iint \frac{\rho(r_1)\rho(r_2)}{r_{12}} dr_1 dr_2$$

$$+ E^{CX}(\rho) \qquad\qquad 3.30$$

Or it can be expressed as:

$$E(\rho) = E^T + E^V + E^J + E^{CX} \qquad\qquad 3.31$$

The first term represents the kinetic energy of the nuclear-electron interactions, the second term signifies the kinetic energy of the non-interacting electrons, the third term is the Coulombic repulsions among the total charge distributions at r_1 and r_2, and last term, known as the

exchange correlation term, represents the correction to the kinetic energy arising from the interacting nature of the electrons, and all non-classic corrections to the electron-electron repulsion energy.

E^{CX} is normally separated into two terms: a correlation term E^C and an exchange term E^X, which can be written as:

$$E^{CX}(\rho) = E^C(\rho) + E^X(\rho) \qquad\qquad 3.31$$

where the correlation term is generally associated with the interactions among the same spin electrons, while the final term represents the interactions among the opposite spin electrons. Note that E^C and E^X are also functional of the electron density. These two terms can be of two distinct types: gradient corrected which depend on the electron density (ρ) and its gradient $(\Delta\rho)$, and local functionals that depend only on the (ρ).

3.5. The Exchange-Correlation Functional

Finding a solution for the Kohn-Sham equations remains one of the greatest tasks for DFT theory. Thus, this section will present some approximations that developed the exchange-correlation functional and in turn can provide some insight into their foundations and limitations.

3.5.1. Local Density Approximation (LDA)

The local density approximation (LDA) constitutes the simplest way to explain the exchange-correlation functional. It was proposed by Dirac in 1930 [293] and improved by the Thomas-

Fermi approach, later known as Thomas-Fermi-Dirac approximation [294]. Consequently, the exchange energy for the uniform electron gas system can be written as:

$$E_{X,Dirac}^{LDA}(\rho) = -C_X \int \rho^{\frac{4}{3}}(\text{r}) \, dr \qquad\qquad 3.32$$

where C_X is a constant and it can read as:

$$C_x = -\frac{3}{4}(\frac{3}{\pi})^{\frac{1}{3}}$$

LDA is based on the assumption that at any point in space, the exchange-correlation energy is a function of the electron density only at that point and can be produced by the electron density of a uniform electron gas of the corresponding density. Generally, calculating the correlation energy separately from the exchange energy using LDA is difficult. However, it can be obtained by employing a suitable interpolation approach that starts from a set of values calculated for the number of various densities in a uniform electron gas. In spite of some typical deficiencies (especially, the inadequate cancellation of self-interaction contributions), LDA approximation results are surprisingly accurate. For instance, LDA works to reduce the atomic- ground state energies, whilst the value of binding energies are normally overestimated [295].

It is important to mention that LDA approximation fails in term of describing the electronic structure and the conduction properties of materials with filled d (or f) shells. Such materials (i.e., transition metal or rare-earth metal ions) typically have a large energy gap between the occupied and unoccupied sub-bands and have well-localized d (f) electrons. When using the

LDA approximation to treat such types of materials with an orbital-independent potential, a partially filled d (f) band associated with itinerant d (f) electrons and a metallic-type electronic structure is located [296].

3.5.2. Generalized Gradient Approximation (GGA)

The Generalized Gradient approximation assumes that the atomic or molecular systems are normally varied from the uniform electron gas. In other words, it has a varying electron density $\rho(r)$. The GGA method bases the correlation and exchange energies not only on the electronic density but also on its gradient $\Delta\rho(r)$ [282]. The gradient expansion for the different uniform electron gas is applied in terms of dimensionless minimized gradient as follow:

$$E_X^{GEA} = -(F_X) \int \rho^{\frac{4}{3}} dr \qquad\qquad 3.33$$

where the constant (F_X) is given by $-[\frac{3}{4}\left(\frac{3}{\pi}\right)^{\frac{1}{3}} + \frac{7}{432\pi(3\pi^3)^{\frac{1}{3}}} X^2 + \cdots]$

However, applying this equation directly for the atomic or molecular systems will cause problems because the electron densities vary slowly. This approximation has been improved by following two developments. The first of such improvements was developed by Becke [280, 297], which is based on numerical fitting procedures including big molecular training sets. Along with this first development of GGA approximation, other exchange functionals following this principle include Perdew-Wang (PW) [298], OptX (O) [299], modified-Perdew-Wang (mPW) [300] and Becke88 (B) [301]. The latter is considered the most commonly used one. Therefore, the simple form of exchange energy for uniform electron gas can be read as:

$$E_X^{GGA}(\rho, X) = -(F_X) \int \rho^{\frac{4}{3}} dr \qquad\qquad 3.34$$

Even though these exchange functionals produce accurate reaction barriers and atomization energies for molecules, they fail to describe several important properties of the system in solid-state physics. The second line of this approximation, which is the more rational-based, was proposed by Perdew [302-304] and is based on the assumption that improvement of exchange-correlation functionals could be anchored in basic principles from quantum mechanics, involving correct limits for high and low densities, scaling relations, and the fulfillment of exact relations on the correlation and exchange holes. There are many exchange functionals of this philosophy involving, Perdew86 (P86) [303], Becke86(B86) [303], modified-Perdew-Burke-Ernzerhof (mPBE) [305], and Perdew-Burke-Ernzerhof (PBE) [306]. Among the functionals of this principle, PBE is considered as the most established. These functionals are more accurate in predicting the solid-state properties compared with the first line functionals. However, these functionals generally also have problems in competing with the fitted functionals for the determination of reaction barriers and atomization energies for molecular reactions.

3.5.3. LDA+*U* Method

As we mentioned before, using the LDA to the exchange-correlation functional that exist in density functional theory for the weakly correlated systems (i.e., ionic solids and covalent semiconductors), will provide reasonable ground-state properties and even band structures, which are excited-state properties. However, this method can be unsuccessful and completely incorrect for the strongly correlated systems in which they usually comprise transition metals or rare-earth metals (practically, they have localized d (f) electrons) [307, 308]. In other words, it neglects the orbital dependence of the Coulomb interaction [309]. For evaluation of these strongly correlated systems, the orbital dependence of the self-energy operators should be applied for both d and f electrons. Even though the presence of methods to incorporate the

strong correlations among d and f electrons (namely, Hartree-Fock method and GW approach) [310, 311], the LDA+U method is the most common. A great extension of the LDA approach in density functional theory was proposed during the last two decades by Anisimov and co-workers [312], based on the Hubbard Hamiltonian model now known as LDA+U method [307, 313]. This approach represents the orbital dependence of the self-energy operators in a relatively crude neglecting the accurate details of the spatial variations of the Coulomb potential. This method can be expressed by adding the interaction terms between the correlation electrons to the total energy functional as [309]:

$$E^{LDA+U}[\rho_\sigma(\mathrm{r}), n_\sigma] = E^{LDA}[\rho_\sigma(\mathrm{r})] + E^U[(n_\sigma) - E_{dc}(n_\sigma)] \qquad 3.35$$

where the first term represents the standard LDA energy functional and the last term is the Coulomb potential among electrons. In equation 3.35, σ is the spin index, $\rho_\sigma(\mathrm{r})$ denotes the electron density for electrons in spin-σ and n_σ signifies the density matrix of the localized d (or f) electrons in spin-σ.

Equation 3.35 can be written in a different form as:

$$E^{LDA+U}[\rho_\sigma(\mathrm{r}), n_\sigma]$$

$$= E^{LDA}[\rho_\sigma(\mathrm{r})] + \frac{1}{2}\sum_{m,\acute{m},\sigma} U_{m\acute{m}}\, n_{m\sigma} n_{\acute{m}-\sigma}$$

$$+ \frac{1}{2}\sum_{m,m,m\neq\acute{m},\sigma} (U_{m\acute{m}} - J_{m\acute{m}}) n_{m\sigma}\, U_{\acute{m}\sigma} - \frac{1}{2} U N(N-1) + \frac{1}{2} J N_\uparrow (N_\uparrow - 1)$$

$$+ \frac{1}{2} J N_\downarrow (N_\downarrow - 1) \qquad 3.36$$

When exchange and non-sphericity are neglected, equation 3.36 can be re-written in simple form as follows:

$$E^{LDA+U}[\rho_\sigma(\text{r}), n_\sigma] = E^{LDA}[\rho_\sigma(\text{r})] + \frac{1}{2} U \sum_{i \neq j} n_i \, n_j - \frac{1}{2} U N(N-1) \qquad 3.37$$

3.6. Transition State Theory

Transition state theory (TST), developed in 1930 [314], constitutes a practical approach to a reaction rate for a rarely occurring elementary reaction. In essence, TST is based on the assumption that the reaction space can be divided into two main states: reactant state (RS), which represented the general state of the system before reacting, and the product state (product state) that defines what is thought of as a product of the reaction. The point between these two states is referred to as the transition state (TS) [315]. The lowest energy configurations in the reactant and product states are indicated as the initial state (IS) and final state (FS) respectively. There are two main assumptions made when applying the transition state theory. The first is based on the hypothesis that the reaction follows up a reaction coordinate and should pass through a maximum point known as the transition state (TS). This state can be usually applied when the initial state is unbounded and the system has had enough time to thermally equilibrate. The second assumption of the transition state theory considers that the concentration of the TS is in equilibrium with the substrate of the reaction, which is governed by the law of thermodynamics [316]. Based on these two assumptions, the equilibrium between the reactants and transition state can be described by and can be expressed in the following equation:

$$TS = e^{\left(\frac{-\Delta G}{RT}\right)}[A][B] \qquad 3.38$$

where $\Delta G, h$ and R signify the variation in Gibbs free energy between the reactants and transition state, and Planck's constant and the molar gas constant, respectively. A and B are the substrates. The concentration of the transition state is therefore defined as:

$$TS = e^{\left(\frac{\Delta S}{R}\right)} e^{\left(\frac{-\Delta H}{RT}\right)} [A][B] \qquad\qquad 3.39$$

As mentioned, the second assumption of the TST that the TS and substrates are in the equilibrium state, the reaction rate is governed not only by the concentration of the TS but also by the frequency in which the TS decomposes to generate the products. It is supposed that the frequency of the decomposition of the transition state is relative to the transmission coefficient and the vibrational frequency of relevance:

$$\sigma_e \frac{k_B T}{h} (TS) = \frac{-\delta [A][B]}{\delta t} \qquad\qquad 3.40$$

where σ_e, k_B and h denote the reaction degeneracy number, the Boltzmann constant and Planck's constant, respectively. So, equation 3.39 can be written as:

$$k = \sigma_e \left(\frac{k_B T}{h}\right) e^{\left(\frac{\Delta S}{R}\right)} e^{\left(\frac{-\Delta H}{RT}\right)} \qquad\qquad 3.41$$

Equation 3.41 is known as the Eyring equation [316].

3.7. Software

Density Functional Theory (DFT) is the most common and efficient way for solving the many-body system problems and is performed in many simulation packages. Variations between these packages might be based on methods applied to solve Kohn-Sham equations and functions employed in constructing Bloch functions. No simulation package is perfect and each has its own advantages and disadvantages. Three simulation packages have been employed to run the quantum calculation in this study: Vienna Ab initio simulation package (VASP), DMol^3 and Phonopy. The use of these packages is well suited to this present study and have been described in recent publications.

3.7.1. The Vienna *Ab initio* Simulation Package (VASP)

The Vienna Ab initio Simulation Package (VASP) is an efficient DFT software developed recently by Georg Kresse and his co-workers [317, 318]. VASP is the most widely used package for studying 3D bulk systems with periodic boundary condition and in applications in key areas of modern solid-state physics and chemistry [317, 319, 320]. VASP uses plane wave basis sets and the ultra-soft pseudopotential approximation or projector augmented wave (PAW) method [321, 322]. The plane wave basis sets are slightly unusual for molecular applications, because of the association of plane wave basis sets with free electron like systems. Although ultra-soft pseudopotential approximation describes the interactions between electrons and ions, VAPS utilizes efficient iterative matrix diagonalization methods, residual minimization with direct inversion of the iterative subspace (RMM-DIIS) and blocked Davidson algorithm, to determine ground state energy. Either or a combination of both can be employed regularly, depending on the size of the system. The blocked Davidson algorithm is stable but slow, whilst RMM-DIIS is considerably faster. For the large systems, the excellent

option is to combine these two methods to first use blocked Davidson algorithm and then RMM-DIIS.

VASP requires a minimum of four input files (namely POSCAR, POTCAR, INCAR, and KPOINTS). The POSCAR file consists of the fractional coordinates and the lattice vector of atomic positions of the system to be applied in calculations. The POTCAR file comprises the pseudopotential for every atomic species used in calculations. For the large system that has two atomic species or even more, the pseudopotentials of atomic species are just concatenated in the POTCAR file and their order should be according to the POSCAR file. The INCAR file is important, and consists of a large number of parameters that determine what and how to calculate. The KPOINTS file comprises k-points selected in calculations.

3.7.2. DMol^3

DMol^3 is a software that utilizes numerical functions on an atom-centred grid as basic functions and can be used for calculations in the gas phase, solution, or solid state [323-325]. DMol^3 uses two sets of the DFT functional: local and non-local functional. The local functionals are PWC and VWN of Perdew and Wang and Vosko el al. [326], respectively, whilst the non-local functional includes PW91 [327] PBE [306], BP [328], BLYP [329], HCTH [330], and RPBE [331]. Along with these sets of the DFT functional, DMol^3 provides various types of atomic orbitals used to specify the basis set ranging from small to large [325]. The basis sets contain: minimal basis set (MIN), double numerical (DN), double numerical plus d-functions (DND), double numerical plus a polarisation p-functions (DNP) and triple numerical plus a polarisation (TNT). DND basis set extends the DN set with a polarisation d-function on all non-hydrogen atoms; the DNP set improves the DND set by including a polarisation p-function on all non-hydrogen atoms and an additional polarisation function is applied on all atoms over the TNP

basis sets. DMol^3 is efficient and accurate for calculating relaxation and geometry optimization, excited states of molecules, potential barriers, interaction energies, Fukui indices thermodynamic properties and vibrational spectra.

3.7.3. Phonopy

The Phonopy package was developed by Togo in 2008 [332] for phonon to determine thermal conductivity and thermodynamic properties. Phonopy code implemented the mixed-space approach which replaced the method of Parliński et al. [333, 334] for calculating phonon properties. In essence, Togo et al. also derived a formulation for the evaluation of the third-order force constants through extending the mixed-space approach [335]. Phonon calculations can be performed by the supercell way and the real-space force constants of supercells can be calculated in the density-functional perturbation theory DFPT performed in the VASP package. Based on a supercell approach, Phonopy software estimates phonon dispersions entailing atomic displacements within the unit cells. Estimated phonon frequencies enable computation of thermodynamic properties, [336, 337] that is, temperature-dependent functions of enthalpies and entropies.
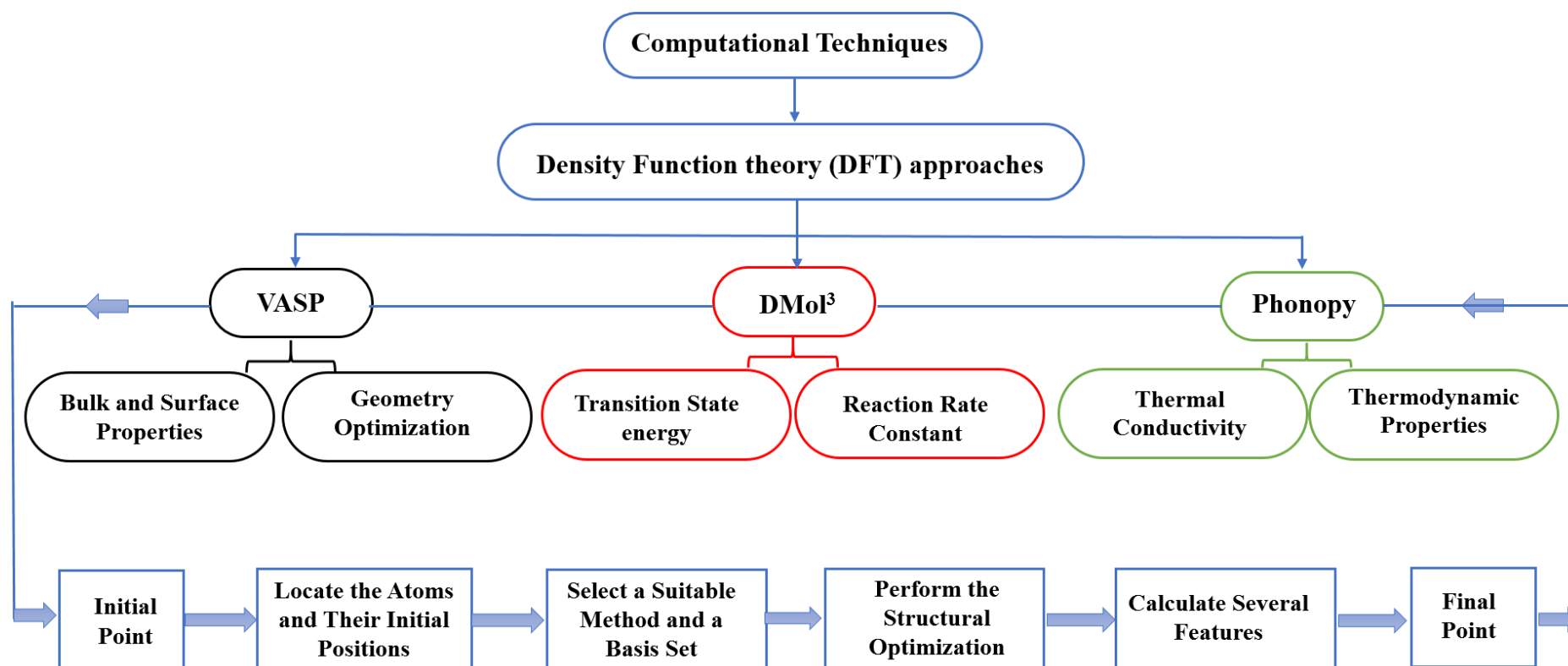
Scheme 3.1: Methodology diagram of the computational work using the DFT approaches.

Chapter 4

Reactions of products from thermal degradation of PVC with nanoclusters of *α*-Fe₂O₃ (hematite)

The following chapter is a modified version of <u>paper I</u>:

Abstract

Polyvinyl Chloride (PVC) plastics constitutes a large fraction of buildings, packaging and electronic devices, whereas, the annual emission electric arc furnace dust (EAFD) from steel manufacturing operations has recently peaked at nearly 6 Mt. Co-pyrolysis of PVC with EAFD currently represents a focal abatement technology for both categories of pollutants. However, despite of several experimental investigations; the mechanisms underlying interaction between EAFD and PVC remain largely speculative. Herein, we examine theoretically reactions of major products from thermal degradation of PVC with nanoclusters of iron (III) oxide, α-Fe_2O_3 (hematite) as a representative model for the various metal oxides in EAFD. The facile nature for the H-Cl bond fission over hematite is in line with experimental findings, pointing out to formation of iron chlorides from pyrolysis of Fe_2O_3-PVC mixtures. Interaction of selected chlorinated C_1-C_3 cuts with the hematite structure preferentially proceeds via a dissociative adsorption pathway. Results from this chapter shall be instrumental to understand, on a precise molecular basis, fixation of halogens on transitional metal oxides; a viable thermal recycling approach for polymeric materials laden with halogenated constituents.

4.1. Introduction

Steel manufacturing facilities annually emit 4.3 - 5.7 Mt of electric arc furnace dust (EAFD) [338]. Designing an effective recycling methodology of EAFD has been a central research theme as it ensures the safeguard of the natural resources as well the environment. Due to the presence of heavy toxic metals such as Cr, Cd and Pb, EAFD imposes serious environmental and health concerns [339, 340]. For example, various metal oxides species in EAFD promote the formation of the notorious environmental persistent free radicals such as phenoxy [66]. The main elements of EAFD are zinc and iron, which vary in the range of 2-46% and 10-45%, respectively. These components mainly present in the form of zincite (ZnO), franklinite ($ZnFe_2O_4$), magnetite (Fe_3O_4), hematite (Fe_2O_3) and might also exist in small concentrations of hydrated zinc chloride [12, 62]. Thus, these high load of precious metals in EAFD have promoted a great deal of research aiming to extract metals from EAFD via both hydro-metallurgical and pyro-metallurgical techniques [339, 341]. The latter processes typical employ energy-intensive operations and necessitate complex clean-up methods [104]. This in turn reduces the economic feasibility of pyro-metallurgical operations. Similarly, applications of hydro-metallurgical procedures on an industrial scale are rather limited due to the accumulations of iron species in deployed acidic solutions that are very selective toward dissolution of zinc and lead [59, 105].

Co-pyrolysis of EAFD with halogen-containing materials has emerged as a promising synchronous recycling methodology for both resources [342]. The underlying derive of this approach relies on the profound fixation ability of halogenated species by metallic oxides constituents in EAFD [41, 239, 253]. Polyvinyl chloride (PVC) represents the largest fraction of the halogenated waste. Owing to superior chemical resistance and flame retardancy behavior, PVC is heavily used in electronic and electrical devices, construction materials, food

packaging and household goods *etc* [6, 343-345]. The global generation of PVC peaked at 61 Mt in 2013 and is projected to triple in 2021[6]. Thermal recycling of PVC-containing waste plastic streams is not a viable option as it results in the generation of the hazardous polychlorinated dibenzo-*p*-dioxins and furan (PCDD/Fs) or dioxins for short [253, 346-348]. Effective Recycling of PVC truly rests on the ability to remove its chlorine content.

TGA-DSC studies on PVC and mixtures of PVC/metallic oxides provide insightful mechanistic insights into their decomposition behavior. Chemical analysis in GC/MS provides temperature-dependent product profiles of the decomposition products while XRD measurements track the change in the elemental composition of EAFD upon its co-pyrolysis with PVC [253, 349]. XRD patterns reported by Al-Harahsheh found that EAFD consists mainly of zincite (ZnO), franklinite ($ZnFe_2O_4$), magnetite (Fe_3O_4) and hematite (Fe_2O_3) [101]. Consensus of opinions from TGA profiles indicate that weight loss curve of pure PVC signifies two main peaks corresponding to elimination of HCl (around 473K) and fission of the carbon bonds in the PVC backbone (~ 633K). In a previous theoretical study [350], we have illustrated that, the common presence of defects in the structure of PVC, in terms of chlorines occupying tertiary positions, increases the reaction rate of the dehydrochlorination initial step (in reference to the ideal PVC structure encompassing secondary chlorines). Our previous kinetic analysis on HCl elimination from model compounds of PVC has also indicated that, rate constants for the dehydrochlorination step are independent of the length of the carbon chain [351].

The presence of EAFD during pyrolysis of PVC significantly reduces the activation energy of the first dehydrochlorination regime. The presence of EAFD enhances the mass loss of PVC in the first stage from 37% to nearly 80%. The additional mass loss was attributed to the formation of metal chlorides (mainly $ZnCl_2$ $PbCl_2$, $FeCl_2$, and $FeCl_3$) [101].

It has been shown that ZnO, La_2O_3, Fe_2O_3 capture the emitted HCl from thermolysis of PVC [241]. The consumed chlorine transforms the metal oxides into metal chlorides. For instance, the addition of ferric oxide during thermal decomposition of PVC waste results in the formation of $FeCl_3$. These iron halides are consequently left in the residue after being subjected to water leaching [59]. Findings by Oleszek et al. has illustrated that, the co-combustion of Fe_2O_3 with tetrabromobisphenol (a majorly deployed brominated flame retardants) [352] assumes a similar role in suppressing formation of HBr and forms iron bromides [263].

An oxidation experiment by Masuda et al. [241] found that, the reaction of hematite (α-Fe_2O_3) with PVC significantly reduces the generation of HCl while enhancing the emission of gaseous products such as CO and CO_2 under various combustion conditions (in reference to neat PVC samples). Moreover, the yield of chlorobenzenes surprisingly increases upon introducing hematite. A plausible explanation is that the formed $FeCl_3$ mediates cyclization of fragmented polyenes into aromatic ring and acts as a chlorinating agent. Higher concentration of chlorobenzene boosts the char formation. More recently, Al-Harahsheh et al. [101] examined extraction of iron in EAFD by pyrolysing it with PVC. They showed that, between 25% and 56% of iron was recovered by leaching with boiling water, while the other remaining percentage represent magnetite and hematite.

Despite of detailed investigations into mixing of PVC with metal oxides over the last few years, the specific underlying mechanism of the reactions of HCl and other chlorinated C_1-C_6 cuts with hematite have remained poorly understood. In light of the importance of thermal recycling of halogenated fuels with hematite as an emerging abatement technology for both categories of pollutants, it is essential to understand the elemental processes governing interactions of halogenated species with metal oxides at a precise atomic scale. The fundamental objective is

to design more efficient catalysts and to optimize the current deployed procedures. In particular, we aim to provide atomic-base insight into the detailed reaction pathways and to identify the key elementary steps that dictate the reaction rates. Many intermediates in the reaction PVC + Fe_2O_3 are expected to be highly transient nature and their presence in the system influences the overall yield of dechlorination process. Thermo-kinetic and mechanistic aspects of the investigated reactions could not be obtained by merely interpreting experimental results. These important aspects could only be obtained via carrying out accurate DFT calculations.

To this end, this chapter reports a theoretical investigation into the reaction of HCl and selected chlorinated hydrocarbons with α-Fe_2O_3, as a model compound for metal oxides in EAFD. This chapter is part of our ongoing effort to investigate thermal recycling of halogenated fuels with Fe_2O_3 and other metallic oxides constituents in EAFD. In a recent study [350], we utilize a cluster model of α-Fe_2O_3 to investigate its reactions with a wide range of brominated alkanes, alkenes and aromatics. Throughout the discussion, we pointed out to the difference in activation energies among the two halogenated systems. Herein, we attempt to map out reaction networks operating during the interaction of a cluster model of dehydrated α-Fe_2O_3 with both HCl and major products from the degradation of PVC. Findings from the current chapter can be useful to understand, on a precise molecular basis, the mechanisms of chlorine fixation on transitional metal oxides in the form of metal chlorides. Such knowledge finds direct application in the pursuit to design effective and viable recycling technologies for halogenated waste steam.

4.2. Computational Method

Total energy and structural optimizations were carried out in the framework of the density functional theory (DFT) using the DMol^3 program package [324, 325]. Local Density Approximation (LDA) along the exchange-correlation of the Padrew and Wang (PAW) functional has been utilized in all calculations [353] . The theoretical methodology comprises a global cut-off of 3.6 Å and a double-polarized numeric basis set of DNP for all electrons [325]. The total energy achieves a tolerance of 1×10^{-6} Hartree. Final calculated energies were corrected via a dispersion correction term based on a methodology developed by Tkatchenko and Scheffle [354]. The complete LST/QST method locates transition states.

The obtained vibrational frequencies enable to estimate thermochemical parameters at elevated temperatures, from which Arrhenius rate parameters can be obtained. Reaction rate constants have been fitted to the Arrhenius equation over a temperature range of 300-1000 K based on the classical transition state theory [355]:

$$k\,(T) = A \exp\left(-E_a\,/\,RT\right) \qquad\qquad 4.1$$

Where A denotes preexponential factor, E_a signifies the activation energy, R stands for the gas constant (1.987 cal K^{-1} mole^{-1}) and T is the temperature in Kelvin [356].

For α-Fe$_2$O$_3$ (0001) surface calculations, A $3 \times 3 \times 1$ Monkhorst-Pack κ-point scheme was used to perform the Brillouin zone integrations. The vacuum region between the adjacent slabs was set to 15 Å along the z-direction to reduce the interaction between the slabs. Throughout surface calculations, the top six layers as well as the adsorbed H and Cl atoms were allowed to relax, whilst the bottom two layers were kept fixed at their bulk positions.

4.3. Results and Discussion

4.3.1. Hematite (α-Fe$_2$O$_3$) Cluster

Hematite nanoparticles adapt a variety of crystallographic forms, for instance, alpha-hematite, beta-hematite and gamma-hematite. Among these different phases, α-Fe$_2$O$_3$ represents the most stable phase and assumes direct applications in many fields [357-360]. Hematite can be formed through oxidation of Fe$_3$O$_4$ at room temperature [361, 362]:

$$O_2 + 4Fe_3O_4 \rightarrow 6Fe_2O_3$$
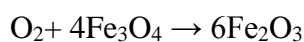
Herein, we adapt the (Fe$_2$O$_3$)$_{n=3}$ cluster utilized in our recent study [350] to model reactions of hematite with brominated motilities. Figure 4.1 depicts optimized structures of the α-Fe$_2$O$_3$ cluster. The optimized structure of α-Fe$_2$O$_3$ comprises three-fold coordinated iron atoms and two-fold coordinated oxygen atoms. To test the computational accuracy of the deployed α-Fe$_2$O$_3$ cluster, our calculated Fe-O interatomic distances, amount to 1.83/2.04 Å. These values reasonably match analogous bulk values sourced from XANES spectra at 1.96/2.08 Å [363]. Our recently estimated Mayer bond orders and Hirshfeld charges provide detailed electronic analysis of the structure. Most importantly, the adapted α-Fe$_2$O$_3$ cluster features surface Fe-O bond that exists in the top layer of the most thermodynamically stable configuration of α-Fe$_2$O$_3$, namely the Fe$_2$O$_3$(001) facet [350]. In addition to well-defined surfaces, Fe$_2$O$_3$ in real systems also exists in the form the nanoparticles [364]. The presence of a particular surface termination in the nanostructures depends on its relative thermodynamic stability. For instance in a recent paper, we constructed a Wulff shape for copper bromide nanoparticles that incorporates more than one Miller index in its facets [365].
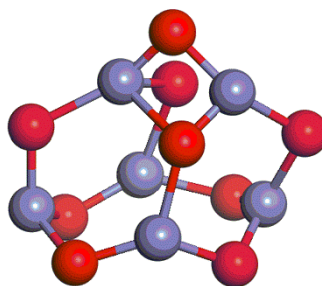
Figure 4.1. Optimized structure of hematite (α-Fe$_2$O$_3$) cluster. Blue spheres denote iron atoms and red spheres signify oxygen atoms. This code of colours applies to all Figures

4.3.2. Dissociative Adsorption of Hydrogen Chloride over α-Fe$_2$O$_3$ Cluster

HCl signifies the initial and the most abundant product from decomposition of PVC. HCl typically accounts for nearly 55% of the total mass loss of PVC during its pyrolysis [366]. Thermodynamic calculations as well as pilot-scale measurements have unequivocally indicated that HCl is the most dominant chlorine species in the gas phase [135]. HCl is truly an inactive chlorinating agent on its own right; yet the so-called Deacon reaction readily transforms it into the active chlorinating agent of molecular chlorine (Cl$_2$) [138]. The growing experimental evidences from TGA-DSC profiles have elucidated that, evolved HCl from PVC converts Fe$_2$O$_3$ into FeCl$_{(n\ =\ 2\text{-}3)}$ [367]. Overall, we find that, HCl reaction with α-Fe$_2$O$_3$ proceeds in a very alike reaction network with that of HBr [350]. Yet, as expected higher bond dissociation energy (BDE) for H-Cl (103.2 kcal mol^{-1}) [135] in reference to H-Br (87.1 kcal mol^{-1}) [367] dictates higher activation energies for the former system.

Figure 4.2 shows reactions encountered in the interaction of HCl with the α-Fe$_2$O$_3$ cluster. Physisorption of HCl on the α-Fe$_2$O$_3$ cluster generates the cluster-molecule adduct M1 that resides 10.6 kcal mol^{-1} below the separated reactants. In the M1 configuration, the H-Cl bond elongates by 7.1%, when compared with the equilibrium distance in the gaseous HCl molecule

(1.39 Å). Dissociation of the adsorbed HCl molecule over Fe-O bond liberates 31.7 kcal mol^{-1} of excess energy and results in the formation of the M2 configuration. Breakage of the H-Cl bond along the reaction M1 → M2 demands a trivial activation energy of 10.3 kcal mol^{-1} via the transition structure TS1. This value slightly overshoots the analogous initial barrier in case of HBr; 8.2 kcal mol^{-1} [350]. The formed Fe-Cl bond length in the M2 structure amounts 2.30 Å, a value that reflects very well the analogous theoretical (2.17 Å) [368] value bond in bulk FeCl$_2$.

Conversion of Fe$_2$O$_3$ into FeCl$_{(n=2-3)}$ occurs through two subsequent steps, further dissociative adsorption of HCl molecules on O-Fe linkages and the release of water molecules. Figure 4.2b maps out these two chemical events. Decomposition of HCl on a neighboring O-Fe bond demands an activation energy of 12.1 kcal mol^{-1} and forms the structure of M4. In a subsequent step, the formation of M5 structure occurs through a slightly exothermic reaction of 5.5 kcal mol^{-1} and it necessitates a relatively sizable barrier of 27.9 kcal mol^{-1} characterized by TS3. This process produces adsorbed H$_2$O molecule via an intramolecular hydrogen transfer between the two hydroxyl groups. Inspection of the M5 structure illustrated in Figure 4.2b reveals that, the ferryl Fe-OH$_2$ bond length (i.e., 2.20 Å) correlates very well with the corresponding distance (2.15 Å) for adsorbed water molecule on the hematite (0001) surface [369]. In the final step of the dissociative uptake of HCl, the water-iron bonded molecule departs the cluster generating the oxychloride structure of M6 via an endothermic reaction of 21.4 kcal mol^{-1}. Clearly, the M6 structure presents a precursor for the transformation of Fe$_2$O$_3$ into iron chlorides. If the two-step process in Figure 4.2b continues, the hematite phase in EAFD is consumed into iron chlorides; in accord with the experimental observations.
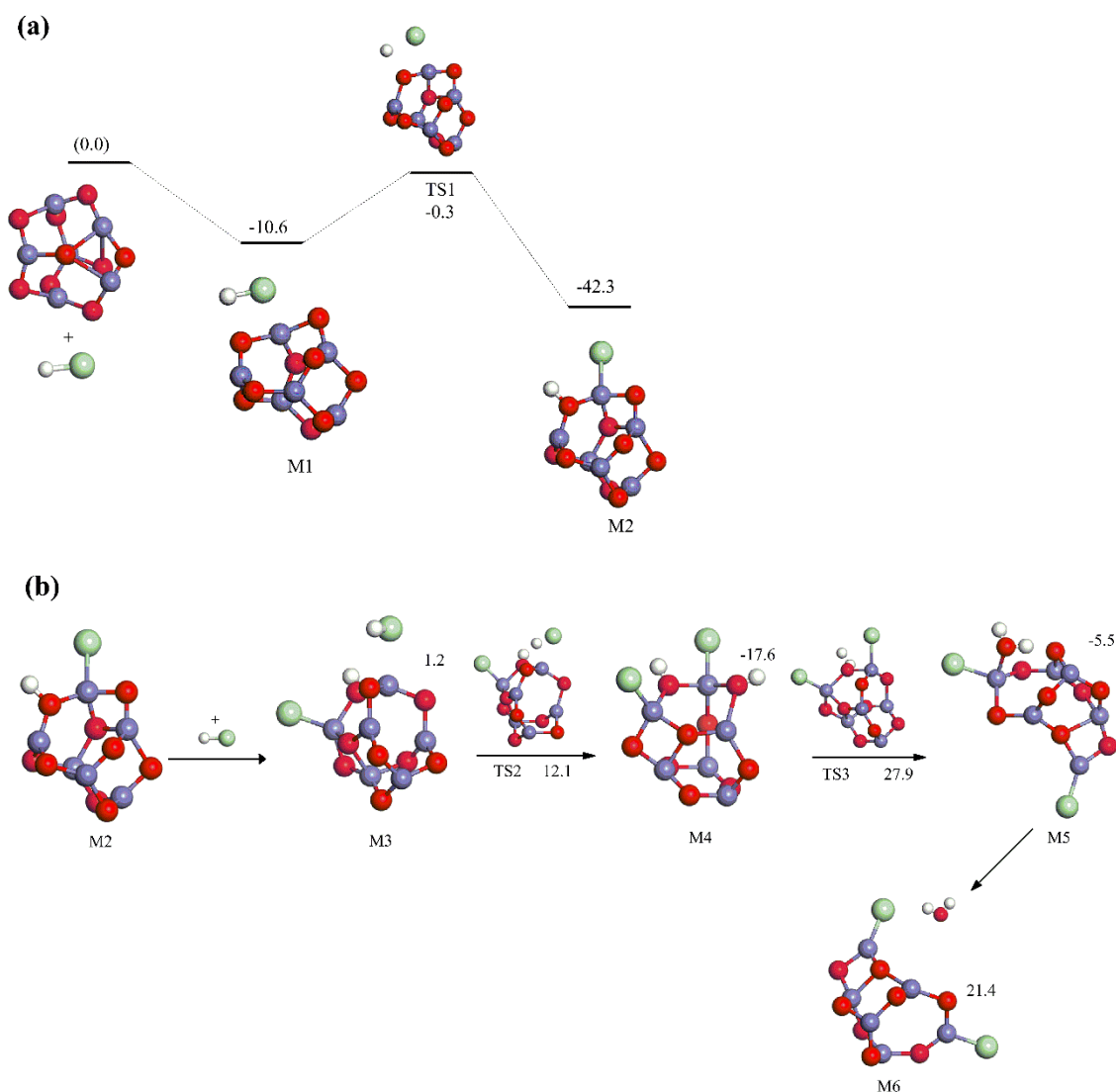
Figure 4.2. Reaction mechanism for HCl molecule and the hematite (α-Fe$_2$O$_3$) cluster. Values are in kcal mol^{-1} with respect to the initial reactant in (a) and to reactants in each step in (b). Large green spheres denote chlorine atoms and white spheres signify hydrogen.

The facile nature of mechanisms in Figure 4.2 indicates that, the formation of iron chlorides occurs simultaneously with the dehydrochlorination of PVC. This finding is in line with the experimental findings of Al-Harahsheh who observed a distinct reversal in the heat flow from an endothermic nature in pure PVC to an exothermic process in the presence of EAFD [101]. The exothermic event revealed by TGA-DSC data was attributed to the formation of new chemical new bonds leading to formation of metal chlorides. A significant 23% increase in the mass residue of the EAFD when co-pyrolysied with PVC was attributed to the fact that captured

HCl does not leave EAFD as volatile iron chlorides [101]. In fact, evaporation of $FeCl_3$ along the reaction $Fe_2O_3 + 6HCl \rightarrow 2FeCl_3 + 3H_2O$ was found to be highly endothermic by ~ 32 kcal/mol at the temperature range of HCl release from PVC; i.e., 700 − 1000 K [59]. Nonetheless, iron volatilization in the form of iron chlorides was reported by Lee and Song who explained that, the rate of iron volatilization depends primarily on the heating rate where a negligible rate was observed at a heating rate below 5 K/min [253].

Table 4.1 lists estimated activation energies and pre-exponential A factor fitted in the temperature region of 300-1000 K for all reactions. Figure 4.3 depicts Arrhenius plots for the two HCl uptake reactions M1 $\rightarrow$ M2 and M4 $\rightarrow$ M5. In reference to the corresponding HBr + Fe_2O_3 system [350], the first dissociative adsorption step in case of HCl is slower by factors of 113.2 and 68.4 at 500 K and 750 K; respectively. Thus, it is inferred, that chlorination of Fe_2O_3 by HCl to be slower than its bromination by HBr. Nonetheless, both halogenation mechanisms adapt similar reaction pathways.

Table 4-1. Kinetic parameters of reactions fitted in the temperature range of 300-1000K

Species	Reaction	A (s^{-1})	Ea (kcal mol^{-1})
Hydrogen chloride	M 1→ M2	3.18×10^{10}	7.9
	M3 → M4	6.65×10^{10}	8.3
	M5 → M6	9.27×10^{10}	22.9
Chloroethene	M7 → M9	3.00×10^{11}	5.8
	M7 → M8 direct elimination	1.12×10^{11}	46.5
	M7 → M8 dissociative adsorption	8.22×10^{10}	73.9
1-Chloro-1-propene	M10 → M12	3.32×10^{11}	13.5
	M10 → M11 direct elimination	3.06×10^{10}	53.1
	M10 → M11 dissociative adsorption	4.82×10^{10}	76.8
Chloroethane	M13 → M14 direct elimination	3.43×10^{9}	30.9
	M13 → M14 dissociative adsorption	1.42×10^{11}	65.1
2-Chloropropane	M16 → M17 direct elimination	2.84×10^{10}	43.8
	M16 → M17 dissociative adsorption	1.77×10^{12}	61.1
Chlorobenzene	M19 → M20	1.99×10^{12}	14.3
2- Chlorophenol	M21 → M23	5.14×10^{15}	20.3
	M21 → M22	7.19×10^{15}	34.2
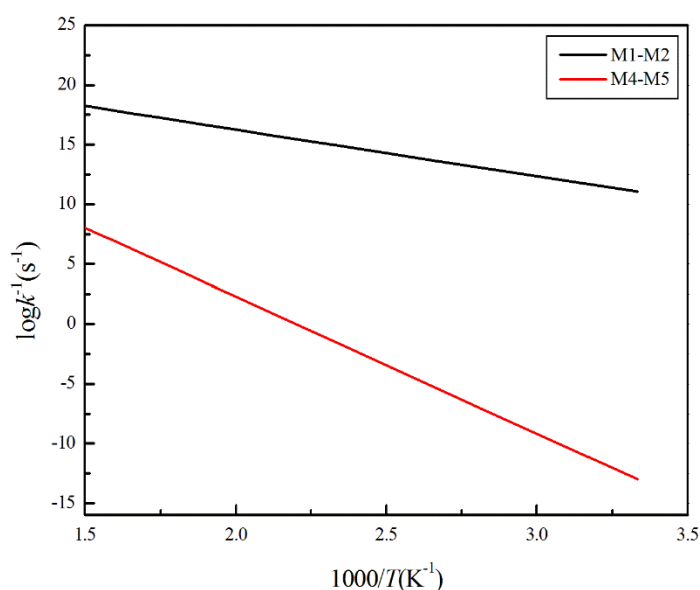
Figure 4.3. Arrhenius plots for reactions between the hematite (α-Fe$_2$O$_3$) cluster and HCl molecules.

It is very-well documented that energies obtained from deploying a cluster model maybe sensitive to the edge effects when contrasted with periodic systems [370]. However, reactions of PVC constituents with the Fe$_2$O$_3$ model occur on the catalytic active sites; that are surface Fe-O bonds which are well represented in the cluster model. In order to provide a structural and energy comparison between a cluster versus a periodic surface model, we utilize a surface model of the α-Fe$_2$O$_3$ (0001) termination to investigate the first reaction step entailing HCl molecule and contrasted obtained values with corresponding results obtained from the cluster model. Figure 4.4 presents energies and structures for the first step in the HCl + Fe$_2$O$_3$ interaction. The following remarks summarise the satisfactory agreement between the two models

1- As illustrated in Figure 4.4, the H-Cl bond of M1$_{Surface}$ configuration is elongated by 6.9% in comparison with the equilibrium distance in the gaseous HCl molecule (1.39 Å). This reasonably corresponds with our finding from the cluster model (i.e. 7.1%).

2- In the dissociative structure (M2$_{Surface}$), the Fe-Cl bond length amounts 2.35 Å, a value that reflects very well the analogous value in the cluster model, i.e. 2.30 Å.

3- Physisorption and chemisorption energies for the reaction of HCl on the α-Fe$_2$O$_3$ (0001) surface (-9.1 and -36.2 kcal mol^{-1}) agree well with the values obtained over the cluster (i.e. -10.6 and -42.3 kcal mol^{-1}).
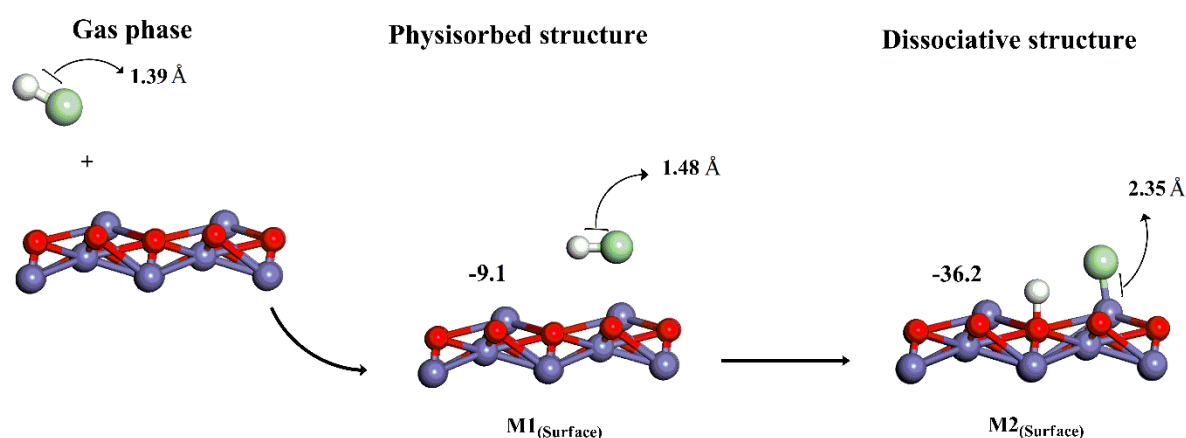
Figure 4.4. Reaction mechanism for HCl molecule and the hematite (α-Fe$_2$O$_3$) surface. Values are in kcal mol^{-1} with respect to the initial reactant. Only the first two Fe layers are shown.

4.3.3. Degradation Mechanisms of Organohalogens

Breakages of carbon linkages in PVC during its pyrolysis produce a wide range of chlorinated compounds [6, 130, 347, 352]. In an analogy to our recent study on thermal recycling of brominated flame retardants using α-Fe$_2$O$_3$ [350], we study the interaction of hematite nanoclusters with various chlorine model molecules; namely (Chloroethene (CH$_2$CHCl), 1-

chloro-1-propene (C_3H_5Cl), chloroethane (CH_3CH_2Cl) and 2-chloropropane (C_3H_7Cl)). These compounds serve as a good representation of chlorinated structural entities stemmed from thermal decomposition of PVC; with corresponding carbon – chlorine BDE falling in the narrow range of 84.6 - 91.2 kcal mol^{-1} [367, 371].

Reaction of chlorinated alkanes and alkenes with α-Fe$_2$O$_3$ cluster can take place through two possible pathways: (i) direct HCl elimination featured with high energy barriers; (ii) low-energy dissociative addition that is followed by a β-hydride elimination step; thereby forming olefins. Lewis acid–base pairs in metal oxides function as potent catalysts for the cleavage of carbon-halogen bonds with greater selectivity if compared with carbon-hydrogen bonds [372, 373]. In this section, we assess the catalytic capacity of α-Fe$_2$O$_3$ toward dehydrochlorination of the selected chlorinated C_2-C_3 cuts with the aim to illustrate chemical phenomena encountered in the co-pyrolysis of EAFD with fragments of PVC.

Figure 4.5 shows both direct elimination and dissociative addition reactions for the catalytic decomposition of vinyl chloride, 1-propenyl chloride, ethyl chloride and 2-propyl chloride on the α-Fe$_2$O$_3$ cluster. In the first step of these reactions, an initial cluster–molecule adduct initiates the Lewis acid–base reaction between α-Fe$_2$O$_3$ cluster and the considered organohalogen molecules. In the initial physisorbed states, carbon–chlorine bonds in the chloroethene, 1-chloro-1-propene, chloroethane and 2-chloropropane are elongated by 23.5%, 5.6%, 6.5% and 15.7%, respectively when compared with the equilibrium distances of their parent gas phase molecules.
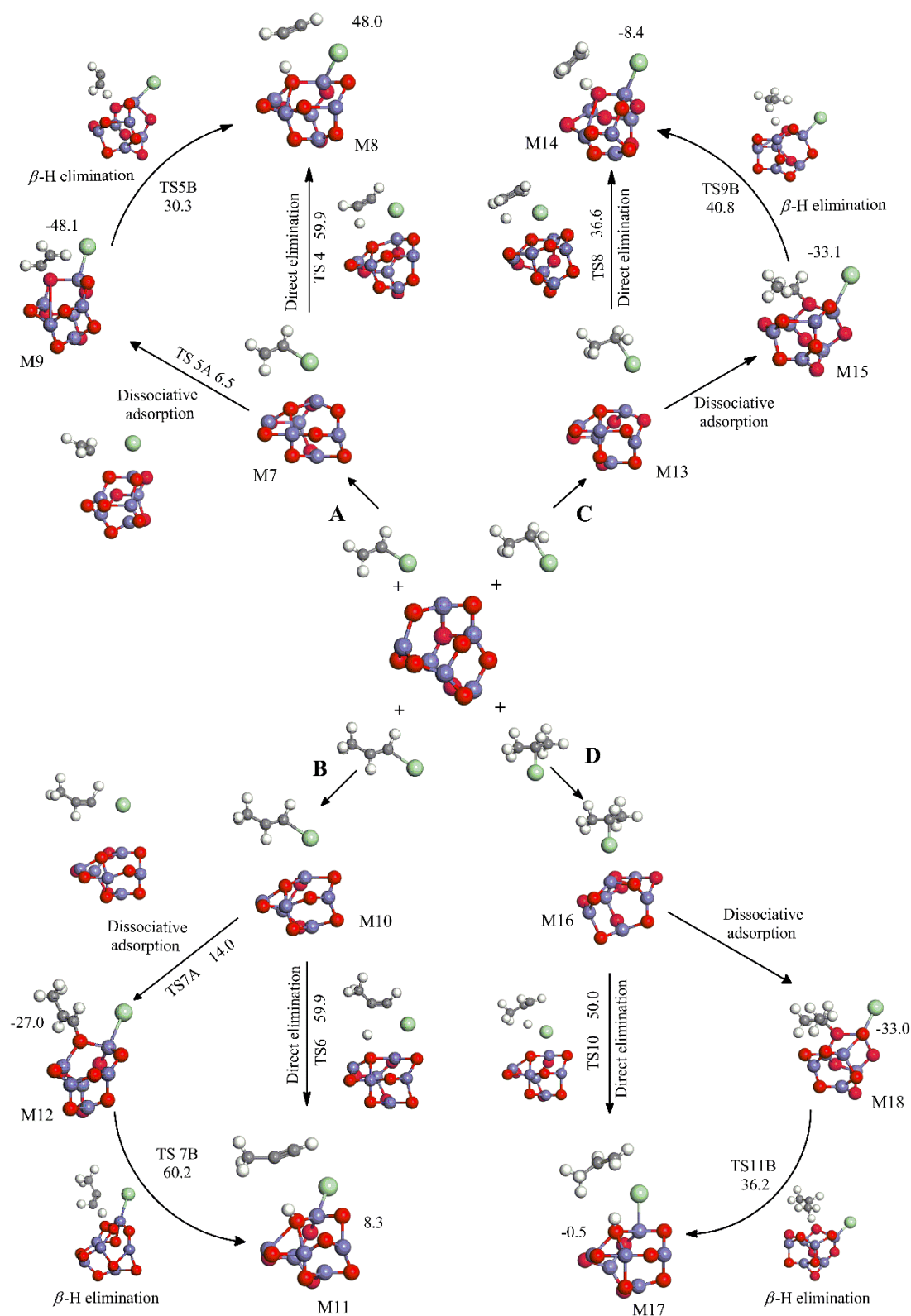
Figure 4.5. Reaction of chloroethene (A), 1-chloro-1-propene (B) chloroethane (C), and 2-chloropropane (D) with the hematite (α-Fe$_2$O$_3$) cluster. Values are in kcal mol^{-1} in reference to the physisorbed M7, M10, M13, M16 structures; respectively.

.

96

α-Fe$_2$O$_3$ cluster displays effectiveness towards dissociative addition pathway in which the surface Fe-O linkages participate in the activation of the C–Cl bond in the first step. Despite of our best efforts, no transition states could be located for the rupture of the C-Cl bonds in chloroethane and 2-chloropropane, while the process proceeds via trivial barriers of 6.5 kcal mol^{-1} (TS5 in Figure 4.5.A) and at 14.0 kcal mol^{-1} (TS7A in Figure 4.5.B) for chloroethene and 1-chloro-1-propene, correspondingly. The next step is the activation of C−H bond followed via a β(H)-hydride transfer to an oxygen site to form an olefin. The β-hydride elimination steps require sizable activation energies varying between 69.2 kcal mol^{-1} for the desorption of CH$_3$CHCH$_2$ molecule (TS11B) to 87.2 kcal mol^{-1} required to form a CH$_3$CCH molecule (TS7B) as shown in panels D and B in Figure 4.5, respectively. Generally, barrier for the desorption of stable molecules via the β(H)-hydride transfer rests not only on the strength of the dissociated C-H bond, but as well on the strength of the O-C bonds [367].

Considering the direct HCl elimination pathway, Fe-O bonds significantly reduces barriers for the dehydrochlorination corridor in reference to the uncatalyzed analogous gas phase process. For example, the formation of ethene through TS8 requires a barrier energy of 36.6 kcal mol^{-1}. This is significantly lower than that for the homogenous HCl elimination from chloroethane, i.e. 57.5 kcal mol^{-1} [374].

Careful examinations of reactions in Figure 4.5, provides three important indications: (i) elimination corridors systematically require higher barrier energies in the range of 36.6– 59.9 kcal mol^{-1} than dissociative addition formation, whose reaction barrier reside in the range of 6.5 - 14.0 kcal mol^{-1}, (ii) while barriers for the direct elimination routes are significantly higher than dissociative addition channels, barriers for the subsequent β-hydrogen transfer incur overall barriers that are comparable with the barriers of the direct elimination pathways, and

(iii) dissociative addition routes undergo the S_N2 category of mechanism, whilst the direct elimination routes undergo the $E2$ mechanisms (bimolecular elimination) similar to the analogous mechanism prevailing in the dehydration of ethanol over Al_2O_3 [375].

Considering the dissociative adsorption channel as a two-step mechanism affording the products of the direct elimination pathway, the dissociative addition channel is expected to predominate the direct elimination route for chloroethene (30.3 kcal mol^{-1} versus 59.9 kcal mol^{-1}) whereas the latter should prevail over the former for chloroethane (36.6 kcal mol^{-1} versus 40.8 kcal mol^{-1}). Both mechanisms incur very similar overall activation barriers for 1-chloro-1-propene (60.2 kcal mol^{-1} versus 59.9 kcal mol^{-1}). Nonetheless, such small difference most likely resides within the expected accuracy margin of the adapted theoretical methodology.

Obtained barriers for the direct elimination pathway seem to positively correlate with the carbon-chlorine BDEs. For instance, as shown from panel C and D in Figure 4.5, the HCl elimination channel in case of chloroethane (C-Cl BDE = 84.2 kcal mol^{-1}) and 1-chloro-propene (C-Cl BDE = 88.6 kcal mol^{-1}) proceeds via very distinct barriers of 36.6 kcal mol^{-1} and 50.0 kcal mol^{-1}; in that order.

Figure 4.6 shows the variation in the rate constant of the two possible pathway reactions between 300 and 1000 K. Reaction rate constants for the two steps in the dissociative adsorption route has been estimated with considering the physisorbed state as the initial reactant. Based on values in Figure 4.6, the dissociative addition pathway predominates the direct elimination channel for the formation of both ethyne as well as propene from chloroethene and 2-chloropropane, respectively. Small chlorine-free hydrocarbons were detected in the experiments of Al-Harahsheh et al. [101]. The formation of these

alkynes/alkenes support the occurrence of the demonstrated dehydrochlorination. On the other hand, the direct elimination pathway represents the only possible route to yield ethene from dehydrohalogenation of chloroethane on the α-Fe$_2$O$_3$ cluster. For instance, in the dissociative addition pathway, the rate reaction constant for chloroethane is less sensitive to the temperature comparing to that for chloroethene. When contrasted with the slow homogenous dehydrochlorination pathway in the gas phase [374], the catalytic-assisted HCl removal demonstrated herein indicates that, iron oxides serve as active catalysts in producing clean olefins streams from chlorinated alkanes; in analogy to the well-documented role of alumina and other metal oxides [376-378].
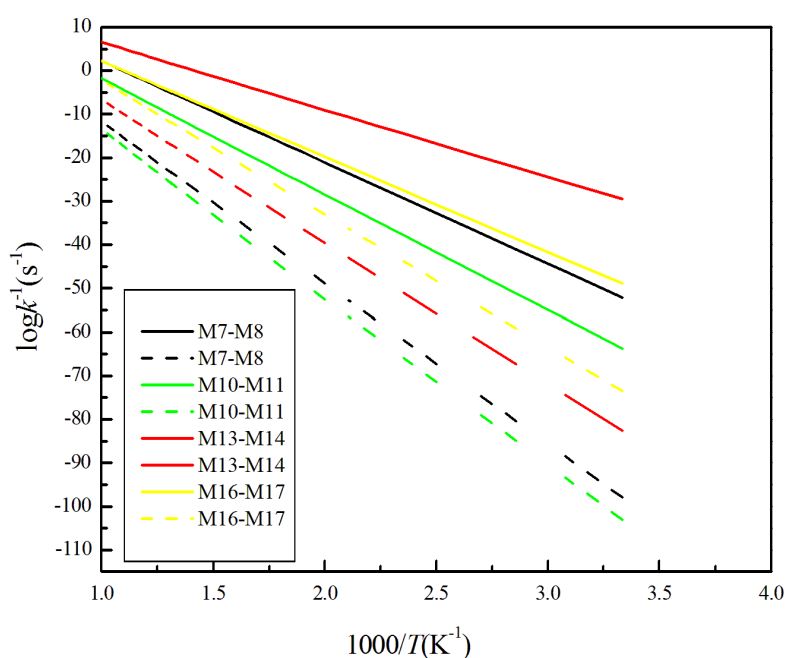
Figure 4.6. Variation of the reactions rates with temperatures for the elimination (solid line) and dissociative addition (dashed line) pathways.

4.3.4. Reaction of α-Fe$_2$O$_3$ Cluster with Chlorobenzene and 2-chlorophenol

Condensation of polyenes produced from PVC yields appreciable concentrations of benzene and other aromatic cyclic compounds [352]. As conveyed earlier, the presence of EAFD promotes the formation of chlorobenzene; presumably mediated by FeCl$_3$. If oxygen exists during thermal degradation of PVC, formed chlorobenzene could be readily oxidized into chlorophenols [379]. Both groups act as direct building blocks for the synthesis of dioxins. Thus, it is insightful to assess the chlorination of chlorobenzenes and chlorophenols over hematite nanoclusters. Herein, we have investigated the interaction of α-Fe$_2$O$_3$ cluster with 1-chlorobenzene and 2-chlorophenol as model compounds for these groups of chlorinated aromatics.

Figure 4.7.a shows that, interaction of chlorobenzene with the α-Fe$_2$O$_3$ cluster forms the M20 moiety in a considerable exothermic reaction of -44.8 kcal mol^{-1}. Fission of the strong aromatic C-Cl bond (95.5 kcal mol^{-1}) via TS12 occurs through an activation barrier of 15.4 kcal mol^{-1}. This value noticeably exceeds the analogous barrier in case of bromobenzene by 4.1 kcal mol^{-1}. Obviously, a weaker aromatic C-Br bond by almost 12.0 kcal mol^{-1} [371] derives this noticeable difference in activation energy for the carbon-halogen bond fission. The formed phenyl ring in the M20 structure is strongly bonded with two neighboring iron atoms. Thus it is highly unlikely for phenyl to desorb. Fragmentation into C$_2$H$_2$ molecules and the coverage of Fe$_2$O$_3$ surfaces with carbonaceous layers may control the fate of the phenyl adduct. Another plausible channel is the cross-linking of two adjacent phenyls into a biphenyl molecule. Subsequent reactions following the formation of an adsorbed phenyl radical on the hematite cluster warrants further investigation.
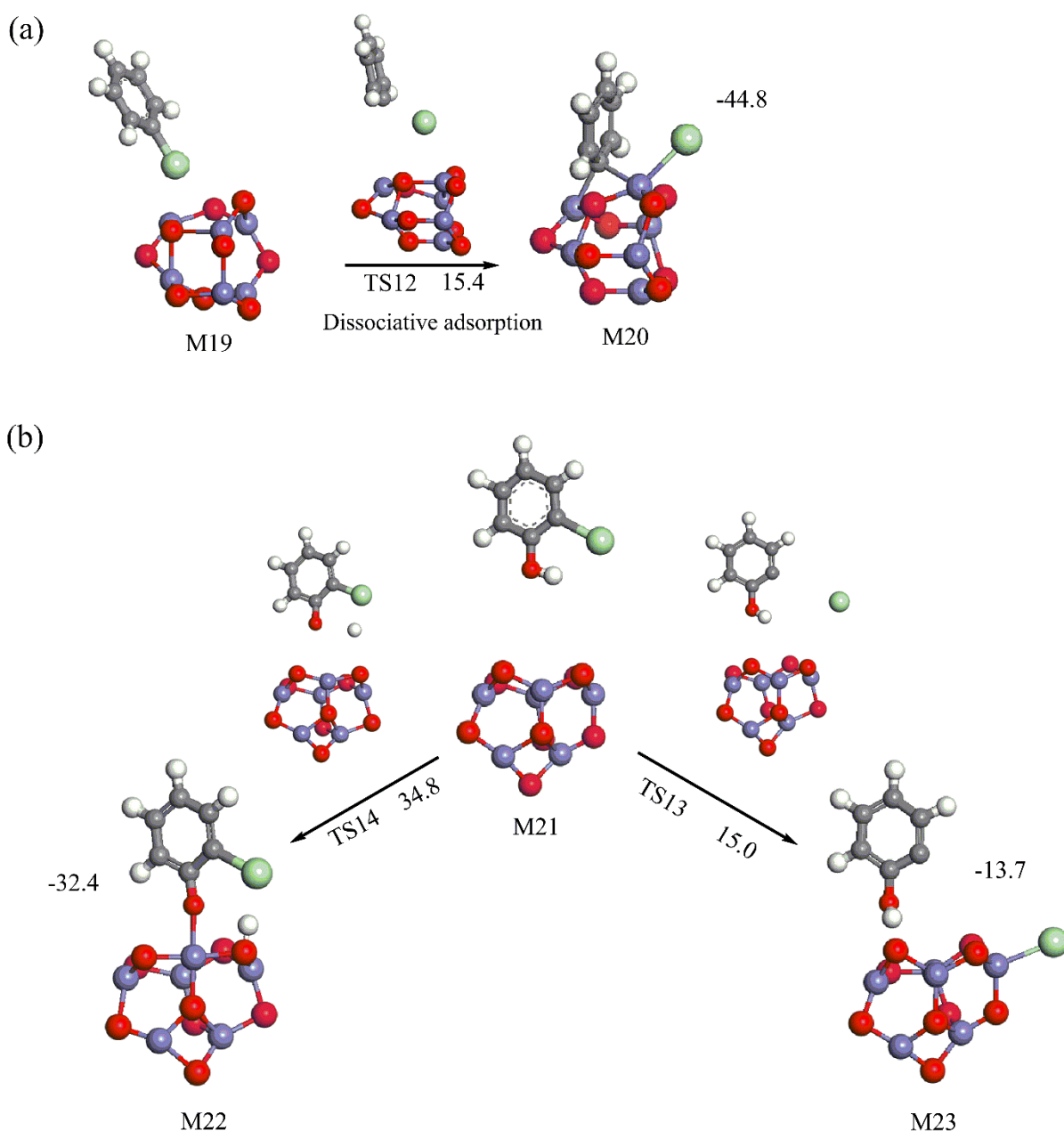
Figure 4.7. Reaction of chlorobenzene (a) and 2-chlorophenol (b) with Hematite (α-Fe$_2$O$_3$) cluster. Values are in kcal mol^{-1} in reference to the initial reactants.

Figure 4.7.b reports the scission of the two weakest bonds in the 2-chlorophenol molecule over the α-Fe$_2$O$_3$ cluster; the hydroxyl O-H bond (89.0 kcal mol^{-1}) [371] and C-Cl bond (95.5 kcal mol^{-1}) [371]. Fission of aromatic C-Cl bond demands a significantly lower activation barrier in reference to the rupture of the fission of the phenol's O-H bond (15.0 versus 34.8 kcal mol^{-1}). It follows that interaction of the chlorophenols solely yields hydroxylated phenyl-type

radicals; rather than phenoxy radicals. Recent theoretical investigations have recently illustrated mechanisms for the homogenous generation of PCDD/Fs from phenyl-type radicals [380]. The weakly adsorbed 2-OH-phenyl radical in the M23 configuration may undergo through Langmuir–Hinshelwood (LH) and Eley–Rideal (ER) mechanisms [138, 381] to yield PCDD/Fs. Therefore, while Fe_2O_3 assumes profound chlorine fixation ability, it could also facilitate generation of direct precursors for the formation of dioxins [26, 381]. The dual role of Fe_2O_3 in dechlorination reactions of aromatics and mediating formation of dioxins require further detailed examination.

4.4. Conclusions and Future Directions

By performing accurate DFT calculations, we have systematically surveyed initial reactions involving a cluster model of α-Fe_2O_3 and major chlorine-bearing species from the fragmentation of PVC. We have demonstrated that, successive uptake of HCl molecules followed by water elimination lead to the formation of a precursor for iron chlorides. Owing to stronger carbon-chlorine bonds in the considered molecules, their dissociative addition corridors assume higher activation barriers in comparison with their brominated counterparts. We found that interaction of hematite nanoclusters with 2-chlorophenol to preferentially form an OH-phenyl radical (via carbon-chlorine bond rupture) rather than 2-chlorophenoxy radical (via O-H bond fission). While results from this chapter provide useful information pertinent to the considered dehydrohalogenation reactions facilitated by hematite, it also suggests that further future work is needed to address some intriguing questions in regard to:

1- The role of Fe_2O_3 as a catalysis in the surface-mediated formations of PCDD/Fs. Relevant experimental studies on co-pyrolysis of PVC with EAFD have mainly

addressed the merits of metal oxides as chlorine fixation agents with little emphasis on the likely potential to generate dioxin compounds.

2- A principal aim for the co-pyrolysis of PVC with EAFD is to extract its high load of zinc content. Zinc in EAFD mainly exists in the form of $ZnFe_2O_4$. It is assumed that formation of the leachable zinc chloride occurs through migration of chlorine from iron chlorides into $ZnFe_2O_4$. It will be informative to examine this mechanistic hypothesis against direct plausible dissociation of HCl on Zn-O bonds.

Chapter 5

Recycling of zincite (ZnO) via uptake of hydrogen halides

The following chapter is a modified version of <u>paper II</u>:

Abstract

Hydrogen halides (HCl/HBr) represent the major halogen fragments from thermal decomposition of halogen laden materials; most notably PVC and brominated flame retardants (BFRs). Co-pyrolysis of halogen-containing solid wastes with metal oxides is currently deployed as a main stream strategy to treat the halogen content as well as to recycle the valuable metallic fraction embedded in electric arc furnace dust (EAFD) and e-waste. However, designing an industrial-scale recycling facility necessitates accurate knowledge on mechanistic and thermo-kinetic parameters dictating the interaction between metal oxides and hydrogen halides. In this contribution, we investigate chemical interplay between HCl/HBr and zincite surfaces, as a representative model for structures of zinc oxides in EAFD by using different sets of functionals, unit cell size and energy cut-off. In the first elementary step, dissociative adsorption of the HCl/HBr molecules affords oxyhalides structures (Cl/Br−Zn, H−O) via modest activation barriers. Conversion of oxyhalides structure into zinc halides occurs through two subsequent steps, further dissociative adsorption of HCl/Br over the same surface Zn atom as well as the release of H_2O molecule. Evaporation (or desorption of zinc halides molecules) signify a bottleneck for the overall halogenation of ZnO. Our Simplified kinetic model on the HCl + ZnO system concurs very well with experimentally reported TGA weigh loss profiles on two grounds; accumulation of oxyhalides till ~ 700 K and desorption of $ZnCl_2$ at higher temperatures. Thermo-kinetic and mechanistic aspects reported herein could be useful in the pursuit to design of a large-scale catalytic upgrading unit that operates to extract the valuable zinc loads from EAFD.

5.1. Introduction

Crude steel manufacturing operations produce large amounts of electric arc furnace dust (EAFD) as by-product solid wastes. It is estimated that nearly 6 Mt of EAFD was emitted globally in 2009 [339]. Sustainable disposal and recycling of EAFD's constituents have been a thematic research topic over the last few years [338, 382, 383]. EAFD is a powder material comprising a vast array of heavy toxic metals such as cadmium, chromium, zinc and nickel as well as small concentrations of chloride compounds including potassium chloride and sodium chloride [91, 105, 384]. Several components in EAFD poses serious environmental and health concerns. Of particular importance, are metal chlorides and oxides in EAFD that are suspected to act as mediators for the formation of notorious pollutants and the so-called persistent free environmental radicals (PEFR) [385-387].

On the other hand, EAFD is opulent in precious metallic oxides and can be employed as secondary feedstock in the production of valuable metals such as iron, zinc and lead [50, 388]. The average concentrations of both iron and zinc in dust vary in the range of 10-45% and 2-46%, respectively and their most common phases are magnetite (Fe_3O_4), hematite (Fe_2O_3), zincite (ZnO) and franklinite ($ZnFe_2O_4$) [50, 101, 389, 390]. 50 to 80% of the total zinc load present in EAFD exists as ZnO, while the rest mainly forms $ZnFe_2O_4$ [391]. Pyro-metallurgical and hydro-metallurgical recycling methods are commonly deployed to extract metals from EAFD [91, 392, 393]. Several drawbacks of these two approaches including intensive energy operations, low selectivity toward the dissolution of lead and zinc; and the involvement of complex clean-up procedures have prompted to explore more efficient recycling technologies of EAFD [338, 394, 395].

The combined treatment or "co-pyrolysis" of both EAFD, and plastic materials bearing organo-halogen compounds (OHCs), has been investigated intensively. The remarkable halogen fixation ability of metallic oxides in EAFD facilitates conversion of metallic oxides into their halogenated counterparts; a process that also significantly lessen the potential for the formation of halogenated pollutants in thermal recycling of polymeric materials laden with halogenated compounds.

Plastic materials comprise two broad categories of organohalogen compounds; polyvinyl chloride (PVC) and brominated flame retardants (BFRs). PVC and BFRs are extensively deployed in countless objects spaning household appliances; building materials, agriculture and electronic equipment [345, 396, 397]. These numerous utilizations have resulted in the generation of an incremented volume of plastics wasts. For instance, in 2013 approximately ~300 Mt of plastics were disposed [398]. Plastic wastes are commonly disposed of through either incineration or landfill [29, 399]. The high energy content embedded in the organic matter of plastics renders the "waste-to-energy" approach to be the mainstream strategy in the disposal of polymeric materials. However, the appreciable halogen contents in halogenated plastics (bromine and chlorine) often lead to synthesis of highly hazardous halogenated hydrocarbons such as polychlorinated dibenzo-p-dioxins and furan (PCDD/Fs) and their brominated counterparts (PBDD/Fs) [400-403].

While metal oxides display catalytic effect toward catalysing important reactions steps during heterogeneous formation of PCDD/Fs and PBDD/Fs; they readily react with hydrogen halides (HCl and HBr) in a process that eliminates the halogen content from the reaction medium [38, 240, 350, 404]. Hydrogen halides represent the major halogen species from thermal degradation of halogen-containing materials. For example, nearly, 60% of the total bromine

content during thermal decomposition of pure Tetrabromobisphenol A (TBBA); a i.e., the most deployed BFRs, is released as HBr [266]. Likewise, HCl signifies by far the major chlorine species during thermal decomposition/oxidation of PVC [266]. The high content of hydrogen halides in the reaction media suggests their prevalent contribution in the halogenation of ZnO alongside with the parent halogenated entities. To account for the experimentally observed halogenation of iron oxides, via means of molecular modelling, we have demonstrated that, dissociative adsorption of HCl and HBr over clusters of α-Fe_2O_3 leading to water elimination and iron chloride/bromide, requires effective activation barriers of 10.3 kcal mol^{-1} and 8.2 kcal mol^{-1}; respectively [350, 405].

Via several laboratory-scale experiments and various scanning calorimetry run, Grabda et al. [266] studied operational conditions that dictate bromination of zinc oxide during thermal decomposition of Tetrabromobisphenol A (TBBA); a i.e., the most deployed BFRs. Their thermal scanning using X-ray diffractometer and an electron probe microanalyzer has indicated that 53-62% of the total bromine content in TBBA is released in the temperature range between 563 and 613 K. Bromination of ZnO displayed high sensitivity with respect to the mixing TBBA:ZnO ratios. For example at TBBA:ZnO mixing ratios of 3.34:1 and 5.17:1; the bromination efficiency attained values of 41-61% and ~ 80%; respectively. It was shown that, the bromination efficiency of ZnO to strongly correlate with the HBr amount co-existing with particles of ZnO [266]. Findings by Terakado et al. [240] have shown that, ZnO commences conversion into zinc bromide during the initial decomposition stage of TBBA-ZnO mixture. This is followed by evaporation of zinc bromide from the quasi-binary $ZnBr_2$–ZnO fluid above 673 K [240]. An analogous formation of $ZnCl_2$ also took place during the co-combustion of PVC with ZnO [406]. In 2007, Lee and Song [253] investigated the influence of many factors such as mixing ratios, heating rate and heat treatment on the recycling of EAFD waste. They

observed that increasing of PVC:ZnO ratios enhance the yield of extracted Zn as zinc chloride vapour [253].

The aforementioned experimental studies have unequivocally pointed out to the facile conversion of ZnO into zinc halides when the former is co-pyrolysied with PVC/BFRs. However, optimising the process toward higher selectivity of extracted Zn necessitates detailed understanding of the surface-mediated capture of HCl/HBr by ZnO leading to zinc halides. The underlying aim of this contribution is to map out reaction corridors leading to halogenation of ZnO; an important chemical phenomenon in the chemical recycling of the zinc content in the EAFD. The layout of the paper is as follows, firstly, geometric and electronic properties of bulk and surfaces ZnO are introduced. This is followed by exploring reaction pathways that operate in the dissociate adsorption of HCl and HBr over a ZnO surfaces and providing governing reaction parameters. Finally, we contract computed conversion into ZnO versus data extracted from weight loss curve for the ZnO + HCl system. It is hoped that thermo-kinetic and mechanistic aspects pertinent to HCl/HBr uptake by ZnO surface can assist in the design of a large-scale catalytic upgrading unit that operates to extract the valuable zinc loads from EAFD.

5.2. Computational Details

All computational calculations were conducted using the Vienna Ab-initio Simulation Package (VASP) [407, 408]. Spin-polarised electronic computations were carried out using the projector augmented wave method (PAW) [409, 410] within the generalized gradient approximation (GGA) approach of Perdew and Wang (PW91) and Perdew, Burke, and Ernzerh (PBE) [319, 411, 412]. The computational methodology comprises a plane-wave basis set with an energy cut-off 320 eV and a κ-points sampling of 3×3×1 automatically generated by the

Monkhorst-Pack scheme. Structures were allowed to relax until total energies and the force constants converge to less than 0.1 meV and 0.05 eV/Å; respectively. It is generally viewed that plane wave basis sets overcome the so-called basis set superposition error (BSSE) shortcoming, often encountered when deploying atomic or Gaussian-based basis sets [413]. Optimisation of bulk ZnO utilises a 12×12×12 κ-points samplings and an energy cut-off at 500 eV.

The ZnO surfaces were constructed from six atomic layer slab and a (2×2) unit cell comprising 48 atoms. During the optimization, the top four layers were allowed to relax, whilst fixing the bottom two layers at their bulk positions. A vacuum region of 20 Å separates slabs along the *z*-direction.

The adsorption energies for all molecular states were estimated according to:

$$E_{adsorption} = E_{molecule} + E_{surface} - E_{surface+molecule}$$

5.1

Where $E_{molecule}$, $E_{surface}$ *and* $E_{surface + molecule}$ signify the total energies of a gas phase molecule, the clean Zn surface and the adsorbate-surface system, respectively. Transition states (TS) along the designated reaction pathways were located using the "climbing image" nudged elastic band (CI-NEB) technique [414, 415]. Surveying of the potential energy surfaces was performed using five minimum energy points (i.e., images) between the reactant and the product where all images were optimized simultaneously based on NEB algorithm.

Estimated vibrational frequencies of physisorbed states and transition states enable to compute thermodynamic functions required to compute kinetic reactions rate constants, $k(T)$, for all

reactions. Arrhenius parameters (*A* and E_a) were fitted in the temperature range from 300 to 1000 K based on the conventional transition state theory (TST) [355]:

$$k\ (T) = \sigma_e \frac{k_B T}{h} \exp\left(\frac{\Delta S}{R}\right) \exp\left(\frac{-\Delta H}{RT}\right) \qquad\qquad 5.2$$

In which σ_e refers the reaction degeneracy number which is taken to be 1.0, k_B, h and R are Boltzmann's, Planck's and the universal gas constants, correspondingly. ΔS and ΔH stands for the entropy and enthalpy of activation [416]. Via the Phonopy code [417], we obtained force constants and corresponding phonon thermodynamic properties. Based on a supercell approach, Phonopy software estimates phonon dispersions entailing atomic displacements within $2 \times 2 \times 2$ unit cells. Estimated phonon frequencies enable to compute thermodynamic properties, [336, 337] i.e., temperature-dependent functions of enthalpies and entropies.

In order to test the convergence of calculated energies with respect to the energy cut-off value, we have investigated the first interaction step of HX molecules over ZnO $(10\bar{1}0)$ surface using a higher energy cut-off of 400 eV. Figure 5. S2 (Appendix A) contrasts energies for the first dissociative adsorption step using energy cut-off of 400 eV. Overall, we found that there are no significant differences between the two sets of parameters 400 eV versus 320 eV. For instance, the chemisorption energies for the first two dissociative structures based on an energy cut-off of 400 eV differ by only 2.89% and 2.83% from their analogues obtained 320 eV values, correspondingly.

In order to test the convergence of calculated energies with respect to the deployed surface unit cell, we have contrasted the energy profile for the first dissociative adsorption step with

considing 2×2 and 3×3 unit cells. As demonstrated in Figure 5. S2 (Appendix A). All values are within (3.5 - 7.7) kcal mol^{-1}.

5.3. Results and Discussion

5.3.1. Zincite (ZnO) $(10\bar{1}0)$ and (0001) Surfaces

Owing to remarkable electronic and structural properties, zincite enjoys a wide array of applications spanning magnetic devices, gas-sensitive materials, adsorbents substance and catalyst or catalytic support materials for many chemical reactions [418-421]. Figure 5. S3.a in the Appendix A portrays the crystal structure of bulk zinc oxide which features hexagonal Zn and O planes with each O^{2-} ion is coordinated with a tetrahedron of Zn^{2+} ions along the c-axis [422, 423]. Table 5.1 displays the calculated lattice constants with other experimental and theoretical data. Our calculated lattice constants for bulk ZnO using PW91 functional depart from their analogous experimental values by only 1.5% (a = b = 3.248 Å) and 1.6% (c = 5.205 Å) [424]. Calculated lattice constants based on BPE functional in this study also reflect very well with previous computational and experimental results [424, 425].

Table 5-1. Computed and experimental values of the lattice constant for bulk ZnO and structural relaxations of the first two surface layers for the nonpolar ($10\bar{1}0$) and polar (0001) surfaces.

Parameters	Calculated			Experimental
Lattice constant	PW91	$a(\text{Å})$	3.298	3.248 [424]
		$c(\text{Å})$	5.289	5.205
	PBE	$a(\text{Å})$	3.195	3.290 [425]
		$c(\text{Å})$	5.102	5.241
Structural relaxations	(0001) surface	Δd_{12}	-23.7%	-25.0% [426] -24.0% [427]
	($10\bar{1}0$) surface	Δd_{12}	-47.0%	-45.0% [428] -44.0% [429]

Depending on the considered Miller indices and the atomic-type termination, ZnO surface exists in various terminations; most notably the polar ($000\bar{1}$)-O and (0001) -Zn, and the nonpolar ($11\bar{2}0$) and ($10\bar{1}0$), configurations [430]. When the crystal is cleaved perpendicular over the c-axis, the two polar surfaces are obtained. Cleaving the same number of Zn - O bonds along the c-axis leads to the two non-polar surfaces which contain an equal number of Zn and O atoms [423, 431]. Several experimental observations have validated that polar (basal) surfaces are unstable owing to the presence of a non-zero dipole moment perpendicular to the surface [426, 432]. Thermal stable configurations by ZnO units were confirmed by X-ray photoelectron spectroscopy (XPS) and combined low-energy electron diffraction (LEED) techniques. It was revealed that these stoichiometric surface terminations are auto compensated because it is covered with both Lewis acid and base sites, i.e., it comprises the same number of zinc and oxygen ions per unit area [423, 433]. Along the same line of enquiry,

result from ab initio atomistic thermodynamics approach have also signified the ZnO $(10\bar{1}0)$ as the most thermodynamically stable ZnO termination across a wide range of accessible temperatures and pressures; including those operating in the co-pyrolysis of EAFD with polymers-bearing hydrocarbons; i.e., $T = 515 - 618$ K and $P = 1$ atm [406, 419, 434]. For example, Meyer et al. [427] carried out a theoretical investigation into the stability of ZnO surfaces in terms of cleavage energy. The authors found that the nonpolar $(10\bar{1}0)$ surface is the most stable face of ZnO among other plausible configurations. Furthermore, we study the interaction of the two hydrogen halides with the polar zinc-terminated Zn-ZnO(0001) surface as an important surface in heterogeneous catalysis, confirmed by highest resolution scanning force microscopy (SFM) [435].

As a benchmark of the structural accuracy of our adapted methodology, it is very instructive to compare the computed electronic relaxation of the surface to other experimental and theoretical values. As shown in Table 5.1, the calculated surface relaxation for the first two layers (Δd_{12}) for $(10\bar{1}0)$ surface is 47%. This value reasonably agrees with values sourced from both LEED analysis (-45%) [428] and a computational investigation at (-44%) [429]. Likewise, the calculated dimer distance between Zn and O atoms ($d_{\text{Zn–O}}$) at the first surface layer amounts to 1.940 Å. This reasonably matches analogous theoretical and experimental data, i.e., $d_{\text{Zn–O}}=$ 1.905 Å and 1.90 Å, [434, 436]; correspondingly. For the Zn-terminated surface, it is clear that the relaxation of the topmost surface layer (Δd_{12}) is in a very good agreement with the findings of previous DFT calculations as given in Table 5.1 [426, 427].

The electrostatic potential of ZnO surface, as illustrated in Figure 5. S3.b, displays that, the exposed zinc cations act as electron acceptors with strong positive potentials, whilst, the

exposed oxygen anions possess strong negative potentials. Thus, Zn-O surface bonds act as acid-base sites for the dissociative uptake of Cl/Br and H atoms; respectively.

5.3.2. Dissociative Adsorption of HCl and HBr over ZnO Surfaces

We start by describing the dissociative adsorption mechanism of HCl and HBr over the ZnO $(10\bar{1}0)$ and (0001) surfaces commencing from their molecularly adsorbed states. Figures 5.1 shows the reacting structures along with prominent interatomic distances while Figures 5.3, 5.4 and 5.5 present pertinent potential energy surfaces.

Figure 5.1 depicts structures for the dissociative adsorption of HCl and HBr molecules over $(10\bar{1}0)$ surface Zn-O bonds; i.e., Lewis acid-base sites. Figure 5.1 shows Cl/Br-H bond elongations (in reference to equilibrium distances in the gas phase) and charge transfer from the surface to the adsorbed molecules. The first step of this reaction characterises weak molecular physisorption states of the two molecules evidenced by marginal binding energies of only 2.4 and 1.3 kcal mol^{-1} for the two surface-molecule adducts $M1_{(Cl)}$ and $M1_{(Br)}$; respectively. Minor elongations of H-Cl and H-Br bond distances and charge transfer from the surface to the physisorbed states of $M1_{(Cl)}$ and $M1_{(Br)}$ (Figure 5.1), account for the very weak interaction with the ZnO surface.
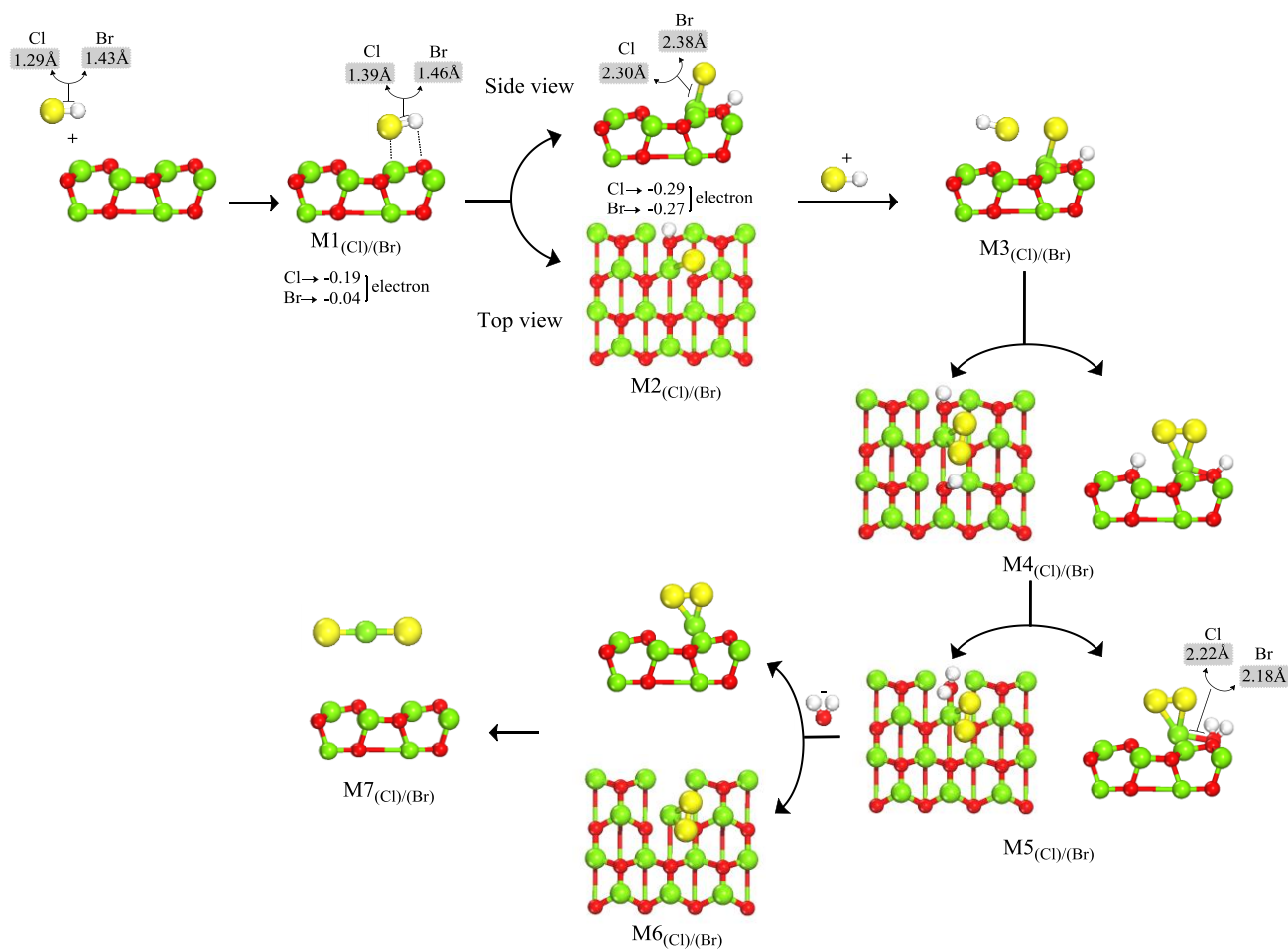
Figure 5.1. Schematic representation of the interaction steps for the decomposition of hydrogen chloride/bromide molecules on zincite ($10\bar{1}0$) surface. Only the first two layers are shown in side views. Large yellow spheres correspond to chloride/bromide atoms and red, green, and white spheres to O, Zn and H atoms, respectively. The net charge transfers from the surface to adsorbed Cl/Br molecule are illustrated.

Dissociation of the H-Cl/H-Br bonds in the second step produces the oxyhalide structures of M2$_{(Cl)}$ and M2$_{(Br)}$ along the reaction:

$$HCl/Br + ZnO(10\bar{1}0) \rightarrow (Cl/Br{-}Zn, H{-}O)/\, ZnO(10\bar{1}0)$$
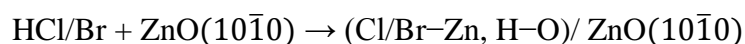
In this reaction, the electronegatively charged atoms Cl and Br atom bind with a surface Zn atom. The bond lengths of Cl –Zn and Br−Zn in M2 $_{(Cl)}$ and M2 $_{(Br)}$ structures attain values of

2.30 Å and 2.38 Å, reflecting very well Cl –Zn and Br–Zn bond lengths in bulk $ZnCl_2$ and $ZnBr_2$ at 2.22 Å and 2.40 Å [437, 438]; correspondingly. As depicted in Figure 5.3, dissociation of HCl and HBr molecules demands modest activation barriers of 17.1 and 8.5 kcal mol^{-1}, correspondingly (in reference to their physisorbed states). Higher activation barriers for fission of the Cl-H in comparison to Br-H concurs with a stronger bond in the former (103.2 versus 87.1 kcal mol^{-1}) [367]. The catalytic capacity of ZnO toward uptake of gas phase hydrogen halides becomes evident when contrasting these low energy barriers with the energy requirements for the uncatalysed bond fission of Cl/Br-H bonds at 103.2 and 87.1 kcal mol^{-1}; respectively [367]. Overall, we find that interaction of HCl with ZnO $(10\bar{1}0)$ surface proceeds via analogous mechanistic steps to that of HBr molecule. These comparable trends are in accord with our recent corresponding findings pointing to the similarity in reactions of products from thermal degradation of PVC and TBBA with nanoclusters of Fe_2O_3 [350, 405]. Nonetheless, catalytic mediated dissociation of carbon-Br bonds systematically demands lower activation energies when contrasted with analogous fission of carbon-Cl bonds.

Dissociative adsorption of HCl and HBr molecules over the ZnO $(10\bar{1}0)$ surface can be viewed as a Lewis acid–base interaction. The chemisorbed hydrogen atom tends to act as a charge donor to a surface oxygen atom to form hydroxyl group. This in turn renders adsorbed chlorine/bromine atom to function as a Lewis acid sites to stabilize the formation of $M2_{(Cl)}$ and $M2_{(Br)}$ configurations via Lewis acid/base interaction. Inspection of charge transfer for the chemisorption states ($M2_{(Cl)}$ and $M2_{(Br)}$) as shown in Figure 5.2, indicates that adsorbed Cl/Br atoms incur a net electronic charge of -0.29/ -0.27. A similar scenario has been observed for dissociative adsorption of HBr over La_2O_3 [439]. A significant charge transfer from the surface to the two adsorbed halogen atoms serves as a signature for the noticeable exothermic nature of HCl/HBr uptake by the ZnO surface (-38.0/-42.4 kcal mol^{-1}). This is in line with Grabda et al. findings [266], who observed strong exothermic peak between 563 − 613 K during

bromination of ZnO from their TGA-DSC measurements. Our previous studies on the decomposition of HCl/HBr over α-Fe$_2$O$_3$ clusters as well analogous previous findings for the dissociation of HCl/HBr molecules on CeO$_2$ (111) surface [440] have also predicted exothermic trends for the first dissociative adsorption step.

(a)   (b)

Figure 5.2. Side views of the charge density distributions for HCl (a) and HBr (b) dissociative adsorption on ZnO ($10\bar{1}0$) surface. Electron charge gain or loss is represented by light yellow and light blue clouds; respectively. Green, Red, blue, brown and white spheres represent Zn, O, Cl, Br and H atoms, respectively. The isosurface density level is 0.005 e/bohr^3.

In order to underpin the influence of the surface termination on the HX molecules dissociation, the adsorption energies and activation energies of hydrogen chloride/bromide molecules on ZnO (0001) surface were also investigated. As illustrated in Figure 5.4, physisrobed interaction of HCl and HBr molecules over the zinc-terminated (0001) surface is found to be more exothermic by 5.9 and 11.5 kcal mol^{-1}, respectively in reference to the non-polar ($10\bar{1}0$) surface. On the other hand, we found that cleavage of Cl/Br-H bonds over (0001) surface request sizable activation barriers of 27.2 and 26.8 kcal mol^{-1} (in reference to ($10\bar{1}0$) surface). By comparing these activation barriers for these two considered terminations, we can see clearly that ($10\bar{1}0$) surface entail lower initial activation energies and hence should be catalytically more active in capturing the hydrogen halides. For this reason, we have limited our investigation on the dissociative adsorption of HX molecules over zincite by utilizing ($10\bar{1}0$) surface only.

In order to illustrate the satsifactory performance of the adapted PW91 functional in predicting reaction barriers, we have compared correponding reacion barriers dictaing the fisrt dissociative adsorption step with analogous values obtained using the PBE method. Moreover, to confirm our limitation and the obtained results, further calculations are performed using the Perdew-Burke-Ernzerhof (PBE) functional for the first interaction step between HX molecules and ZnO $(10\bar{1}0)$ surface. The following remarks summarise the satisfactory agreement between these two functionals:

1- As illustrated in Figure 5.5, formation of $M10_{(Cl)}$ and $M10_{(Br)}$ structures require very weak physisorption energies. This reasonably corresponds with values obtained using the PW91 functional method.

2- Chemisorption energies for the reaction of HCl and HBr molecules using PBE functional method (37.1 and 40.2 kcal mol^{-1}, correspondingly) concur very well with the values obtained using PW91 functional (i.e. -38.0 and -42.4 kcal mol^{-1}).

3- Dissociation of the H-Cl and H-Br requires activation barriers of 21.1 and 6.6 kcal mol^{-1}, respectively. These values reflect very well analogous estimates using the PW91 functional.

In the subsequent dissociative addition reactions of HCl/Br molecules over corresponding oxyhalide configurations of $M2_{(Cl)}$ and $M2_{(Br)}$ as Figure 5.1 depicts, molecular physisorption leads to the intermediates $M3_{(Cl)}$ and $M3_{(Br)}$ structures. As it the case for interaction of HCl/HBr over pure zincite surface, adsorption of HCl was found to be slightly exothermic at -4.9 kcal mol^{-1} whereas, adsorption of HBr endures thermodynamically neutrality. As depicted in Figure 5.1, scission of the H-Cl/Br bonds yielding $M4_{(Cl)}$ and $M4_{(Br)}$ configurations request activation

energies of 11.8 and 5.7 kcal mol^{-1} via the transition structures of TS2$_{(Cl)}$ TS2$_{(Br)}$, respectively (in reference to their physisorbed states). These two values are approximately close to activation barriers for the first dissociation reactions (16.9 and 8.5 kcal mol^{-1}), indicating a minimal effect for the presence of pre-adsorbed halide atoms in facilitating subsequent dissociative adsorptions.

In M4$_{(Cl)}$ and M4$_{(Br)}$ structures, the Cl/Br atoms attach with the same surface Zn atom, forming a surface ZnCl$_2$/Br$_2$ site while the dissociated H atom forms another hydroxyl group with a surface O atom. The second Cl/Br-H dissociation reaction is accompanied with reaction energies of 2.1 and -21.7 kcal mol^{-1}, sequentially. In the M4 $_{(Cl)}$ and M4 $_{(Br)}$ structures, the involved Zn atoms slightly deviate from planarity of the surface facilitating its subsequent departure as zinc halide by evaporation as found experimentally by Grabda et al. [266] and Zhang et al. [406]. By analysing the deviation of TG-MS and Deferential Scanning Calorimetry (DSC) curves, it was revealed that chlorination/bromination of Zn proceeds via the direct interaction between zincite and PVC/TBBPA and their halogenated fragments [266, 406]. Our molecular modeling herein supports these experimental findings and confirms that, both hydrogen chloride/bromide function as an excellent chlorinating /brominating agent for ZnO.

Subsequently, intramolecular hydrogen transfers from a surface OH group to the adjacent hydroxyl group produces water molecules. Formation of M5$_{(Cl)}$ via this process is endothermic by 3.4 kcal mol^{-1} whilst synthesis of the M5$_{(Br)}$ structures is an exothermic reaction by -5.5 kcal mol^{-1}. Generation of water through these processes takes place through energy barriers of 23.4 and 16.3 kcal mol^{-1}; characterised by the transition states TS3$_{(Cl)}$ and TS3$_{(Br)}$; respectively. Desorption of a water molecule from the M5$_{(Cl)}$ structure takes place without encountering a

reaction barrier through an endothermic reaction of 19.4 kcal mol^{-1}. Elimination of water molecules clearly leads to the formation of surface zinc chlorides/bromides entities symbolized by M6 $_{(Cl)}$ and M6 $_{(Br)}$. In the M5$_{(Cl)}$ and M5$_{(Br)}$ configurations, water resides 2.22 Å and 2.18 Å above the surface; respectively. These two values reasonably agree with a recent theoretical estimate for water adsorption on a pure ZnO(1010) surface at 2.07 Å [433]. In the final step of these reactions, the adsorbed zinc chloride/bromide molecules desorb from M6$_{(Cl)}$ and M6$_{(Br)}$ structures to yield the configurations M7$_{(Cl)}$ and M7$_{(Br)}$ in a relatively sizable endothermic reactions of 60.6 and 67.3 kcal mol^{-1}; respectively. It has been demonstrated that gaseous zinc halides exist as monomers rather than dimers [441]. Figure 5.S4 in the Appendix A shows the optimized structure of gaseous ZnCl$_2$ and ZnBr$_2$ molecules. In these structures, the Zn-Cl and Zn-Br bond length attain values of 2.07 Å and 2.21 Å, respectively. These values are in good agreement with analogous experimental estimates (i.e, 2.0 Å and 2.19 Å) [442].

We now attempt to interpret the experimental observations pertinent to halogenation of ZnO based on the potential energy surfaces (PES) portrayed in Figure 5.3. Via deploying TG–MS measurements, Zhang et al. [406] investigate thermal decomposition of ZnO -PVC mixture, Zhang et al. [406] revealed that PVC particle size has a significant role in the chlorination of ZnO. They observed that the weight loss of the ZnO-PVC mixture occurs in four distinctive stages featuring water elimination (473 – 555 K), dehydrochlorination of PVC/chlorination of ZnO (555 – 618 K, further degradation of PVC (618 – 688 K) and vaporisation of ZnCl$_2$ (688 – 873 K). Figure 5.S6.a in the Appendix A reproduces the weight loss curve reported by Zhang et al. [406]. Two concluding remarks can be inferred from contrasting our HCl-PES in Figure 5.3 and Figure 5.S6.a:
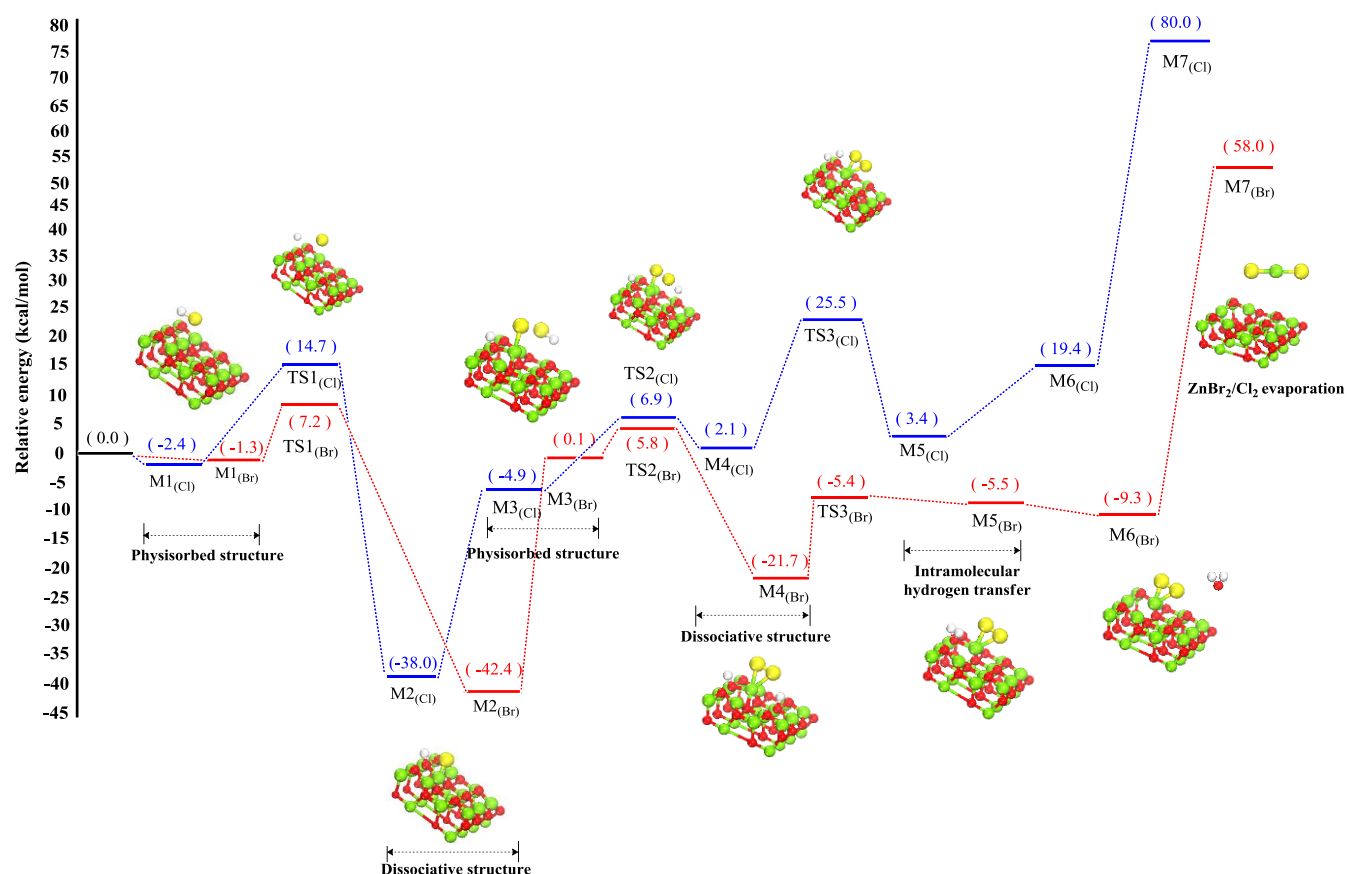
Figure 5.3. Relative energy profile diagram for the first addition step of HCl (Blue) and HBr (Red) molecules over zincite ($10\overline{1}0$) surface. Values are in kcal mol^{-1} with respect to reactants in each step.

- The majority of evolved HCl from dehydrochlorination of PVC (stage 2) does not yield a net weight loss as it is captured by ZnO in a process that leads to the formation of oxychlorides. This corresponds to the facile formation of M4$_{(Cl)}$ − M6$_{(Cl)}$ structures in Figure 5.3 via an overall reaction barrier of only 25.5 kcal mol^{-1}. Water evaporation in the first and second stages most likely originate from two sources, namely, physically adsorbed water molecules on ZnO surfaces and water formed by the intramolecular hydrogen transfer.

- The fact that the main weight loss (~ 45%) occurs at relatively high temperatures coincides with the significant energy penalty required from the desorption for ZnCl$_2$ moiety from the surface; i.e., 60.6 kcal mol^{-1}. Thus, the rate determining step in

chlorination of ZnO into $ZnCl_2$ signifies desorption of $ZnCl_2$ molecules from oxychlorides. The energy requirement for this step overshoots the reported value for sublimation of zinc chloride at 32.3 kcal mol^{-1} [441] along the reaction $ZnCl_2(s) \rightarrow ZnCl_2(g)$.

The HBr/ZnO reacting system exhibit a similar behaviour in regard to the accumulation of oxybromides prior to evaporation of $ZnBr_2$. Figure 5.S6.b in the Appendix A is reproduced from the study by Oleszek et al. [264] who used X-ray diffraction and electron probe microanalysis techniques to trace zinc speciation during co-pyrolysis of ZnO with TBBA. As shown in Figure 5.S6.b, surface bromination of the zinc content in zincite peaks at 70% around 550 K, however, evaporation of $ZnBr_2$ remains very negligible and reaches only ~ 5% at 700 K. Clearly, this indicates rapid surface bromination (i.e., commencing with $M1_{(Br)} \rightarrow M2_{(Br)}$) and thermodynamic hindrance toward evaporation of zinc bromide (i.e., departure on $ZnBr_2$ from the surface along the reaction $M6_{(Br)} \rightarrow M7_{(Br)}$).
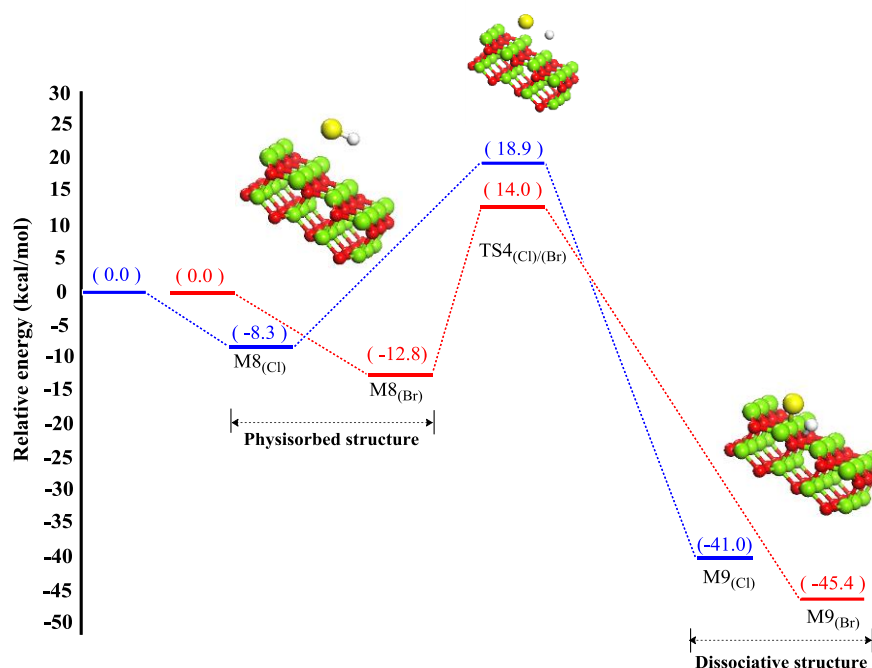
Figure 5.4. Relative energy profile diagram for the first addition step of HCl (Blue) and HBr (Red) molecules over ZnO ($\mathbf{0001}$) surface.

In addition to exploring reaction pathways for the dissociate adsorption of HX molecules over ZnO surface, as mentioned above, further studies are needed to underpin various intriguing aspects:

- The roles of zincite in mediating degradation of organohalogens released from thermal decomposition of PVC and BFRs.

- We have limited our analysis on a perfect ZnO structure; that is the $(10\bar{1}0)$ surface. The presence of structural defects or atomic-type impurities often enhances catalytic decomposition capacities for environmental-bases catalysts. Thus, it is insightful to assess the effect of these factors on the catalytic decomposition performance of ZnO.

- We have shown here that ZnO captures the largely inert halogenation agents HCl and HBr. However, it is greenery viewed that metal halides act as shuttle to transfer chlorine into aromatic compounds; a process that substantially increases their overall toxicity. It will be instructive to explore the mechanistic and kinetic parameters for the halogenation mechanism of aromatic pollutants by zinc halides. Such information will be informative to assess the overall merits of deploying metal oxides in general to capture the halogen content in solid waste streams; including EAFD and e-waste.
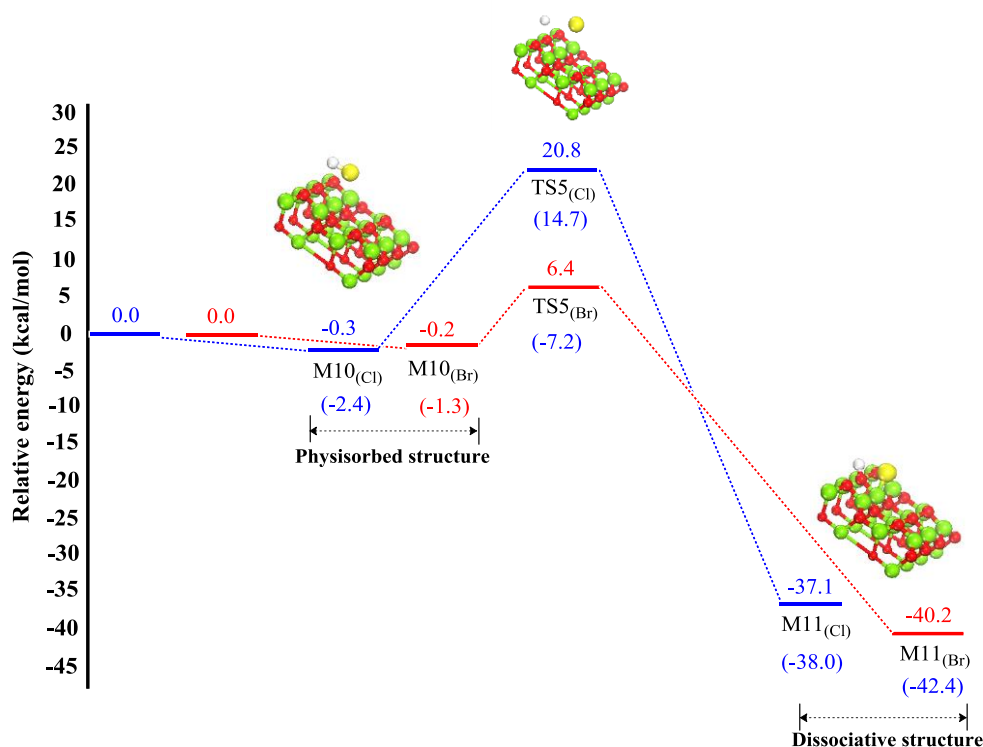
Figure 5.5. Relative energy profile diagram for the first addition step of HCl (Blue) and HBr (Red) molecules over ZnO ($10\overline{1}0$) surface using BPE functional. Values in brackets are for PW91 functional.

5.3.3. Kinetics Model

Table 5.2 enlists reaction rate constants parameters for reactions pathways depicted in Figures 5.1, while Figure 5.S5 in the Appendix A shows their Arrhenous plots. At a temperature of 515K (The onset temperature for the dissociative adsorption of HCl) [406], the rate constant for HCl uptake by ZnO is approximately three fold slower than that of HBr. This observation stems from higher activation barriers embedded in the dissociation of HCl when contrasted with the analogous steps for HBr. Based on the estimated reaction rate constants, intramolecular hydrogen transfer releasing water molecules represent a bottle neck in halogenation of zinc atoms into surface islands of zinc halides.

Table 5-2. Kinetic parameters of reactions at a temperature range of 300-1000 K.

Species	Reaction	A (s^{-1})	E_a (kcal mol^{-1})
ZnO + HCl	M1$_{(Cl)}$ → M2$_{(Cl)}$ k_1	1.16×10^{10}	13.4
	M3$_{(Cl)}$ → M4$_{(Cl)}$ k_2	8.67×10^{10}	12.8
	M5$_{(Cl)}$ → M6$_{(Cl)}$ k_3	6.42×10^{9}	20.3
ZnO + HBr	M1$_{(Br)}$ → M2$_{(Br)}$	2.22×10^{10}	6.2
	M3$_{(Br)}$ → M4$_{(Br)}$	5.74×10^{10}	3.5
	M5$_{(Br)}$ → M6$_{(Br)}$	3.07×10^{8}	19.5

Next, we turn our attention to constructing a simplified kinetic model that accounts for the weight loss behaviour for PVC:ZnO mixtures reported by Zhang et al. [406] (Figure 5.S6.a) based on the reaction rate constants listed in Table 5.2. Via considering a batch reactor model and by assuming that HCl molecules exist in great excess with the ZnO surface, the mole balance equations of the chlorination reaction sequence:

$$M1_{(Cl)} \xrightarrow{k_1(T)} M3_{(Cl)} \xrightarrow{k_2(T)} M5_{(Cl)} \xrightarrow{k_3(T)} M6_{(Cl)} \xrightarrow{k_4(T)} M7_{(Cl)} \qquad 5.3$$
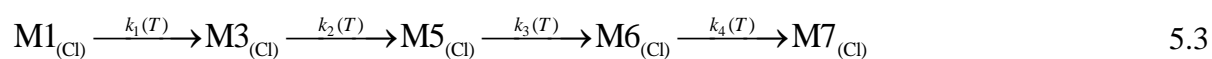
can be arranged into:

$$\frac{d[\text{M1}_{\text{Cl}}]}{dt} = -k_1[\text{M1}_{\text{Cl}}]$$

$$\frac{d[\text{M3}_{\text{Cl}}]}{dt} = k_1[\text{M1}_{\text{Cl}}] - k_2[\text{M3}_{\text{Cl}}]$$

$$\frac{d[\text{M5}_{\text{Cl}}]}{dt} = k_2[\text{M3}_{\text{Cl}}] - k_3[\text{M5}_{\text{Cl}}]$$

$$\frac{d[\text{M6}_{\text{Cl}}]}{dt} = k_3[\text{M5}_{\text{Cl}}] - k_4[\text{M6}_{\text{Cl}}]$$

$$\frac{d[\text{M7}_{\text{Cl}}]}{dt} = k_4[\text{M6}_{\text{Cl}}]$$

A-factor for the step M6 → M7 was assumed to be $1.00 \times 10^{12}\,\text{s}^{-1}$, (a commonly deployed value for unimolecular reactions) with an activation energy taken to be the desorption energy at 60.6 kcal mol^{-1}. These sets of ordinary differential equations were solved with the aid of the PolyMath code.[81]

Conversion profiles of the M1$_{(\text{Cl})}$ configuration are depicted in Figure 5.6 for a reaction time of 3 s between 300 – 900 K. The model predicts desorption of ZnCl$_2$ to commence at ~ 800 K and to account for nearly 36% to the initial M1$_{(\text{Cl})}$ at 900 K. These findings are in qualitative agreement with the temperature window of stage 4 in Figure 5.S6.a; (688 – 873 K) and reported mass loss associated with ZnCl$_2$ evaporation; i.e., 45%. Another salient feature of the model is the formation of the oxychloride phase as the dominant reaction product at temperature as low as 500 K. This clearly coincide with the interpretation of Zhang et al. [406] in regard to the occurrence of ZnO chlorination between 555 – 618 K (stage 2).
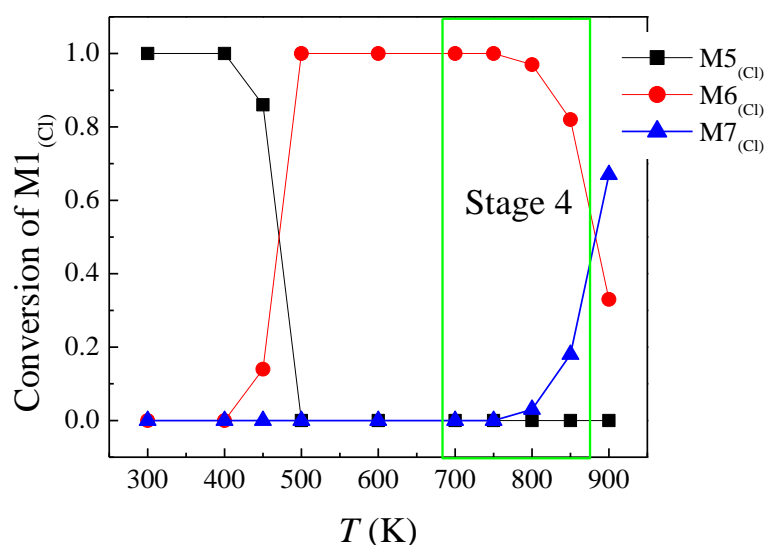
Figure 5.6. Modeled product profiles from the reaction of ZnO + HCl.

5.4. Conclusions

In the current work, a systematic theoretical thermo-kinetic study was performed to investigate dissociate adsorption of HCl//Br molecules over ZnO surfaces. Convergence tests using different sets of functionals, unit cell size and energy cut-off ensures the accuracy of all reported energy profiles. Calculated results indicate that conversion of ZnO into zinc chlorides and bromides take place through two subsequent dissociative adsorption steps, followed by intramolecular hydrogen transfer. Our results show that fission of a H-Cl bond over zincate surface requires reaction barriers in reference to H-Br, reflecting the noticeable difference in their bond dissociation energies in the gas phase. Desorption of $ZnCl_2$ and $ZnBr_2$ as gas phase molecules occur via relatively accessible desorption energies. We found that the nonpolar ZnO ($10\bar{1}0$) surface displays higher catalytic activity for dissociative adsorption of HX molecules in comparison to zinc-terminated (0001) surface. Our theoretical calculations support the previous experimental observations that HX molecules have great potentials to serve as a perfect chlorinating /brominating agent for recycling of zincite.

Chapter 6

Catalytic De-chlorination of Products from PVC degradation by Magnetite (Fe$_3$O$_4$)

The following chapter is a modified version of <u>paper IV</u>:

Abstract

This contribution provides a systematic theoretical thermo-kinetic study of the initial reactions between Fe_3O_4(111) surface, as a representative model for metal oxides in electric arc furnace dust (EAFD) with HCl and selected chlorinated hydrocarbons, as major products from thermal degradation of PVC. Formation of the experimentally observed iron chloride occurs by subsequent dissociative addition of HCl molecules followed by H migration into a surface hydroxyl group. We provided Arrhenius parameters for reactions dictating the conversion of iron oxide into its chloride. In the course of the interaction of chlorinated alkanes and alkenes with the Fe_3O_4 surface, the opening channel in the dissociative addition route requires lower activation barriers in reference to the direct HCl elimination pathways. However, sizable activation barriers are encountered in the subsequent β C-H bond elimination step. Estimated electronic charges confirm the nature of surface Fe-Cl bonds as Lewis acid−base pair. The obtained accessible reaction barriers for reactions of chlorinated alkanes and alkenes with the title iron oxide demonstrate that the latter serve as active catalysts in producing clean olefins streams from chlorinated alkanes. Results from this study should be instrumental to understand, on a precise atomic scale, mechanisms operating in fixation of halogens on transitional metal oxides; a viable thermal recycling approach for polymeric materials laden with halogenated constituents.

6.1. Introduction

Polyvinyl chloride (PVC) is the main component in thermoplastics, piping systems and a wide array of household and industrial applications [117, 122, 443]. PVC is widely employed in various long- and short- service life products such as electrical and electronic equipment's, and construction materials [122, 444, 445]. Global consumption of PVC has steadily grown over the last decades to reach 35.3 Mt in 2007 with a projected increase of about 3% per year [446]. However, the profusion of PVC-based generate gigantic undesirable amounts of halogenated wastes that accumulated all over the world engendering safe and effective disposal of these chlorinated items a truly daunting task [347]. Landfilled and thermal methods are the most common as well as the widely utilized processes [6, 130, 447]. A number of factors including decrease of landfills capacity, high equipment costs and release of hazardous chlorinated compounds have altered the scientific community to design a more sustainable method for the disposal of PVC-containing objects [6, 31, 448].

In recent years, catalytic co-pyrolysis of halogenated polymers with metallic oxides, sourced from electric arc furnace dust (EAFD) was pioneered as a lower temperature operation to transform halogen-bearing plastics into potentially useful liquid and gaseous products [35, 59, 101, 245, 449-451]. Thermal stability of the pyrolysate mixture, fixation of light halogen gases and low temperature operation signify major merits of the catalytic co-pyrolysis scheme [452-454]. Notwithstanding, to our knowledge, there is insufficient understanding at the molecular level for reactions operating in the course of simultaneous pyrolysis mechanism of PVC with metal oxides.

EAFD accounts for ~15 to 20 kg per ton of produced steel and its constitutes the main environmental burden for steel manufacturing operations [42, 87]. EAFD is classified as a

131

toxic waste because of the presence of significant amounts of heavy metals such as zinc, cadmium, and lead [91, 106]. In addition to these metals, EAFD contains a considerable amount of Cl, which triggers the formation of hazardous chlorinated compounds (most notably polychlorinated dibenzo-*p*-dioxins, and polychlorinated dibenzofurans, PCDD/Fs) [381, 455-459]. These metals, in turn, can be used as secondary raw materials in the production of iron, lead and zinc [50, 59, 68, 96, 105].

Consensus of opinions in the literature has indicated that, the metal oxides present during thermal degradation of PVC-containing plastic materials work as dechlorinating agent and can inhibit the formation of chlorinated hydrocarbons and convert the metal oxides to their respective chlorides. The latter are readily soluble in water or are volatile at low temperature [101, 241, 253, 343]. It has been shown, in our recent theoretical investigations, that zincite surfaces and hematite clusters capture the released hydrogen halides and organohalogens from thermal degradation of PVC and brominated flame retardants (BRFs) plastic materials leading to metal chloride/bromine formation accompanied with water elimination [350, 460-462], as was predicted by experimental studies. Chemical analysis in GC/MS by Blazso and Jakab [255] found that among various metal oxides, iron oxides would be able to dehydrochlorinate PVC (i.e. they initially worked as a catalyst and then acted as a sorbent).

Among iron phases, magnetite represents a potentially effective dechlorination catalyst because of its recycling capability and its high surface area [463, 464]. Pervious experimental investigations demonstrated a robust catalyst behavior of Fe_3O_4 toward degradation and dechlorination of PVC based plastic material [256, 397]. For example, Uddin et al. [256] investigated degradation and dechlorination of PVC using a variety of metals. They found that the average concentration of chlorine-containing in PVC is nearly 53 wt % using gas chromatography with an atomic emission detector (GC-AED). ~91 to 96 wt % of these

amounts were released as gaseous hydrogen chloride, while the rest condensed as a liquid. Among the various considered metals, it has been shown that FeOOH and Fe_3O_4 are very effective species in fixing released HCl.

To the best of our knowledge, literature presents no mechanistic or kinetics information at the molecular level interaction mechanisms of HCl and other chlorinated C_1-C_6 over magnetite surface. To this end, this work reports a comprehensive computational study of the initial reactions between $(Fe_3O_4)(111)$ surface and selected chlorinated hydrocarbons. We first discuss the geometric, structure and electronic properties of the bulk and the clean (Fe_3O_4) (111) surface. We then compare the catalytic effect of both Fe_{Oct2} and Fe_{Tet1} terminated magnetite (111) surface toward dissociative adsorption of HCl molecule. Finally, we provide a significant insight into the possible interaction pathways of the selected chlorinated hydrocarbons over magnetite (111) surface. Results reported herein manuscript shall be instrumental in efforts aiming to optimize a unit operation for the concurrent treatment of the title two categories of waste materials; i.e., EAFD and PVC.

6.2. Computational Method

All energy calculations and geometry optimizations were carried out using the plane-wave periodic DFT code Vienna *Ab* initio Simulation Package (VASP) [317, 318]. Spin polarized Perdew-Wang91 (PW91) functional of the generalized gradient approximations (GGA) was deployed as the electronic-energy correlational functional correlation energies and electron exchange [327, 465]. The calculations have taken into account the ferromagnetism character of iron atoms. VASP uses scalar relativistic projected augmented wave (PAW) pseudopotentials to describe A plane-wave kinetic energy cut-off was set to 400 eV to treat the

valence electron [321]. For the structural optimization of bulk Fe_3O_4, a κ-mesh sampling of $12\times 12\times 12$ and a cutoff energy of 500 eV were utilized.

For the clean Fe_3O_4 (111) surface, a (2×2) unit cell comprising four atomic layers of iron and four layers of oxygen atoms were utilized. A 20 Å vacuum gap was used to separate the slabs along the z-direction. Integration of the irreducible part of Brillouin's zone was carried out based on a 3×3×1 Monkhorst−Pack mesh κ-points. Relaxation of the gas-phase molecules was computed through placing them in a 20 Å × 20 Å × 20 Å unit cell. Charge transfer from the surface to the adsorbate was estimated within Bader formalism [466].

A van der Waals (vdW) correction, using Grimme's [467] semi-empirical DFT-D2 force-field method, was applied in all calculations to account for contributions of dispersion interactions to adsorption energies and activation barriers. This approach accurately characterizes the interaction between the solid surfaces and organic molecules. In the DFT-D2 formalisms, the total energy of the system can be defined as a sum of the semi-empirical dispersion correction (E_{dsip}) and the self-consistent Kohn−Sham energies.

$$E_{DFT-D2} = E_{disp} + E_{KS-DFT} \qquad\qquad 6.1$$

In order to precisely account for the strong electronic correlation of the Fe $3d$ states and their over-delocalisation in the standard DFT methods, a Hubbard correction parameter was applied in all calculations based on the DFT+U formalism of Liechtenstein and Dudarev [468, 469].

Moreover, to determine the transition states (TS) and the minimum energy reaction paths for all structures presented in our study, climbing image nudged elastic band (CI-NEB) technique

was performed [414, 470, 471]. Generally, five images were generated between the states of initial reactants and final products based on nudged elastic band (NEB) method. When the interaction had an intermediate minimum present, the closest energy point was allowed for full relaxation to define if the minimum was a true minimum. Activation energies for all interaction mechanisms were calculated by applying the following equation:

$$E_{activation} = E_{surface} + E_{molecule} - E_{transition\,state} \qquad 6.2$$

where $E_{surface}$, $E_{molecule}$, and $E_{transition\,state}$ denote the energies of substrate, gas phase molecule and the transition state, respectively.

Calculated vibrational frequencies enable to estimate thermodynamic parameters at high temperatures (300-1000K), from which Arrhenius parameters (E_a and A) can be computed. based on the transition state theory (TST), reaction rate constants $k(T)$ are computed from enthalpy (ΔH) and entropy (ΔS) of activation [416, 472]:

$$k\,(T) = \sigma_e \frac{k_B T}{h}\, e^{\frac{\Delta S}{R}} e^{-\frac{\Delta H}{RT}} \qquad 6.3$$

In this formula, h and k_B are Planck and Boltzmann constants, respectively; T is the temperature in Kelvin (K), R denotes the universal gas constant, and σ_e signifies the reaction deration number (i.e., = 1.0).

Finally, Phonopy software [332, 473] was employed to estimate phonon spectra (i.e., vibrational free energies). Phonopy code computes the real-space force constants by introducing displacements to supercells based on atomic limited displacement method. Hence,

calculated force constants enable to obtain both phonon frequencies and thermodynamic properties [417, 474]. The latter was used to calculate reaction rate constants based on the TST as explained above.

6.3. Results and Discussion

6.3.1. Bulk, Surface and Gas Phase Molecules

Nanoparticles of Fe_3O_4 with inverse spinel structure have been widely applied in a variety of fields such as tincture colour and heterogeneous catalysts due to their non-toxicity, chemical stability and profound redox performance [451, 475-478]. The crystal structure of magnetite is an inverse spinel pattern with equally mixture of Fe^{2+} and Fe^{3+} ions in the octahedral sites and with Fe^{3+} ions in the tetrahedral sites [479, 480]. Figure 6.S2 (Appendix B) depicts the optimized structure of Fe_3O_4. The calculated lattice parameter amounts to 8.150 Å. This value agrees reasonably well with other previous theoretical and experimental results of 8.140 Å and 8.396 Å, correspondingly [481, 482].

Perpendicular cleavage of magnetite unit cell affords three low-Miller distinct surface terminations indicated as (100), (110) and (111) configurations. Among these surfaces, Fe_3O_4 (111) configuration is found to follow the experimentally observed natural growth and to be the more thermodynamically stable configuration [483-486]. In this work, we have adapted the Fe_{Oct2} and Fe_{Tet1} terminated surfaces as the most thermal stable faces of Fe_3O_4 (111) validated by numerous experimental and theoretical investigations. Based on low-energy electron diffraction (LEED) and scanning tunnelling microscopy (STM) techniques, it was confirmed that these terminated surfaces are the most energetically favored faces among other possible terminations. For example, Lennie et al. [483] carried out an experimental investigation on a natural single-crystal of Fe_3O_4 (111), cleaned and annealed using cycles of

500-eV Ar^+ bombardment and electron-beam heating (UHV) at 1070 K , respectively. Using the STM images, they found that several surface terminations of Fe_3O_4 have been observed under oxidation and reducible annealing conditions; i.e. T= 1173 K and 1073 K but the two outmost layers (Fe_{Oct2} and Fe_{Tet1}) are the most thermodynamically stable. A similar observation was made by Grillo et al. [487] via performed a theoretical investigation to study Fe_3O_4 (111) structure in a temperature range of 298 to1200 K.

In order to examine the Fe_3O_4 surface structure adopted in our study, it is of interest to calculate the dimer distance between iron and oxygen atoms and to contrast these distances with those of previous works. As shown in Table 6.S1 (Appendix B), our computed $Fe_{oct-tet}$ -O bond lengths match analogous theoretical and experimental values obtained from GGA+U functional method and LEED analysis [487-489]. Moreover, we calculate surface relaxation of the topmost layers of Fe atoms to gain a benchmark of accuracy of our adapted methodology. We find Fe_{Oct2} and Fe_{Tet1} relaxation to correspond to 67% and 41%, respectively inward to the underneath O layer. Our calculations reflect very well with the previous computational and experimental results [486, 488, 490].

Furthermore, a Bader charge analysis was calculated to evaluate the surface electrostatic potential. As shown in Figure 6.S2, the exposed Fe_{Oct2} cations containing the first layer possess strong positive potentials and thereby act as effective electron acceptors whilst, Fe_{Tet1} atoms in the second topmost layer are highly charged deficient because of their surrounded oxygen atoms. Hence, it can be expected from these electrostatic characteristics that Fe_{Oct2} site is the main target for any molecular adsorption.

Finally, we have computed bond dissociation energies (BDEs) for the selected molecules in order to contrast them with their well-documented gas-phase thermochemistry values in the literature. As illustrated in Figure 6.S3 (Appendix B) the calculated BDEs for fission H/C-Cl bonds of the gaseous molecules selected in this study show excellent consistency with the BDEs values reported in the literature [367, 371].

6.3.2. Dissociation Adsorption of HCl over Fe_3O_4 (111) Surface

As an outset point of this section, we investigated the three subsequence stages of dissociation adsorption of HCl on both Fe_{Oct2} and Fe_{Tet1} sites of Fe_3O_4 (111) surface: (i) physisorption state leading to surface-molecule adducts M1 (over Fe_{Oct2}) and M1* (over Fe_{Tet1}) formation; (ii) decomposition step producing oxychloride structures of M2 and M2*; and (iii) transition state of the HCl dissociation step.

As illustrated in Figure 6.1, HCl molecule can be adsorbed either on the top of Fe_{Oct2} or Fe_{Tet1} surface atoms. The adsorption energy of HCl at the Fe_{Oct2} site is calculated as -13.5 kcal mol^{-1}, which is lower than that (-8.8 kcal mol^{-1}) on Fe_{Tet1} of Fe_3O_4 (111) surface, indicating a strong molecular physisorption state of the Fe_{Oct2} site. In order to further reveal this strong nature of Fe_{Oct2} reactivity, we analysed both the geometric and electronic structural properties on both sites. As an initial state of HCl interaction over Fe_{Oct2} and Fe_{Tet1} sites, the Cl fragment is attached to surface Fe atoms with bond of 2.195Å and 2.440Å, respectively. This is accompanied with a sizable H-Cl bond extension by 130% and 51% on the Fe_{Oct2} and Fe_{Tet1} sites, respectively, in comparison to the equilibrium distances in the gaseous HCl molecule (1.298Å) at the Fe_{Tet1} side. Therefore, the considerable H-Cl bond elongation indicates a strong chemical activation of the HCl molecule over the Fe_{Oct2} site.

Likewise, as depicted in Figure 6.1, higher electron transferred from Fe atom to chlorine atom at the Oct2 site in reference to the Tet1 site (-0.08e versus -0.02e) represents another signature for the stronger adsorption state over the Fe$_{Oct2}$ site in comparison with that over Fe$_{Tet1}$ site. Interestingly, our findings are consistent with the previous computational results [491, 492], which reported that, molecular adsorption on a surface Fe$_{Oct2}$ atoms has the most energetic preference in reference to Tet1 atoms.
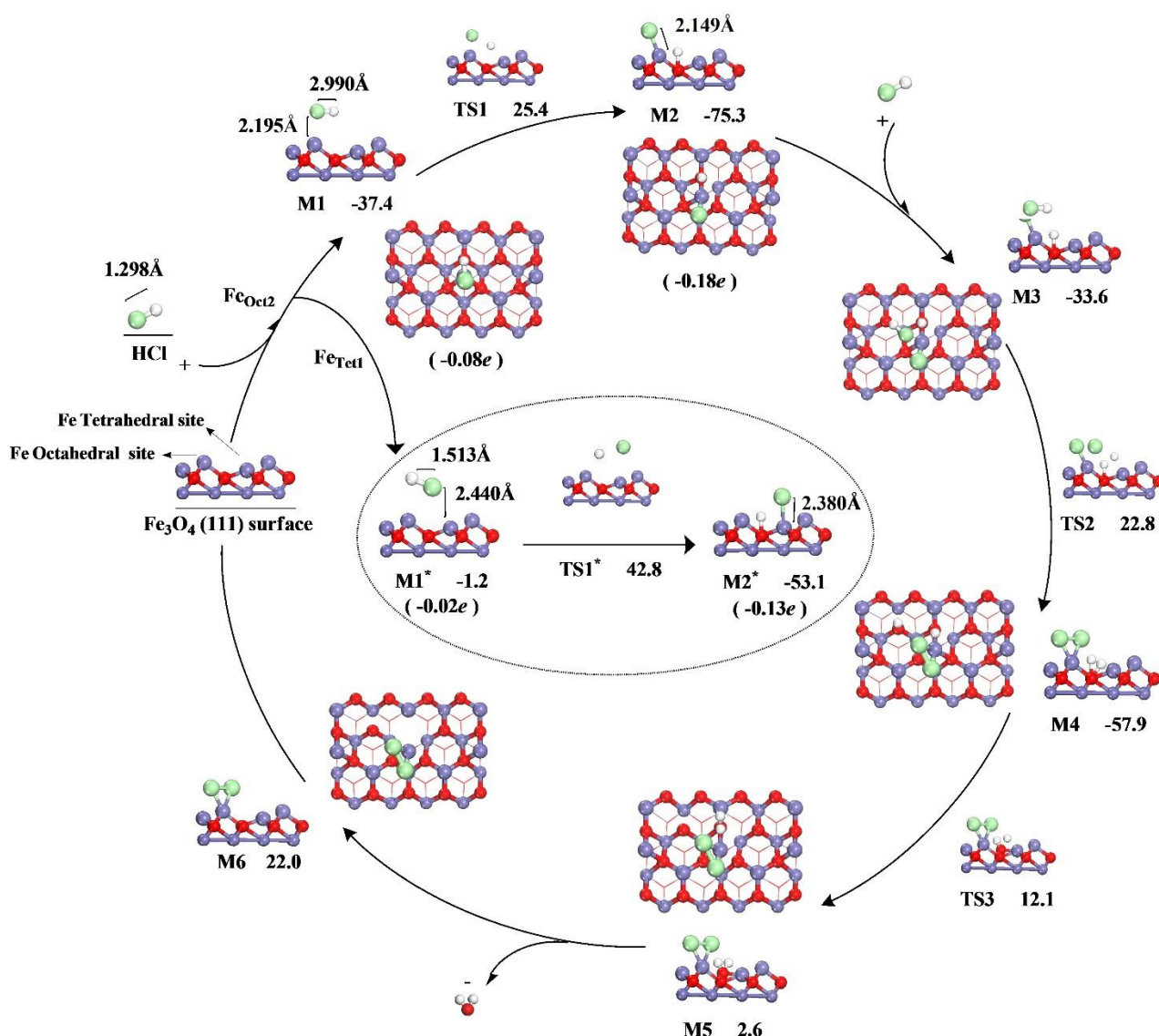
Figure 6.1. Reaction steps for the decomposition of hydrogen chloride molecules on both Fe$_{Oct2}$ and Fe$_{Tet1}$ sites of magnetite (111) surface. Only the first two layers are shown in side views. The net charge transfers from the surface to adsorbed Cl molecule are illustrated.

Additional insight into understanding the interaction between molecularly adsorbed HCl over both the Fe_{Oct2} and Fe_{Tet1}-terminated can be obtained by analyzing the electronic properties of the system. Figure 6.2 illustrates the spin-polarized density of state (DOS) and partial density of states (PDOS) spectra onto the d-orbitals of Fe_3O_4 (111) surface and for those two different terminations calculated at the DFT-U level rather than DFT. DFT-U presents a better description of the half-metallic electron structure above the Verwey transition and it considers to be most relevant for electron transport spin polarization measurements. For the clean Fe_3O_4 (111) surface, it is obvious that the total DOS is very similar to the bulk DOS [493] and the low laying states of this clean surface (Figure 6.2.a) is dominated by d-orbitals of iron, which is in a good agreements with previous results [491]. It is also found from panels b and c, for both clean Fe_{Oct2} and Fe_{Tet1} terminations, that the iron contributions to surface PDOS of Fe_{Oct2} termination are more dominant than those of the Fe_{Tet1} termination, in specific around the Fermi level, and this agrees well with previous theoretical results based on PBE functional [494]. This high domination, in turn, indicates that the Fe_{Oct2} termination is very sensitive to the adsorption of gas species.

For investigation of the bonding mechanisms for the adsorption of HCl molecular over Fe_{Oct2} and Fe_{Tet1} sites, we first analyse the DOS of free HCl molecule. Figure 6.2 (d) displays the DOS of the gaseous HCl. In this panel, the electronic states *A*, *B* and *C* originate from Cl-H bonds and chlorine lone pair [495]. However, in the state of HCl dissociation over the Fe_{Oct2} and Fe_{Tet1} terminations, it is clear that these bands shift downward the Fermi level, which implies the charge transfer from the Fe_{Oct2} atoms to HCl molecule. Moreover, from panels e and f, the appearance of a new peak near -10 eV and the split of the *B* band into two peaks over the both sites indicates a generation of new Cl-Fe bond accompanied with a change in the H-Cl molecular bonding. By comparing the PDOS schemes for dissociative adsorption of HCl

molecular over these terminations, as shown in panels e and f, we can conclude the following focal points:

1- The level of the split in the case of Fe_{Oct2} is higher than that of the case Tet side. This indicates that the adsorption of HCl molecular over Oct2 site incurs higher stability than that of the Tet site. This corresponds with the general observations from the previous work [496] and with our findings for the formation of M2 and $M2^*$ configurations in Figure1 that bonding of Cl with Fe_{Oct2} atom is considerably stronger than the Tet site (-54.8 kcal mol^{-1} versus -36.1 kcal mol^{-1}) and (2.149 Å versus 2.380 Å).

2- The high peaks shifting of the HCl dissociative adsorption over Fe_{Oct2} termination below the Fermi level in reference to the Fe_{Tet1} termination, as shown in panels e and f, implies a higher electron transfer from Fe_{Oct2} atoms to adsorbed Cl atom (-0.18 versus -0.13).
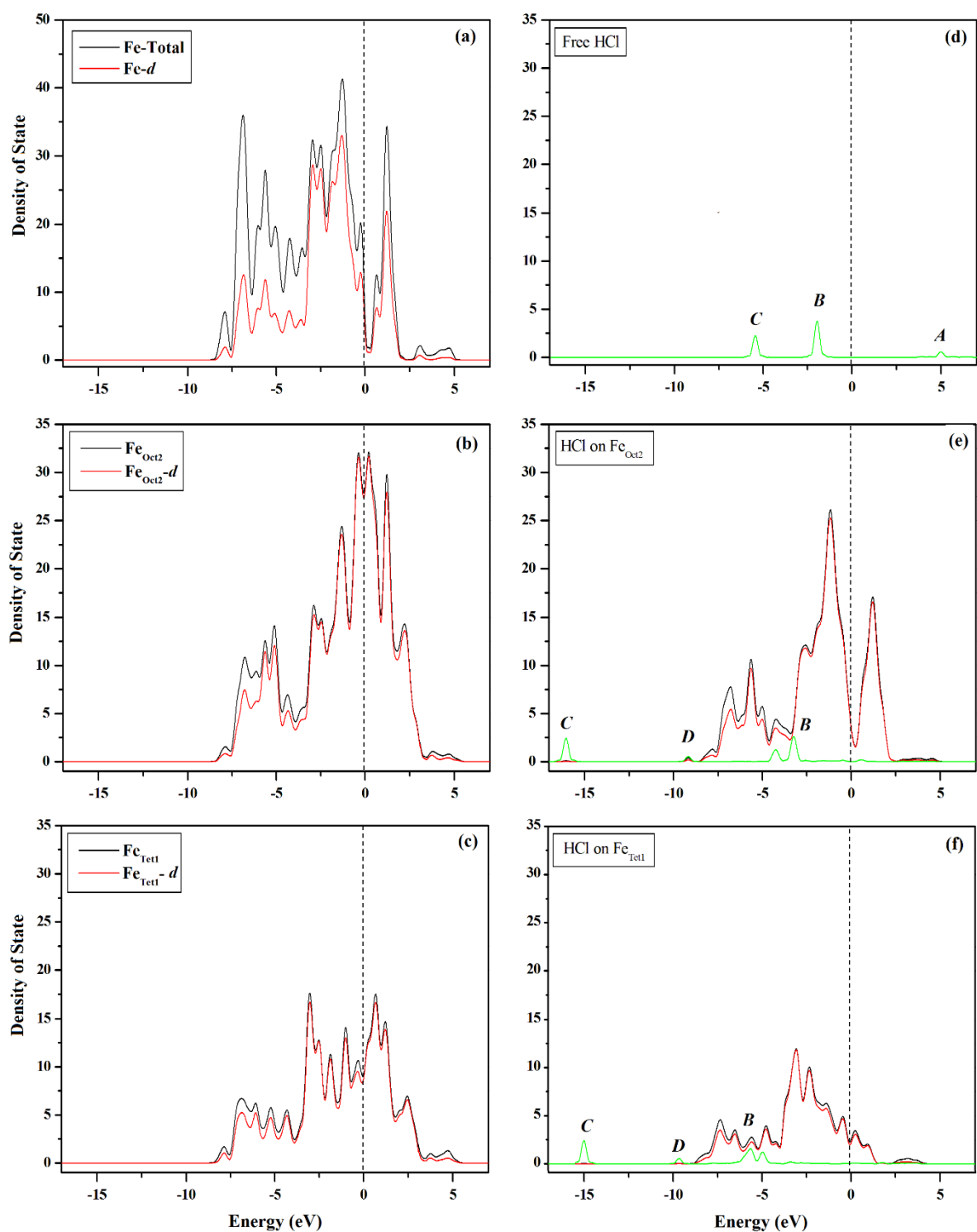
Figure 6.2. DOS and PDOS of (a) clean $Fe_3O_4(111)$ surface, (b) clean Fe_{Oct2} termination, (c) clean Fe_{Tet1} termination (d) free HCl molecular (e) the adsorbed HCl on Fe_{Oct2} termination, and (f) the adsorbed HCl on the Fe_{Tet1} termination.

As mentioned earlier, the second step is the decomposition reaction. The Fe_{Oct2} site also delivers superior activity than Fe_{Tet1} from thermodynamic and kinetics aspects. HCl molecular dissociation upon Fe_{Oct2} is exothermic by 54.8 kcal mol^{-1} with a modest activation barrier of 26.3 kcal mol^{-1}. On the other hand, dissociation energy of HCl on Fe_{tet1} site of Fe_3O_4 (111) is exothermic by 36.1 kcal mol^{-1}, with a higher barrier energy of 43.2 kcal mol^{-1}. This larger value of chemisorption energy over Fe_{Oct2} site is in line with Zhou et al.'s result [491], who observed that, water molecule dissociativelly adsorb over Fe_{Oct2} site with a high energy value in reference to Fe_{Tet1} site. Moreover, this exothermic trend for the first decomposition stage reflects very well with our recent investigations for reaction of HCl/HBr over α-Fe_2O_3 clusters and ZnO surface.[350, 460, 461] In this step, HCl molecule dissociates heterolytically on a surface oxygen atom as well as both Fe_{Oct2} and Fe_{Tet1} sites leading to the migration of both hydrogen and chloride atoms, forming hydroxyl species and oxychloride configurations of M2 (Fe_{Oct2}-Cl) and M2* (Fe_{Tet1}-Cl), with interatomic distances by 2.149 Å and 2.380 Å, correspondingly. Compared to the Fe_{Tet1}-Cl, Fe_{Oct2}-Cl bond length reflects very well with the analogous theoretical value of the bulk $FeCl_2$ and that can be attributed to a strong Fe_{Oct2} chemisorption energy (-54.8 kcal mol^{-1}) [368]. By comparing these activation barriers for the two considered sites of Fe_3O_4 (111) surface with the energy requirement for H-Cl bond scission in gas phase (i.e., 103.2 kcal mol^{-1}) [371], it becomes evident that Fe_{Oct2} site requires significantly lower energy and hence should be catalytically very effective in fixing Cl atom. In support of this finding, the existing literature points out that more than 90% of chlorine compounds, released from thermal degradation of PVC mixed plastic, has been fixed in the presence of Fe_3O_4 and form ferrous chlorides [256].

Bader's charge analysis for dissociative adsorption of HCl over Fe_{Oct2} and Fe_{Tet1} sites in Fe_3O_4 (111) can also provide an effective theoretical prediction for the ability of the Cl atom (formed

by dissociative adsorption) to function as a Lewis acid–base pair. This could be achieved by determining electron transfer between HCl molecule and the magnetite surface. As illustrated in Figure 6.1, the net electronic charge transfer from Fe_{Oct2} and Fe_{Tet1} sites to adsorbed Cl atoms are -0.18 and -0.13, respectively. Clearly, Cl serves as a charge acceptor and hence the Fe-Cl acts as a Lewis acid–base pair.

The extent of the transferred charge from Fe_{Oct2} (M2) is relatively sizable (in reference to Fe_{Tet1} site, M2*). This demonstrates a stronger interaction with the strong reaction with Fe_{Oct2} site in comparison with the Fe_{Tet1} site of Fe_3O_4 (111) surface. Such similar behaviours have also been found when HCl dissociates on CeO_2 and ZnO surface [440, 461]. Therefore, based on the analysis above for the dissociative adsorption of HCl on both Fe_{oct2} and Fe_{tet1} sites, we will limit our further analysis and discussions for HCl decomposition and the dissociative adsorption of the selected chlorinated hydrocarbons only on the Fe_{Oct2} site.

6.3.3. Subsequent Addition of HCl over Fe_3O_4 (111) Surface

The second interaction mechanism examined here is a dissociative adsorption of a hydrogen chloride molecule. In this interaction, we began with addition another HCl molecule to the oxychloride configuration of M2 to form a ferric chloride. Energies and structures for this mechanism are shown in Figure 6.1. First, a second HCl molecule is attracted to the Fe-O bond in M2 with a physisorption energy of -16.3 kcal mol^{-1} to yield the intermediate M3 configuration. Next, the H-Cl bond is broken over a surface Fe-O bond and the M4 structure is formed via TS2. This step is largely irreversible with an activation energy barrier of 20.9 kcal mol^{-1} accompanied with an exothermic reaction energy of 36.9 kcal mol^{-1}. In the course of M4 formation, the Cl atom combines with the same surface Fe atom whereas, H atom forms a hydroxyl group via binding with a different surface oxygen atom, as pictured in Figure 6.1.

The barrier of TS2 matches very well that of TS1 (20.9 versus 26.3 kcal mol^{-1}). This indicates that the existence of the pre-adsorbed chloride atoms displays a minimal influence in facilitating further dissociative adsorption.

In the next step, a hydrogen atom from a surface hydroxyl group migrates to an O atom from a neighbouring hydroxyl group forming an adsorbed water molecule as shown in structure M5. This intramolecular H transfer process is slightly endothermic by 6.4 kcal mol^{-1}. The latter values are very close to an analogous value at of 3.5 kcal mol^{-1} reported by Huang et al. [492], who investigated H$_2$ interaction with the Fe$_3$O$_4$ surface. Moreover, our previous investigations have predicted the same endothermic trends over hematite cluster and zincite surface [350, 461]. This process entails an accessible activation energy of 16.9 kcal mol^{-1} through TS3. Similar low activation barriers were also calculated in our previous studies on hematite clusters and zincite surfaces [350, 461]. As hydrogen atoms recombination mechanism involves generation of a water molecule, the calculated length of the Fe-OH$_2$ bond (i.e., 2.23 Å) from the M5 structure is in accord with the corresponding bond length (2.15Å) [497] obtained for H$_2$O adsorption on the hematite surface and is also in a good agreement with our analogous estimate (i.e., 2.20 Å) for hematite clusters [460].

The final stage of HCl + Fe$_3$O$_4$ interaction is water desorption process from the M5 configuration leading to form M6 structure via a barrierless reaction. This process was found to be exothermic with the computed desorption energy of -4.4 kcal mol^{-1}, as shown in Figure 6. 1. This is in line with Al-Harahsheh et al. [101] findings, who observed an exothermic event during the thermal decomposition of PVC and EAFD mixture. Clearly, desorption of water marks the final step in the conversion of iron oxide into iron chloride via interaction of HCl. Chromatograph with a thermal conductivity detector was used by Uddin et al. [256] to

investigate the effect of iron oxides on the removal of Cl from thermal decomposition of PVC. They observed that more than 90% of chlorine had been adsorbed using Fe_3O_4 and FeOOH. This in turn indicates that Fe_3O_4 and FeOOH are very effective in fixing Cl in their structural framework, presumably along the illustrated mechanism in Figure 6.1. Moreover, X-ray diffractometer has been utilized to determine the crystalline structure of the formed iron chloride, in which no crystalline phase of $FeCl_2$ can be observed, but it can be present only on iron oxides as a monolayer. Furthermore, findings by Al-Harahsheh et al. [384] have demonstrated that combining treatment of metal oxides with PVC lead to the formation of a new solid phase product (i.e., iron chloride) that can act as an HCl removal agent. Therefore, we conclude that the captured Cl from thermal degradation of PVC does not leave the hematite surface as a volatile iron chloride.

Reaction rate constants for steps in Figure 6.1 were computed according to the TST as explained in section 6.2. The reaction rate parameters for these reactions (portrayed in Figure 6. 1) are listed in Table 6.S2, whilst the panels in Figure 6.3 depict Arrhenius plots between 300-1000 K for the rates of decomposition of hydrogen chloride molecules over the Fe_3O_4(111) surface.
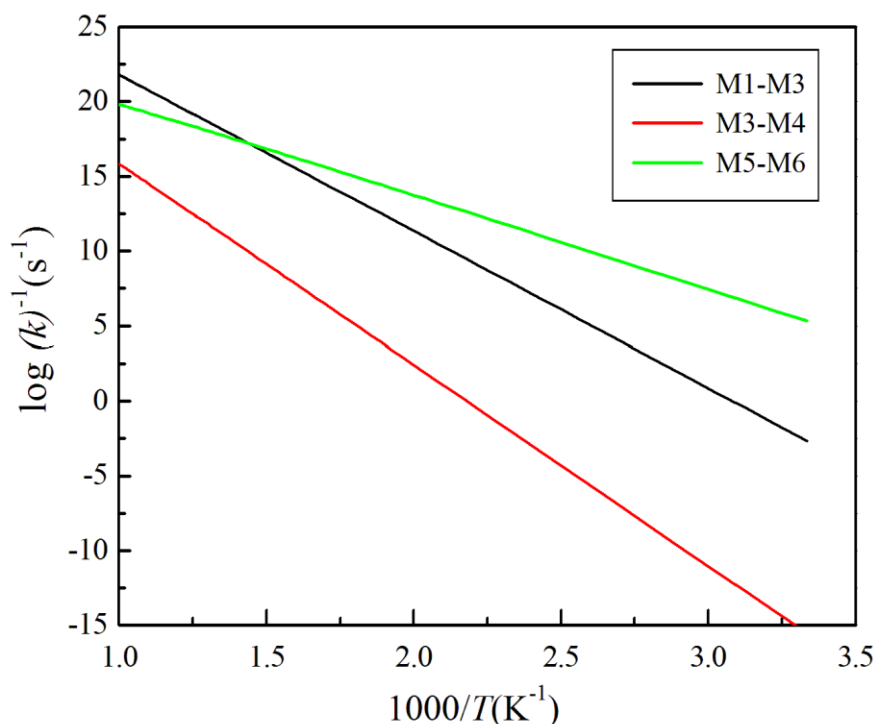
Figure 6.3. Arrhenius plots for reactions of $Fe_3O_4(111)$ surface with HCl molecules.

.

6.3.4 Decomposition of Organochlorinated Compounds over Fe_3O_4 (111) Surface

The interaction of alkyl halogens with metallic oxide catalysts (dehydrohalogenation process, in particular) represents one of the most promising methods for the industrial production of olefins [498]. This process, in turn, has significant environmental and economic benefits pertinent to recovery of chlorine emitted from thermal decomposition of from halogenated wastes as metallic chloride. The mechanism proposed for the reaction of halogenated alkanes and alkenes with metal oxides consists of two essential competing channels: direct elimination and dissociative addition.

In our earlier works, we indicated that α-Fe_2O_3 cluster act as an active catalyst in generating clean olefins flows from both the brominated and chlorinated compounds [350, 460]. Continuing these studies, we evaluate the catalytic activity of magnetite in the

dehydrochlorination of the selected compounds with the aim to device an approach for mild conditions in the recycling of halogenated waste steam.

Molecular adsorption of the considered chlorinated compounds over the magnetite (111) surface in the first step can be viewed as a Lewis-acid / base reaction leading to generate the surface-molecular adducts M7, M10, M13 and M16 for the adsorption of chloroethane, 2-chloropropane, 1-chloro-1-propene and chloroethene, respectively. Through this step, magnetite surface activates the carbon-halogen bonds thereby elongating C-Cl bond by 0.16%, 2.83%, 4.48% and 4.63%, respectively (in reference to equilibrium distances of their parent gas phase molecules). In order to reveal this reaction nature, we utilize the Bader's charges to determine whether the adsorbed species are Lewis acid or a Lewis base. Table 6.1 lists the Bader's charges of the adsorbed Cl atoms. In the physisorbed structures, Cl atoms are positioned over Fe_{oct2} sites in the surface as shown in the top views of Figures 6.4- 6.7. The negative values for the net charge transfer as presented in Table 6.1, indicate that the Cl atoms for all the surface-molecular adducts incur electronic charge. Previous computational investigations have illustrated that, the presence of a Lewis base over a metal oxide surface enhances the adsorption energy of a Lewis acid.[440, 499] The net charge transferred from magnetite surface, as shown in Table 6.1, positively correlate with the elongation of the C-Cl bonds.

Table 6-1. Electronic and structural properties for molecular and dissociative adsorption structures

Species	Elongation of Cl -C bonds (%)	Charge transfer from the surface to adsorbed Cl molecules (e) (Physisorption)	Adsorption energy (kcal mol^{-1})
Chloroethane	0.16	-0.13	-12.4
2-Chloropropane	2.83	-0.19	-15.1
1-Chloro-1-propene	4.48	-0.21	-9.5
Chloroethene	4.63	-0.32	-14.4

Figures 6.4- 6.7 portray the catalytic decomposition of the selected chlorinated compounds. Calculations have shown that the direct elimination of HCl from the selected molecules proceeds though activation barriers of 6.9 kcal mol^{-1}, 21.4 kcal mol^{-1}, 35.0 kcal mol^{-1}, and 48.5 kcal mol^{-1} for chloroethane, 2-chloropropane, 1-chloro-1-propene and chloroethene, correspondingly. It should be pointed out that, these values seem to positively consistent with the BDE values of carbon-chlorine elimination in the gas phase [367, 371]. It is obvious that, the surface Fe-O bonds lower the activation energies for the dehydrochlorination corridor when contrasted with the uncatalyzed analogous gas phase pathways. For instance, HCl elimination from chloroethane molecule demands an activation barrier of 6.9 kcal mol^{-1}. This is significantly less than the value sourced from a DFT investigation Ahubelem et al [374] who found that formation of ethene from chloroethane requires a sizable barrier of 57.5 kcal mol^{-1}.
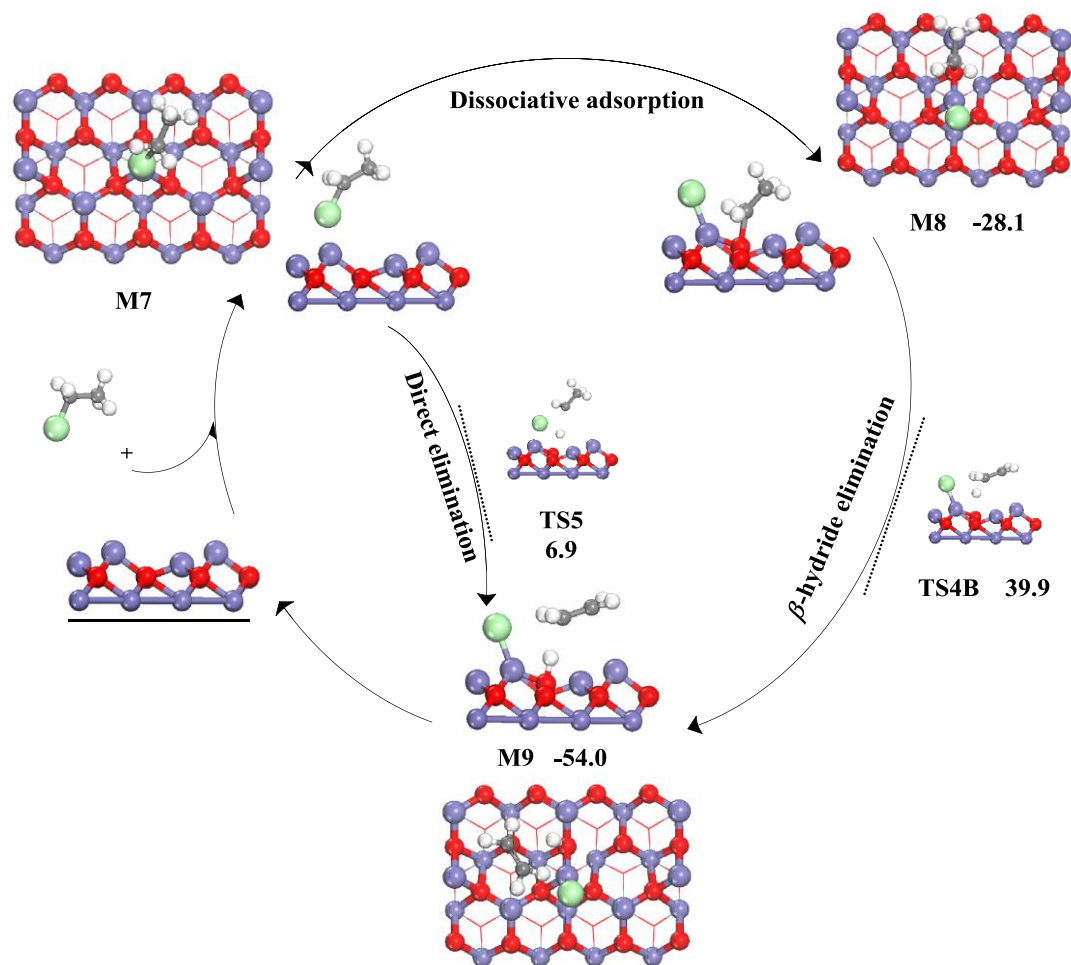
Figure 6.4. Reaction of chloroethane molecule with the magnetite (111) surface. Values are in kcal mol^{-1} in reference to the initial physisorbed structure, M7.

As alternative mechanism to the direct elimination route is the dissociative addition pathway. This pathway proceeds in two steps; the direct scission of carbon-chlorine bond in the adsorbed radicals, followed by β C-H bond elimination to afford the same products from elimination route. The first is the fission of a C-Cl bond either through a low activation barrier of 18.2 kcal mol^{-1} and at 24.6 kcal mol^{-1} for 1-chloro-1-propene and chloroethene, respectively or via a barrierless interaction for chloroethane and 2-chloropropane. This stage leads to produce an alkoxy or alkoxide intermediate over the oxygen atoms of magnetite surface where the positively charged C atoms combine with the surface O atoms, while the Cl atoms bind with Fe atoms as shown in structures M14 and M17 in Figures 6.6 and 6.7. The second step signifies

the formation of chlorine-free olefins by activating the carbon-hydrogen bond characterised by the transfer of a hydrogen atom to a surface oxygen via a β-hydride elimination step. The subsequent migration of hydrogen atoms occurs via very sizable activation barriers that vary from 37.3 kcal mol^{-1} (TS6B in Figure 6.5) for the expulsion of propene (one of the previously experimentally detected compounds from co-pyrolysis of PVC with EAFD) as a gas phase radical to 83.3 kcal mol^{-1} (TS10B in Figure 6.7) for formation of an ethyne molecule. Overall, the expulsion of olefins as a gas phase supports earlier experimental measurements of Al-Harahsheh et al. [59] who found that, the co-pyrolysis of both EAFD and PVC at temperatures higher 623 K lead to form alkyne molecules such as propyne.

Figure 6.5. Reaction of 2-chloropropane molecule with the magnetite (111) surface. Values are in kcal mol^{-1} in reference to the initial physisorbed structure, M10.

From the above analysis, we can indicate that, the direct elimination channel is likely to satisfy the so-called E2 mechanism presented by a recent theoretical study for ethanol dehydration by Al_2O_3 clusters [500], while the dissociative addition channel follows the S_N2 type of mechanism.
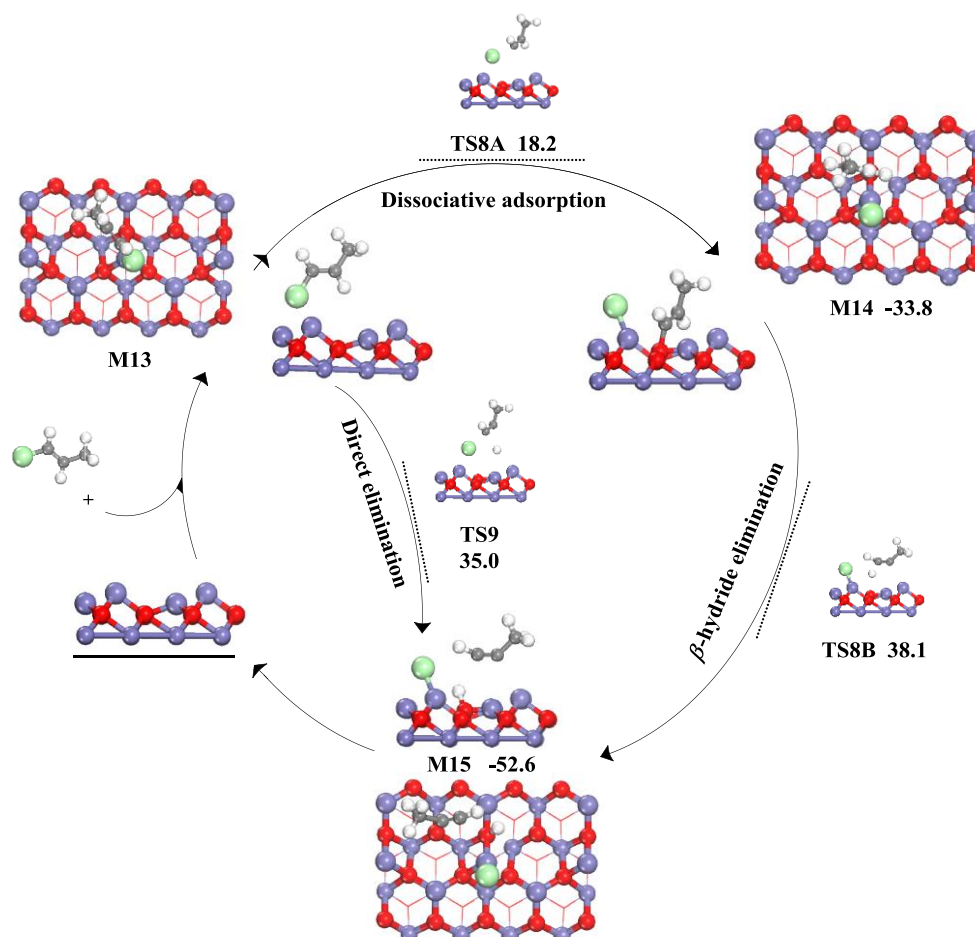
Figure 6.6. Reaction of 1-chloro-1-propene molecule with the magnetite (111) surface. Values are in kcal mol^{-1} in reference to the initial physisorbed structure, M13.

Next, we turn our attention to compare the overall activation barriers for the β-hydride elimination step (i.e., in reference to the initial physisorption states) with those values of the direct elimination routes. From Figure 6.4- 6.7, we infer the following focal points:

1- Dissociative addition pathway is expected to predominate the direct elimination route for the formation of propene and ethyne. This corresponds with our finding for the dehydrochlorination of organochlorinated compounds over α-Fe$_2$O$_3$ clusters as well as with an analogous previous theoretical account for the dehydrohalogenation of halogenated alkanes by Al$_2$O$_3$ cluster [460, 501].

2- Direct elimination route represents the only feasible pathway for formation of ethene. A similar trend has been observed from our recent investigations on the interaction of a wide range of brominated/chlorinated compounds with hematite cluster [350, 460].

3- Reaction barrier for the direct HCl elimination route (35.0 kcal mol^{-1} for 1-chloro-1-propene) matches an analogous overall barrier for its dissociative adsorption pathway i.e., 38.1 kcal mol^{-1}.

This trend supports the general consensus pertinent to the significance of the dissociative addition pathway for producing pure stream of olefins [498]. The above conveyed analysis demonstrates that, iron oxides act as effective catalysts and sorbent for the chlorine emitted from the decomposition of PVC.
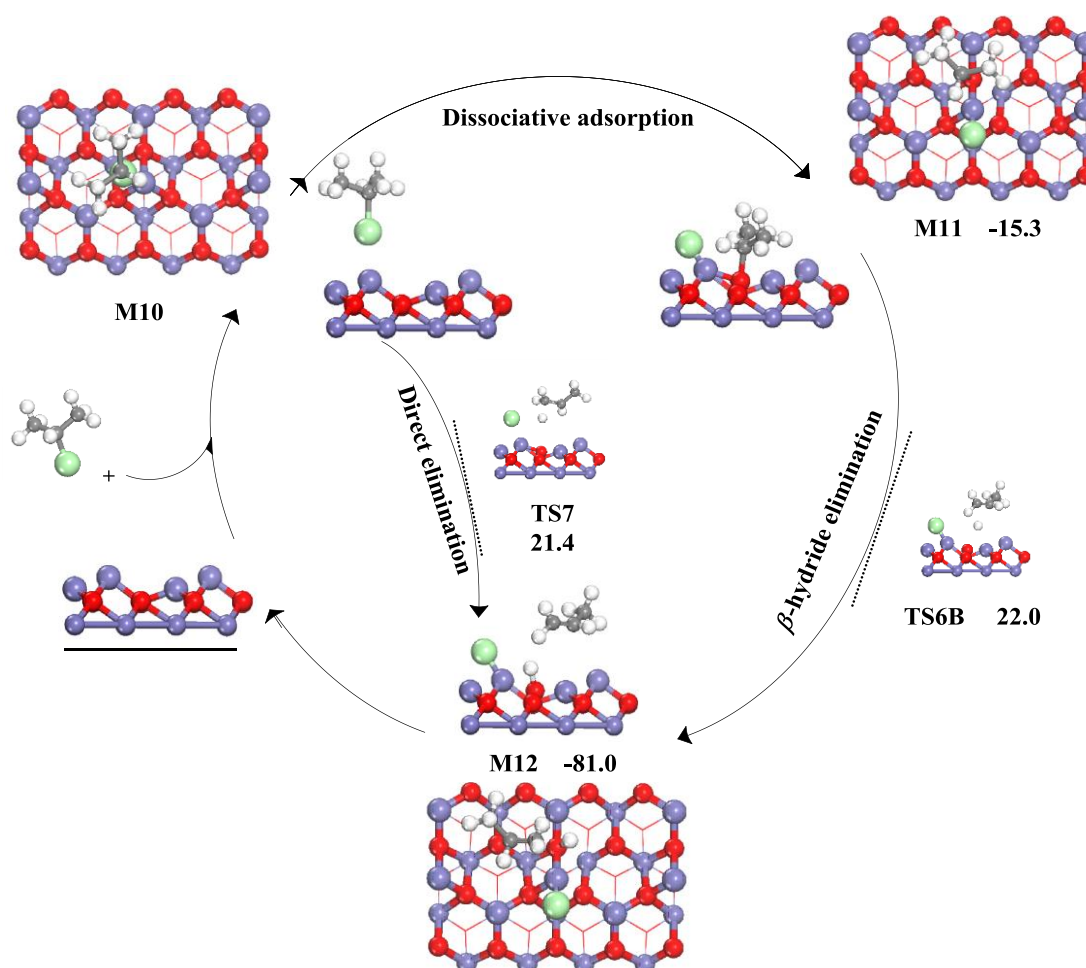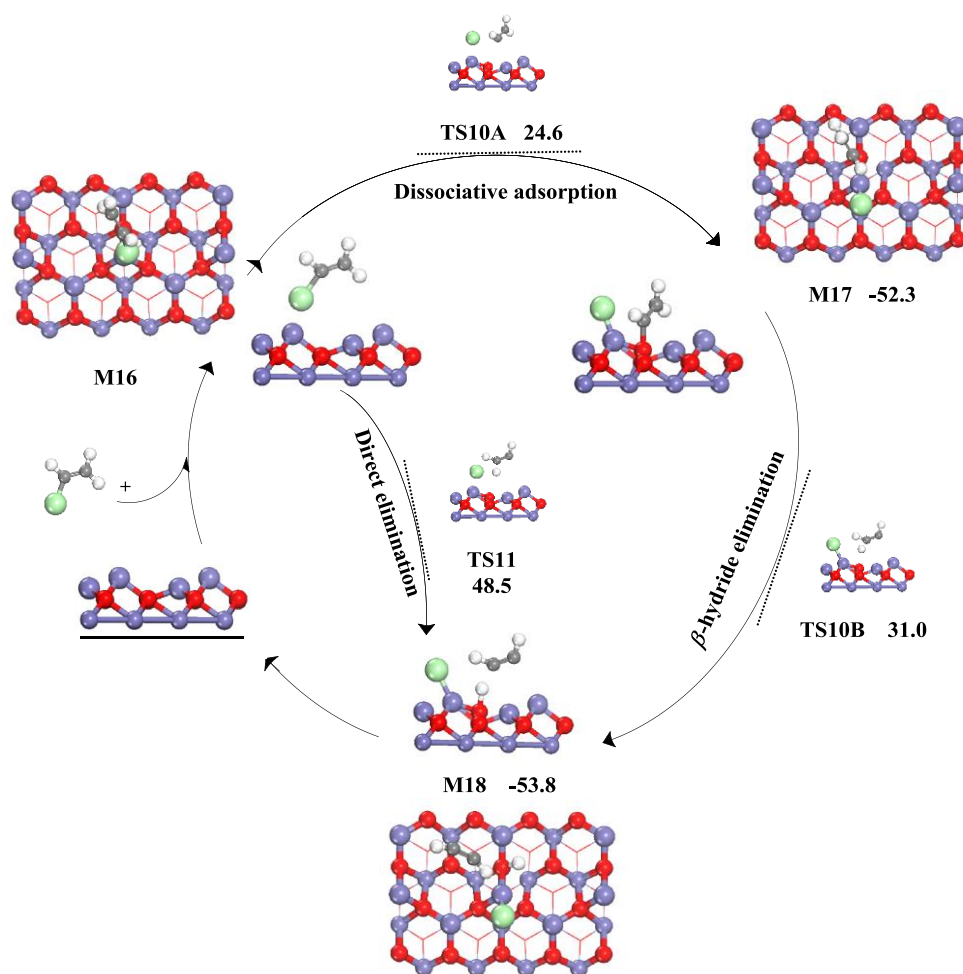
Figure 6.7. Reaction of chloroethene molecule with the magnetite (111) surface. Values are in kcal mol^{-1} in reference to the initial physisorbed structure, M16.

6.4. Conclusions and Future Directions

Throughout this manuscript, we have performed accurate DFT calculations to study dechlorination and dehydrochlorination mechanism of hydrogen chloride and organochlorinated compounds over magnetite Fe_3O_4 (111) surface. We started the study by a comprehensive accuracy benchmarking of the adapted methodology against literature reporting electronic and structural properties for bulk and surface of Fe_3O_4 as well as for the BDE in the investigated molecules. Results show that, dechlorination mechanism involved the formation of ferrous ferric chloride proceed via two subsequent stages, further dissociative adsorption of hydrogen chloride molecules on strong Lewis acid metal oxide site and followed by liberation

of H_2O molecules. We find that the dissociative adsorption of HCl over Fe_{Oct2} sites requires remarkably lower activation energy than that over the Fe_{Tet1} sites of Fe_3O_4 (111) surface. Herein, we investigated two competing channels for the reaction of halogenated alkanes and alkenes with the Fe_3O_4 surface; the direct HCl elimination route and the dissociative addition pathway. Products from the latter channel are significantly lower in energy, which supports the general consensus related to the significance of the dissociative addition pathway in producing a pure stream of olefins.

Chapter 7

Catalytic De-halogenation of Alkyl Halides by Copper Surfaces

The following chapter is a modified version of <u>paper III</u>:

Abstract

The interplay of halogenated compounds with metal surfaces has been the focus of many experimental and theoretical studies. These investigations have mainly aimed to illustrate the potential dual role of transition metals and their oxides in mediating formation of toxic halogenated aromatics as well as their catalytic-assisted decomposition over these surfaces. An initial and prominent step in conversion of these precursors into heavier halogenated aromatics signifies their dissociative adsorption on metallic species readily present in the combustion media. This contribution represents a systematic computational study to examine thermo-kinetic parameters underlying rupture of Cl/Br-C bonds in halogenated model compounds (namely; 2-chloropropane, chloromethane, chloroethyne, chloropropene, chlorobenzene, 2-bromopropane, bromomethane, bromoethyne, bromopropene, and bromobenzene) over the Cu (100) surface. These compounds adapt very weak physisorbed molecular states evidenced by marginal adsorption energies and minimal structural changes in reference to their gas phase molecules. The calculated reaction barriers for Cl/Br-C bond fissions are scattered in the range of 8.3 - 37.2 kcal mol^{-1}. Stronger Cl – C bonds in reference to Br – C bonds (in the gas phase) translate into higher corresponding reaction barriers for the former. The calculated reaction rate constants and activation energies reveal faster rate for the decomposition of the brominated species. Our calculations of the activation energies accord very well with the experimental analogues values.

7.1. Introduction

Brominated flame retardants (BFRs) are broad groups of chemicals that are extensively used to delay/prevent the inset of ignition in treated objects via releasing bromine atoms [16, 459, 502, 503]. The latter readily captures hydroxyl radicals from the progressively established combustion medium. BFRs are widely employed in a vast array of commercial and consumer products such as textiles, furniture, plastics and electronic and electrical equipment [22, 504]. Due to the relatively short life span of treated objects (i.e., printed circuit boards), the extensive uses of BFRs has resulted in a gigantic volume of halogenated wastes that poses a significant concern, not only on the environment but also on the public health of human and other living organisms [502, 505-507]. Likewise, polyvinyl chloride (PVC) is the most widely used polymers with a production that has peaked at 60 Mt in 2013 and is estimated to reach ~180 Mt in 2021 [6]. The "waste-to-energy" approach is now widely deployed as a mainstream strategy in the safe and economically effective disposal of the polymeric constitutes of halogenated polymeric wastes. The organic matter in halogenated wastes is embedded with high energy content. The recyclability of halogenated polymers into important industrial feedstocks (olefins, in particular) heavily relies on near complete removal of their bromine/chlorine content [212, 508].

Destroying of the carbon frameworks in bromine/chlorine-containing polymers through thermal methods such as, incineration and thermal degradation is a truly daunting task as it often necessitates a very high temperature under well-enclosed combustion chambers [6, 130]. An incomplete combustion of these wastes may result in the formation of notably hazardous halogenated compounds such as polybrominated dibenzo-*p*-dioxins, and dibenzofurans (PBDD/Fs) and their chlorinated counterparts [7, 26, 509]. Catalytic pyrolytic upgrading has emerged as a viable alternative for the commonly utilized high-temperature combustion based

on two compelling grounds [219, 510]. Catalytic upgrading proceeds at a significantly lower temperature, and it is feasible to fine-tune operational conditions toward favouring striping the halogen content while keeping the carbon skeleton intact [511-513]. Catalytic dehalogenation reaction involves the cleavage of carbon-halogen bond as the elementary step. This process has been employed to generate alkyl groups, linked on catalyst-surfaces [512, 514]. Consequently, numerous studies investigated direct de-halogenation reactions over many potential surfaces. For example, through several laboratory-scale experiments, Buelow et al.,[512] examined the carbon-halogen bond breaking over Pd(111) and Al(111) surfaces under ultra-high-vacuum conditions. Their kinetics measurements using XPS and thermal desorption spectroscopy provided an estimate for the involved activation energies in the C-Cl/I bond cleavage. The authors found that, the reaction rate constants for the C-Cl/I bond cleavage over the aforementioned two surfaces are relatively small in the range of (15.7/6.2-17.0/11.7 kcal mol^{-1}) at temperature range of 250 –350 K.

The carbon-halogen bond sessions was assumed to take place via homolytic transition structures [512]. Temperature-programmed reaction (TPR) and high-resolution electron energy loss (HREEL) spectrometer measurements reported by Lin and his co-workers [515, 516] provided insightful evidence for the surface-assisted cleavage of C-Br/Cl bonds of bromoethane, 1-bromopropane, 2-bromopropane and their chlorinated counterparts yielding adsorbed radicals, such as, ethyl and i-propyl groups. The authors also found that, the activation energies of the alkyl halide molecules' decomposition over the copper surface amount to ~10-19% of their gas phase values (gas phase fission of C-Br/Cl bonds). These significant reductions in energy remain without theoretical verification. In our opinion, the vacuum conditions deployed in these very delicate conditions may entail a significant discrepancy when compared with real scenarios that typically entail high loads of both copper

species and gaseous halogenated alkanes. In this regard, open burning of e-waste often pollutes surrounding areas with high loads of elemental copper and halogenated compounds [517]. Simulation of catalytic reactions has now been widely deployed to acquire elucidation into experimental measurements [518, 519].

Among several tested surfaces, copper represents a potentially effective catalyst owing to its high selectivity toward the occurrence of the dehydrohalogenation reaction leading to the formation of corresponding non-halogenated carbon cuts [520, 521]. In this context, copper enjoy some interesting features over other transition metals such as, high natural abundance, and the avoidance of halogen side-products (other than hydrogen halides) [522-524]. Despite of various previous studies that have addressed reaction of halogenated short unbranched hydrocarbons with copper surface from different views, [525, 526] a detail mechanistic understanding of its role in surface-mediating rupture of carbon-halogen bond remains unexplained on a precise atomic scale. It is of a fundamental importance to identify and investigate the elementary steps that govern the degradation of multiple halogenated hydrocarbons over a copper surface. This, in turn, will provide an atomic-based insight into mechanistic and thermo-kinetic aspects that might not be easily acquired through just explicating the experimental measurements.

The complex reaction medium engenders experimental identification of involved species and the exact energy requirement to be a daunting task. Quantum chemical calculations are the only means to describe the very transient nature of intermediates. To this end, this contribution reports comprehensive density functional (DFT) study into the mechanistic steps and kinetic factors dictating fission of Br/Cl-C bond in a selected group of halogenated compounds. In the first part of this study, we benchmarked calculated parameters for bulk and copper surface with

analogous experimental and other calculated values. This is followed by surveying energy requirements for the fission of Cl/Br-C bonds in the title compounds (2-chloropropane, chloromethane, chloroethyne, chloropropene, chlorobenzene, and their brominated counterparts). Finally, we present Arrhenius parameters for the bond scission reactions. It is hoped that findings from the current work can provide an insight into chemical phenomena operating in the recycling the polymeric fraction of e-waste and other severely halogenated fuels.

7.2. Computational Details

All electronic structure calculations presented in this work were performed using the Vienna ab initio simulation package (VASP) that is based on the DFT formalism [407, 408]. The calculation methodology encompass a spin-polarized generalized gradient approximation (GGA) along with the exchange-correlation functional described by Perdew and Wang (PW91) [319, 527]. In structural optimizations, the plane-wave basis set with energy cut off of 400 eV was applied. The κ-point meshes of 12×12×12 and 6×6×1 generated using the Monkhorst-Pack method were employed in the κ-space integrations for bulk and (100) surface; respectively. The total energies on each ion were converged to less than 10^{-5} eV and the structures were deemed to be fully relaxed until the force constants on every ion were all less than 0.05 eV/Å. A dipole correction was applied along the z direction in all surface calculations.

To create a solid reference system for the molecular adsorption of the selected halogenated compounds over copper surface, we first benchamrked structural properties of the bulk Cu and its clean (100) surface (lattice constant and surface relaxation) aginst experimental analogous values. Our optimized lattice constant of for bulk Cu at 3.653Å departs from the analogous

experimental value by only 0.4% [528]. It is also in an accord with other reported values in previous theoretical studies [529, 530]. Also, the surface relaxation for the first two topmost layers was calculated according to the following function:

$$\Delta d_{12} = \frac{d_{12} - d}{d} \qquad\qquad 7.1$$

where d_{12} signifies the surface atomic layer distance between the subsequent layers 1 and 2 while d represents the corresponding distance in the bulk. Our inward surface relaxation of -2.6% obtained is in a good agreement with the previous theoretical estimates at -2.8% and -3.1% [528, 529].

A six-layer symmetric slab and a p (2×2) unit cell were utilized. During the optimization, atoms in the bottommost two layers were held fixed during the optimization in their bulk positions, whilst all other ions for the top four layers were allowed to relax. Throughout this study, the vacuum region between the adjacent slabs was set to 15 Å along the z-direction to eliminate any plausible interaction between vertically adjacent slabs, while in the x and y directions, it was repeated periodically. Gas-phase molecules were optimized via placing them in a 20 Å $\times$ 20 Å $\times$ 20 Å unit cell.

The Bader's formalism [466] affords atomic charge analysis in envistgated systems. In this regard, the atomic charge diffierence upon adsorption is calculated as:

$$\Delta Q = Q_{\text{surface+molecule}} - (Q_{\text{surface}} + Q_{\text{molecule}}) \qquad\qquad 7.2$$

where $Q_{\text{surface+molecule}}$, Q_{surface} and Q_{molecule} signify the charge on the adsorbed system, the clean surface's atoms and the adsorbed molecules, respectively.

Molecular adsorption and activation energies for all interaction mechanisms were determined as the energy difference between the initial states and, products and transition states, respectively, calculated according to the following expressions:

$$E_{\text{adsorption}} = E_{\text{surface+molecule}} - (E_{\text{surface}} + E_{\text{molecule}}) \qquad 7.3$$

$$E_{\text{activation}} = E_{\text{transition state}} - (E_{\text{surface}} + E_{\text{molecule}}) \qquad 7.4$$

where E_{surface}, E_{molecule}, $E_{\text{surface + molecule}}$ and $E_{\text{transition state}}$ denote the energies of substrate, gas phase molecule, substrate together with the gas phase and the transition state; respectively. It is generally obvious that, the more negative value of adsorption energy indicates a stronger and a thermodynamically favourable interaction.

The transition states (TS) along the reaction pathway were carried out using the "climbing image" nudged elastic band (CI-NEB) technique [414, 415]. This was performed using sixteen images between the reactant and the product states in each step where all images were optimized individually based on the nudged elastic band algorithm. In the CINEB calculations, the particular number of images was carefully adjusted in each transition-state to smothen the tangent along the designated reaction potential energy surface. When the interaction had an intermediate minimum present, the closest energy point was allowed to fully relax to define if the minimum was a true minimum. Confirmed transition states contain one and only one negative vibrational frequency along the designated reaction pathway.

Finally, as a benchmark of the thermochemistry accuracy of the adopted molecules in our study, it is very instructive to calculate bond dissociation energies (BDEs) for the selected molecules in order to contrast them with their well-documented gas-phase thermochemistry values in the literature. The calculated BDEs for fission C-Cl/Br bonds, as documented in Figure 7.1, amount to 85.8/67.0 kcal mol^{-1} (2-chloro/bromo-propane), 79.1/67.6 kcal mol^{-1} (chloro/bromo-methane), 97.3/99.6 kcal mol^{-1} (chloro/bromo-ethyne), 88.9/89.7 kcal mol^{-1} (chloro/bromo-propene) and 100.4/89.9 kcal mol^{-1} (chloro/bromo-benzene), respectively. These results math very well analogous experimental estimates reported in the literature (i.e., 87.8/65.5 kcal mol^{-1}, 83.7/70.3 kcal mol^{-1}, 104.1/98.1 kcal mol^{-1}, 88.6/89.4 kcal mol^{-1}, and 97.6/86.5 kcal mol^{-1}, correspondingly) [367, 371].
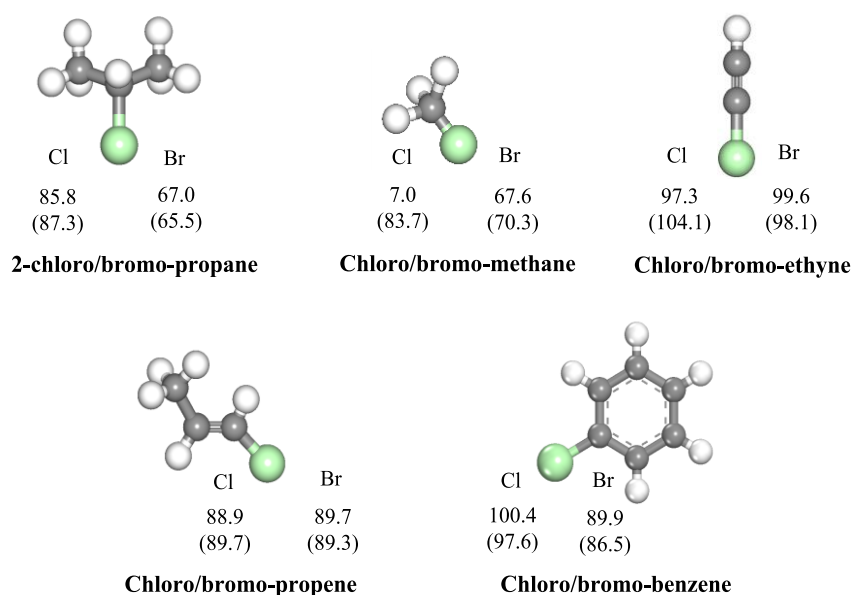
Figure 7.1. Optimized structures of the selected gaseous molecules. Values represent bond dissociation energies in kcal mol^{-1}. Values in brackets denote experimental values [367, 371]. Large green spheres denote chlorine/bromine atoms.

7.3. Results and Discussion

The five selected compounds feat7.ure five distinct types of carbon-halogen bonds; methyl (chloromethane); secondary (2-chloropropane); allylic (chloropropene); vinylic (chloroethyne) and aromatic (chlorobenzene). For the five chloro- and bromo-containing compounds, the BDEs scatter within 87.3-97.6 and 65.5-86.5 kcal/mol^{-1}; respectively. This noticeable variation in the BDEs values enables to assess the influence of the atomic bonding environment on estimated thermodynamics and kinetic parameters as the next section portrays.

7.3.1. Interaction of Halogenated Short-Chain Hydrocarbons with the Cu (1 0 0) Surface

Studying of surface-alkyl halide molecular adduct becomes an essential tool for fine chemical synthesis. Generally, alkyl halides have been demonstrated to be capable of coordinating with Cu surface's hallow sites via dissociative adsorption pathway.

Catalytic removal of halogen atoms from alkanes and olefins generally proceed via two pathways; direct elimination, or dissociative adsorption followed by hydrogen transfer to the surface:
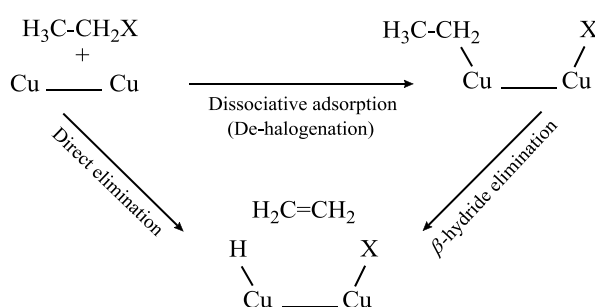
From our recent work on the interaction of halogenated C_1-C_3 cuts with clusters of α-Fe$_2$O$_3$ (hematite), [48, 49] it became apparent that the dissociative adsorption channel systematically requires lower opening barrier in reference to the direct elimination channel. Nonetheless, high

barriers for subsequent hydrogen transfer from *β*-carbon to the surface (releasing non halogenated entities) renders dissociative decomposition and direct elimination channel to incur very similar overall activation barriers in the alkyne family. For instance, we find that both channels assume comparable reaction rates in formation of acetylene from vinyl bromide. Herein, we limit our analysis on the first step in the dissociative adsorption channel. Removal of the adsorbed hydrocarbon adduct from the surface following surface-assisted fission of the Cl/Br-C bond may in principle occur via reactions that do not involve the intramolecular hydrogen transfer into the surface. If oxygen is pre-adsorbed on the surface, it could initiate conversion of these moieties into their corresponding alcohol compounds for instance [531].

We first present geometries for the initial reactant and the final products following the dissociative adsorption channel as depicted in Figures 7.2 and 7.3. The corresponding potential energy surfaces are shown in Figures 7.4 and 7.5. We find that physisorption of the four considered chlorinated species over the Cu (100) surface are slightly exothermic affording very negligible reaction energy in the range from -2.1 to -0.1 kcal mol^{-1}. In the surface-adduct structures ($M1_{(Cl)}$, $M3_{(Cl)}$, $M5_{(Cl)}$ and $M7_{(Cl)}$), the C-Cl bonds differ from their analogous gas phase bonds by only 1.25-0.60%. Likewise, the physisorption energies for brominated species reside in the narrow range of 0.8 to -2.6 kcal mol^{-1}.

Table 7.1 summarises values of bond elongations and adsorption energies for all physisorbed structures. The marginal Cl/Br-C bond stretching is in line with the computed low values of adsorption energies. The very weak interaction reported in Table 7.1 is in accord with an analogues DFT findings by Barbosa et al. [521] in their study on the interaction of trichloethene molecule on two different Cu(110) surfaces. It should be emphasised though that the computed low energies are most likely to be within the accuracy limit of the adapted methodology. It can

be concluded herein that the four title C1-3 halogenated molecules interact rather weakly with the Cu(100) surface in their physisorbed states.

Table 7-1. Electronic and structural properties for molecular and dissociative adsorption structures

Species	Elongation of Cl/Br-C bonds (%)	Charge transfer from the surface to adsorbed Cl/Br molecules (e)(Chemisorption)	Adsorption energy (kcal mol^{-1})
2-Chloropropane	1.25	-0.27	-2.1
Chloromethane	0.60	-0.29	-1.1
Chloroethyne	7.05	-0.44	-1.0
Chloropropene	0.60	-0.36	-0.1
Chlorobenzene	1.00	-0.34	0.5
2-Bromopropane	1.19	-0.20	-1.8
Bromomethane	1.68	-0.33	-2.0
Bromoethyne	11.84	-1.46	-2.6
Bromopropene	0.89	-0.49	0.8
Bromobenzene	1.78	-0.40	0.4

New are now in a position to examine reaction for the dissociative adsorption interaction underpinning catalytic de-halogenation of the selected C_1-C_3 halogenated species. As shown in Figures 7.2 and 7.3, we portray the side and top perspectives for products arising from

scission of the C-Cl/Br bonds in the selected four molecules. In all structures, we consider that all dissociated halogen atoms occupy a hollow site. We have shown previously that dissociated Cl atom from the fragmentation of a 2-chlorophenol molecule prefers adsorption at the hollow site in comparison to on-top and bridge sites [529]. The produced hydrocarbon adducts are attached to the surface via bonding of the free carbon radical centre to the surface Cu atom. Fission of the C-Cl bonds in the 2-chloropropane, chloromethane, chloroethyne and chloropropene molecules results in the formation $M2_{(Cl)}$, $M4_{(Cl)}$, $M6_{(Cl)}$ and $M8_{(Cl)}$ adducts, respectively. In reference to the physisorbed configurations, $M2_{(Cl)}$, $M4_{(Cl)}$, $M6_{(Cl)}$ and $M8_{(Cl)}$, dissociative adsorption leading to fission of the C-Cl bonds entail an exothermicity of -12.0, -22.3, -50.9 and -27.9 kcal mol^{-1}; respectively. The catalytic effect of the Cu(100) becomes more comprehensible when contrasting this predicted surface-assisted exothermicity with the highly endothermic direct cleavage of C-Cl bonds in the gas phase. These reactions demand considerable energies of 87.3, 83.7 104.1, and 89.7 kcal mol^{-1} for 2-chloropropane, chloromethane, chloroethyne, and chloropropene, in that order [367, 371]. Therefore, whilst thermodynamic factors in terms of the exothermic nature of the surface-mediated C-Cl bond rupture, predict a spontaneous process, the potential for the occurrence of the bond fission reactions truly rests on underlying kinetic considerations, embedded in activation energies. We find that dissociation of Cl from the selected chlorinated molecules proceeds via activation barriers of 11.8 (TS1), 8.8 (TS2), 37.2 (TS3) and 25.4 kcal mol^{-1} (TS4) for 2-chloropropane, chloromethane, chloroethyne and chloropropene physisorbed states, respectively. It should be indicated that, these energies seem to positively concur with the energy requirements for the C-Cl bond scission in gas phase, i.e., 87.3, 83.7 104.1, and 88.7 kcal mol^{-1}, correspondingly [367, 371]. Interatomic distances of Cl-Cu and Br-Cu in $M2_{(Cl)/(Br)}$, $M4_{(Cl)/(Br)}$, $M6_{(Cl)/(Br)}$, and $M8_{(Cl)/(Br)}$, structures reside within the range of (2.305 – 2.382Å), reflecting very well Cl-Cu and Br-Cu bond lengths of bulk $CuCl_2$ and $CuBr_2$ at 2.380 Å and 2.390 Å [532-535].
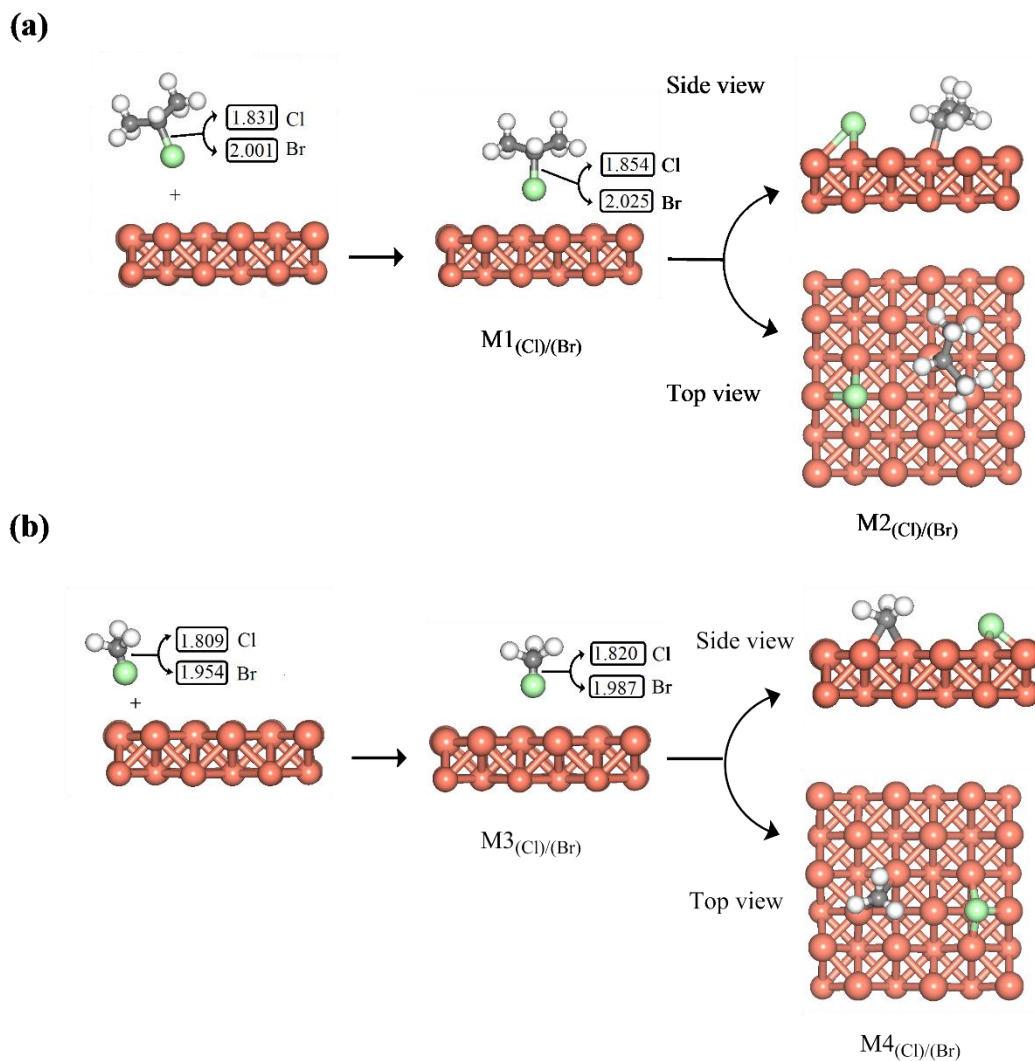
Figure 7.2. Schematic representation for the decomposition of (a) 2-chloropropane/bromopropane molecules and (b) chloromethane/bromomethane over the Cu (100) surface. Only the first two layers are shown in side views. Large green spheres correspond to chloride/bromide atoms and brown, gray, and white spheres to Cu, H and C atoms, respectively. This color code applies in Figures 3 and 6. Values are C-Cl/Br distances in Å.
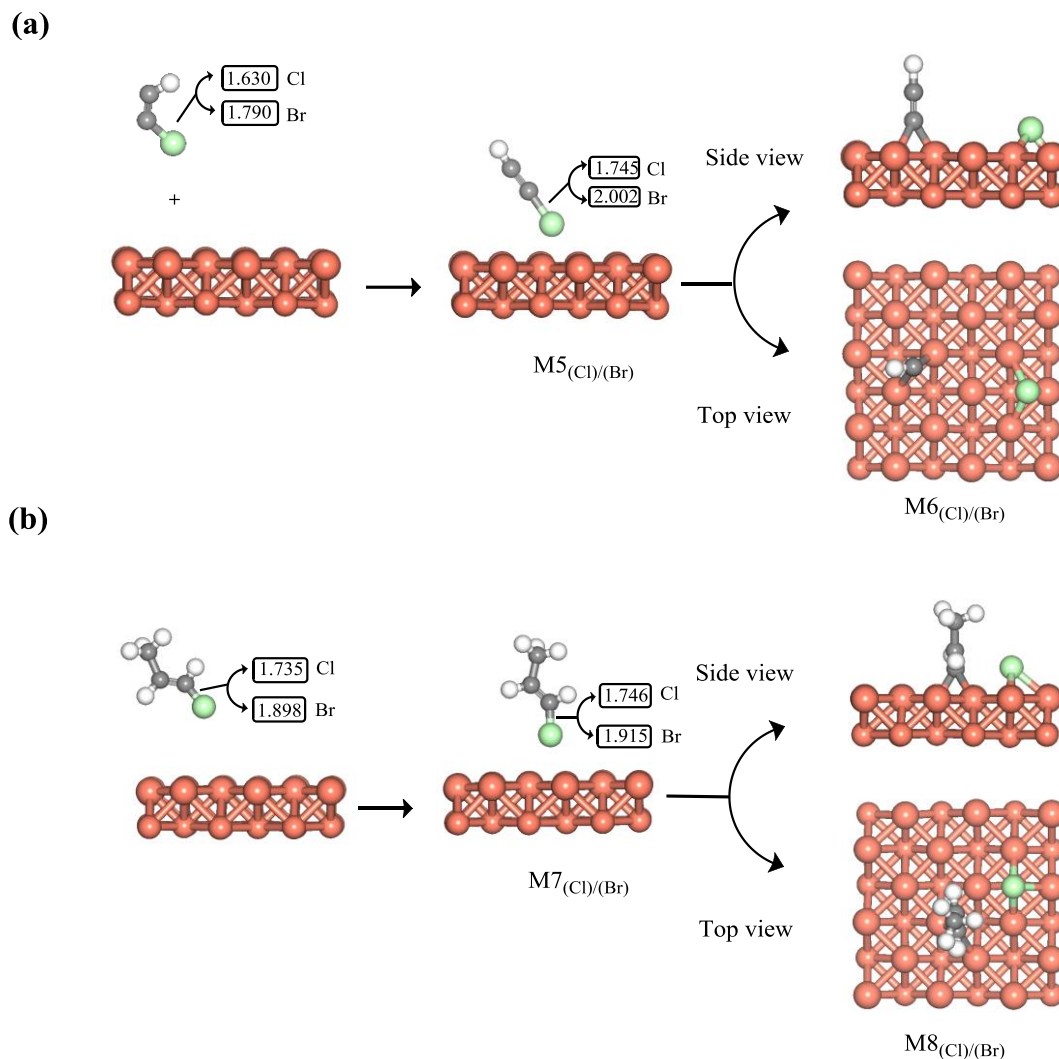
Figure 7.3. Schematic representation of the decomposition of (a) chloroethyne/bromoethyne moleculesand (b) chloropropene/bromopropene over Cu (100) surface. This color code applies in Figures 7.3 and 7.6. Values are C-Cl/Br distances in Å.

The interaction of the corresponding brominated species with the Cu (100) surface proceeds through similar thermodynamic and kinetic trends. Surface-mediated fission of the Br-C bonds requires activation energy barriers that vary between 8.3 kcal mol^{-1} (TS7 in Figure 7.5) for the de-bromination of bromoethyne to 19.1 kcal mol^{-1} (TS8 Figure 7.5) for bromopropene de-bromination process. These steps are accompanied with exothermic reaction energies varying between -17.7 kcal mol^{-1} (M2 $_{(Br)}$) to -57.8 kcal mol^{-1} (M6 $_{(Br)}$), as shown in Figure 7.5. The catalytic capacity of the Cu surface toward de-bromination of the selected gas phase molecules

becomes very evident by comparing these low values with the reaction energies required to break the C-Br bonds in the gas phase (i.e., 65.5, 70.3, 98.1, and 89.3 kcal mol^{-1} for 2-bromopropane, bromomethane, bromoethyne, and bromopropene, respectively.) [367, 371].

By comparing the higher activation energy barriers for the scission of the C-Cl bonds for almost all the selected chlorinated species with those for C-Br bonds, we can see obviously that these values concur with the stronger bonds in the former [367, 371]. The only exception to these trends constitutes the dissociative adsorption of chloromethane versus the bromomethane molecule. Examination of the transition state values for the intermediate structures M4$_{(Cl)}$ and M4$_{(Br)}$ show that the required barrier energy for the cleavage of C-Cl bond of chloromethane is ~1.6 kcal/mol lower than analogous value for the C-Br bond scission of bromomethane. Interestingly, our results herein are consistent with the experimental work performed on the similar molecules by Zhou et al. [536] over the Ag(111), in which it was reported that dehalogenation of chloromethane is more facile than that of bromoethane.

Overall, inspection of the relative energy profile diagrams displayed in Figures 7.4 and 7.5 leads to the following focal points:

1- Dissociative adsorption of the selected brominated species is generally more exothermic in comparison to their chlorinated counterparts. For example, the fragmented structures M2 $_{(Cl)}$ resides in a well-depth 12.0 kcal mol^{-1} in reference to its non-interacting state. This is significantly lower than that for the analogous M2 $_{(Br)}$ structure (i.e., -17.7 kcal mol^{-1}). This responsibly corresponds with the general observations from the previous investigations in the literature that bonding of brominated compounds with metal surfaces are slightly stronger than their chlorinated counterparts [515].

171

2- Transition states of the dissociate adsorption of the four chlorinated species (Figure 7.4) are consistently higher than their analogous values for brominated species (Figure 7.5). Stronger C-Cl bonds in reference to C-Br in gas phase molecules engender higher activation barriers. These results are consistent with the general observation from previous experimental investigations in the literature [515, 516] as well as with our recent findings on the dissociative adsorption of several brominated [350] and chlorinated compounds [460] over α-Fe$_2$O$_3$ nanoclusters.
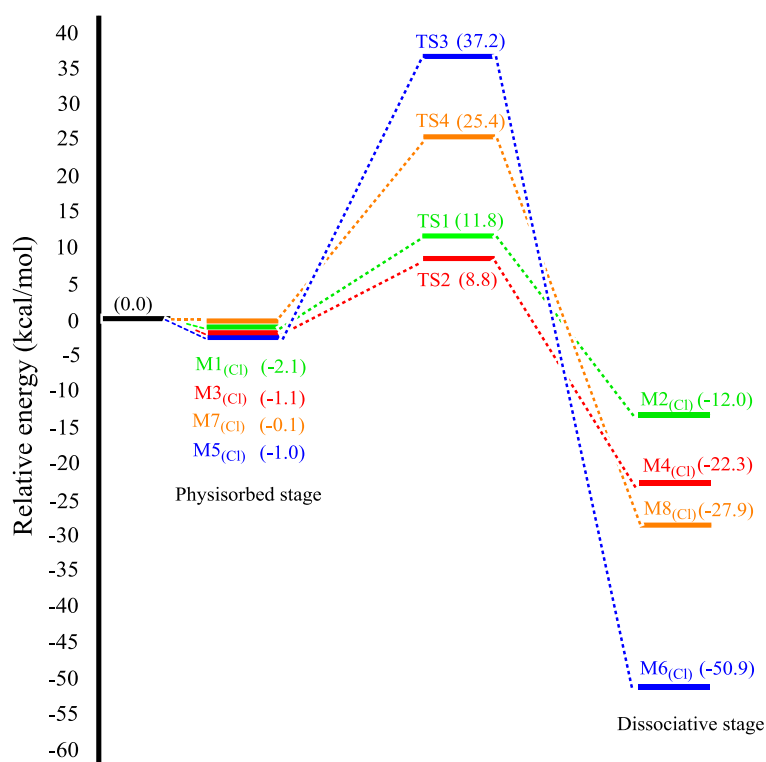
Figure 7.4. Potential energy surface for the C-Cl bond fissions in 2-chloropropane (Green), chloromethane (Red), chloroethyne (Blue), and chloropropene (Orange) molecules over the Cu(100) surface. Values are in kcal mol^{-1} with respect to the initially separated reactants.

Analysis of charge transfer assists in comprehending whether the adsorbed fragments constitutes Lewis base (donates electron) or Lewis acid (received electrons). Table 7.1 presents the Bader's charges of the chemisorbed Cl/Br atoms (i.e., the net electronic charges transfer

from copper surface to molecules). The negative values presented in Table 7.1, discloses that the halogen atoms for M2$_{(Cl/Br)}$, M4$_{(Cl/Br)}$, M6$_{(Cl/Br)}$ and M8$_{(Cl/Br)}$ structures acquire electron charge when they adsorb over a surface's hallow side, and thus acting as Lewis acid. The relatively significant transferred charge from the copper substrate to chlorine/ bromine atoms is in line with the remarkable strong exothermic reactions between both the substrate and the adsorbate in the final chemisorbed structures. The noticeable charge transfer from the surface positively correlates with the estimated dissociative energies. Overall, accessible activation energies, significant charge transfer and profound exothermecity all consistently indicate that copper surfaces incur high catalytic capacity toward dehalogenation of unbranched hydrocarbon cuts.
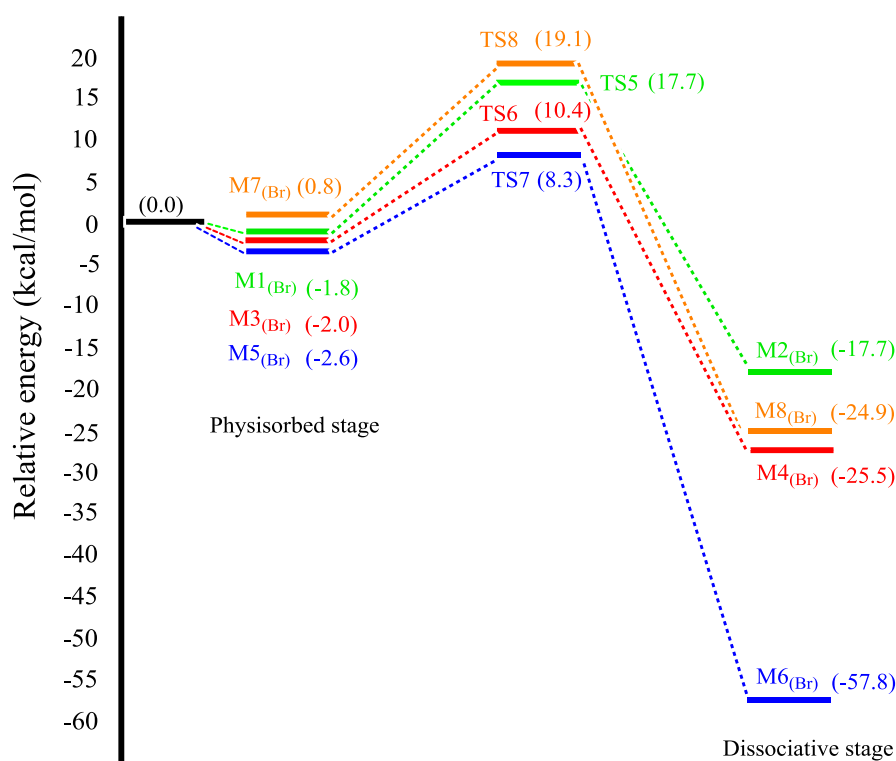
Figure 7.5. Potential energy surface for the C-Br bond fissions in 2-bromopropane (Green), bromomethane (Red), bromoethyne (Blue), and bromopropene (Orange) over Cu (100) surface. Values are in kcal mol^{-1} with respect to the initially separated reactants.

7.3.2. Decomposition of Aromatic Halogen Compounds over Cu (100) Surface

Herein, we investigated the three elementary stages of chlorobenzene and bromobenzene molecules dissociation over the Cu(100) surface. In Figure 7.6 and 7.7, we illustrate that, both molecules share the same principal dissociation mechanism stages, albeit with various energy profiles. The chlorobenzene/bromobenzene is physisorbed in the initial reaction stage, whilst both the halogen atom (hollow site) and the phenyl ring are chemisorbed in the final reaction stage. Starting with the non-dissociative molecular adsorption state, binding energies for the initial physisorbed structures of chlorobenzene and bromobenzene molecules over Cu surface amount to only 0.5 and 0.4 kcal mol^{-1} for chlorobenzene and bromobenzene, respectively. This endothermic trend for the first step reflects well with Björk et al., [537] findings for the interaction of some aromatic compounds with metallic surfaces. Moreover, this behaviour is accompanied with minor extension of C-Cl/Br bond by only 1.0 and 0.89%, correspondingly, when compared with the equilibrium distances in the gaseous C_6H_5Cl/Br molecules (i.e., 1.749 and 1.910 Å). Thus, those low C-Cl/Br bond elongations represent another signature for the weak physisorption process over the Cu surface. Consequently, physisorption of the two haloaromatic compounds over the surface does not result in their activation. Very weak adsorption energies were also obtained in the course of the interaction of the 2-chlorophenol molecule over the Cu(100) [529] and Cu(111) surfaces [509].
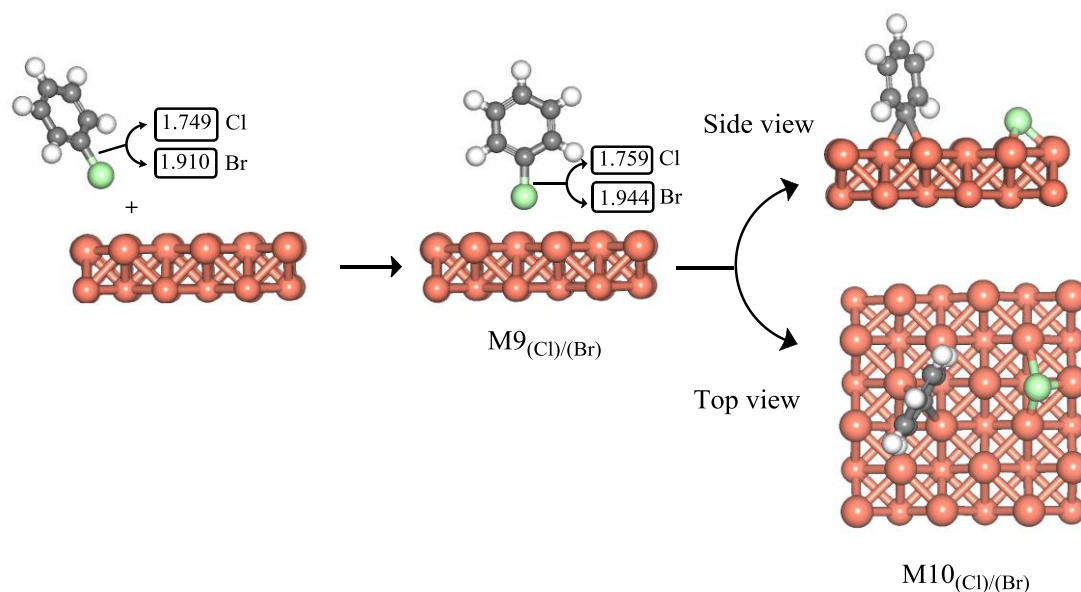
Figure 7.6. Schematic representation for the dissociative decomposition of chorobenzene /bromobenzene molecules over Cu (100) surface. Values are C-Cl/Br distances in Å.

Chlorobenzene/bromobenzene molecule dissociates hetrolytically in the final stage leading to adsorption of the halogen atom in a surface hollow side whilst, the adsorbed phenyl ring with its unsaturated carbon in structures M10$_{(Cl)}$ and M10 $_{(Br)}$ form bridges with two adjacent copper substrate atoms. Therefore, desorption of phenyl rings into the gas phase is unlikely to occur. The most prevalent scenario is decomposition of the phenyl ring affording smaller fragments, most notably acetylene. As depicted in Figure 7.7, dissociation of halobenzene molecules in both reactions are exothermic, that is reflected by the negative values of the final stage energies in reference to their physisorbed states., -19.2 and -34.2 kcal mol^{-1} for chlorobenzene and bromobenzene, respectively. Moreover, this exothermic trend for the final stage is in line with our recent investigations for decomposition of brominated/ chlorinated benzene over clusters of α-Fe$_2$O$_3$ [350, 460].

Inspection of TS9 and TS10 as shown in Figure 7.7, indicate that fission of aromatic C-Cl/C-Br bonds proceeds via activation barriers of 22.8 kcal mol^{-1} for dissociation of chlorobenzene and 20.2 kcal mol^{-1} for bromobenzene. Lower energy barriers for scission of the C-Br bond in

comparison to C-Cl concur with the weaker bond in the former (86.5 versus 97.6 kcal mol^{-1})

[371]. The strong catalytic effect of Cu(100) surface on the de-halogenation of gas phase of

halobenzene molecules becomes clear when contrasting those modest barrier energies with the

sizable reaction energies required to break the C-Cl/Br bonds in the gas phase, 97.6 and 86.0

kcal mol^{-1} for C_6H_5Cl/Br, respectively [371]. Obviously, the Cu(100) surface significantly

decreases the activation barriers and thus considerably lower the operational temperature

required to de-halogenate aromatic compounds in general.
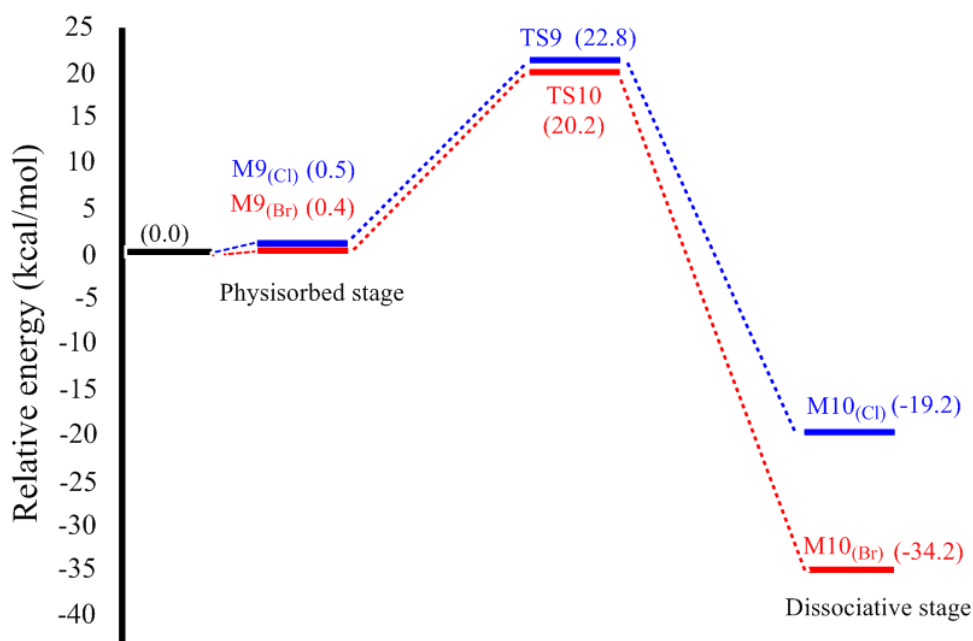
Figure 7.7. Relative energy for reaction of chlorobenzene (Blue) and bromobenzene (Red) over Cu (100) surface. Values are in kcal mol^{-1} with respect to the initial reactant.

Binding of the electronegatively charged Cl and Br atoms with the surface Cu atoms produces

charge transfer and redistribution which can be explained effectually using Linus Pauling

electronegativity method. It is predictable that the electron charge transfers occurs from the

less electronegative atom (i.e., Cu atoms, its Pauling electronegativity = 1.90) toward the more

electronegative atom (i.e., Br/Cl, their Pauling electronegativity = 2.96 and 3.16, respectively).

Bader's charge analysis for the chemisorption states (M10$_{(Cl)}$ and M10 $_{(Br)}$) as listed in Table

7.1, indicates that Cl/Br surface atoms incur a net electronic charge of -0.34/ -0.40. We compute very similar charge transfer to C/Br atoms upon dissociative adsorption of the two hydrogen halides over zincite surface [461]. Coupling of two adjacent phenyl rings via consequent reaction steps over copper surface leads to the formation of biphenyl molecule via the well-known Ullmann reaction [525, 537]. The kinetics for Ulmman reaction over copper and other transitional metal surfaces will be investigated in a due course.

7.3.3. Kinetics Consideration

Finally, based on the results presented so far, it is important to investigate how the interaction kinetic are affected by the thermodynamic parameters. The reaction rate constants of all dehalogenation processes were estimated based on the transition state theory (TST) [538]:

$$k\ (T) = A \exp\ (-E_a\ /\ RT) \tag{7.5}$$

in which E_a signifies the activation energy, R stands for the gas constant (1.987 cal K^{-1} $mole^{-1}$) and T is the temperature in Kelvin [356]. Herein, we used the Phonopy software [417, 539] to calculate vibrational frequencies, which enable us to obtain phonon-related thermodynamic properties (enthalpies and entropies of activation as a function of temperature). The latter two quantities are then utilized to obtain the fitted pre-exponential factor A and energy of activation E_a.

Panels shown in Figures 7.8 and 7.9 characterize the variation in the reaction rate constant over the temperature region of 300 and 1000 K for all investigated molecules, while Table 7.2 listed their Arrhenius parameters. As expected, we find that C-Cl cleavage reactions to consistently incur lower reaction rates in reference to C-Br bond fission. Accordingly, the Cu(100) surface

catalytic de-bromination is predicted to occur at lower temperatures. These thermodynamic and kinetic preference for the de-bromination process supports the prior experimental findings of Lin et al., [515, 516] who found that, copper-mediated scission of C-Cl/Br bonds require substantially higher energy requirements if contracted with the unanalysed gas phase reaction. Our calculated activation energies for the formation ($M2_{(Cl/Br)}$, $M4_{(Cl/Br)}$, $M6_{(Cl/Br)}$, $M8_{(Cl/Br)}$ and $M10_{(Cl/Br)}$) amount to 14.6/20.4, 10.3/13.1, 34.3/8.6, 28.3/22.2, and 21.6/17.6 kcal mol^{-1}, respectively. These values constitute 8-31% of corresponding C-Cl/Br BDEs in the gas phase. This compares very well with the analogues reduction in energy requirement for surface-assisted versus direct bond fissions in the gas phase reported by Lin et al.; (10-19%).
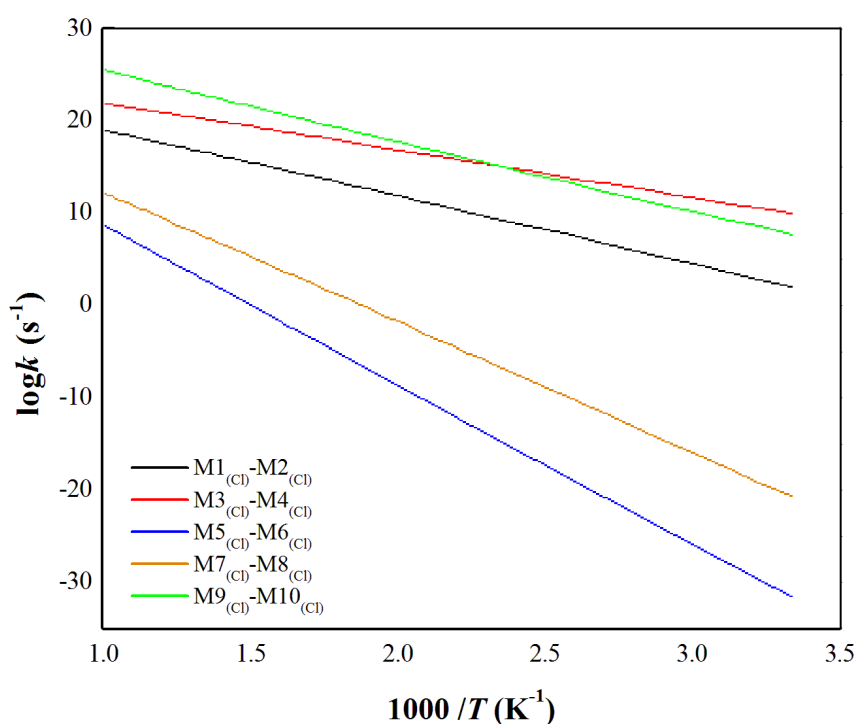
Figure 7.8. Arrhenius plots for C-Cl bond ruptures over the Cu(100) surface.

In order to illustrate the high catalytic performance of copper (100) surface toward dehalogenation of alkyl halides, we have compared the results obtained for some of the alkyl

halides considered in our study with analogous theoretical and experimental values obtained over (i) other copper surface terminations, and (ii) over various metal surfaces:

(i)   In order to underpin the catalytic capacity of copper-terminated (100) surface than other copper terminations, we have contrasted our obtained activation energies for dissociation reactions in selected halogenated hydrocarbons molecules with corresponding values ensued over another copper termination surface (i.e., Cu(410)) [540]. Figure 7.S1 (in the Appendix C) shows that fission of the C-Cl bond in the CH_3Cl molecule over copper-terminated (410) required slightly higher activation barrier (10.3 kcal mol^{-1}) in reference to the value calculated here for the clean Cu(100) surface; i.e., 8.3 kcal mol^{-1}.

(ii)   The Cu(100) surface-mediated fission of halogen-carbon bonds in the CH_3Cl or CH_3Br molecules entails a modest barrier of 8.8 and 10.4 kcal mol^{-1}, respectively. In Figure 7.S2, we compared these values with analogous literature reported values for other metallic systems. Our calculated activation energies are consistently lower than activation barriers for fission of CH_3-Cl and CH_3-Br bonds over other metallic surfaces, i.e, 13.3 kcal mol^{-1} (Ru) [541], 11.2 kcal mol^{-1} (Pd) [542], and 11.2 kcal mol^{-1} (Ru) [543]. Thus, it is inferred herein that the C-Cl/Br bonds of methyl halides can be easily activated by the Cu(100) surface in a rate that is very comparable if not faster than other surfaces.
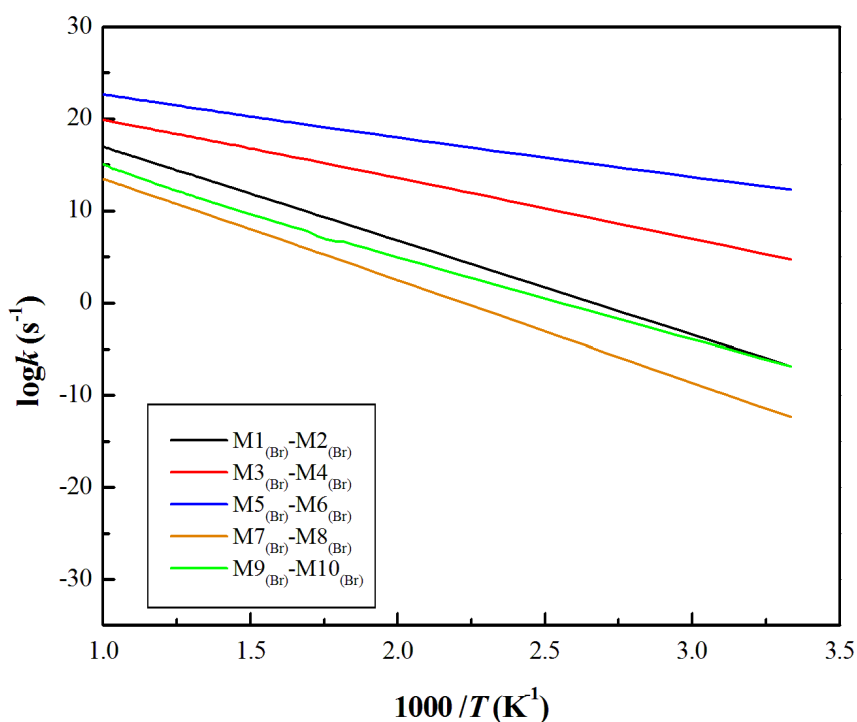
Figure 7.9. Arrhenius plots for C-Br bond ruptures over the Cu(100) surface

Next, we move to compare our computed activation barrier for the de-halogenation of the bromobenzene molecule over Cu(100) with the corresponding value of activation energy obtained previously over the Au(111) [537]. As illustrated in Figure 7.S3, Au-mediated fission of the aromatic C-Br bond requires an activation barrier of 23.5 kcal mol^{-1}; slightly higher than the analogous value over the Cu(111) surface. Thus, copper surfaces display a comparable performance in activation of aromatic C-Br bonds in reference to Nobel metals.

Table 7-2 Kinetic parameters fitted in the temperature range of 300-1000K.

Species	Reaction	A (s^{-1})	E_a (kcal mol^{-1})
2-Chloropropane	M1$_{(Cl)}$ → M2$_{(Cl)}$	3.70×10^{11}	14.6
Chloromethane	M3$_{(Cl)}$ → M4$_{(Cl)}$	7.48×10^{11}	10.3
Chloroethyne	M5$_{(Cl)}$ → M6$_{(Cl)}$	1.55×10^{11}	34.3
Chloropropene	M7$_{(Cl)}$ → M8$_{(Cl)}$	3.70×10^{11}	28.3
Chlorobenzene	M9$_{(Cl)}$ → M10$_{(Cl)}$	1.85×10^{11}	21.6
2-Bromopropane	M1$_{(Br)}$ → M2$_{(Br)}$	6.43×10^{11}	20.4
Bromomethane	M3$_{(Br)}$ → M4$_{(Br)}$	4.21×10^{11}	13.1
Bromoethyne	M5$_{(Br)}$ → M6$_{(Br)}$	3.58×10^{11}	8.6
Bromopropene	M7$_{(Br)}$ → M8$_{(Br)}$	5.25×10^{10}	22.2
Bromobenzene	M9$_{(Br)}$ → M10$_{(Br)}$	6.46×10^{9}	17.6

7.4. Conclusions

We performed a systematic theoretical study of the catalytic dehalogenation mechanism of selected halogenated compounds over Cu (100) surface. Our study sought to identify the initial stages that dictate the de-halogenation mechanism. We examined the thermo-kinetic parameters underlying the split off halogen atoms from chlorinated/brominated alkyl chloride/bromide and chloro/bromo-benzene molecule. The analysis of the structural properties and binding energies in the elementary physisorption stage for each surface-adduct structure discloses that investigated halogenated compounds interact rather very weakly with the Cu (100) surface. Activation barriers for C-Cl bond fission are systematically higher than

their analogous C-Br values, largely following their respective bond strengths in gas phase molecules. Surface Cl/Br-Cu bonds mimic the corresponding bonds in bulk $CuCl_2$/$CuBr_2$.

Chapter 8

Formation of Phenoxy-type Environmental Persistent Free Radicals (EPFRs) from Dissociative Adsorption of Phenol on Cu/Fe and their Partial Oxides

Abstract

The interplay of phenolic molecules with 3*d* transition metals, such as Fe and Cu, and their oxide surfaces, provide important fingerprints for environmental burdens associated with thermal recycling of *e*-waste and subsequent generation of notorious dioxins compounds and phenoxy-type Environmental Persistent Free Radicals (EPFRs). DRIFTS and EPR measurements established a strong interaction of the phenol molecule with transition metal oxides via synthesis of phenolic- and catecholic-type EPFRs intermediates. In this contribution, we comparatively examined the dissociative adsorption of a phenol molecule, as the simplest model for phenolic-type compounds, on Cu and Fe surfaces and their partially oxidized configurations through accurate density functional theory (DFT) studies. The underlying aim is to elucidate the specific underpinning mechanism forming phenoxy- or phenolate-type EFPRs. Simulated results show that, the phenol molecule undergoes fission of its hydroxyl's O-H bond via accessible activation energies. These values are lower by 46.5 - 74.1% when compared with the analogous gas phase value. Physisorbed molecules of phenol incur very low binding energies in the range of -2.1– -5.5 over clean Cu/Fe and their oxides surfaces. Molecular attributes based on charge transfer and geometrical features are in accord with the very weak interaction in physisorbed states. Thermo-kinetic parameters established over the temperature region of 300 and 1000 K, exhibit a lower activation energy for scission of phenolic's O-H bonds over the oxide surfaces in reference to their pure surfaces (24.7 and 43.0 kcal mol^{-1} *vs* 38.4 and 47.0 kcal mol^{-1}).

8.1. Introduction

The essential role of the phenol molecule (and its halogenated isomers) in the synthesis of the notorious "dioxins" compounds is well-established in the literature [138, 166]. Via a synergistic experimental-theoretical approach over the last decade, we have demonstrated a wide array of chemical phenomena that dictate condensation of phenolic molecules into halogenated dioxins. A central step in commonly discussed phenol → "dioxins" mechanisms is the conversion of phenol molecules into gas phase phenoxy radicals or surface-bounded phenolate anions. With a strong hydroxyl's O-H bond at ~ 85 kcal mol^{-1} [138], a direct thermal bond fission assumes a negligible importance when compared with H abstraction reactions operated by O/H radicals in the combustion media [458]. Depending on the operational conditions in the gas phase medium (most notable the temperature window and pyrolytic versus oxidative environment); self-coupling of phenoxy radicals branches into either dibezno-*p*-dioxin or dibenzofuran molecules [544]. However, the homogenous route contributes by less than 30% of the total yields of dioxins. Heterogeneous pathways characterised by the so-called "de novo synthesis" and surface-assisted coupling of adsorbed phenoxy radicals (or phenolate anions) constitute the prevailing synthesis corridors. The most effective species in catalyzing formation of dioxins from isomers of phenols are transition metals and their oxides.

With deploying more stringent emission criteria and abatement technologies, emission of dioxins from thermal systems has systematically reduced. However, interaction of phenolic-type molecules with metallic surfaces has continued to enjoy a profound interest derived by serious health hazards [545-547]. Dissociative adsorption of phenol molecules over these metals facilitates rupture of their hydroxyls O-H bonds affording phenolate-type Environmental Persistent Free Radicals (EPFRs) [548, 549]. Phenolate-type EPFRs endure prolonged life spans and were shown to cause chronic respiratory illnesses [550, 551]. Electron

paramagnetic Resonance (EPR) measurements consistently detected signals that correspond to oxygen-centred surface-bounded phenoxy radicals from the interaction of phenol molecules with transition metal oxides; most notably Fe_2O_3 [552] and CuO [553]. A higher oxidation potential for Fe_2O_3 in reference to CuO produced higher concentration of phenoxy-type EPFRs [552, 553]. Seemingly unreacted silica surfaces also facilitate rupture of the phenolic's O-H bond [554]. In our recent theoretical studies [66], we illustrated thermo-kinetics parameters for the dissociative adsorption of phenol yielding adsorbed phenolate species over surfaces of dehydroxylated alumina and OH-alumina clusters. The metal (M) – oxygen (O) linkages in these surfaces serve as a Lewis-acid pair in facilitating rupture of phenolic's O-H bonds. In this regard, copper and iron species largely dominate the metallic content in systems pertinent to surface-catalysed formation of phenolic-type EPFRs such as particulates matters generated from combustion operations and [555] municipal waste incinerations [556].

In a related work, Lu et al.[557] investigated the adsorption of phenol onto Pt(111) surface with low-energy electron diffraction (LEED), high-resolution electron energy loss (HREELS) and anger electron spectroscopy (AES). These authors reported that phenol initially adsorbs molecularly, horizontal to the Pt(111) surface, at a temperature below 200 K before undergoing a fission of its O-H bond affording surface-bounded phenolate and a hydrogen atom. Molecular dissociative adsorption is sustained by a pairing of the odd electron with electron density of the metal. Along the same line of enquiry, Richardson and his co-worker [558] examined the O-H bond scission over Cu(110) surface at room temperature. By using the HREELS and AES data, the authors attributed the absence of C-OH associated vibrations in the phenol molecule to a potential rupture of the O-H bond.

Theoretically, Hensley et al. [559] carried out density functional theory (DFT) calculations to explore the adsorption mechanism of phenol over Fe(110) and Pd(111) surfaces with the inclusion of van der Waals corrections. They examined this process via two reactions; parallel and perpendicular configurations. They reported that phenol adsorption through the aromatic ring (parallel) side is significantly more favourable than through the oxygen functional group (perpendicular) side. The authors concluded that preference of the parallel side can be ascribed to an enhancement in the amount of charge transfer between the surface and adsorbate in the parallel orientation via the aromatic ring. Altarawneh et al. [381, 560] studied fragmentation of a 2-chlorophenol molecule over Cu(100) and Cu(111), but without attempting to calculate pertinent intrinsic reaction barriers. For he thermodynamically most stable copper oxides, Altarawneh et al. [456] attained a reaction barrier at 8.2 kcal mol^{-1} for fission of the phenolic's O-H bonds over the $Cu_2O(110)$ surface. Notwithstanding these numerous experimental measurements and computational calculations, several mechanistic aspects dictating formation of phenoxy-type EPFR remain poorly understood; most notably regarding the operating reaction barriers prevailing over pure metallic surfaces and their partially oxides states.

To this end, this study investigates reaction mechanisms and energy barriers for the formation of phenoxy-type EPFRs over surfaces of pure Cu(100) and Fe(100) and their oxygen-covered configurations. The prime focus is to contrast the catalytic capacity of the aforementioned reactions of the title reaction with analogues values reported in the literature for transition metal oxides. Lastly, we provide kinetics parameters for all investigated reactions. It is hoped that results provided herein to be useful in the continuous pursuit to understand the transformation chemistry of phenol → phenoxy-type EPFRs.

8.2. Computational Details

Periodic DFT calculations have been widely utilized to accurately describe various aspects of heterogenous catalysis; namely in establishing reaction mechanisms and in constructing kinetics models. This approach simulates the surface-assisted chemical reactions by considering active sites. Periodic surfaces eliminate the presence of edge effects that often prevail in corresponding cluster models. Periodic density functional theory (DFT) calculations were performed utilizing the Vienna ab Initio Simulation Package (VASP) code [317, 318]. Projector augmented wave method (PAW) was employed to represent the spin-polarised electronic computations and the core-valence interactions [321]. The generalized gradient approximation (GGA) functional of Perdew and Wang (PW91) was used to describe the electron exchange and the electronic-energy correlation effect [527]. The energy cut-off of the plane wave basis set was fixed at 400 eV. Pure metallic surfaces and their partially oxidized configurations [i.e., Cu(100), Fe(100), Cu(100)_O_1 and Fe(100)_O_1] were modelled with six-layer thick surface and p (2×2) unit cell separated with a 20 Å of vacuum gap to accommodate the monocyclic aromatic molecule of phenol along the z-direction. The bottommost two-layer metal ions were fixed at their corresponding bulk positions whilst the top four layers together with the adsorbate phenol molecule were allowed to fully relax. Figure 1 portrays side and top views of Cu(100), Fe(100) and Cu(100)_O_1 and Fe(100)_O_1 surfaces.

A dipole correction was also imposed along the z direction due to potentially significant effect of dipole interactions between the consecutive supercells. Integration of the irreducible part of the Brillouin's zone was carried out based on a 12×12×12 and 6×6×1 Monkhorst-Pack mesh k-points for bulk and surfaces calculations, correspondingly. The total energy was converged to at least 10^{-5} eV on each ion in the system and the systems were deemed to be fully optimized when the force constants on each ion were less than 0.05 eV/Å.

The adsorption energy, defined as the binding energy of the phenol molecule with the surface, was calculated by using the following expression [561]:

$$BE_{(Ads)} = E_{(Ads/Slab)} - E_{(Slab)} - E_{(Ads)}$$
8.1

where $BE_{(Ads)}$ signifies the binding energy, $E_{(Ads/Slab)}$ is the total energy of the adsorbate on the metal slab, E_{Slab} denotes the energy of the clean slab and E_{Ads} is the energy of the gas phase adsorbate. The negative values of the binding energy imply that the adsorption is exothermic (practically, the more negative value of binding energy indicates a favourable adsorption), whilst the positive values correspond to an endothermic adsorption.

The activation energies of the interaction characterize the energy difference between the reactant (the initial physisorbed state) and the transition state. Climbing Image Nudged Elastic Band (CINEB) technique was applied to obtain geometries and energies of transition states (TS) [414, 562]. In implementing the CINEB procedure, we utilized 16 images between the initial and the final (the dissociative structures) states of each recanting system. Each of these images were optimized separately based on CINEB formalism. Computing the vibrational frequencies of the reactants and transition state structures enable to calculate their thermodynamic parameters (entropy, $\Delta S^{\#}$, and enthalpy, $\Delta H^{\#}$, of activation) at high temperatures between 300 and 1000K. Reaction rate constants, $k(T)$, were obtained using the classical transition state theory (TST) [416, 472]:

$$k(T) = \sigma_e \left(\frac{k_B T}{h}\right) e^{\left(\frac{\Delta S\#}{R}\right)} e^{\left(\frac{-\Delta H\#}{RT}\right)}$$
8.2

where σ_e, k_B, T and h denote the reaction degeneracy number (set to 1 in all reactions), the Boltzmann's constant, the reaction temperature, and the Planck's constant; respectively.

8.3. Results and Discussion

8.3.1 Bulk and Surface Properties

It is of a prime importance to first demonstrate the anticipated accuracy level of the adapted theoretical framework against experimentally measured values. In our recent studies, we have thoroughly compared DFT-computed values with a wide array of structural and thermochemical properties reporting a rather very good agreement (a difference in the range of 2-6% in reference to experimental measurements) [365, 374, 563, 564]. Contrasted properties encompass bond dissociation enthalpies, reaction rate constants, pk_A values, solvation energies, lattice constants; and electronic bang gaps. In order to establish an accuracy benchmark of our adapted theoretical methodology herein, we first compute structural parameters of the bulk Cu/Fe and for their clean (100) surfaces, namely, lattice parameter, and surface relaxations. Table1 contrast calculated lattice constants with other analogous literature computational and experimental values. Our calculated lattice constants for bulk Cu and Fe depart from their analogous experimental values by only 0.46% -0.28%, respectively [565, 566]. As Table 8.1 shows, computed lattice constants are in accord with other theoretical values [559, 567].

Table 8-1. Computed and experimental values of the lattice constant for bulk Cu/Fe and structural relaxations of the clean Cu(100) and Fe(100) surfaces. $\Delta d_{12} = (d_{12} - d)/d$, where d_{12} is the surface atomic layer distance between the subsequent layers **1 and 2** while d represents the corresponding distance in the bulk.

Parameters	This work			Theoretical	Experimental
Lattice	Cu	$a(\text{Å})$	3.653	3.646 [567]	3.636 [565]
constant	Fe	$a(\text{Å})$	2.825	2.832 [568]	2.833 [566]
Structural	Cu(100)	Δd_{12}	-2.8%	-3.1% [569]	-2.8% [570]
relaxations	Fe(100)	Δd_{12}	-2.5%	- 2.72% [559]	-1.4± 3 % [571]

Likewise, our computed structural relaxation between the first and second layers ($\Delta d_{12)}$ in clean Cu(100) and Fe(100) surfaces are in accord with literature values at -2.8% [570] and -1.4±3% [571]; respectively. These values were sourced from low-energy electron diffraction (LEED) measurements. Similarly, computed Δd_{12} values are very comparable with other theoretically obtained values [567-569]. We conclude this section by comparing structural parameters of gas-phase phenol molecule with literature values (Table 8.2) in which an excellent agreement is obtained [66, 572].

Table 8-2. The equilibrium bond distances in the gas-phase phenol molecule along with a comparison with literature values.

Parameters	This work	Theoretical [66]	Experimental [572]
d(C–H)/Å	1.09	1.09	1.08
d(C–C)/Å	1.39	1.39	1.39
d(C–O)/Å	1.37	1.38	1.37
d(O–H)/Å	0.97	0.97	0.96

8.3.2 Surface-Assisted Fission of Hydroxyl's OH bonds over Cu(100) and Fe(100) Surfaces

This section presents three stapes dictating the surface-mediated session of the phenolic O-H bond over the clean Cu(100) and Fe(100) surfaces. Figure 8.2 and 8.3 reveals the geometric structures of physisorption, chemisorption and desorption states, denoted as M_nA, M_nC and M_nD; respectively, while the corresponding potential energy surfaces are displayed in Figure 8.4. A closer look at the optimized structures of physisorbed M_1A and M_2A states from Figures 8.3 and 8.4 reveals that the OH group slightly tilts toward the surfaces in which the distances between the oxygen atom and the nearest Cu and Fe surface atoms are 3.002 Å and 3.171 Å, respectively. As shown in Figure 8.2 and 8.3, intermediates and products in the dissociative

adsorption mechanisms over the two surfaces share very similar geometries. Albeit with distinct energy profiles.
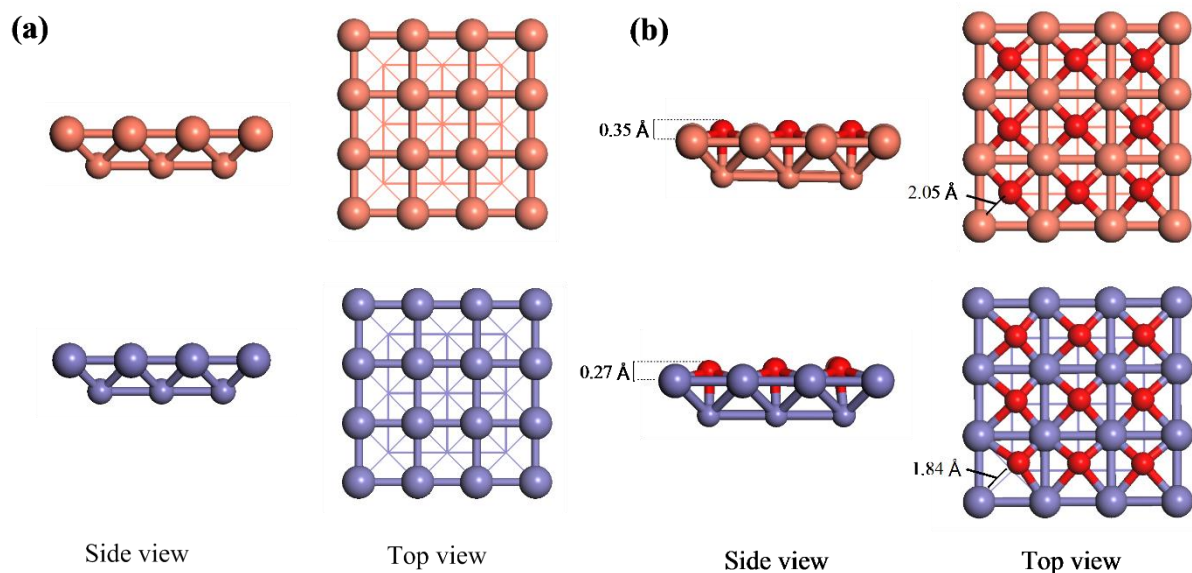
Figure 8.1. Top and side view of the first two layers of (a) clean Cu(100) and Fe(100) surfaces, and (b) Cu(100) $\_O_1$ and Fe(100) $\_O_1$ surfaces.

The adsorption energy of molecular phenol over the clean Cu(100) substrate is calculated to be -2.4 kcal mol^{-1}, a value that is very close with the analogous estimate at 2.1 kcal mol^{-1} over the Fe(100) surface. Bearing in mind uncertainty limits in the adapted methodology, we can conclude that that the phenol molecule interacts rather weakly with the two surfaces. The binding energy of phenol on the clean Cu(100) surface computed herein is in a good agreement with a corresponding value of -2.76 kcal mol^{-1} [573] obtained for a Cu(111) surface constructed by (4×4) unit cells. Likewise, our estimated weak binding energy of the phenol molecule over the iron surface matches very well analogous literature value at -2.30 kcal mol^{-1} using the Vienna ab initio simulation package with the four-layer close-packed $p(4 \times 4)$ slabs [573].
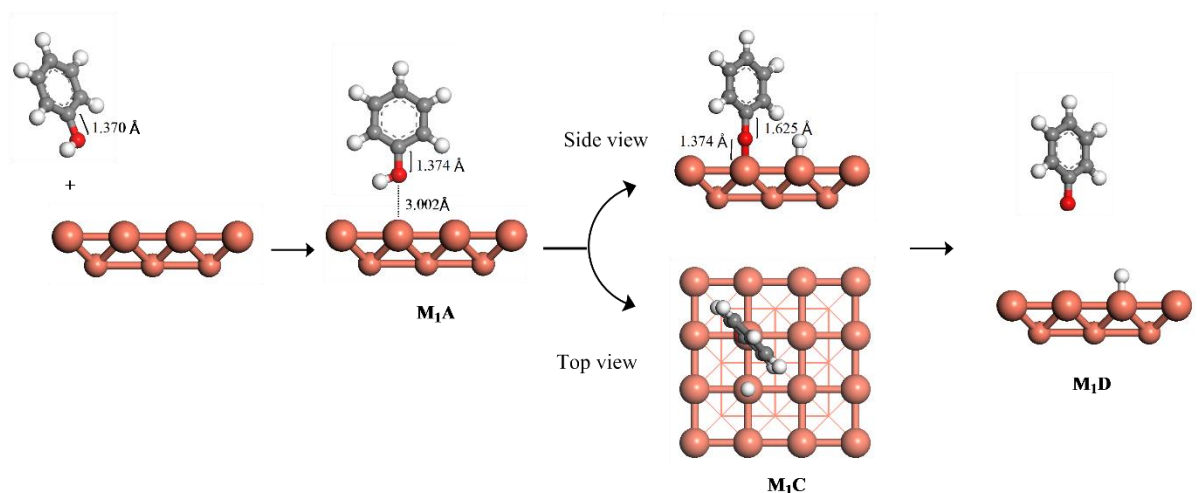
Figure 8.2. Structures of the physisorbed (M_1A), chemisorbed (M_1C) and desorption (M_1D) states over the Cu(100) surface. Only the first two layers are shown in side views. Red spheres are oxygen atoms, grey spheres are carbon, and white spheres denote hydrogen atoms.

In order to elucidate an insight into the weak interaction between the phenol molecules and the clean Cu and Fe surfaces, we present in Table 8.3 the % O-H's bond elongation and charge transfer from the surface to the phenol molecule. The minimal elongation of O-H bonds in adsorbed phenol (0.41% and 0.20% in reference to the equilibrium bond length in the gaseous phenol molecule), concurs with the very weak binding energies for physisorbed states. Similarly, the net amount of the charge transferred from Cu(100) and Fe(100) surfaces to the phenol upon adsorption is found to be 0.16e and 0.10e, respectively. These minor values largely reflect the weal interactions in the surface-adduct structures of M_1A and M_2A.

Table 8-3. Elongation of O-H bond (in reference to a gas-phase molecule), charge transfer and binding energy.

Structure	Elongation of O-H bond (%)	Charge transfer from the surface to the O phenolic's atom (e)	Binding energy (kcal mol^{-1})
M$_1$A [Cu(100) + phenol]	0.41	-0.16	-2.4
M$_2$A [Fe(100) + phenol]	0.20	-0.08	-2.1
M$_3$A [Cu(100)_O$_1$ + phenol]	0.61	-0.33	-5.5
M$_4$A [Fe(100)_O$_1$ + phenol]	0.30	-0.25	-3.1

Figures 8.3 and 8.4 reveals side and top perspectives for the optimized chemisorption structures of phenolate adduct and hydrogen atom following fission of the hydroxyl's O-H bond. In comparison with the horizontally adsorbed molecular phenol in the physisorbed states, the aromatic ring is vertically adsorbed in the chemisorbed states, forming phenolate-type EPFRs. We found that the vertical orientation adapted by the adsorbed phenolate on top of a surface Cu atom is unaltered when the phenolate occupies a four-fold hollow position. The formed Cu-O and Fe-O bonds with the adsorbed phenolate adduct amounts to 1.347 Å and 1.926 Å; correspondingly. In reference to a gaseous phenoxy radical, the C-O bonds in structures M$_1$C and M$_2$C, elongates by 18.2% and 7.7%, correspondingly. The C$_6$H$_5$O adduct is attached to the clean metallic surfaces through bonding of the free oxygen radical centre to the nearest surface atoms. Corresponding elongation for the C-O bonds in adsorbed phenolate on other surfaces incur similar values in the range 4.4%- 12.4% [456, 559, 574]. Based on computed Bader's charges, the O atoms in the adsorbed phenolate accumulate charges of 1.43e (M$_1$C) and 1.27e (M$_2$C). These values are significantly higher than the partial atomic charge localised at a gas phase phenoxy's O [138]. The predicted value of electron transfer from Fe surface atoms calculated herein is in accord with analogous value computed previously (i.e., 1.36e) in case of interaction of the phenol molecule with the Fe(110) surface [559]. The significance C-

O elongation in M_1C and M_2C and higher negative charges on phenoxy's O atom unequivocally point out to the formation of adsorbed phenolate-EPFR structure rather than a highly phenoxy radical.
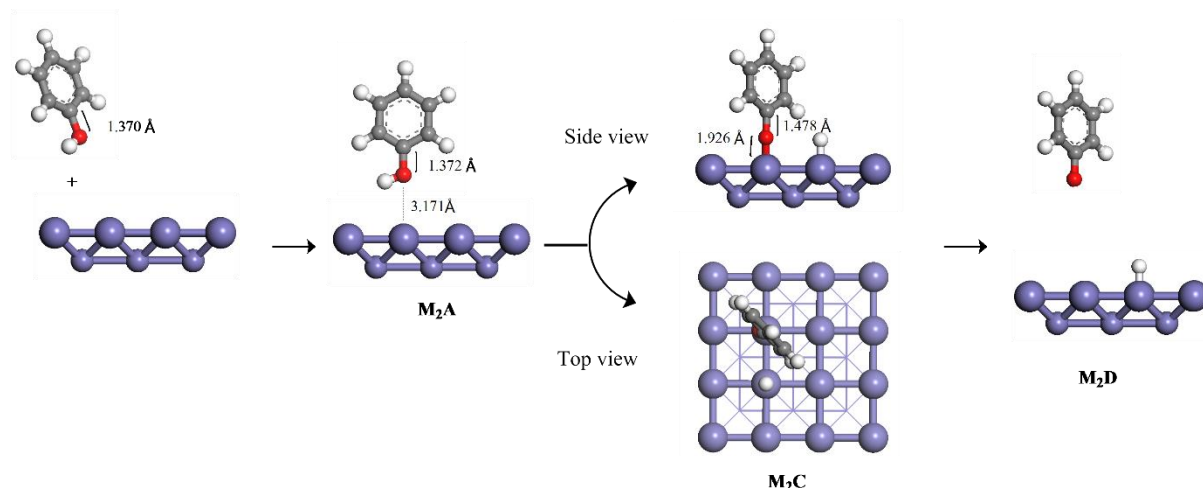
Figure 8.3. Structures of the physisorbed (M_2A), chemisorbed (M_2C) and desorption (M_1D) states over the Fe(100) surface. Only the first two layers are shown in side views.

In the M_1C and M_2C configurations, both the hydrogen atom and the produced phenolate-type EPFR are attached to a surface Cu or Fe atom. The obtained reaction energy of the surface-assisted conversion of phenol into phenolate adducts are -20.9 kcal mol^{-1} on Cu(100) and 9.1 kcal mol^{-1} on Fe(100). The Cu-O distance (1.374 Å) is significantly shorter than that of Fe-O (1.926 Å). Nonetheless, desorption of the surface-bound phenolate from the Fe(100) surfaces into a gas phase phenoxy radical demands a significant larger desorption energy at 48.3 kcal mol^{-1} in reference to the analogous value for the Cu(100) surface; 24.2 kcal mol^{-1}. This finding is in line with a higher concentration and lifetimes of phenolate-type EPFR over Fe surfaces in comparison to Cu surfaces [552, 553].
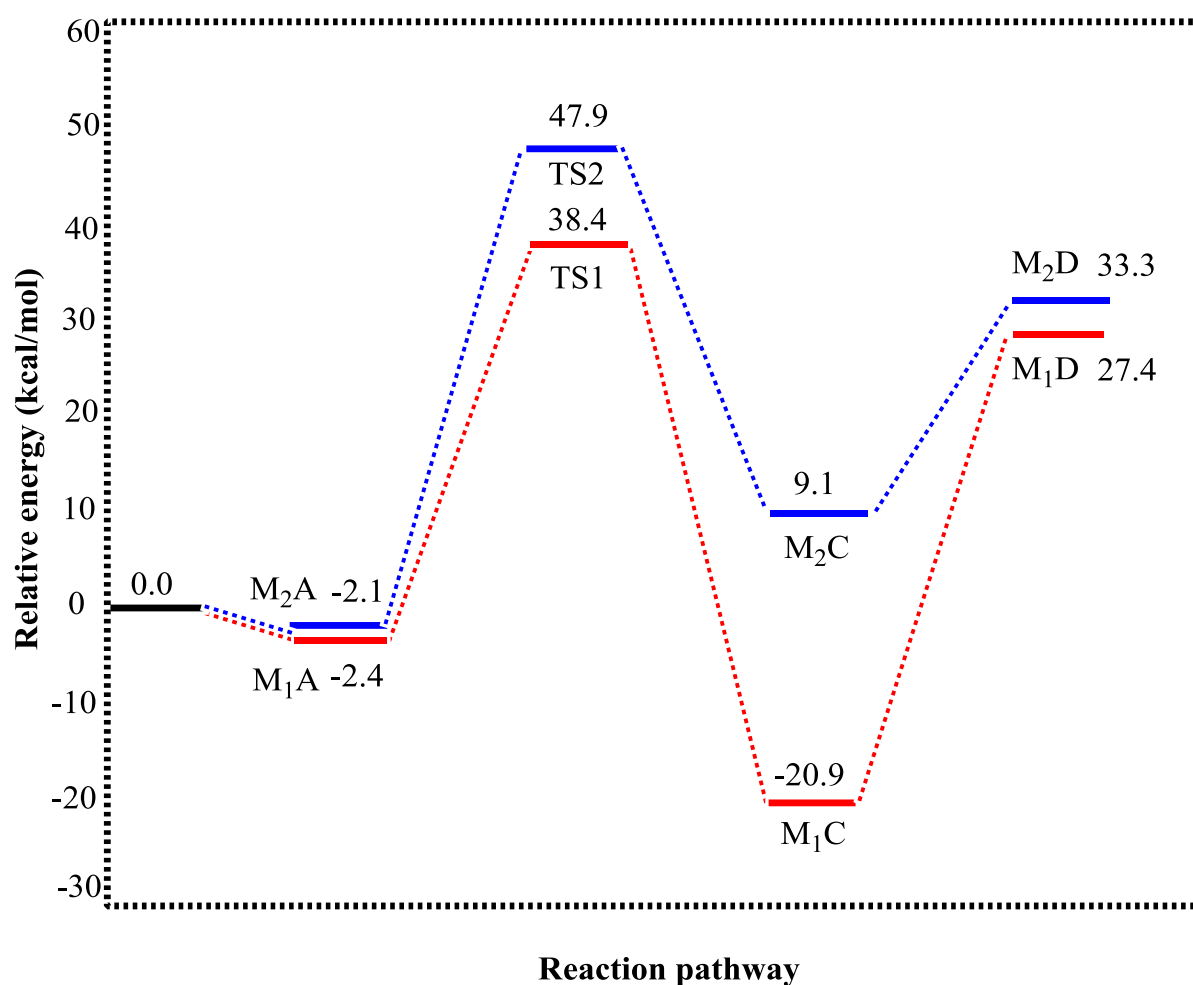
Figure 8.4. Relative energy profile diagram for the interaction of the phenol molecule with the Cu(100) and Fe(100) surfaces.

To further investigate prevailing electronic attributes of the adsorption mechanism, Figure 8.5 displays the projected density of states (PDOS) spectra onto the *3d*-orbitals of the Fe(100) surface. We first examined the PDOS of both the clean Fe surface's atom and the free phenolic's O atom before contrasting them with analogous plots for the chemisorbed (M$_2$C) and physisrobed state (M$_2$A). Figure 8.5 (a) illustrated the PDOS of the free phenolic's O. In Figure 8.5b, the PDOS of a surface Fe atom exhibits to a large extent bulk PDOS and is in agreement with previous theoretical studies [559, 575]. The Fermi level is set at 0 eV.

From the PDOS of both physisorption and chemisorption structures (panels c and d in Figure 8.5), it is obvious that the split bands of spin-up for the *3d*-orbitals of Fe atom in the range of 0 to -5 eV are broader than those of the clean Fe surface's atom (panel b) and shift toward the Fermi level. However, the modest increase in the peak widths of the physisorption state in panel (c) indicates less covalent effect between the surface Fe atom and molecularly adsorbed phenol in comparison to the chemisorption state. The latter displays higher peak widths. Furthermore, from the panels c and d, the bands shifting of the O phenolic's atom downward the fermi level suggests that O atom withdraws charges from the *3d*-orbitals of Fe surface's atom. This trend satisfactorily correlate with our recent work for the interaction of HCl molecular over Fe_3O_4 surface [576]. Indeed, two concluding remarks can be inferred from contrasting the adsorption mechanism in panel c and d:

1- The significant overlaps in the case of chemisorption state between the *3d*-orbitals of Fe surface's atom and the *2p* orbital of phenolic O atom in reference to the physisorption state, indicates stronger bonding interaction between Fe and O atoms. This trend concur very well with the calculated energy values of M_2A and M_2C configurations in Figure 8.4 (-2.1 kcal mol^{-1} versus -20.9 kcal mol^{-1}) and with the previous finding by Li et al. [574] for the dissociation of phenol molecular over the Pd(111) surface.

2- The split of phenolic O atom band in the range of 0 to -3 eV into two peaks for both cases implies that there is a change in the phenol molecular bonding and formation a new Fe-O bond.
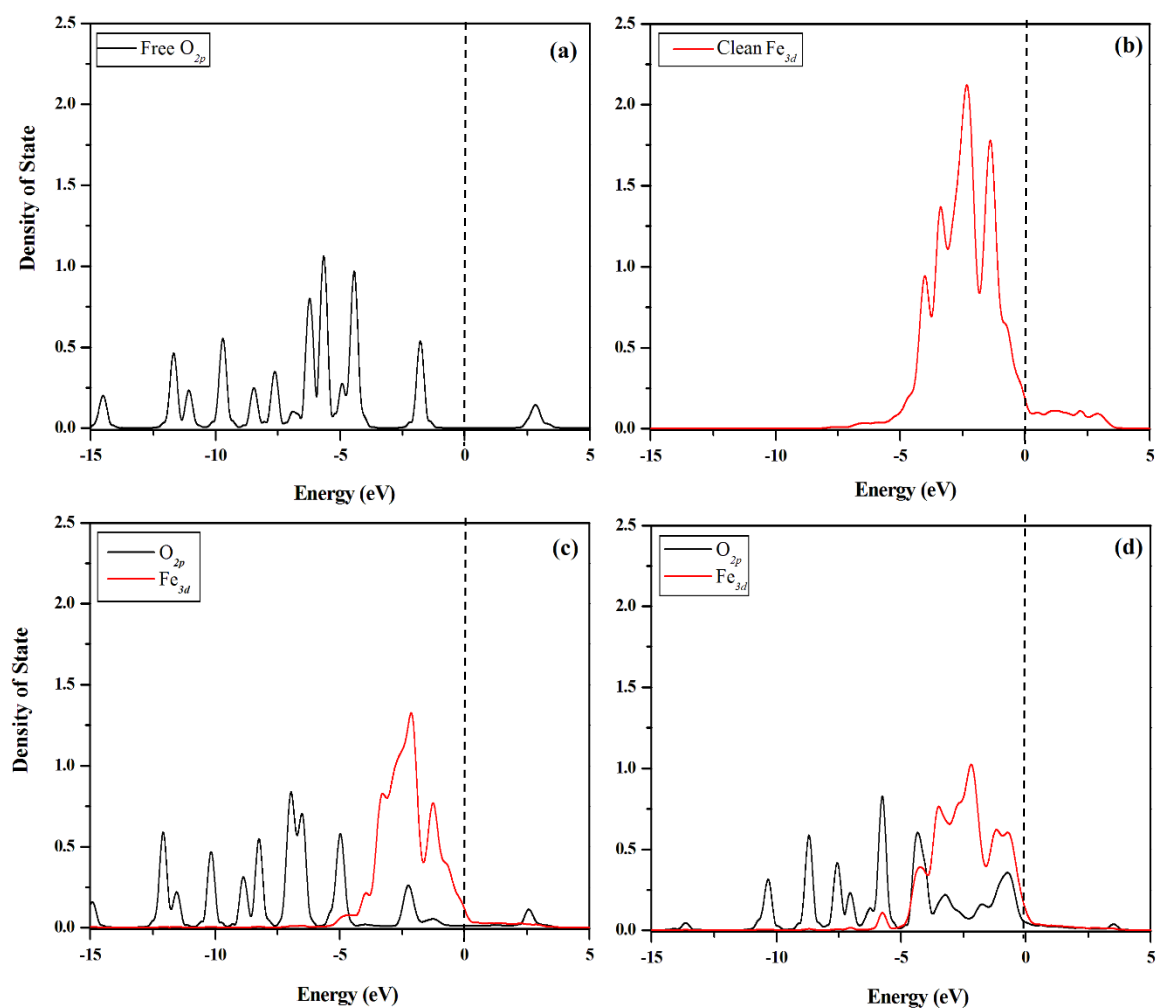
Figure 8.5. PDOS of (a) free phenolic's O, (b) clean Fe atom, (c) phenolic's O and the nearest Fe atom in the M$_2$A state (physisorbed), and (d) phenolic's O and the nearest Fe atom in the M$_2$C state (chemisorbed).

Assessing the catalytic capacity of Cu(100) and Fe(100) toward dissociative adsorption of phenol to surface-bounded phenolate truly rests on underpinning kinetics parameters, most notably the intrinsic reaction barriers. As shown in Figure 8.4, fission of the O-H bond in physisrobed phenol ensues via an activation energy of 38.4 kcal mol^{-1} over the Cu(100) surface and 47.9 kcal mol^{-1} on Fe(100). The catalytic capacity of these surfaces toward fission of the hydroxyl's OH bond in the phenol molecule becomes evident when contrasting these calculated

energy barriers with the highly endothermic direct cleavage of O-H bond in the in the gas phase that scatter in the narrow range of 87.5 - 89.5 kcal mol^{-1} [371, 577]. Clearly, catalytic transformation of phenol molecule into phenolate-type EPFRs on the clean Cu(100) surface is thermodynamically and kinetically more favourable than on the Fe(100) surface. To further elaborate on the kinetic feasibility for the surface-mediated formation of phenolate-type EPFR over clean Cu(100) and Fe(100) surfaces, we carried out a simplified batch reactor model along reaction pathways depicted in Figure 8.4 at a reaction time of 60 s. This simplified model utilizes reaction rate expressions enlisted in Table 8.4. Reaction rate constants for the final desorption step deployed a t typical *A*-factor of 1×10^{13} s^{-1} and the desorption energy as the activation barrier. Computed conversion of M_1A configuration (adsorbed phenol molecule over the Cu(100) surface) into the M_1D structure (a gas phase phenoxy radical) attains values of 0.74 and 1.00 at 600 and 700 K respectively. Corresponding conversion over the Fe(100) surface entail similar values of 0.57 (600 K) and 1.00 (700 K). The predicted high conversion of adsorbed phenol molecules into gaseous phenoxy-type EPFR unequivocally points out to a kinetic feasibility at temperatures encountered in the post-combustion zone; 650 – 700 K [138, 166].

The significant reduction in energetic requirements described herein pinpoints a kinetics feasibility for the synthesis of surface-bounded phenolate-type EPFR in systems pertinent to co-combustion of phenolic-containing polymers and Cu/Fe species. Typical thermal systems encompass thermal recycling of e-waste [166] and municipal waste incineration [138].

Table 8-4. Kinetic parameters for the surface-assisted dissociation reactions at a temperature range of 300-1000K.

Reaction	A (s^{-1})	E_a (kcal mol^{-1})
$M_1A \rightarrow M_1C$	1.58×10^{11}	33.2
$M_2A \rightarrow M_2C$	1.97×10^{13}	41.6
$M_3A \rightarrow M_3C$	2.71×10^{12}	22.2
$M_4A \rightarrow M_4C$	7.48×10^{11}	43.3

8.3.3 The Effect of the Oxygen: Cu(100)_O$_1$ and Fe (100)_O$_1$ Surfaces

Among notable transition meal oxides in PM$_{2.5}$ are CuO and Fe$_2$O$_3$ [578]. These oxides host and serve as major carriers for phenoxy-type EPFR adsorbed on PM$_{2.5}$. Cu species in particular are the most abundant transition metals in particulate matters in the atmosphere [579]. Likewise, Cu(II) and Fe(III) were reported to act as redox centres in course of synthesis of EPFR on montmorillonite ; a key mineral component in PM$_{2.5}$ [580, 581]. EPR and X-ray absorption near edge measurements confirmed formation and stabilisation of phenoxy- and catecholic-type EPFR on CuO and Fe$_2$O$_3$. Phenoxy-type EPFR endures a significantly longer lifetime over Fe$_2$O$_3$ surfaces when contrasted with CuO surfaces [578]. Formation of phenoxy-type EPFR over these surfaces typically occur over hydroxylated surfaces of these oxides. Nonetheless, de-hydroxylated surfaces persist at higher temperatures. Thus, it is of interest to examine energetics requirements for production of phenoxy-type EPFR on these oxides. Herein, we simulate the structures of the CuO and Fe$_2$O$_3$ oxides by considering oxygen pec-covered surfaces of Cu(100) and Fe(100) denote as Cu(100)_O$_1$ and Fe(100)_O$_1$ surfaces. In the latter, all 4-fold hollow sites are occupied with oxygen atoms. In case of copper, it was shown that the surface oxygen adsorption serves as a precursor for the formation of the two copper oxide phases, Cu$_2$O and CuO [582, 583]. It was found that oxygen atoms preferentially adsorbs on hollow sites of Cu(100) and Fe(100) surfaces, rather than bridge or atop site [584,

585]. From another perspective, surface Cu/Fe-O dimers function as redox centres that triggers fission of the O-H bond in the phenol molecule. Inner Cu/Fe-O bonds in oxides are expected to play a rather negligible role in a truly surface phenomenon.

Figure 8.1.b depicts optimized structures for the oxygen doped configurations Cu(100)_O_1 and Fe(100)_O_1. The calculated dimer distance between Cu/Fe and O atoms ($d_{Cu/Fe-O}$) at the first surface layers amount to 1.84 Å and 2.05 Å respectively. These estimates agree quite well with the analogous theoretical and experimental data (i.e., $d_{Cu/Fe-O}$ = 1.94 Å and 2.05Å, correspondingly) [586, 587]. O atoms in Cu(100)_O_1 and Fe(100)_O_1 configurations reside 0.35Å and 0.27Å above the first layer; respectively.

Figure 8.6 and 8.7 present the optimized structures for reactants, transition states and products along with prominent interatomic distances, whilst Figure 8.8 illustrate pertinent potential energy surfaces. Molecular adsorption of the phenol molecule assumes a marginal binding energy of only -5.5 and -3.1 kcal mol^{-1} for the two surface-molecule adducts M_3A and M_4A; correspondingly as listed in Table 8.3. Despite of a minor O-H bond elongation at slightly of 0.61% and 0.30%, a noticeable charge transfer from the surface is reported with values at 0.33e and 0.25e. In all, the phenol molecule interacts very weakly with oxygen pre-covered surfaces of Cu(100) and Fe(100). While the very small differences in binding energies between clean and pre-covered oxygen configurations are most likely to be within the accuracy margin of the adapted methodology, hydrocarbon molecules were found to incur higher binding energies on transition metal oxides in reference to clean metallic surfaces [582].
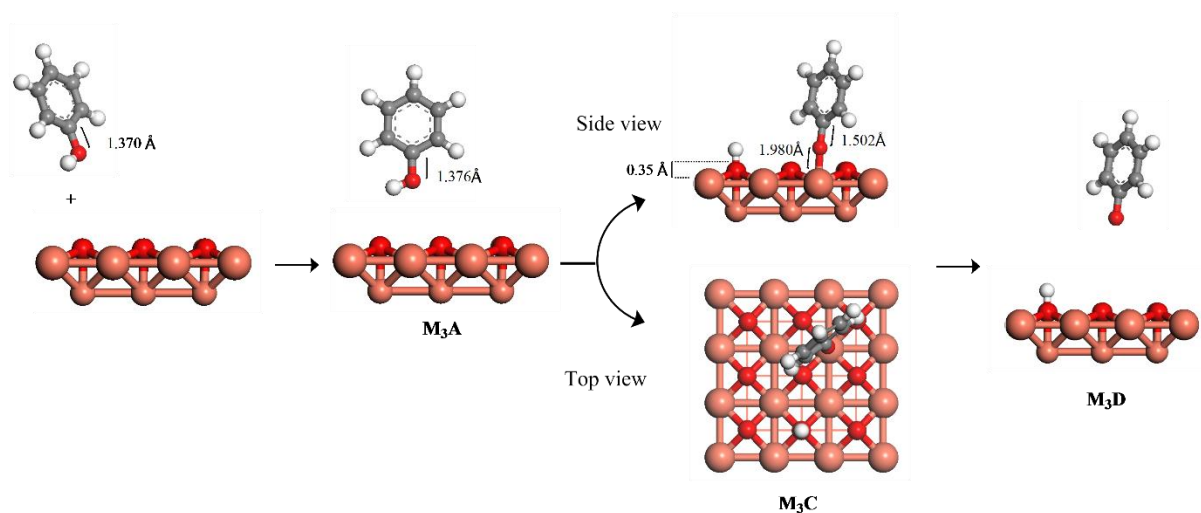
Figure 8.6. Structures of the physisorbed (M₃A), chemisorbed (M₃C) and desorption (M₁D) states over the clean Cu(100)_O₁ surface. Only the first two layers are shown in side views.
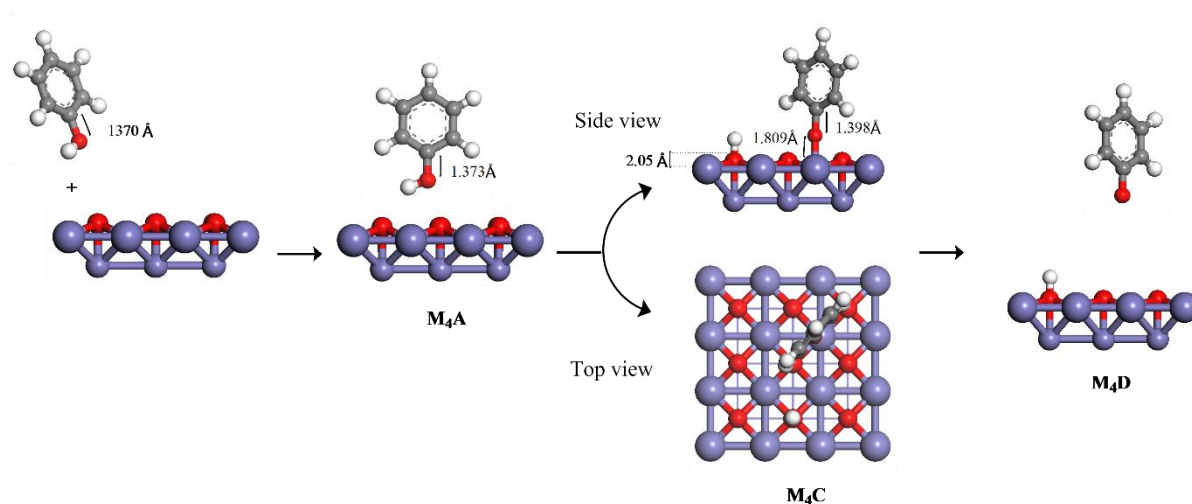
Figure 8.7. Structures of the physisorbed (M₄A), chemisorbed (M₄C) and desorption (M₁D) states over the the clean Fe(100)_O₁ surface. Only the first two layers are shown in side views.

Following the weak adsorption of the phenol molecule, rupture of the O-H bond occurs heterolytically in which the phenoxy adduct is attached to atop Cu/Fe site and the dissociated hydrogen atom forms a link with an oxygen surface atom. The formed surface hydroxyl groups entail O-H distances of 0.98 Å and 1.01 Å over the Cu(100)_O₁ and Fe(100)_O₁ configurations, respectively. These calculated values concur very well with corresponding distances (0.98 Å and 0.97 Å) reported from theoretical investigations for adsorbed hydroxyl groups over CuO

(011) and $Fe_3O_4(111)$ surfaces, respectively [487, 586]. Further interaction of a phenol molecule with surface Cu/Fe-OH islands may yield the experimentally observed catecholic-type EPFR [588].
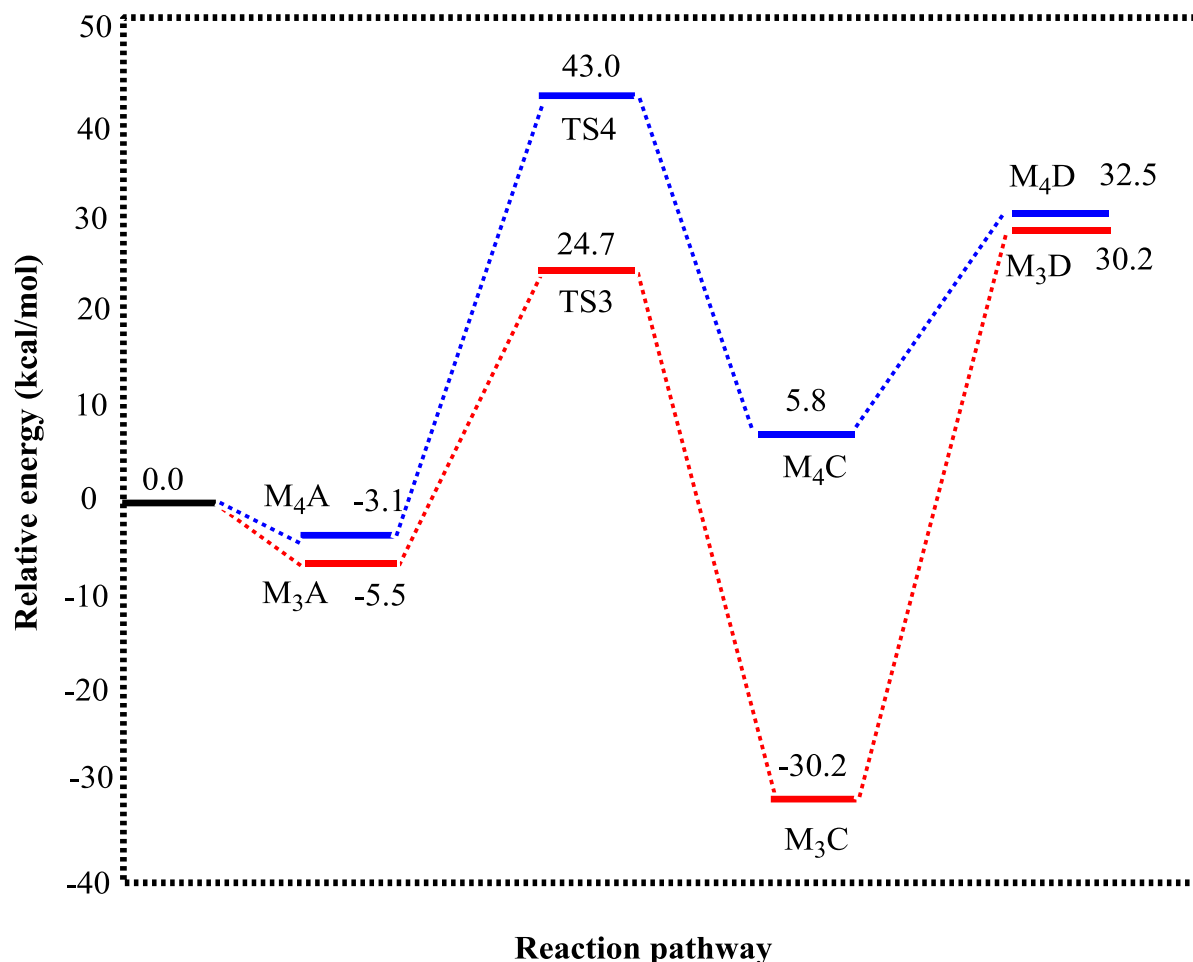
Figure 8.8. Relative energy profile diagram for the dissociative adsorption of the phenol molecule over the Cu(100) $\_O_1$ and Fe(100) $\_O_1$ surfaces.

In the M_3C and M_4C structures, the phenoxy's O binds to surface Cu and Fe atoms at a separation of 1.980 Å and 1.809 Å in that order. These two values depart by 44.1% and -5.5% from their analogous bond distances in the dissociative structures M_1C and M_2C, respectively. The bond length of phenoxy's O-Cu/Fe surface atoms in M_3C and M_4C structures are quite similar to the length of Cu-O and Fe-O bonds at 1.960 and 1.857 Å, reported from recent invistigations for dissociation of phenole molecule over the same surfaces [456, 589]. Fission

of the phenolic's O-H bond over the Cu(100)_O_1 surafce is noticably exothermic by 30.2 kcal/mol while the process ensues via a minor endothermecity of only 5.8 kcal/mol above the Fe(100)_O1 configuration. In this regard, we find that phenol chemisorption on oxygen doped Cu and Fe surfaces is significantly stronger when contrasted with their clean surfaces. The surface-mediated fission of the O-H bond necessitates modest activation barriers of 24.7 and 43.0 kcal mol^{-1} over Cu(100)_O_1 and Fe(100)_O_1 surfaces, correspondingly. In comparison with the clean Cu(100) surface, the presence of the oxygen atom in the hollow site in the Cu(100)_O_1 configuration, noticeably reduces the reaction barrier by 13.7 kcal mol^{-1}. The corresponding reduction in activation energy for Fe(100) versus Fe(100)_O_1 appears very minor at 3.9 kcal mol^{-1}

In Table 8.5, we assemble literature reported activation barriers for the fission of phenolic O-H bond over metallic and metal oxide surfaces [66, 456, 554, 574, 589, 590]. It is evident that the clean Fe and Cu surfaces and their partially oxidized configuration require higher activation energies to transform phenol into a surface-bound phenolate. Nonetheless, the high temperature in thermal processes pertinent to co-existence of PM$_{2.5}$ with phenolic constituents should suffice to overcome the relatively sizable activation barriers for the title reaction reported herein.

Table 8.4 lists reaction rate constants for all these reactions. It is obvious that the cleavage of the O-H bond in the phenol molecular incur lower reaction rates over the clean surfaces in reference to their partially oxidized surfaces. These data shall be useful to predict the uptake of phenol molecules by Cu- and Fe-PM$_{2.5}$ constituents

Table 8-5. Activation energies for breaking the phenolic O-H bond over different metallic and metallic oxides surfaces

Metallic surfaces	Activation energy (kcal mol^{-1})	Metallic surface oxides	Activation energy (kcal mol^{-1})
Pt(111) [574]	11.1	α-Al$_2$O$_3$ [66]	11.4
Pd(111) [574]	4.6	SiO$_2$ [554]	7.6
Pt(111) [590]	15.9	Cu$_2$O(110) [456]	8.2
Rh(111) [590]	15.2	Fe-MMT [589]	8.5
		Ca-MMT [589]	12.6
		Na-MMT [589]	56.9

It is important to mention herein that the final step of the dissociative adsorption of phenol molecule over all the four selected surfaces in our study is desorption of phenoxy molecule from these surfaces. As illustrated from Figures 8.2, 8.3, 8.6 and 8.7, surface-bound phenolate desorb from M$_1$C, M$_2$C, M$_3$C and M$_4$C structures to yield gas-phase free phenoxy radicals in M$_1$D, M$_2$D, M$_3$D and M$_4$D configurations through sizable endothermic process of 48.3, 24.2, 60.4 and 25.7 kcal mol^{-1}; respectively. It is obvious that the energy requirements for the final desorption step appear significantly lower in reference to desorption energies of 2-chlorophenoalte from a neat SiO$_2$ surface [554] (91 kcal mol^{-1}), and phenol over hydroxylated α-Al$_2$O$_3$ clusters [591] (89 kcal mol-1) and α-Al$_2$O$_3$ surface [66]. Higher stability of phenolate-EPFRs on Fe/Cu surfaces enable their subsequent surface-assisted coupling into dioxins compounds via the so-called Langmuir–Hinshelwood (LH)[138] and Eley–Rideal (ER)[592] mechanisms.

We conclude this section by assessing the feasibility for the transformation of an adsorbed phenolate adduct into that catecholic-type intermediates of *o*-semiquinone (*o*-SQ). Figure 8.9 describes a plausible pertinent mechanism. In the first step, a hydroxyl group transfer from surface into an ortho carbon atom followed by a loss of an ipso hydrogen atom affords a

surface-attached a *o*-SQ adduct. However, the high energy barriers for the two involved transition states (TS5 and TS6) suggest a plausible existence for alternative lower energy barriers. Thee potential pathways may involve the formation of an ortho carbon centred radical proper to migration of a surface OH group to the vacant radical site. Mechanisms operating in the likely formation of catecholic-type intermediates warrant further investigations.
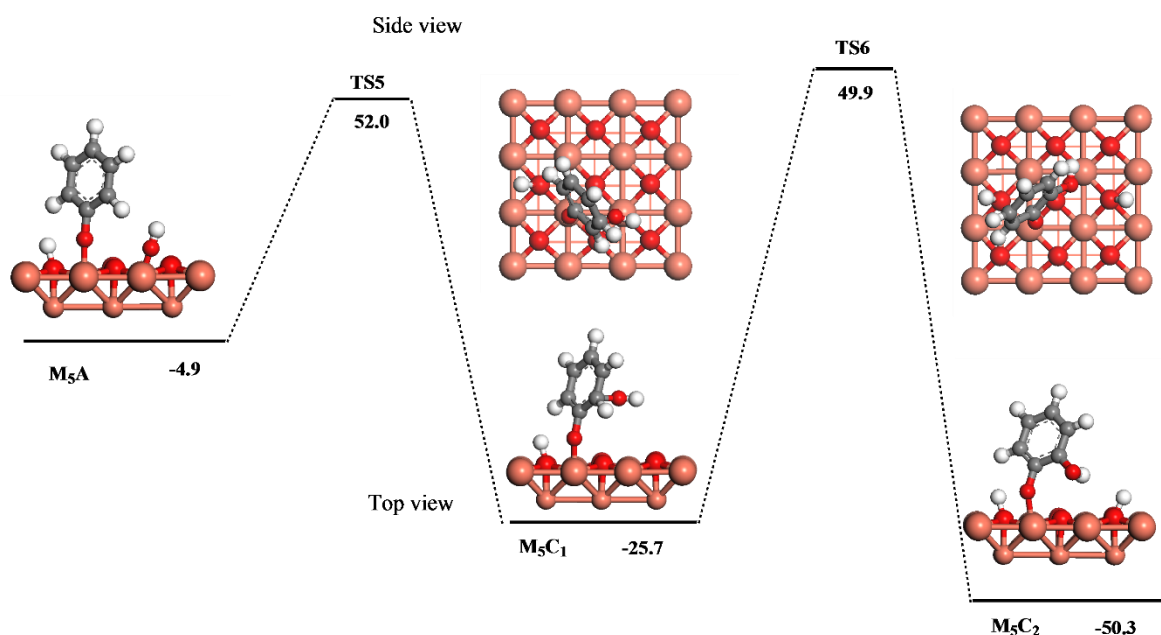
Figure 8.9. Structures for the physisorbed (M$_5$A) and chemisorbed (M$_5$C$_1$ and M$_5$C$_2$) states of hydroxyl group over the Cu(100)_O$_1$ surface. Only the first two layers are shown in side views.

8.3.4 Catalyzed Formation of Phenolic-Type EPFR From Catechol and Cresol

In addition to phenol, other hydroxylated derivatives of benzenes, namely catechol and cresol; constitutes the major decomposition products from the various structural entities in biomass (most notably cellulose and lignin) [593]. Thus, generation of phenolic-type EPFR from combustion of biomass entails catalyzed interaction of hydroxylated benzenes with the trace metallic content in biomass [594]. For this reason, we report in Figures 8.10 and 8.11 energy profiles for the interaction of catechol and cresol with the Cu(100)_O1 surface; in that order. Fission of the first O-H bond in the catechol molecule demands a sizable energy barrier of 41.5 kcal/mol via the transition structure TS7 (Figure 8.10). This barrier is in line with the

corresponding value computed for the O-H bond fission in the phenol molecule at 40.8 kcal/mol (Figure 8.4; TS1). Clearly, the tremendous activation barrier embedded in TS8 (45.3 kcal/mol) largely hinders fission of the second O-H bond into an adsorbed o-quinone adduct (the structure M_6C_2). In Figure 8.11, secession of the methyl's C-H bond in cresol prevails over the fission of the hydroxyl's O-H bond (26.8 kcal/mol versus 36.9 kcal/mol). It follows, that dissociative adsorption of cresol preferentially produces a carbon-bounded species rather than a phenolic-type EPFR moiety.
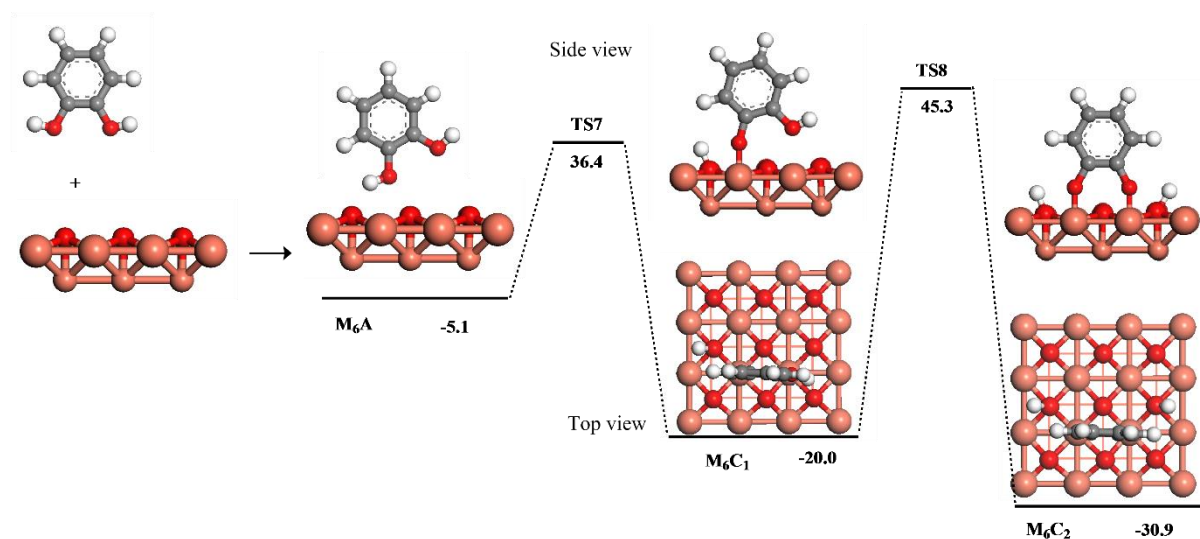
Figure 8.10. Structures for the physisorbed (M_6A) and chemisorbed (M_6C_1 and M_6C_2) states of catechol molecule over the Cu(100)_O_1 surface. Only the first two layers are shown in side views.
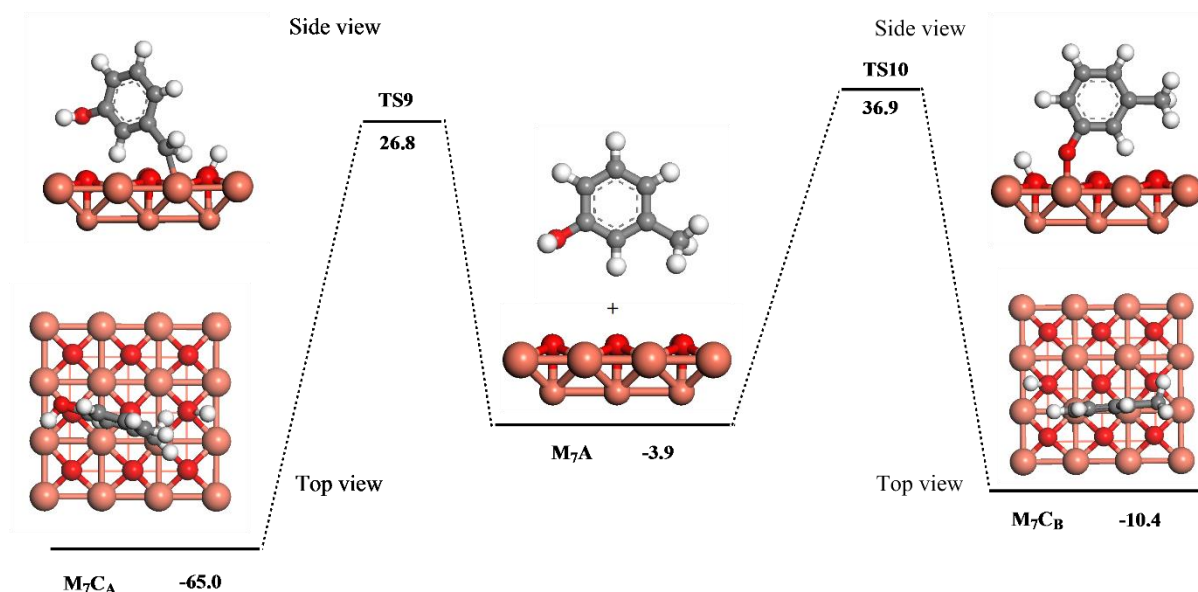
Figure 8.11. Structures for the physisorbed (M$_7$A) and chemisorbed (M$_7$C$_A$ and M$_7$C$_B$) states of cresol molecule over the Cu(100)_O$_1$ surface. Only the first two layers are shown in side views.

8.4. Conclusions

Utilizing accurate DFT calculations, we systematically exanimated the dissociative adsorption mechanism of an aromatic oxygenate compound (phenol molecule) on 3d transition metal surfaces and their partially oxidized configurations [Cu(100), Fe(100), Cu(100) _O$_1$, and Fe(100) _O$_1$]. The main objective of the present contribution is to elucidate, on a precise atomic scale, the specific underlying mechanism of the title reaction and the kinetics feasibility to germane to generate phenolate-type EFPRs. It is found that dissociative adsorption of the phenol molecule is kinetically and thermodynamically preferred over the partially oxidized configuration in reference to neat Cu and Fe surfaces. Desorption of the surface-bound phenolate adduct from surfaces demand desorption energies in the range of 24 – 48 kcal mol-1. Computed charge transfer and DOS indicates accumulation of spin density on the phenolic's O following fission of the O-H bond. Calculated kinetics parameters herein shall be useful to predict lifetimes of phenolate-EPFR in Cu/Fe-rich PM2.5.

Chapter 9

Conclusion and Recommendations

9.1. Conclusion

The aim of this research was to understand the potential dual role of modelling structures of 3d transition metals and their oxides within the framework of density functional theory (DFT) calculations in the catalytic de-halogenation of halogen-containing solid wastes and their mediating generation of notorious dioxin compounds and phenoxy-type environmental persistent free radicals (EPFRs). The major findings of the research include:

(i) Determination of the mechanistic and thermo-kinetic aspects that govern the decomposition of hydrogen halides molecules and multiple halogenated hydrocarbons over transition metals and their oxide configurations

(ii) Identification, on a precise molecular basis, of mechanisms that determined the fixation of halogen molecules on transitional metals and their oxides

(iii) Elucidation of comprehensive specific underpinning mechanisms to generate phenolate-type EFPRs.

Chapter 4 investigated the initial reactions for a cluster model of hematite and major chlorine-bearing species from the fragmentation of polyvinyl chloride (PVC). It was demonstrated that successive uptake of HCl molecules followed by water elimination led to the formation of a precursor for iron chlorides. Owing to stronger carbon-chlorine bonds in the considered molecules, their dissociative addition corridors assume higher activation barriers in comparison with their brominated counterparts. It was found that interaction of α-Fe$_2$O$_3$ nanoclusters with 2-chlorophenol preferentially form an OH-phenyl radical (via carbon-chlorine bond rupture) rather than a 2-chlorophenoxy radical (via O-H bond fission).

Chapter 5 reported the findings of a theoretical thermo-kinetic study to investigate dissociative adsorption mechanism of hydrogen halide molecules on zincite surfaces. Convergence tests

using various sets of functionals, unit cell size and energy cut-off ensures the accuracy of all reported energy profiles. Calculated findings show that transformation of ZnO into zinc halide take place through two subsequent dissociative adsorption steps, followed by intramolecular hydrogen transfer. Results showed that cleavage of a H-Cl bond over a zincate surface requires reaction barriers in reference to H-Br, reflecting the noticeable difference in their bond dissociation energies in the gas phase. Desorption of $ZnCl_2$ and $ZnBr_2$ as gas phase molecules occur through relatively accessible desorption energies. It was also found that the nonpolar ZnO $(10\bar{1}0)$ surface displays higher catalytic activity for dissociative adsorption of HX molecules in comparison to a zinc-terminated (0001) surface. The theoretical calculations in this chapter support previous experimental observations that HX molecules have great potential to serve as a perfect chlorinating /brominating agent for recycling of zincite.

Chapter 6 reported the de-chlorination and de-hydrochlorination mechanisms of HCl molecule and organochlorinated compounds over a magnetite surface. The chapter began with a comprehensive benchmarking of the adapted methodology against literature that reported electronic and structural features of bulk and surface of magnetite as well as for the BDE in the investigated molecules. Results showed that de-chlorination mechanism involved the formation of ferrous ferric chloride proceeding through two subsequent stapes, further dissociative adsorption of hydrogen chloride molecule on strong Lewis acid metal oxide site, followed by liberation of water molecules. It was observed that the dissociative adsorption of HCl over Fe_{oct2} sites requires remarkably lower activation energy than that over the Fe_{tet1} sites of the Fe_3O_4(111) surface. The chapter also reported the findings of the investigation of two competing channels for the reaction of halogenated alkanes and alkenes with the Fe_3O_4 surface: the direct HCl elimination route and the dissociative addition pathway. Products from the latter

channel were significantly lower in energy, which supports the general consensus related to the significance of the dissociative addition pathway in producing pure steam of olefins.

Chapter 7 established the results of the investigation of the catalytic de-halogenation mechanism of selected alkyl halides molecules over a Cu(100) surface. The study sought to identify the initial stages that dictate the de-halogenation mechanism. The thermo-kinetic parameters underlying the split off halogen atoms from chlorinated/brominated alkyl chloride/bromide and chloro/bromo-benzene molecules were examined. The analysis of the structural properties and binding energies in the elementary physisorption stage for each surface-adduct structure disclosed that the investigated halogenated compounds interacted rather weakly with the Cu(100) surface. Activation barriers for C-Cl bond fission were systematically higher than their analogous C-Br values, largely following their respective bond strengths in gas phase molecules. Surface Cl/Br-Cu bonds mimicked the corresponding bonds in bulk $CuCl_2$/$CuBr_2$.

Finally, chapter 8 discussed the dissociative adsorption mechanism of aromatic oxygenate compounds on 3d transition metal surfaces and their partially oxidized configurations [Cu(100), Fe(100), Cu(100) _O1, and Fe(100) _O1]. The main objective of the present contribution was to illustrate, on a precise molecular basis, the specific underlying mechanism of the title reaction and kinetics feasibility germane to generating phenolate-type EFPRs. It was found that dissociative adsorption of the phenol molecule is kinetically and thermodynamically preferred over the partially oxidized configuration in reference to neat Cu and Fe surfaces. Desorption of the surface-bound phenolate adduct from surfaces demands desorption energies in the range of 24–48 kcal mol^{-1}. Computed charge transfer and DOS indicates accumulation of spin density on the phenolic's O following fission of the O-H bond.

Calculated kinetics parameters shall be useful to predict lifetimes of phenolate-EPFR in Cu/Fe-rich PM2.5.

9.2. Recommendations

In light of the results reported in this dissertation, further work is needed to address questions that continue to surround the following issues.

- ➤ The role of Fe_2O_3 as a catalysis in the surface-mediated formations of PCDD/Fs, PBDD/Fs in addition to mixed polychlorinated/brominated dibenzo-*p*-dioxins, and furans (PXDD/Fs; X = Cl, Br). Relevant experimental investigations on co-pyrolysis of halogen-containing solid wastes with EAFD have mainly addressed the merits of metal oxides as halogen fixation agents with little emphasis on the likely potential to generate dioxin compounds.

- ➤ A principal aim for the co-pyrolysis of PVC and BFRs with EAFD is to extract its high load of zinc content. Zinc in EAFD mainly exists in the form of $ZnFe_2O_4$. It is assumed that formation of leachable zinc halide occurs through migration of halides from iron halides into $ZnFe_2O_4$. It will be informative to examine this mechanistic hypothesis against direct plausible dissociation of HCl/HBr on Zn-O bonds.

- ➤ The roles of zincite in mediating decomposition of organohalogens released from thermal degradation of PVC and BFRs.

- ➤ As reported in chapter 5, analysis was limited to a perfect ZnO structure (i.e., $(10\bar{1}0)$ surface). The presence of structural defects or atomic-type impurities often enhances

catalytic decomposition capacities for environmental-bases catalysts. Therefore, it will be useful to investigate the effect of these factors on the catalytic decomposition performance of ZnO.

➢ Identification of the mechanistic and kinetic parameters for the halogenation mechanism of aromatic pollutants by zinc halides. Such informative investigations will assess the overall merits of deploying metals and their oxides to capture the halogen laden materials in solid waste streams; including e-waste and EAFD.

➢ Thermal recycling is currently represented as a major stream strategy in the safe disposal of objects laden with halides, most notably the polymeric fraction in electronic and electrical waste (e-waste). Therefore, it is essential to comprehend the combustion chemistry underpinning the reaction of chlorinated and brominated constituents with common polymeric entities. (Appendix D displays the preliminary results of this investigation).

➢ Future studies need to be carried out to investigate the mechanistic and thermo-kinetic aspects that govern the formation of other types of EPFR such as phenyl and para-dihydroxybenzneses over other transition metal oxides such as Si_2O_3 and Fe_2O_3.

➢ Determine the thermal stability of materials laden with new-generation brominated hydrocarbons, collectively known as novel brominated flame retardants (NBFRs) and their interactions with metal oxides present in potential catalysts (i.e., those in the EAFD). Decomposition profiles of pure NBFRs, NBFRs-containing mixtures and

mixtures of BFRs with metal oxides provide valuable safety information, including the onset of the thermal decomposition stages of decomposition.

➢ Investigation of the potential use of EAFD as an inexpensive catalyst in upgrading pyrolysis oil requires co-pyrolysis of EAFD with plastics laden with NBFRs.

Appendix

Appendix A (Chapter 5)
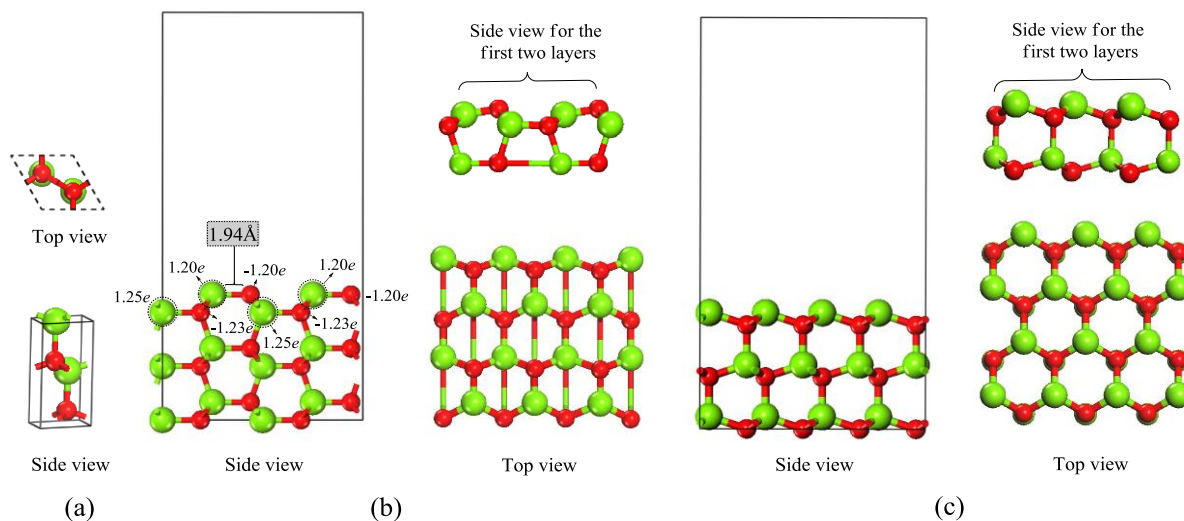
Figure 5.S1. Slab models of ZnO(10$\bar{1}$0) and (0001) surfaces. (a) ZnO unit cell; (b) side and top view ZnO(10$\bar{1}$0); (c) side and top view ZnO (0001). The green and red spheres represent zinc and oxygen atoms, respectively.
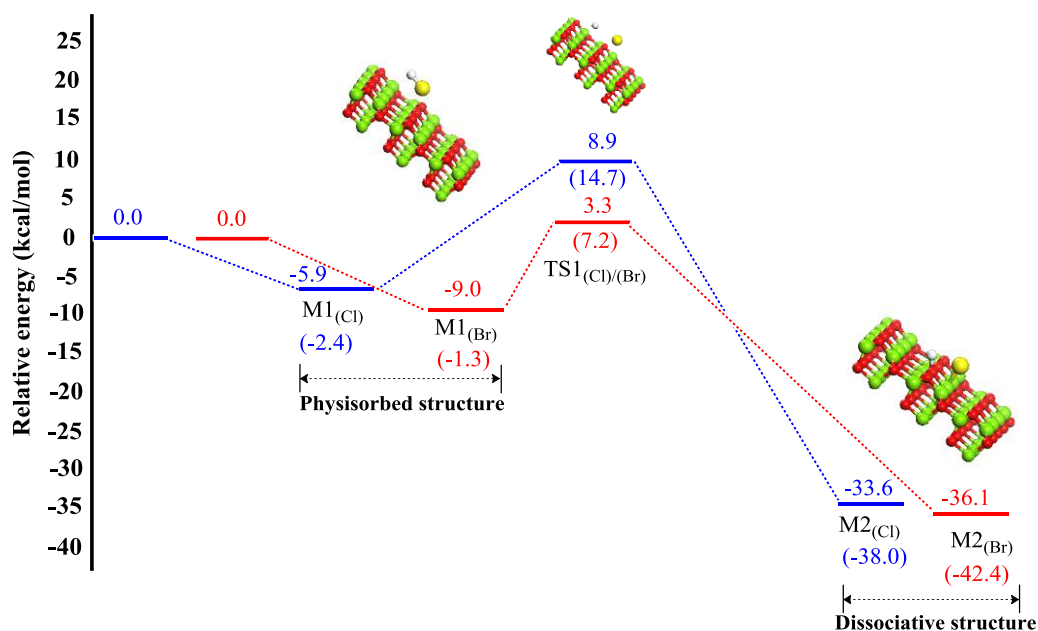
Figure 5.S2. Relative energy profile diagram for the first addition step of HCl (Blue) and HBr (Red) molecules over ZnO (10$\bar{1}$0) surface using a (3 × 3) unit cell. Values in brackets are for (2 × 2) unit cell.
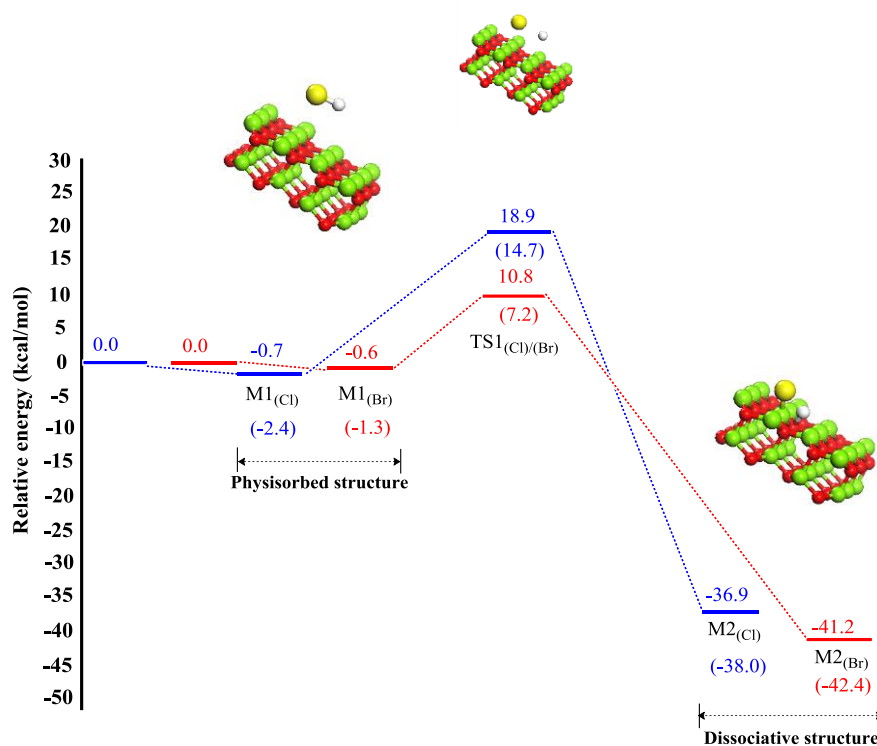
Figure 5.S3. Relative energy profile diagram for the first addition step of HCl (Blue) and HBr (Red) molecules over ZnO $(10\bar{1}0)$ surface using the energy cut-off of 400 eV. Values in brackets are for cut-off of 320 eV.
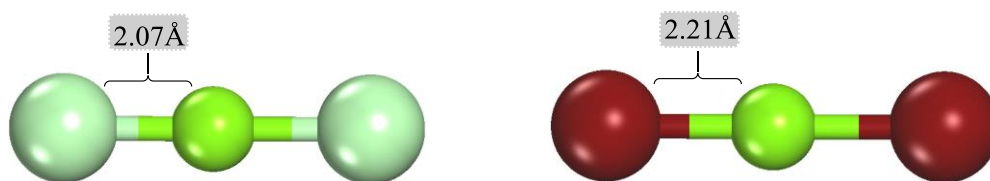
Figure 5.S4. Optimized structures of gaseous $ZnCl_2$ (left) and $ZnBr_2$ (right) molecules.
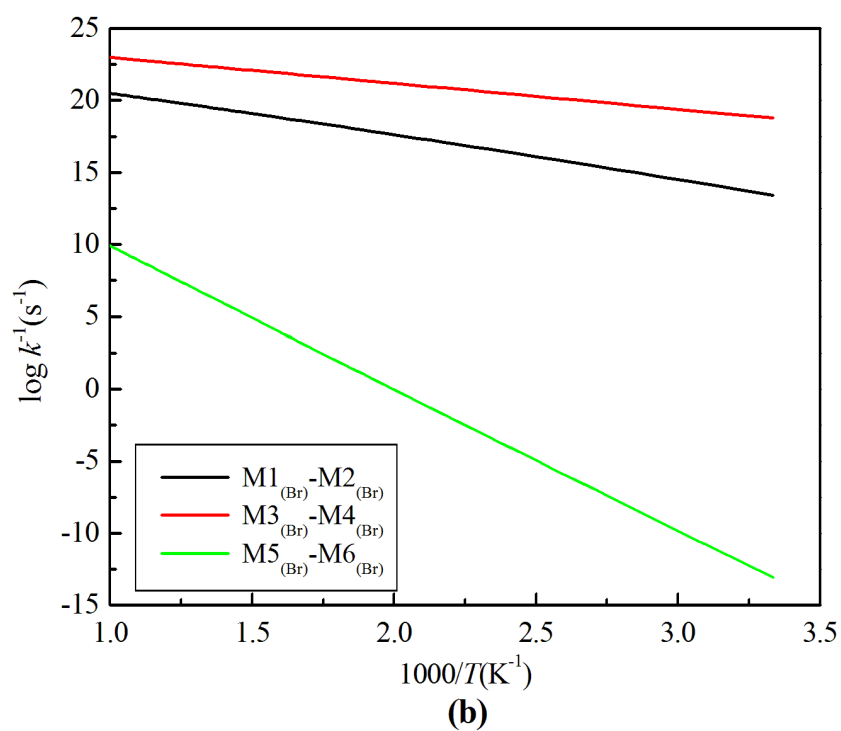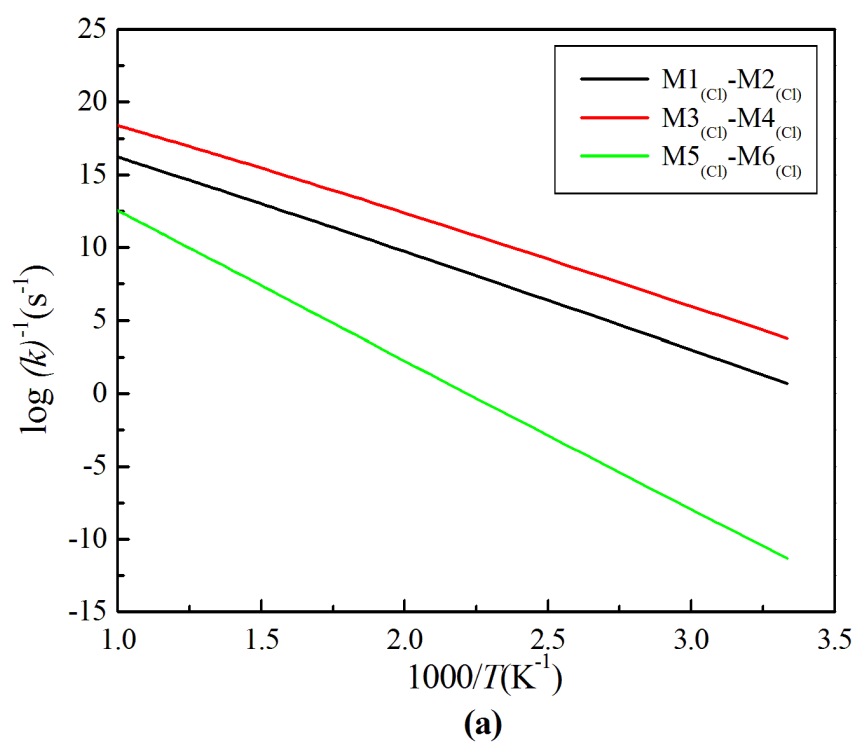
Figure 5.S5. Arrhenius plots for reactions of zincite $(10\bar{1}0)$ surface with HCl molecules (a) and HBr molecules (b).
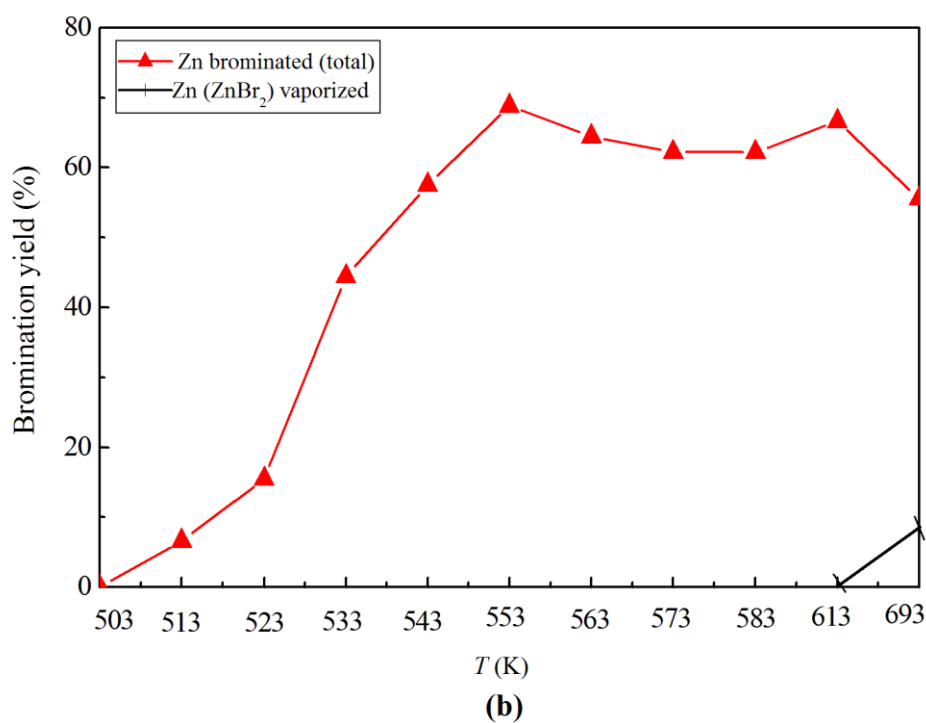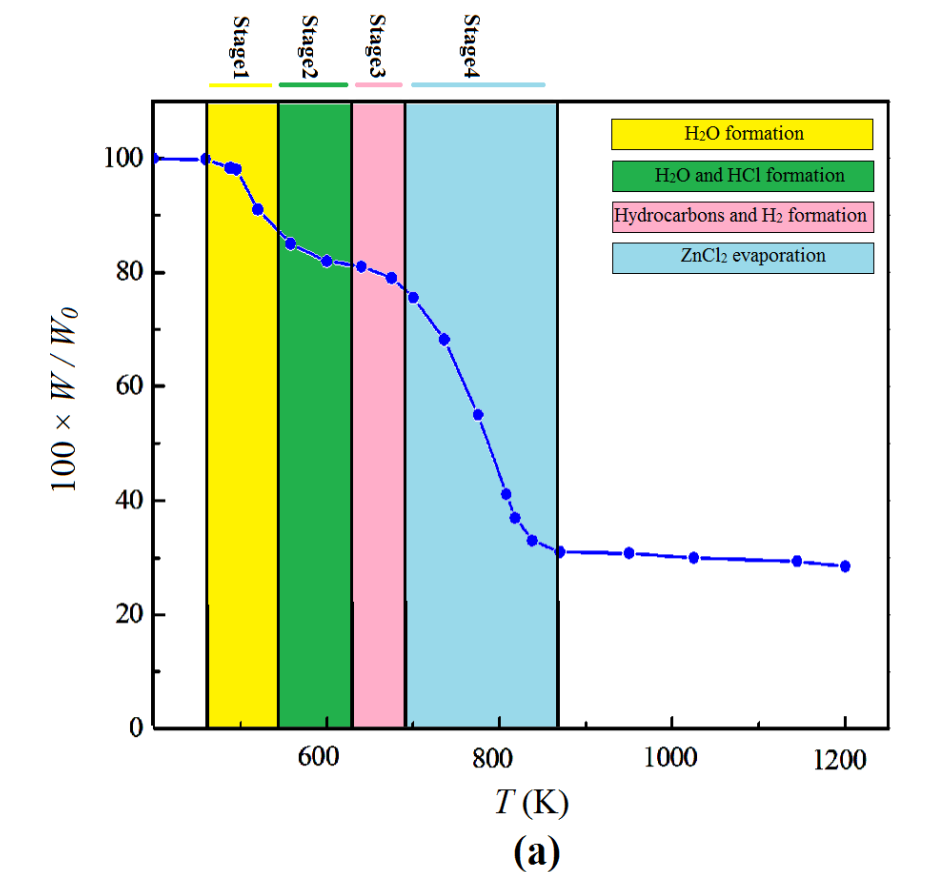
Figure 5.S6. (a) TG-DTG curve of ZnO-PVC mixture, (b) Effect of temperature on effectiveness of zinc bromination released from TBBPA during thermal treatment of ZnO:TBBPA [406, 440].

Appendix B (Chapter 6)

Table 6.S1. Computed and previous experimental and theoretical values of Fe-O interatomic distances. Values are in Å.

Atomic species	Calculated	Theoretical [487]	Experimental [488, 489]
Fe_{oct2}-O	1.986	2.111	2.020
Fe_{tet1}-O	1.846	1.811	1.820
Fe_{oct2}-O	1.973	1.953	1.920
Fe_{tet1}-O	1.842	1.900	1.870

Table 7.S2. Kinetic parameters for the reactions of HCl with the Fe_3O_4(111) surface at a temperature range of 300-1000K.

Species	Reaction	A (s^{-1})	Ea (kcal mol^{-1})
Hydrogen chloride	M1→ M2	10.05×10^{14}	20.9
	M3 → M4	5.22×10^{12}	26.8
	M4 → M5	2.69×10^{12}	12.5
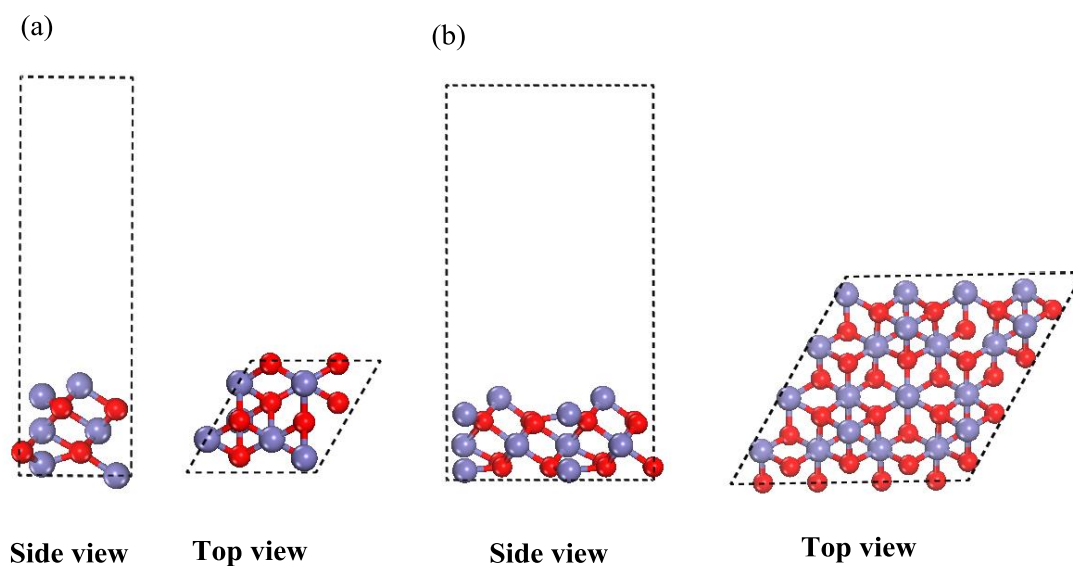
Figure 6.S1. Side and top view of the Fe₃O₄(111) (a) (1×1) unit cell and (b) (2×2) unit cell.
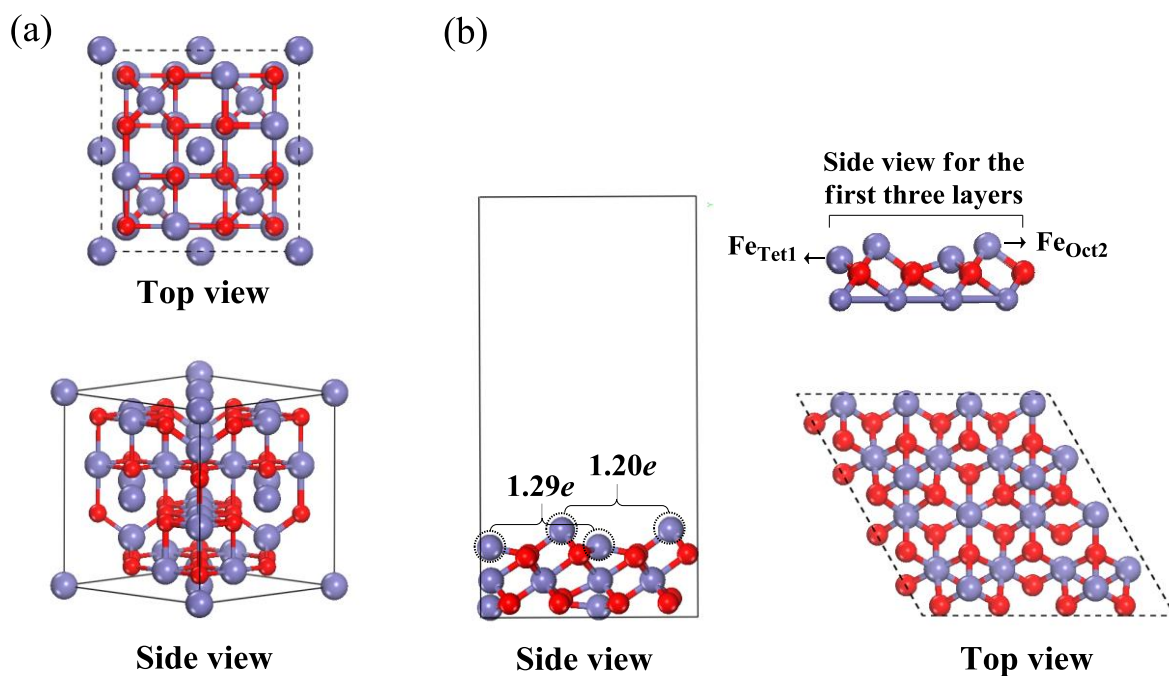
Figure 6.S2. Slab models of (Fe₃O₄) (111) surface. (a) Fe₃O₄ unit cell; (b) side and top views for the Fe₃O₄-111 surface. The blue and red spheres represent iron and oxygen atoms, respectively.

(103.2)

105.3

Hydrogen chloride

(85.0)

84.8

Chloroethane

(87.3)

85.8

2-chloropropane

(89.7)

88.9

1-chloro-1-propene

(92.7)

92.2

Chloroethene
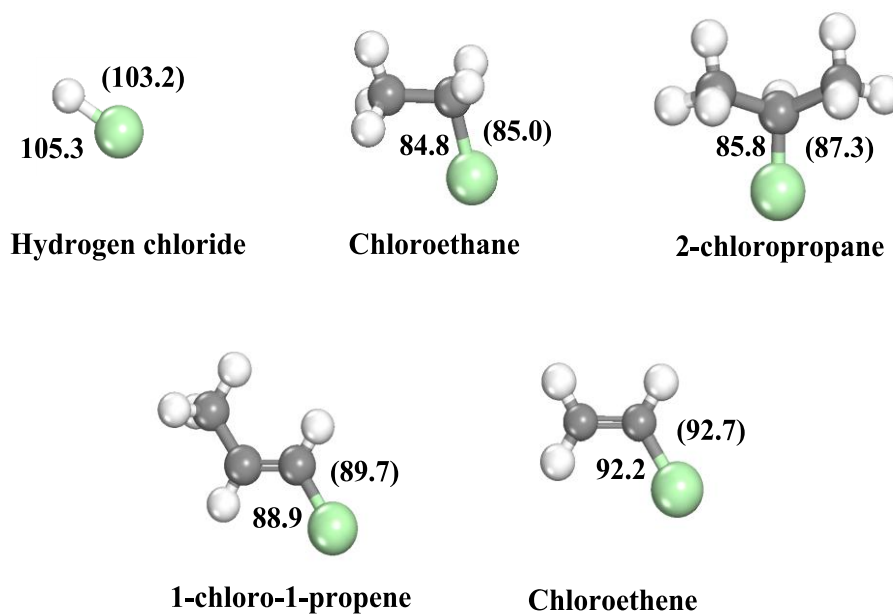
Figure 6.S3. Optimized structures of the selected gaseous molecules. Values represent BDE in kcal mol^{-1}. Values in brackets are for experimental findings [367, 371]. Large green spheres denote chlorine atoms.
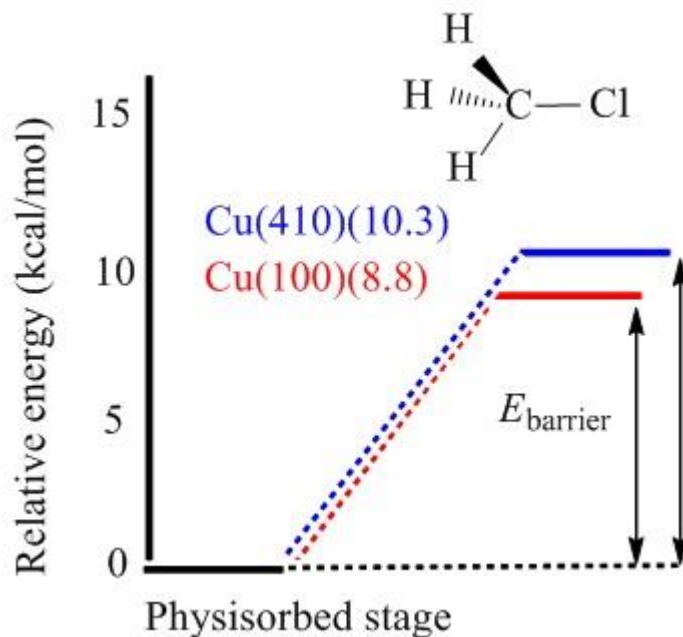
Figure 7.S1. Potential energy surface for the C-Cl bond fissions in Chloromethane over Cu (100) (Red) surface and Cu (410) [595] (Blue). Values are in kcal mol^{-1} with respect to initial state.
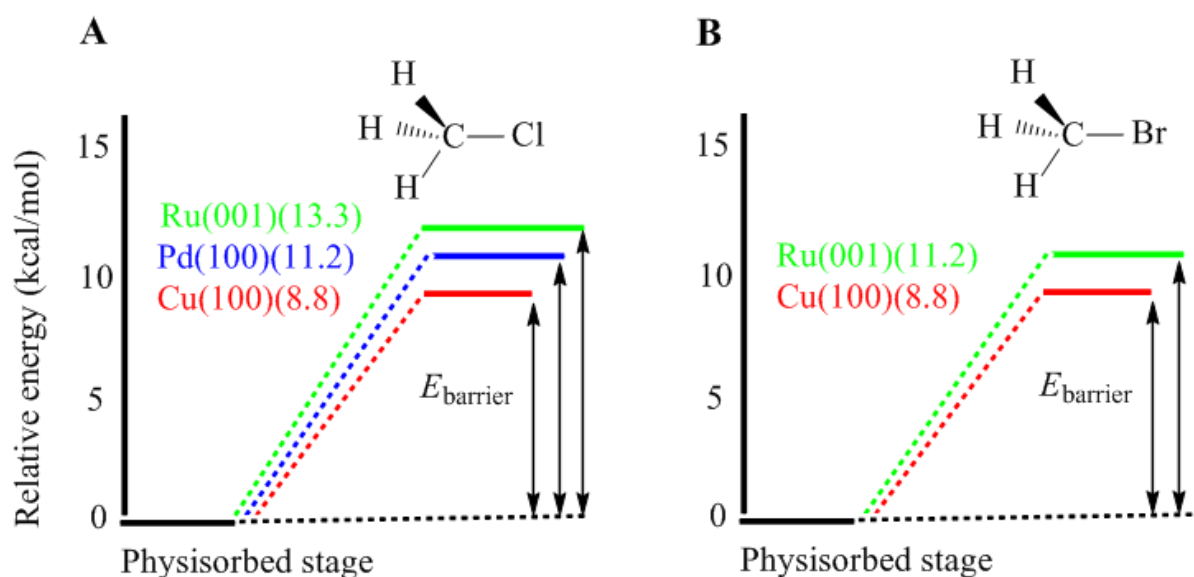
Figure 7.S2. Potential energy surface for the C-Cl/Br bond fissions in (A) Chloromethane over Cu (100), (Red), Ru(001) [596], (Green) and Pd(100) [597] surfaces. (B) Bromomethane over

Cu (100) (Blue) and Ru(001) [598] (Green) surfaces. Values are in kcal mol⁻¹ with respect to initial state.
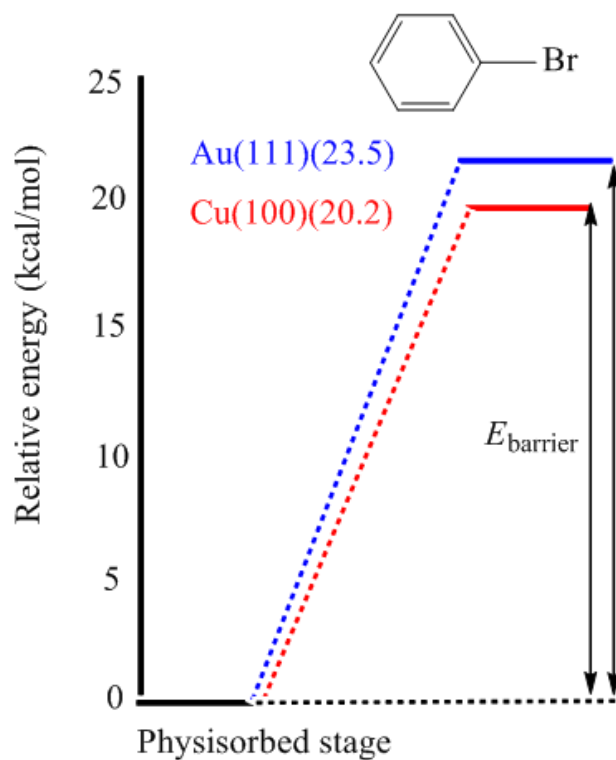
Figure 7.S3. Potential energy surface for the C-Br bond fissions in bromobenzene over Cu (100) (Red) and Au (111) [599] (Blue) surfaces. Values are in kcal mol⁻¹ with respect to initial state.

Appendix D (Future Work)
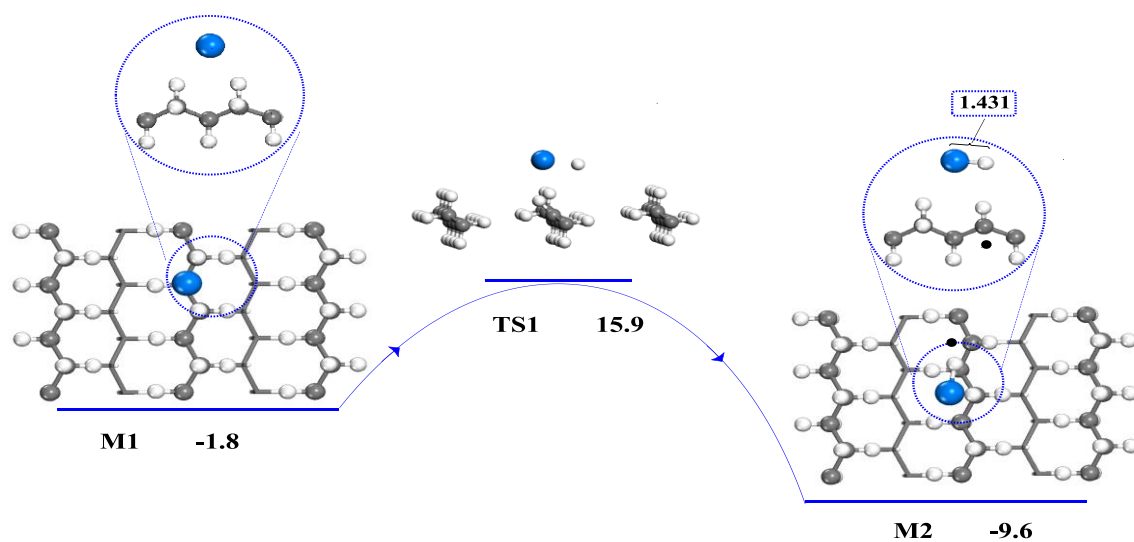
Figure F1. Reaction of bromine atom over a polyethylene (PE) surface. Values are in kcal mol^{-1} with respect to initial state. Large blue spheres denote bromine atoms, grey spheres are carbon, and white spheres denote hydrogen atoms.
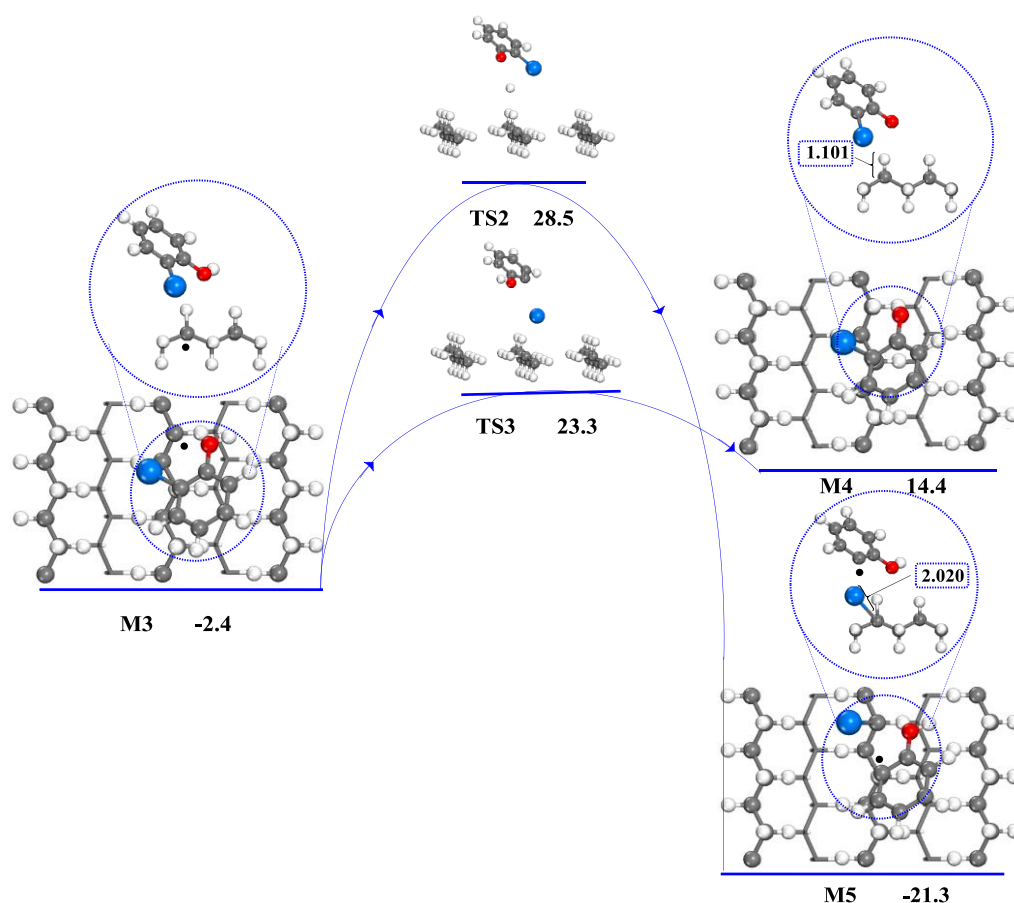
Figure F2. Reaction of a 2-bromophenol molecule with the radical site in polyethylene (PE) surface. Values are in kcal mol^{-1} with respect to initial state. Large blue spheres denote bromine atoms, grey spheres are carbon, white spheres signify hydrogen atoms and red spheres are oxygen atoms,
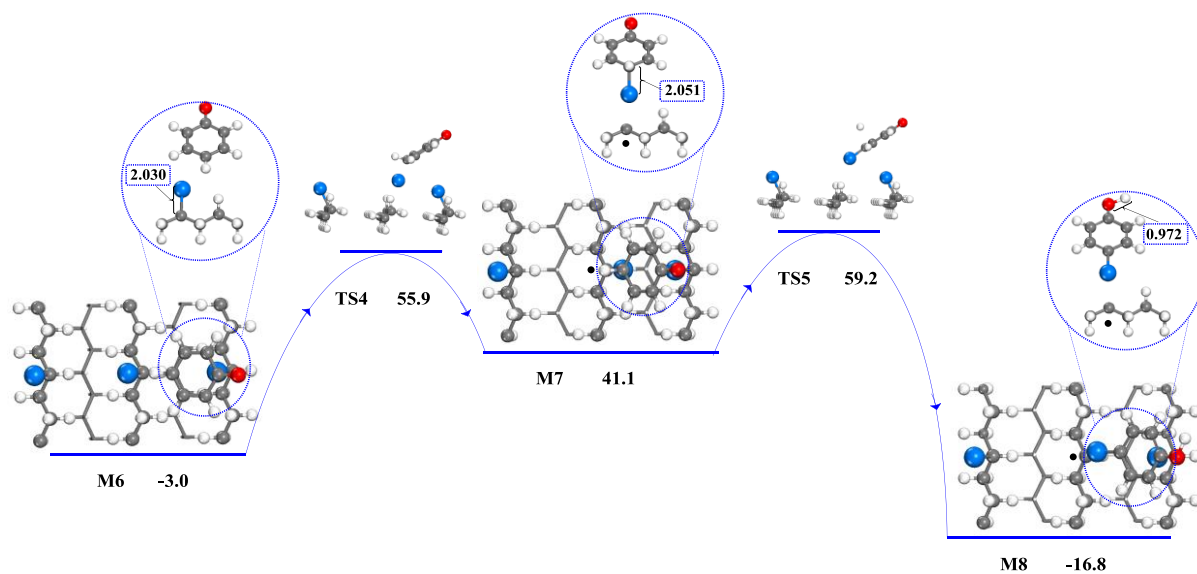
Figure F3. Reaction of phenoxy radical over a brominated polyethylene (Br-PE) surface. Values are in kcal mol⁻¹ with respect to initial state. Large blue spheres denote bromine atoms, grey spheres are carbon, white spheres signify hydrogen atoms and red spheres are oxygen atoms,
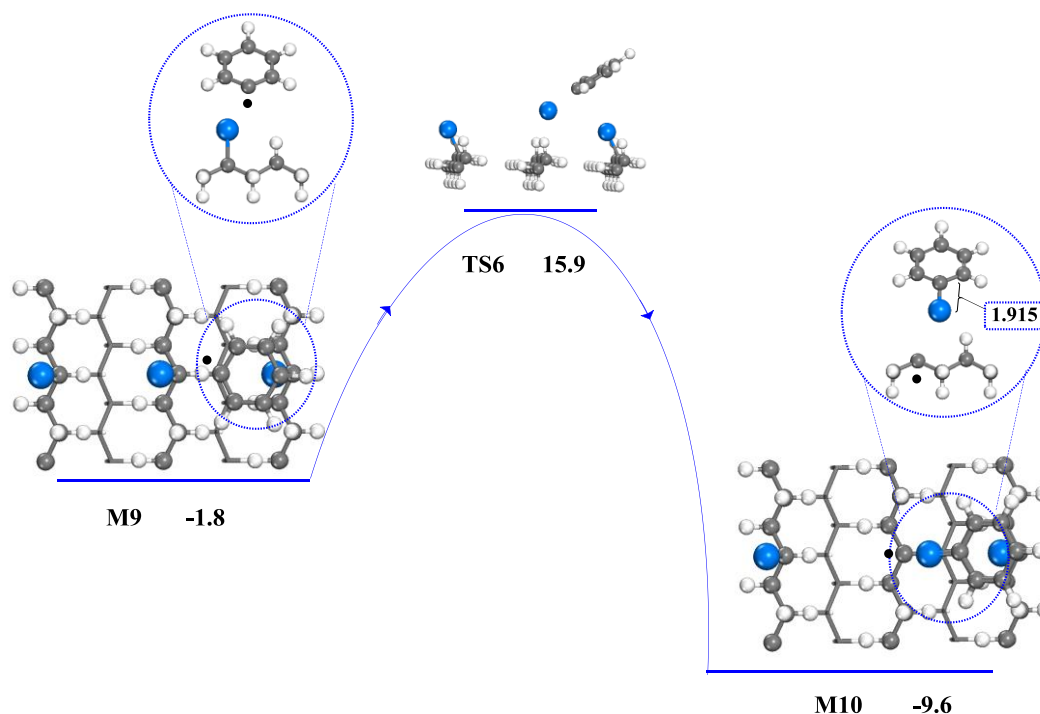
Figure F4. Reaction of phenyl radical over a brominated polyethylene (Br-PE) surface. Values are in kcal mol⁻¹ with respect to initial state. Large blue spheres denote bromine atoms, grey spheres are carbon and white spheres signify hydrogen atoms.
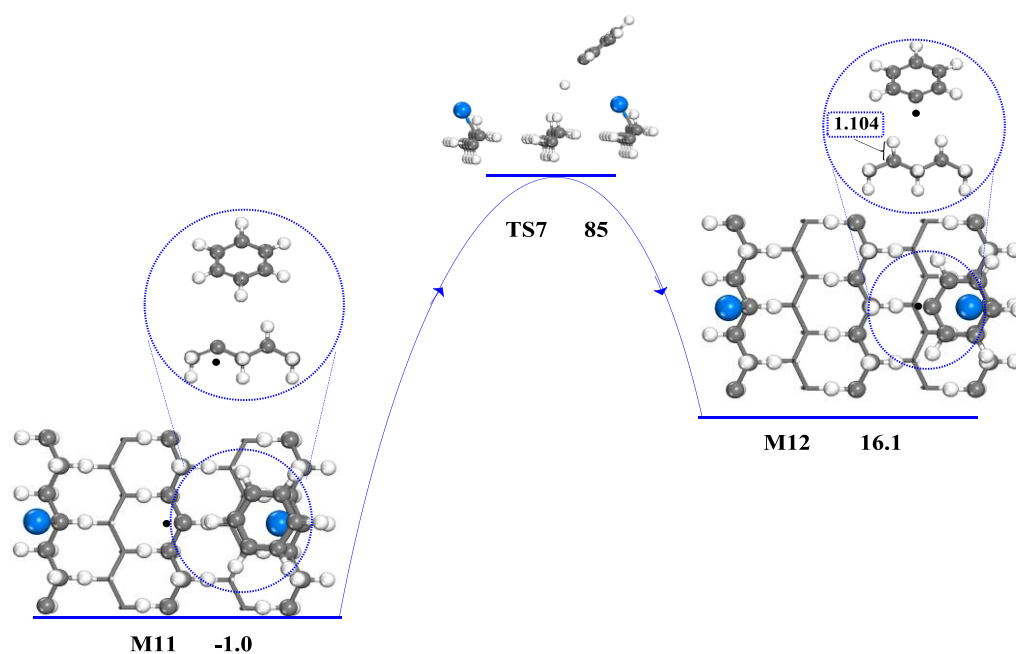
Figure F5. Reaction of benzene molecule with the radical site in polyethylene (PE) surface. Values are in kcal mol^{-1} with respect to initial state. Large blue spheres denote bromine atoms, grey spheres are carbon and white spheres signify hydrogen atoms.
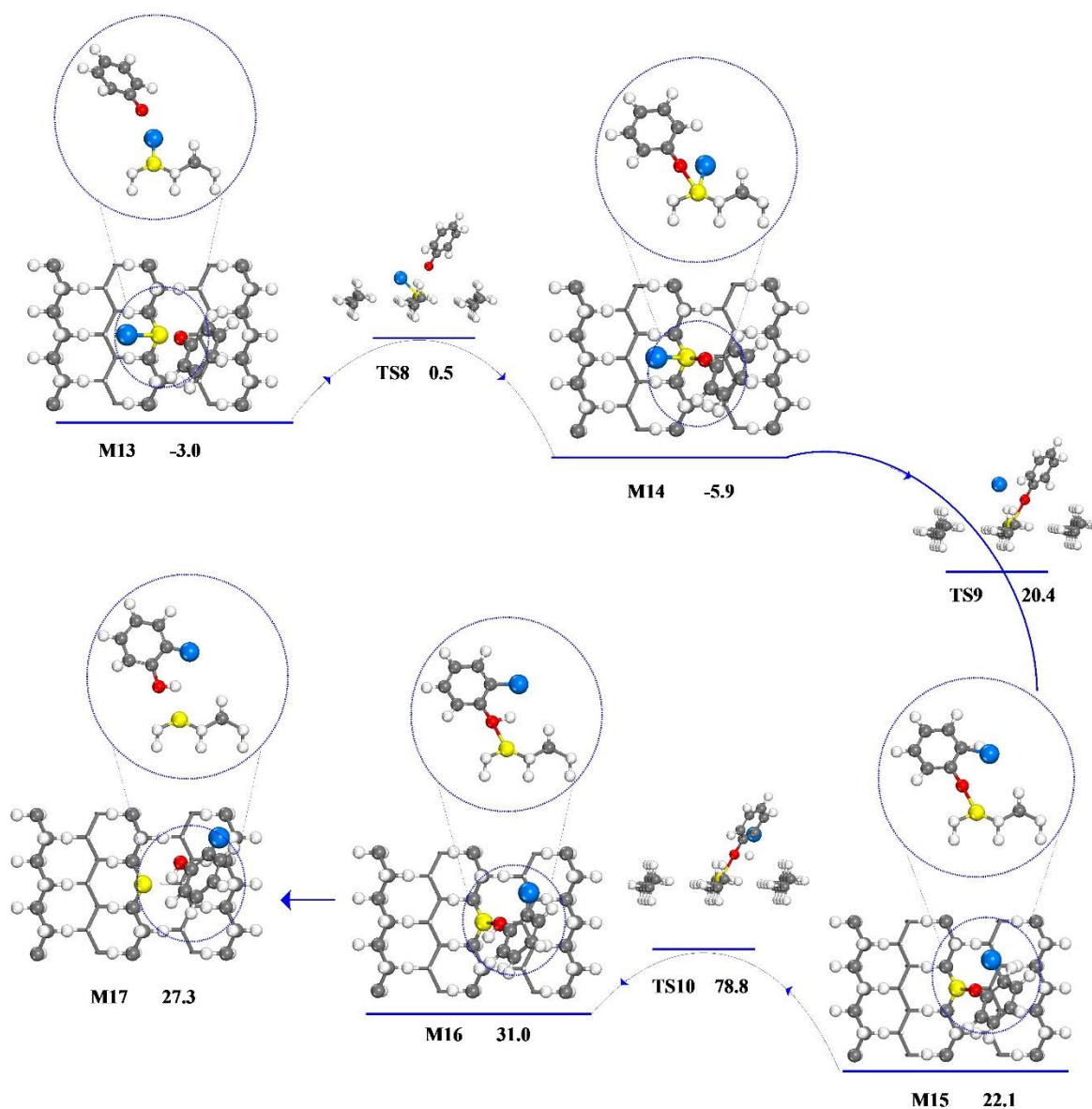
Figure F6. Reaction of a phenoxy radical over a brominated copper polyethylene (Br-CuPE) surface. Values are in kcal mol^{-1} with respect to initial state. Large blue spheres denote bromine atoms, grey spheres are carbon, white spheres signify hydrogen atoms, yellow spheres are copper atoms and red spheres are oxygen atoms.

Table F1: Kinetic parameters fitted in the temperature range of 300-1000 K.

Reaction	A (s^{-1})	E_a (kcal mol^{-1})
M1$\rightarrow$ M2	2.7×10^{17}	18.6
M3$\rightarrow$ M4	9.0×10^{11}	21.9
M3$\rightarrow$ M5	6.0×10^{11}	30.7
M6$\rightarrow$ M7	5.6×10^{10}	56.3
M7$\rightarrow$ M8	1.4×10^{11}	66.4
M9$\rightarrow$ M10	2.1×10^{14}	15.8
M11$\rightarrow$ M12	1.0×10^{11}	92.6

References

[1] L. Zeng, R. Yang, Q. Zhang, H. Zhang, K. Xiao, H. Zhang, Y. Wang, P.K.S. Lam, G. Jiang, Current Levels and Composition Profiles of Emerging Halogenated Flame Retardants and Dehalogenated Products in Sewage Sludge from Municipal Wastewater Treatment Plants in China, Environ. Sci. Technol., 48 (2014) 12586-12594.

[2] A. Salamova, R.A. Hites, Brominated and Chlorinated Flame Retardants in Tree Bark from Around the Globe, Environ. Sci. Technol., 47 (2013) 349-354.

[3] A. Covaci, S. Harrad, M.A.E. Abdallah, N. Ali, R.J. Law, D. Herzke, C.A. de Wit, Novel brominated flame retardants: A review of their analysis, environmental fate and behaviour, Environ. Int., 37 (2011) 532-556.

[4] S. Kumagai, G. Grause, T. Kameda, T. Yoshioka, Simultaneous Recovery of Benzene-Rich Oil and Metals by Steam Pyrolysis of Metal-Poly(ethylene terephthalate) Composite Waste, Environ. Sci. Technol., 48 (2014) 3430-3437.

[5] A. Kumar, M.P. Sharma, GHG emission and carbon sequestration potential from MSW of Indian metro cities, Urban Clim., 8 (2014) 30-41.

[6] J. Yu, L. Sun, C. Ma, Y. Qiao, H. Yao, Thermal degradation of PVC: A review, Waste Manage., 48 (2016) 300-314.

[7] K. Chen, D. Wojtalewicz, M. Altarawneh, J.C. Mackie, E.M. Kennedy, B.Z. Dlugogorski, Formation of polychlorinated dibenzo-p-dioxins and dibenzofurans (PCDD/F) in oxidation of captan pesticide, Proc. Combust. Inst., 33 (2011) 701-708.

[8] S. Birnbaum Linda, F. Staskal Daniele, Brominated flame retardants: cause for concern?, Environ. Health Perspect., 112 (2004) 9-17.

[9] C. Ma, J. Yu, B. Wang, Z. Song, J. Xiang, S. Hu, S. Su, L. Sun, Chemical recycling of brominated flame retarded plastics from e-waste for clean fuels production: A review, Renew. Sustain. Energy Rev., 61 (2016) 433-450.

[10] C. Vasile, M.A. Brebu, T. Karayildirim, J. Yanik, H. Darie, Feedstock recycling from plastics and thermosets fractions of used computers. II. Pyrolysis oil upgrading, Fuel 86 (2007) 477-485.

[11] S.M. Al-Salem, A. Antelava, A. Constantinou, G. Manos, A. Dutta, A review on thermal and catalytic pyrolysis of plastic solid waste (PSW), J. Environ. Manage., 197 (2017) 177-198.

[12] T. Havlík, B.V.e. Souza, A.M. Bernardes, I.A.H. Schneider, A. Miškufová, Hydrometallurgical processing of carbon steel EAF dust, J. Hazard. Mater., 135 (2006) 311-318.

[13] J.A. de Araújo, V. Schalch, Recycling of electric arc furnace (EAF) dust for use in steel making process, J. Mater. Res. Technol., 3 (2014) 274-279.

[14] I. van der Veen, J. de Boer, Phosphorus flame retardants: Properties, production, environmental occurrence, toxicity and analysis, Chemosphere 88 (2012) 1119-1153.

[15] H. Hakk, R.J. Letcher, Metabolism in the toxicokinetics and fate of brominated flame retardants-a review, Environ. Int., 29 (2003) 801-828.

[16] E. Boyles, H. Tan, Y. Wu, C.K. Nielsen, L. Shen, E.J. Reiner, D. Chen, Halogenated flame retardants in bobcats from the midwestern United States, Environ. Pollut., 221 (2017) 191-198.

[17] M. Alaee, P. Arias, A. Sjödin, Å. Bergman, An overview of commercially used brominated flame retardants, their applications, their use patterns in different countries/regions and possible modes of release, Environ. Int., 29 (2003) 683-689.

[18] M. Venier, Y. Ma, R.A. Hites, Bromobenzene Flame Retardants in the Great Lakes Atmosphere, Environ. Sci. Technol., 46 (2012) 8653-8660.

[19] C.A. de Wit, D. Herzke, K. Vorkamp, Brominated flame retardants in the Arctic environment-trends and new candidates, Sci. Total Environ., 408 (2010) 2885-2918.

[20] A. Sjödin, H.a. Carlsson, K. Thuresson, S. Sjölin, Å. Bergman, C. Östman, Flame Retardants in Indoor Air at an Electronics Recycling Plant and at Other Work Environments, Environ. Sci. Technol., 35 (2001) 448-454.

[21] C.A. de Wit, An overview of brominated flame retardants in the environment, Chemosphere 46 (2002) 583-624.

[22] J. Ebert, M. Bahadir, Formation of PBDD/F from flame-retarded plastic materials under thermal stress, Environ. Int., 29 (2003) 711-716.

[23] I. Watanabe, S.-i. Sakai, Environmental release and behavior of brominated flame retardants, Environ. Int., 29 (2003) 665-682.

[24] J. Guo, J. Guo, Z. Xu, Recycling of non-metallic fractions from waste printed circuit boards: A review, J. Hazard. Mater., 168 (2009) 567-590.

[25] C. Thomsen, E. Lundanes, G. Becher, Brominated flame retardants in plasma samples from three different occupational groups in Norway, J. Environ. Monit., 3 (2001) 366-370.

[26] M. Altarawneh, D. Carrizo, A. Ziolkowski, E.M. Kennedy, B.Z. Dlugogorski, J.C. Mackie, Pyrolysis of permethrin and formation of precursors of polychlorinated dibenzo-p-dioxins and dibenzofurans (PCDD/F) under non-oxidative conditions, Chemosphere 74 (2009) 1435-1443.

[27] Q. Bu, D. Wu, J. Xia, M. Wu, X. Liu, Z. Cao, G. Yu, Polybrominated diphenyl ethers and novel brominated flame retardants in indoor dust of different microenvironments in Beijing, China, Environ. Int., 122 (2019) 159-167.

[28] G. Yu, Q. Bu, Z. Cao, X. Du, J. Xia, M. Wu, J. Huang, Brominated flame retardants (BFRs): A review on environmental contamination in China, Chemosphere 150 (2016) 479-490.

[29] F. Pinto, P. Costa, I. Gulyurtlu, I. Cabrita, Pyrolysis of plastic wastes. 1. Effect of plastic waste composition on product yield, J. Anal. Appl. Pyrolysis, 51 (1999) 39-55.

[30] U. Lee, J. Han, M. Wang, Evaluation of landfill gas emissions from municipal solid waste landfills for the life-cycle analysis of waste-to-energy pathways, J. Cleaner Prod., 166 (2017) 335-342.

[31] W.R. Lea, Plastic incineration versus recycling: a comparison of energy and landfill cost savings, J. Hazard. Mater., 47 (1996) 295-302.

[32] R. Verma, K.S. Vinoda, M. Papireddy, A.N.S. Gowda, Toxic Pollutants from Plastic Waste- A Review, Procedia Environ. Sci., 35 (2016) 701-708.

[33] A. Nizami, M. Rehan, O.K. Ouda, K. Shahzad, Y. Sadef, T. Iqbal, I.M. Ismail, An argument for developing waste-to-energy technologies in Saudi Arabia, Chem. Eng. Transact., 45 (2015) 337-342.

[34] P. Costi, R. Minciardi, M. Robba, M. Rovatti, R. Sacile, An environmentally sustainable decision model for urban solid waste management, Waste Manage., 24 (2004) 277-295.

[35] R. Miandad, M. Rehan, A.-S. Nizami, M.A. El-Fetouh Barakat, I.M. Ismail, The Energy and Value-Added Products from Pyrolysis of Waste Plastics, in: O.P. Karthikeyan, K. Heimann, S.S. Muthu (Eds.) Recycling of Solid Waste for Biofuels and Bio-chemicals, Springer Singapore, Singapore, 2016, pp. 333-355.

[36] G. Grause, A. Buekens, Y. Sakata, A. Okuwaki, T. Yoshioka, Feedstock recycling of waste polymeric material, Journal of Material Cycles and Waste Manage. 13 (2011) 265-282.

[37] M. Syamsiro, H. Saptoadi, T. Norsujianto, P. Noviasri, S. Cheng, Z. Alimuddin, K. Yoshikawa, Fuel Oil Production from Municipal Plastic Wastes in Sequential Pyrolysis and Catalytic Reforming Reactors, Energy Procedia, 47 (2014) 180-188.

[38] J. Korpas, V. Slovák, K. Wichterle, Capture of hydrogen chloride by copyrolysis of polyvinyl chloride waste materials with steelmaking dust.

[39] O. Terakado, Y. Takahahsi, M. Hirasawa, Influence of metal oxide on the fixation of chlorine in thermal decomposition of poly (vinylidene chloride co vinyl chloride), igh Temp. Mater. Processes, 28 (2009) 133-140.

[40] P.J.W.K.d. Buzin, N.C. Heck, A.C.F. Vilela, EAF dust: An overview on the influences of physical, chemical and mineral features in its recycling and waste incorporation routes, J. Mater. Res. Technol., 6 (2017) 194-202.

[41] B. Gui, Y. Qiao, D. Wan, S. Liu, Z. Han, H. Yao, M. Xu, Nascent tar formation during polyvinylchloride (PVC) pyrolysis, Proc. Combust. Inst., 34 (2013) 2321-2329.

[42] T. Sofilić, A. Rastovčan-Mioč, Š. Cerjan-Stefanović, V. Novosel-Radović, M. Jenko, Characterization of steel mill electric-arc furnace dust, J. Hazard.Mater.,109 (2004) 59-70.

[43] C.M.F. Vieira, R. Sanchez, S.N. Monteiro, N. Lalla, N. Quaranta, Recycling of electric arc furnace dust into red ceramic, J. Mater. Res. Technol., 2 (2013) 88-92.

[44] A.-G. Guézennec, J.-C. Huber, F. Patisson, P. Sessiecq, J.-P. Birat, D. Ablitzer, Dust formation in Electric Arc Furnace: Birth of the particles, Powder Technol., 157 (2005) 2-11.

[45] B. Cubukcuoglu, S. Ouki, The use of alternative constituents in cement-based solidification/stabilization of electric arc furnace dust, Proceedings of the 7th international conference on sustainable management of waste and recycled materials in construction, WASCON Lyon, 2009, pp. 3-5.

[46] A.C. Bayraktar, E. Avşar, İ. Toröz, K. Alp, A. Hanedar, Stabilization and solidification of electric arc furnace dust originating from steel industry by using low grade MgO, Arch. Environ. Prot., 41 (2015) 62-66.

[47] M.A. Alsheyab, SEM analysis on electron arc furnace dust (EAFD) and EAFD-asphalt mixture, Environ. Nat. Resour. Res., 3 (2013) 147.

[48] R.A. Janjua, Optimisation of electric arc furnace dust recycling and zinc recovery by scrap de-zincing, (2008).

[49] P.E. Tsakiridis, P. Oustadakis, A. Katsiapi, S. Agatzini-Leonardou, Hydrometallurgical process for zinc recovery from electric arc furnace dust (EAFD). Part II: Downstream processing and zinc recovery by electrowinning, J. Hazard. Mater., 179 (2010) 8-14.

[50] N. Leclerc, E. Meux, J.-M. Lecuire, Hydrometallurgical recovery of zinc and lead from electric arc furnace dust using mononitrilotriacetate anion and hexahydrated ferric chloride, J. Hazard. Mater., 91 (2002) 257-270.

[51] S. Polsilapa, P. Wangyao, Glassification of electric arc furnace dust by using fly ash or bagasse ash, J. Met. Mater. Miner., 17 (2017).

[52] P. Popielska-Ostrowska, J. Siwka, A. Sorek, M. Niesler, Dust arising during steelmaking processes, J. Achiev. Mater. Manuf. Eng., 55 (2012) 772-776.

[53] C. Delhaes, A. Hauck, D. Neuschütz, Mechanisms of dust generation in a stainless steelmaking converter, Steel Res., 64 (1993) 22-27.

[54] Gu, eacute, A.G. zennec, J.C. Huber, F. Patisson, P. Sessiecq, J.P. Birat, D. Ablitzer, Dust Formation by Bubble-burst Phenomenon at the Surface of a Liquid Steel Bath, ISIJ Int., 44 (2004) 1328-1333.

[55] C. Rizescu, Z. Bacinschi, E. Stoian, A. Polinescu, Characterisation of steel mill electric-arc furnace dust, Adv. waste manage., (2010).

[56] J. Zhang, J.J.J. Chen, N. Zhou, Characteristics of jet droplet produced by bubble bursting on the free liquid surface, Chem. Eng. Sci., 68 (2012) 151-156.

[57] Z. Han, L. Holappa, Bubble bursting phenomenon in Gas/Metal/Slag systems, Metall. Mater. Trans. B, 34 (2003) 525-532.

[58] C. Sikalidis, Mitrakas, and Tsitouridou,Immobilization of electric arc furnace dust toxic elements within the matrix of concrete based products, Glob. NEST J. 12 (2010) 373-378.

[59] M. Al-Harahsheh, A. Al-Otoom, L. Al-Makhadmah, I.E. Hamilton, S. Kingman, S. Al-Asheh, M. Hararah, Pyrolysis of poly(vinyl chloride) and-electric arc furnacedust mixtures, J. Hazard. Mater., 299 (2015) 425-436.

[60] A.K. Biswas, Principles of Blast Furnace Ironmaking, Theory and Practice, Steel Times 211.

[61] C.A. Pickles, Thermodynamic analysis of the selective chlorination of electric arc furnace dust, J. Hazard. Mater., 166 (2009) 1030-1042.

[62] D.K. Xia, C.A. Picklesi, Microwave caustic leaching of electric arc furnace dust, Min. Eng., 13 (2000) 79-94.

[63] S. Sukonthanit, Zinc metal recovery from electric arc furnace dust, Chulalongkorn University1998.

[64] E.A. Domínguez, R. Ullman, 'Ecological bricks' made with clays and steel dust pollutants, Appl. Clay Sci., 11 (1996) 237-249.

[65] D.K. Xia, C.A. Pickles, Caustic roasting and leaching of electric arc furnace dust, Can. Metall. Q., 38 (1999) 175-186.

[66] N.W. Assaf, M. Altarawneh, I. Oluwoye, M. Radny, S.M. Lomnicki, B.Z. Dlugogorski, Formation of Environmentally Persistent Free Radicals on α-Al$_2$O$_3$, Environ. Sci. Technol., 50 (2016) 11094-11102.

[67] N. Tsubouchi, H. Hashimoto, N. Ohtaka, Y. Ohtsuka, Chemical characterization of dust particles recovered from bag filters of electric arc furnaces for steelmaking: Some factors influencing the formation of hexachlorobenzene, J. Hazard. Mater., 183 (2010) 116-124.

[68] P. Oustadakis, P.E. Tsakiridis, A. Katsiapi, S. Agatzini-Leonardou, Hydrometallurgical process for zinc recovery from electric arc furnace dust (EAFD): Part I: Characterization and leaching by diluted sulphuric acid, J. Hazard. Mater., 179 (2010) 1-7.

[69] M.B. Chang, H.C. Huang, S.S. Tsai, K.H. Chi, G.P. Chang-Chien, Evaluation of the emission characteristics of PCDD/Fs from electric arc furnaces, Chemosphere, 62 (2006) 1761-1773.

[70] T. Wang, D.R. Anderson, D. Thompson, M. Clench, R. Fisher, Studies into the formation of dioxins in the sintering process used in the iron and steel industry. 1. Characterisation of isomer profiles in particulate and gaseous emissions, Chemosphere, 51 (2003) 585-594.

[71] S. Figueira, J. Gomes, Emissions of dioxin and dibenzofuran from electric arc furnaces, Rev. Metal., 41 (2005) 164-168.

[72] T. Öberg, T. Öhrström, J. Bergström, Metal catalyzed formation of chlorinated aromatic compounds: A study of the correlation pattern in incinerator fly ash, Chemosphere, 67 (2007) S185-S190.

[73] T. Murakami, M. Shimura, E. Kasai, Formation of Hexachlorobenzene from Dusts of an Electric Arc Furnace Used in Steelmaking: Effect of Temperature and Dust Composition, Environ. Sci. Technol., 42 (2008) 7459-7463.

[74] S. Kuzuhara, H. Sato, N. Tsubouchi, Y. Ohtsuka, E. Kasai, Effect of Nitrogen-Containing Compounds on Polychlorinated Dibenzo-p-dioxin/Dibenzofuran Formation through de Novo Synthesis, Environ. Sci. Technol., 39 (2005) 795-799.

[75] M. Al-Harahsheh, J. Al-Nu'airat, A. Al-Otoom, H. Al-jabali, M. Al-zoubi, Treatments of electric arc furnace dust and halogenated plastic wastes: A review, Cement and Concrete Res., 7 (2019) 102856.

[76] T. Lis, K. Nowacki, Determination of physical and chemical properties of electric arc furnace dusts for the purposes of their utilization, Ste. Res. Intern., 83 (2012) 842-851.

[77] P.J.W.K. de Buzin, N.C. Heck, A.C.F. Vilela, EAF dust: An overview on the influences of physical, chemical and mineral features in its recycling and waste incorporation routes, J. Mate. Res. Technol., 6 (2017) 194-202.

[78] C. Lanzerstorfer, Electric arc furnace (EAF) dust: Application of air classification for improved zinc enrichment in in-plant recycling, J. Clean. Prod., 174 (2018) 1-6.

[79] G. AG, H. JC, F. Patisson, P. Sessiecq, B. JP, D. Ablitzer, Dust formation by bubble-burst phenomenon at the surface of a liquid steel bath, ISIJ Intern., 44 (2004) 1328-1333.

[80] M.C. Arnold, A.S. de Vargas, L. Bianchini, Study of electric-arc furnace dust (EAFD) in fly ash and rice husk ash-based geopolymers, Adva. Pow. Technol., 28 (2017) 2023-2034.

[81] C. Barreneche, A.I. Fernández, M. Niubó, J.M. Chimenos, F. Espiell, M. Segarra, C. Solé, L.F. Cabeza, Development and characterization of new shape-stabilized phase change material (PCM-Polymer including electrical arc furnace dust (EAFD), for acoustic and thermal comfort in buildings, Energy Build., 61 (2013) 210-214.

[82] M. Niubó, A. Fernández, J. Chimenos, L. Haurie, A possible recycling method for high grade steels EAFD in polymer composites, J. Hazard. Mater., 171 (2009) 1139-1144.

[83] M. Al-Harahsheh, M. Aljarrah, F. Rummanah, K. Abdel-Latif, S. Kingman, Leaching of valuable metals from electric arc furnace dust-tetrabromobisphenol A pyrolysis residues, J. Analy. Appl. Pyrolysis, 125 (2017) 50-60.

[84] G. Laforest, J. Duchesne, Stabilization of electric arc furnace dust by the use of cementitious materials: Ionic competition and long-term leachability, Cement and Concrete Res., 36 (2006) 1628-1634.

[85] A.J.B. Dutra, P.R.P. Paiva, L.M. Tavares, Alkaline leaching of zinc from electric arc furnace steel dust, Min. Eng., 19 (2006) 478-485.

[86] M.-t. Tang, J. Peng, B. Peng, D. Yu, C.-b. Tang, Thermal solidification of stainless steelmaking dust, T. Nonferr. Metal. Soc., 18 (2008) 202-206.

[87] Z. Youcai, R. Stanforth, Integrated hydrometallurgical process for production of zinc from electric arc furnace dust in alkaline medium, J. Hazard. Mater., 80 (2000) 223-240.

[88] F. Kukurugya, T. Havlik, Characterization of fine-grained wastes generated during carbon steel and stainless steel production, (2013).

[89] C. Caravaca, A. Cobo, F.J. Alguacil, Considerations about the recycling of EAF flue dusts as source for the recovery of valuable metals by hydrometallurgical processes, Resou. Cons. Recycl., 10 (1994) 35-41.

[90] G. Ma, A.M. Garbers-Craig, Stabilisation of Cr(VI) in stainless steel plant dust through sintering using silica-rich clay, J. Hazard. Mater., 169 (2009) 210-216.

[91] C. Sikalidis, M. Mitrakas, R. Tsitouridou, Immobilization of electric arc furnace dust toxic elements within the matrix of concrete based products, Global NEST J., 12 (2010) 368-373.

[92] S. Wannakamb, S. Manuskijsamrun, W. Buggakupta, The use of electric arc furnace dust from steel recycling in ceramic glaze, J. Sci. Technol., 20 (2013) 329-337.

[93] F. Pinakidou, E.C. Paloura, X-ray absorption spectroscopies: A novel tool for the nanostructural characterization of stabilized industrial waste, J. Alloys Compd., 483 (2009) 670-675.

[94] R.L. Nyirenda, The processing of steelmaking flue-dust: A review, Min. Eng., 4 (1991) 1003-1025.

[95] D. Zunkel, What to do with your EAF dust, Steel Times Int., 20 (1996) 46.

[96] M.C. Mantovani, C. Takano, P.M. Büchler, EAF and secondary dust characterisation, Ironmak. Steelmak., 31 (2004) 325-332.

[97] J.R. Donald, C.A. Pickles, A Kinetic study of the reaction of zinc oxide with iron powder, Metall. Mater. Trans. B, 27 (1996) 363-374.

[98] M. Černík, A. Mašlejová, L. Hrabčáková, X–ray diffraction analysis of sludge and dust produced in steelworks, Acta Metall. Slov., 19 (2013) 206-211.

[99] P.J. Nolasco-Sobrinho, D.C.R. Espinosa, J.A.S. Tenório, Characterisation of dusts and sludges generated during stainless steel production in Brazilian industries, Ironmak. Steelmak., 30 (2003) 11-17.

[100] H. Matsuura, T. Hamano, F. Tsukihashi, Removal of Zn and Pb from Fe2O3 & ZnFe2O4 & ZnO & PbO Mixture by Selective Chlorination and Evaporation Reactions, ISIJ Int., 46 (2006) 1113-1119.

[101] M. Al-harahsheh, S. Kingman, L. Al-Makhadmah, I.E. Hamilton, Microwave treatment of electric arc furnace dust with PVC: Dielectric characterization and pyrolysis-leaching, J. Hazard. Mater., 274 (2014) 87-97.

[102] C.A. Pickles, Reaction of electric arc furnace dust with molten iron containing carbon, Min. Process. Extract. Metall., 112 (2003) 81-89.

[103] N. Menad, J.N. Ayala, F. Garcia-Carcedo, E. Ruiz-Ayúcar, A. Hernández, Study of the presence of fluorine in the recycled fractions during carbothermal treatment of EAF dust, Waste Manage., 23 (2003) 483-491.

[104] M.K. Jha, V. Kumar, R.J. Singh, Review of hydrometallurgical recovery of zinc from industrial wastes, Resources, Conserv. Recycl., 33 (2001) 1-22.

[105] G. Orhan, Leaching and cementation of heavy metals from electric arc furnace dust in alkaline medium, Hydrometallurgy, 78 (2005) 236-245.

[106] J.G.M.S. Machado, F.A. Brehm, C.A.M. Moraes, C.A.d. Santos, A.C.F. Vilela, J.B.M.d. Cunha, Chemical, physical, structural and morphological characterization of the electric arc furnace dust, J. Hazard. Mater., 136 (2006) 953-960.

[107] G. Ma, A.M. Garbers-Craig, Cr(VI) containing electric furnace dusts and filter cake from a stainless steel waste treatment plant: Part 1 – Characteristics and microstructure, Ironmak. Steelmak., 33 (2006) 229-237.

[108] H. Shen, E. Forssberg, U. Nordström, Physicochemical and mineralogical properties of stainless steel slags oriented to metal recovery, Resources, Conserv. Recycl., 40 (2004) 245-271.

[109] G. Ma, A.M. Garbers-Craig, A review on the characteristics, formation mechanisms and treatment processes of Cr (VI)-containing pyrometallurgical wastes, J. South. Afr. Inst. Min. Metall., 106 (2006) 753-763.

[110] M. Morcali, O. Yucel, A. Aydin, B. Derin, Carbothermic reduction of electric arc furnace dust and calcination of waelz oxide by semi-pilot scale rotary furnace, J. Min. Metall. B: Metall., 48 (2012) 173-184.

[111] J. Liu, Y. Su, J. Peng, X. Zhao, Y. Zhang, Y. Dong, Z. Jiang, Preparation and Performance of Antifouling PVC/CPVC Blend Ultrafiltration Membranes, IIndust. Eng. Chem. Res., 51 (2012) 8308-8314.

[112] D. Garcia, R. Balart, J.E. Crespo, J. Lopez, Mechanical properties of recycled PVC blends with styrenic polymers, J. Appl. Polym. Sci., 101 (2006) 2464-2471.

[113] S. Ulutan, A recycling assessment of PVC bottles by means of heat impact evaluation on its reprocessing, J. Appl. Polym. Sci., 69 (1998) 865-869.

[114] H. Stichnothe, A. Azapagic, Life cycle assessment of recycling PVC window frames, Resources, Conserv. Recycl., 71 (2013) 40-47.

[115] P. Plus, Everything about PVC from manufacturing to recycling.

[116] A. Lopez-Urionabarrenechea, I. de Marco, B.M. Caballero, M.F. Laresgoiti, A. Adrados, Catalytic stepwise pyrolysis of packaging plastic waste, J. Anal. Appl. Pyrol., 96 (2012) 54-62.

[117] W.H. Starnes, Structural and mechanistic aspects of the thermal degradation of poly(vinyl chloride), Prog. Polym. Sci., 27 (2002) 2133-2170.

[118] N. Yarahmadi, I. Jakubowicz, L. Martinsson, PVC floorings as post-consumer products for mechanical recycling and energy recovery, Polym. Degrad. Stabil., 79 (2003) 439-448.

[119] J. Leadbitter, PVC and sustainability, Prog. Polym. Sci., 27 (2002) 2197-2226.

[120] I. Janajreh, M. Alshrah, S. Zamzam, Mechanical recycling of PVC plastic waste streams from cable industry: A case study, Sustain. Cities Soc., 18 (2015) 13-20.

[121] A.C. Shah, D.J. Poledna, Review of specialty PVC resins, J. Vinyl Addit. Technol., 8 (2002) 214-221.

[122] M. Sadat-Shojai, G.-R. Bakhshandeh, Recycling of PVC wastes, Polym. Degrad. Stabil., 96 (2011) 404-415.

[123] R. Lin, A.P. Amrute, J. Pérez-Ramírez, Halogen-Mediated Conversion of Hydrocarbons to Commodities, Chem. Rev., 117 (2017) 4182-4247.

[124] T. Somheil, Study: Global PVC demand to grow 3.2% annually through 2021, Resin Princing, Building Costruction (2014).

[125] M.K. Patel, E. Jochem, P. Radgen, E. Worrell, Plastics streams in Germany—an analysis of production, consumption and waste generation, Resources, Conserv. Recycl., 24 (1998) 191-215.

[126] I.S. Arvanitoyannis, 15 - Waste Management in Food Packaging Industries, in: I.S. Arvanitoyannis (Ed.) Waste Management for the Food Industries, Academic Press, Amsterdam, 396 (2008) 941-1045.

[127] D. Braun, Poly(vinyl chloride) on the way from the 19th century to the 21st century, J. Polym. Sci. A: Polym. Chem., 42 (2004) 578-586.

[128] D.J. Lisk, Environmental effects of landfills, Sci. Total Environ., 100 (1991) 415-468.

[129] N. Miskolczi, L. Bartha, A. Angyal, Pyrolysis of Polyvinyl Chloride (PVC)-Containing Mixed Plastic Wastes for Recovery of Hydrocarbons, Energy & Fuels 23 (2009) 2743-2749.

[130] R. Miranda, H. Pakdel, C. Roy, H. Darmstadt, C. Vasile, Vacuum pyrolysis of PVCII: Product analysis, Polym. Degrad. Stabil., 66 (1999) 107-125.

[131] E. Wikström, G. Löfvenius, C. Rappe, S. Marklund, Influence of Level and Form of Chlorine on the Formation of Chlorinated Dioxins, Dibenzofurans, and Benzenes during Combustion of an Artificial Fuel in a Laboratory Reactor, Environ. Sci. Technol., 30 (1996) 1637-1644.

[132] H. Zhou, A. Meng, Y. Long, Q. Li, Y. Zhang, A review of dioxin-related substances during municipal solid waste incineration, Waste Manage., 36 (2015) 106-118.

[133] R. Addink, K. Olie, Role of oxygen in formation of polychlorinated dibenzo-p-dioxins/dibenzofurans from carbon on fly ash, Environ. Sci. Technol., 29 (1995) 1586-1590.

[134] A. Saeed, M. Altarawneh, B.Z. Dlugogorski, Formation of mixed halogenated dibenzo-p-dioxins and dibenzofurans (PXDD/Fs), Chemosphere, 137 (2015) 149-156.

[135] E. Wikström, S. Ryan, A. Touati, M. Telfer, D. Tabor, B.K. Gullett, Importance of Chlorine Speciation on de Novo Formation of Polychlorinated Dibenzo-p-dioxins and Polychlorinated Dibenzofurans, Environ. Sci. Technol., 37 (2003) 1108-1113.

[136] B.R. Stanmore, The formation of dioxins in combustion systems, Combust. Flame, 136 (2004) 398-427.

[137] L. Stieglitz, G. Zwick, J. Beck, W. Roth, H. Vogg, On the de-novo synthesis of PCDD/PCDF on fly ash of municipal waste incinerators, Chemosphere, 18 (1989) 1219-1226.

[138] M. Altarawneh, B.Z. Dlugogorski, E.M. Kennedy, J.C. Mackie, Mechanisms for formation, chlorination, dechlorination and destruction of polychlorinated dibenzo-p-dioxins and dibenzofurans (PCDD/Fs), Prog. Energy Combust. Sci., 35 (2009) 245-274.

[139] S. Nakamura, K. Nakajima, Y. Yoshizawa, K. Matsubae-Yokoyama, T. Nagasaka, Analyzing Polyvinyl Chloride in Japan With the Waste Input−Output Material Flow Analysis Model, J. Ind. Ecol., 13 (2009) 706-717.

[140] F. Burat, A. Güney, M. Olgaç Kangal, Selective separation of virgin and post-consumer polymers (PET and PVC) by flotation method, Waste Manage., 29 (2009) 1807-1813.

[141] M.A. Keane, Catalytic conversion of waste plastics: focus on waste PVC, J. Chem. Technol. Biotechnol., 82 (2007) 787-795.

[142] N. Sombatsompop, S. Thongsang, Rheology, morphology, and mechanical and thermal properties of recycled PVC pipes, J. Appl. Polym. Sci., 82 (2001) 2478-2486.

[143] B.A. Hegberg, W.H. Hallenbeck, G.R. Brenniman, Plastics recycling rates, Resources, Conserv. Recycl., 9 (1993) 89-107.

[144] T. Kameda, Y. Fukuda, G. Grause, T. Yoshioka, Chemical modification of rigid poly(vinyl chloride) by the substitution with nucleophiles, J. Appl. Polym. Sci., 116 (2010) 36-44.

[145] S.M. Al-Salem, P. Lettieri, J. Baeyens, Recycling and recovery routes of plastic solid waste (PSW): A review, Waste Manage., 29 (2009) 2625-2643.

[146] G. Wu, J. Li, Z. Xu, Triboelectrostatic separation for granular plastic waste recycling: A review, Waste Manage., 33 (2013) 585-597.

[147] S.M. Al-Salem, P. Lettieri, J. Baeyens, The valorization of plastic solid waste (PSW) by primary to quaternary routes: From re-use to energy and chemicals, Prog. Energy Comb. Sci., 36 (2010) 103-129.

[148] P. Lettieri, S.M. Al-Salem, Chapter 17 - Thermochemical Treatment of Plastic Solid Waste, in: T.M. Letcher, D.A. Vallero (Eds.) Waste, Academic Press, Boston, (2011), 233-242.

[149] S. Honus, S. Kumagai, V. Molnár, G. Fedorko, T. Yoshioka, Pyrolysis gases produced from individual and mixed PE, PP, PS, PVC, and PET-Part II: Fuel characteristics, Fuel 221 (2018) 361-373.

[150] F.P. La Mantia, Recycling of plastic materials, ChemTec Publishing 1993.

[151] C.-H. Wu, C.-Y. Chang, J.-L. Hor, S.-M. Shih, L.-W. Chen, F.-W. Chang, Two-Stage pyrolysis model of PVC, Can. J. Chem. Eng., 72 (1994) 644-650.

[152] H.M. de A. M. M. S. Machado, G.R. Filho, R.M.N. De Assunção, H.M. Soares, A.P. Cangani, D.A. Cerqueira, C.d.S. Meireles, Chemical recycling of poly(vinyl chloride): Application of partially dehydrochlorinated poly(vinyl chloride) for producing a chemically modified polymer, J. Appl. Polym. Sci., 115 (2010) 1474-1479.

[153] X. Hu, J.M. Calo, Plastic particle separation via liquid-fluidized bed classification, AIChE J., 52 (2006) 1333-1342.

[154] G. Dodbiba, J. Sadaki, K. Okaya, A. Shibayama, T. Fujita, The use of air tabling and triboelectric separation for separating a mixture of three plastics, Min. Eng., 18 (2005) 1350-1360.

[155] M. Brits, J. de Vos, J.M. Weiss, E.R. Rohwer, J. de Boer, Critical review of the analysis of brominated flame retardants and their environmental levels in Africa, Chemosphere, 164 (2016) 174-189.

[156] N. Ortuño, J. Moltó, J.A. Conesa, R. Font, Formation of brominated pollutants during the pyrolysis and combustion of tetrabromobisphenol A at different temperatures, Environ. Pollut., 191 (2014) 31-37.

[157] Å. Bergman, A. Rydén, R.J. Law, J. de Boer, A. Covaci, M. Alaee, L. Birnbaum, M. Petreas, M. Rose, S. Sakai, N. Van den Eede, I. van der Veen, A novel abbreviation standard for organobromine, organochlorine and organophosphorus flame retardants and some characteristics of the chemicals, Environ. Int., 49 (2012) 57-82.

[158] H. Fromme, G. Becher, B. Hilger, W. Völkel, Brominated flame retardants – Exposure and risk assessment for the general population, Int. J. Hyg. Environ. Health, 219 (2016) 1-23.

[159] L.S. Birnbaum, D.F. Staskal, Brominated flame retardants: cause for concern?, Environ. Health Perspect., 112 (2004) 9-17.

[160] M. Zhang, A. Buekens, X. Li, Brominated flame retardants and the formation of dioxins and furans in fires and combustion, J. Hazard. Mater., 304 (2016) 26-39.

[161] D. Santillo, P. Johnston, K. Brigden, The presence of brominated flame retardants and organotin compounds in dusts collected from Parliament buildings from eight countries, Greenpeace Research Laboratories, dated March (2001).

[162] P. Mikula, Z. Svobodova, Brominated flame retardants in the environment: their sources and effects (a review), Acta Vet. Brno., 75 (2006) 587-599.

[163] K.K. Kefeni, J.O. Okonkwo, O.I. Olukunle, B.M. Botha, Brominated flame retardants: sources, distribution, exposure pathways, and toxicity, Environ. Rev., 19 (2011) 238-253.

[164] O. Hutzinger, H. Thoma, Polybrominated dibenzo-p-dioxins and dibenzofurans: the flame retardant issue, Chemosphere, 16 (1987) 1877-1880.

[165] A. Covaci, S. Voorspoels, J. de Boer, Determination of brominated flame retardants, with emphasis on polybrominated diphenyl ethers (PBDEs) in environmental and human samples—a review, Environ. Int., 29 (2003) 735-756.

[166] M. Altarawneh, A. Saeed, M. Al-Harahsheh, B.Z. Dlugogorski, Thermal decomposition of brominated flame retardants (BFRs): Products and mechanisms, Pro. Energy Comb. Sci., 70 (2019) 212-259.

[167] A.I. Balabanovich, A. Hornung, D. Merz, H. Seifert, The effect of a curing agent on the thermal degradation of fire retardant brominated epoxy resins, Polym. Degrad. Stabil., 85 (2004) 713-723.

[168] A. Sepúlveda, M. Schluep, F.G. Renaud, M. Streicher, R. Kuehr, C. Hagelüken, A.C. Gerecke, A review of the environmental fate and effects of hazardous substances released from electrical and electronic equipments during recycling: Examples from China and India, Impact Assess. Rev., 30 (2010) 28-41.

[169] H. Destaillats, R.L. Maddalena, B.C. Singer, A.T. Hodgson, T.E. McKone, Indoor pollutants emitted by office equipment: A review of reported data and information needs, Atmo. Environ., 42 (2008) 1371-1388.

[170] R.C. Hale, M.J. La Guardia, E. Harvey, T. Matt Mainor, Potential role of fire retardant-treated polyurethane foam as a source of brominated diphenyl ethers to the US environment, Chemosphere, 46 (2002) 729-735.

[171] A.F.H. ter Schure, C. Agrell, A. Bokenstrand, J. Sveder, P. Larsson, B.N. Zegers, Polybrominated diphenyl ethers at a solid waste incineration plant II: atmospheric deposition, Atmo. Environ., 38 (2004) 5149-5155.

[172] M. Karlsson, A. Julander, B. van Bavel, L. Hardell, Levels of brominated flame retardants in blood in relation to levels in household air and dust, Environ. Int., 33 (2007) 62-69.

[173] S. Harrad, M.A.-E. Abdallah, N.L. Rose, S.D. Turner, T.A. Davidson, Current-Use Brominated Flame Retardants in Water, Sediment, and Fish from English Lakes, Environ, Sci, Technol., 43 (2009) 9077-9083.

[174] U. Jans, Emerging Brominated Flame Retardants in Sediments and Soils: a Review, Current Pollut. Rep., 2 (2016) 213-223.

[175] P.O. Darnerud, Toxic effects of brominated flame retardants in man and in wildlife, Environ. Int., 29 (2003) 841-853.

[176] L.T.M. Van der Ven, T. Van de Kuil, A. Verhoef, C.M. Verwer, H. Lilienthal, P.E.G. Leonards, U.M.D. Schauer, R.F. Cantón, S. Litens, F.H. De Jong, T.J. Visser, W. Dekant, N. Stern, H. Håkansson, W. Slob, M. Van den Berg, J.G. Vos, A.H. Piersma, Endocrine effects of tetrabromobisphenol-A (TBBPA) in Wistar rats as tested in a one-generation reproduction study and a subacute toxicity study, Toxicol., 245 (2008) 76-89.

[177] M. Rose, A. Fernandes, Are BFRs responsible for brominated dioxins and furans (PBDD/Fs) in food, Proceedings of the 5th international symposium on brominated flame retardants, 2010.

[178] G. Suzuki, M. Nakamura, C. Michinaka, N.M. Tue, H. Handa, H. Takigami, Dioxin-like activity of brominated dioxins as individual compounds or mixtures in in vitro reporter gene assays with rat and mouse hepatoma cell lines, Toxicol. Vitro., 44 (2017) 134-141.

[179] R. Weber, B. Kuch, Relevance of BFRs and thermal conditions on the formation pathways of brominated and brominated–chlorinated dibenzodioxins and dibenzofurans, Environ. Int., 29 (2003) 699-710.

[180] L.-C. Wang, G.-P. Chang-Chien, Characterizing the Emissions of Polybrominated Dibenzo-p-dioxins and Dibenzofurans from Municipal and Industrial Waste Incinerators, Environ. Sci. Technol., 41 (2007) 1159-1165.

[181] M. Zhang, A. Buekens, X. Li, Open burning as a source of dioxins, Critical Reviews in Environ. Sci. Technol., 47 (2017) 543-620.

[182] M. Zhang, A. Buekens, De novo synthesis of dioxins: a review, Int. J. Environ. Pollut., 60 (2016) 63-110.

[183] R. Luijk, H.A.J. Govers, The formation of polybrominated dibenzo-p-dioxins (PBDDs) and dibenzofurans (PBDFs) during pyrolysis of polymer blends containing brominated flame retardants, Chemosphere 25 (1992) 361-374.

[184] R. Luijk, H. Wever, K. Olie, H.A.J. Govers, J.J. Boon, The influence of the polymer matrix on the formation of polybrominated dibenzo-p-dioxins (PBDDs) and polybrominated dibenzofurans (PBDFs), Chemosphere, 23 (1991) 1173-1183.

[185] H. Huang, A. Buekens, On the mechanisms of dioxin formation in combustion processes, Chemosphere, 31 (1995) 4099-4117.

[186] B. Du, M. Zheng, H. Tian, A. Liu, Y. Huang, L. Li, T. Ba, N. Li, Y. Ren, Y. Li, S. Dong, G. Su, Occurrence and characteristics of polybrominated dibenzo-p-dioxins and dibenzofurans in stack gas emissions from industrial thermal processes, Chemosphere, 80 (2010) 1227-1233.

[187] N. Ortuño, J.A. Conesa, J. Moltó, R. Font, De Novo Synthesis of Brominated Dioxins and Furans, Environ. Sci. Technol., 48 (2014) 7959-7965.

[188] J. Vehlow, B. Bergfeldt, K. Jay, H. Seifert, T. Wanke, F.E. Mark, Thermal treatment of electrical and electronic waste plastics, Waste Manage. Res., 18 (2000) 131-140.

[189] R. Dumler, D. Lenoir, H. Thoma, O. Hutzinger, Thermal formation of polybrominated dibenzofurans and dioxins from decabromodiphenyl ether flame retardant: Influence of antimony(III) oxide and the polymer matrix, Chemosphere, 20 (1990) 1867-1873.

[190] D. Lenoir, B. Zier, D. Bieniek, A. Kettrup, The influence of water and metals on PBDD/F concentration in incineration of decabrombiphenyl ether in polymeric matrices, Chemosphere, 28 (1994) 1921-1928.

[191] M. Al-Harahsheh, M. Altarawneh, M. Aljarrah, F. Rummanah, K. Abdel-Latif, Bromine fixing ability of electric arc furnace dust during thermal degradation of tetrabromobisphenol: Experimental and thermodynamic analysis study, J. Anal. Appl. Pyroly., 134 (2018) 503-509.

[192] J. Piskorska-Pliszczyńska, S. Maszewski, Brominated dioxins: little-known new health hazards-a review, Bull. Vet. Inst. Pulawy, 58 (2014) 327-335.

[193] F. Barontini, K. Marsanich, L. Petarca, V. Cozzani, The Thermal Degradation Process of Tetrabromobisphenol A, IInd. Eng. Chem. Res., 43 (2004) 1952-1961.

[194] A. Marongiu, G. Bozzano, M. Dente, E. Ranzi, T. Faravelli, Detailed kinetic modeling of pyrolysis of tetrabromobisphenol A, J. Anal. Appl. Pyroly., 80 (2007) 325-345.

[195] F. Barontini, V. Cozzani, K. Marsanich, V. Raffa, L. Petarca, An experimental investigation of tetrabromobisphenol A decomposition pathways, J. Anal. Appl. Pyroly., 72 (2004) 41-53.

[196] F. Sasse, G. Emig, Chemical Recycling of Polymer Materials, Chem. Engi. Technol., 21 (1998) 777-789.

[197] T.F. Astrup, D. Tonini, R. Turconi, A. Boldrin, Life cycle assessment of thermal Waste-to-Energy technologies: Review and recommendations, Waste Manage., 37 (2015) 104-115.

[198] J. Aguado, D.P. Serrano, J.M. Escola, Fuels from Waste Plastics by Thermal and Catalytic Processes: A Review, Ind. Eng. Chem. Res., 47 (2008) 7982-7992.

[199] K. Hamad, M. Kaseem, F. Deri, Recycling of waste from polymer materials: An overview of the recent works, Polym. Degrad. Stabil., 98 (2013) 2801-2812.

[200] A.A. Garforth, S. Ali, J. Hernández-Martínez, A. Akah, Feedstock recycling of polymer wastes, Curr. Opin. Solid State Mater. Sci., 8 (2004) 419-425.

[201] O.K.M. Ouda, S.A. Raza, A.S. Nizami, M. Rehan, R. Al-Waked, N.E. Korres, Waste to energy potential: A case study of Saudi Arabia, Renew. Sust. Energy Rev., 61 (2016) 328-340.

[202] K. Ragaert, L. Delva, K. Van Geem, Mechanical and chemical recycling of solid plastic waste, Waste Manage., 69 (2017) 24-58.

[203] T. Bhaskar, T. Matsui, J. Kaneko, M.A. Uddin, A. Muto, Y. Sakata, Novel calcium based sorbent (Ca-C) for the dehalogenation (Br, Cl) process during halogenated mixed plastic (PP/PE/PS/PVC and HIPS-Br) pyrolysis, Green Chem., 4 (2002) 372-375.

[204] Y. Shen, R. Zhao, J. Wang, X. Chen, X. Ge, M. Chen, Waste-to-energy: Dehalogenation of plastic-containing wastes, Waste Manage., 49 (2016) 287-303.

[205] C. Wu, P.T. Williams, Advanced Thermal Treatment of Wastes for Fuels, Chemicals and Materials Recovery, Waste as a Resource, The Royal Society of Chemistry Cambridge(2013) 1-43.

[206] A. Buekens, Introduction to feedstock recycling of plastics, Feedstock recycling and pyrolysis of waste plastics 6 (2006) 1-41.

[207] B. Kunwar, H.N. Cheng, S.R. Chandrashekaran, B.K. Sharma, Plastics to fuel: a review, Renew. Sust. Energy Rev., 54 (2016) 421-428.

[208] S.M. FakhrHoseini, M. Dastanian, Predicting Pyrolysis Products of PE, PP, and PET Using NRTL Activity Coefficient Model, J. Chem., 2013 (2013) 5.

[209] A.V. Bridgwater, Review of fast pyrolysis of biomass and product upgrading, Biomass and Bioenergy 38 (2012) 68-94.

[210] F. Abnisa, W.M.A. Wan Daud, A review on co-pyrolysis of biomass: An optional technique to obtain a high-grade pyrolysis oil, Energy Convers. Manage., 87 (2014) 71-85.

[211] W.J. Hall, P.T. Williams, Fast Pyrolysis of Halogenated Plastics Recovered from Waste Computers, Energy & Fuels 20 (2006) 1536-1549.

[212] W.J. Hall, P.T. Williams, Removal of organobromine compounds from the pyrolysis oils of flame retarded plastics using zeolite catalysts, J. Anal. Appl. Pyroly., 81 (2008) 139-147.

[213] H. Bockhorn, A. Hornung, U. Hornung, P. Jakobströer, M. Kraus, Dehydrochlorination of plastic mixtures, J. Anal. Appl. Pyroly., 49 (1999) 97-106.

[214] A. López, I. de Marco, B.M. Caballero, M.F. Laresgoiti, A. Adrados, Influence of time and temperature on pyrolysis of plastic wastes in a semi-batch reactor, Chem. Eng. J., 173 (2011) 62-71.

[215] A. López, I. de Marco, B.M. Caballero, M.F. Laresgoiti, A. Adrados, Dechlorination of fuels in pyrolysis of PVC containing plastic wastes, Fuel Process. Technol., 92 (2011) 253-260.

[216] H. Kuramochi, D. Nakajima, S. Goto, K. Sugita, W. Wu, K. Kawamoto, HCl emission during co-pyrolysis of demolition wood with a small amount of PVC film and the effect of wood constituents on HCl emission reduction, Fuel, 87 (2008) 3155-3157.

[217] A. López, I. de Marco, B.M. Caballero, M.F. Laresgoiti, A. Adrados, A. Aranzabal, Catalytic pyrolysis of plastic wastes with two different types of catalysts: ZSM-5 zeolite and Red Mud, Appl. Cataly. B: Environ., 104 (2011) 211-219.

[218] H.M. Zhu, X.G. Jiang, J.H. Yan, Y. Chi, K.F. Cen, TG-FTIR analysis of PVC thermal degradation and HCl removal, J. Anal. Appl. Pyroly., 82 (2008) 1-9.

[219] X. Yang, L. Sun, J. Xiang, S. Hu, S. Su, Pyrolysis and dehalogenation of plastics from waste electrical and electronic equipment (WEEE): A review, Waste manage., 33 (2013) 462-473.

[220] T. Bhaskar, W.J. Hall, N.M.M. Mitan, A. Muto, P.T. Williams, Y. Sakata, Controlled pyrolysis of polyethylene/polypropylene/polystyrene mixed plastics with high impact polystyrene containing flame retardant: Effect of decabromo diphenylethane (DDE), Polym. Degrad. Stabil., 92 (2007) 211-221.

[221] N.M.M. Mitan, T. Bhaskar, W.J. Hall, A. Muto, P.T. Williams, Y. Sakata, Effect of decabromodiphenyl ether and antimony trioxide on controlled pyrolysis of high-impact polystyrene mixed with polyolefins, Chemosphere, 72 (2008) 1073-1079.

[222] F. Ateş, N. Miskolczi, N. Borsodi, Comparision of real waste (MSW and MPW) pyrolysis in batch reactor over different catalysts. Part I: Product yields, gas and pyrolysis oil properties, Biores. Technol., 133 (2013) 443-454.

[223] D.S. Achilias, C. Roupakias, P. Megalokonomos, A.A. Lappas, E.V. Antonakou, Chemical recycling of plastic wastes made from polyethylene (LDPE and HDPE) and polypropylene (PP), J. Hazard. Mater., 149 (2007) 536-542.

[224] S.Y. Lee, J.H. Yoon, J.R. Kim, D.W. Park, Catalytic degradation of polystyrene over natural clinoptilolite zeolite, Polym. Degrad. Stabil., 74 (2001) 297-305.

[225] J. Aguado, D. Serrano, J. Escola, Catalytic upgrading of plastic wastes, Feedstock recycling and pyrolysis of waste plastics: converting waste plastics into diesel and other fuels (2006) 73-110.

[226] S.R. Ivanova, E.F. Gumerova, K.S. Minsker, G.E. Zaikov, A.A. Berlin, Selective catalytic degradation of polyolefins, Prog. Polym. Sci., 15 (1990) 193-215.

[227] R.W.J. Westerhout, J.A.M. Kuipers, W.P.M. van Swaaij, Experimental Determination of the Yield of Pyrolysis Products of Polyethene and Polypropene. Influence of Reaction Conditions, Ind. Eng. Chem. Res., 37 (1998) 841-847.

[228] B. Saha, A.K. Ghoshal, Thermal degradation kinetics of poly(ethylene terephthalate) from waste soft drinks bottles, Chem. Eng. J., 111 (2005) 39-43.

[229] R. Aguado, R. Prieto, M.a.J.S. José, S. Alvarez, M.n. Olazar, J. Bilbao, Defluidization modelling of pyrolysis of plastics in a conical spouted bed reactor, Chem, Eng, Process., 44 (2005) 231-235.

[230] E. Butler, G. Devlin, D. Meier, K. McDonnell, A review of recent laboratory research and commercial developments in fast pyrolysis and upgrading, Sustain. Energy Rev., 15 (2011) 4171-4186.

[231] F. Pinto, P. Costa, I. Gulyurtlu, I. Cabrita, Pyrolysis of plastic wastes: 2. Effect of catalyst on product yield, J. Anal. Appl. Pyroly., 51 (1999) 57-71.

[232] J. Aguado, D.P. Serrano, J.M. Escola, A. Peral, Catalytic cracking of polyethylene over zeolite mordenite with enhanced textural properties, Journal of Analytical and Applied Pyrolysis 85 (2009) 352-358.

[233] J. Aguado, D.P. Serrano, J.M. Escola, A. Peral, Catalytic cracking of polyethylene over zeolite mordenite with enhanced textural properties, J. Anal. Appl. Pyroly., 85 (2009) 352-358.

[234] W.J. Hall, N. Miskolczi, J. Onwudili, P.T. Williams, Thermal Processing of Toxic Flame-Retarded Polymers Using a Waste Fluidized Catalytic Cracker (FCC) Catalyst, Energy Fuels 22 (2008) 1691-1697.

[235] N.S. Akpanudoh, K. Gobin, G. Manos, Catalytic degradation of plastic waste to liquid fuel over commercial cracking catalysts: Effect of polymer to catalyst ratio/acidity content, J. Mol. Catal. A Chem., 235 (2005) 67-73.

[236] M. Olazar, G. Lopez, M. Amutio, G. Elordi, R. Aguado, J. Bilbao, Influence of FCC catalyst steaming on HDPE pyrolysis product distribution, J. Anal. Appl. Pyroly., 85 (2009) 359-365.

[237] K.-H. Lee, Thermal and catalytic degradation of pyrolytic oil from pyrolysis of municipal plastic wastes, J. Anal. Appl. Pyroly., 85 (2009) 372-379.

[238] S.-H. Jung, S.-J. Kim, J.-S. Kim, Fast pyrolysis of a waste fraction of high impact polystyrene (HIPS) containing brominated flame retardants in a fluidized bed reactor: The effects of various Ca-based additives (CaO, Ca(OH)$_2$ and oyster shells) on the removal of bromine, Fuel 95 (2012) 514-520.

[239] M. Sarker, M.M. Rashid, Waste plastics mixture of polystyrene and polypropylene into light grade fuel using Fe$_2$O$_3$ catalyst, Int. J. Renew. Energy Technol. Res., 2 (2013) 17-28.

[240] O. Terakado, R. Ohhashi, M. Hirasawa, Thermal degradation study of tetrabromobisphenol A under the presence metal oxide: Comparison of bromine fixation ability, J. Anal. Appl. Pyroly., 91 (2011) 303-309.

[241] Y. Masuda, T. Uda, O. Terakado, M. Hirasawa, Pyrolysis study of poly(vinyl chloride)–metal oxide mixtures: Quantitative product analysis and the chlorine fixing ability of metal oxides, J. Anal. Appl. Pyroly., 77 (2006) 159-168.

[242] M. Blazsó, E. Jakab, Effect of metals, metal oxides, and carboxylates on the thermal decomposition processes of poly(vinyl chloride), J. Anal. Appl. Pyroly., 49 (1999) 125-143.

[243] N. Lingaiah, M. Azhar Uddin, A. Muto, Y. Sakata, T. Imai, K. Murata, Catalytic dechlorination of chloroorganic compounds from PVC-containing mixed plastic-derived oil, Appl. Catal., A, 207 (2001) 79-84.

[244] K.-B. Park, S.-J. Oh, G. Begum, J.-S. Kim, Production of clean oil with low levels of chlorine and olefins in a continuous two-stage pyrolysis of a mixture of waste low-density polyethylene and polyvinyl chloride, Energy, 157 (2018) 402-411.

[245] M. Al-Harahsheh, Thermodynamic Analysis on the Thermal Treatment of Electric Arc Furnace Dust-PVC Blends, Arab. J. Sci. Eng., 43 (2018) 5757-5769.

[246] T. Karayildirim, J. Yanik, M. Yuksel, M. Saglam, C. Vasile, H. Bockhorn, The effect of some fillers on PVC degradation, J. Anal. Appl. Pyroly., 75 (2006) 112-119.

[247] A. Ballistreri, S. Foti, P. Maravigna, G. Montaudo, E. Scamporrino, Effect of metal oxides on the evolution of aromatic hydrocarbons in the thermal decomposition of PVC, J. Polym. Sci., 18 (1980) 3101-3110.

[248] E.D. Owen, K.J. Msayib, Catalyzed degradation of poly(vinylchloride). III. Zinc(II) chloride catalysis, J. Polym. Sci. A: Polym. Chem., 27 (1989) 399-408.

[249] B. Zhang, X.-Y. Yan, K. Shibata, T. Uda, M. Tada, M. Hirasawa, Thermogravimetric-Mass Spectrometric Analysis of the Reactions between Oxide (ZnO, Fe_2O_3 or $ZnFe_2O_4$) and Polyvinyl Chloride under Inert Atmosphere, Mater. Trans., JIM 41 (2000) 1342-1350.

[250] B. Zhang, X. Yan, K. Shibata, M. Tada, M. Hirasawa, Novel Process for Recycling Metallic Elements from Mixtures of Metal Oxide Wastes and Waste Polyvinyl Chloride, High Temp. Mater. Proc., 1999, pp. 197.

[251] H. Matsuura, F. Tsukihashi, Chlorination kinetics of ZnO with Ar-Cl2-O2 gas and the effect of oxychloride formation, Metall. Mater. Trans. B, 37 (2006) 413-420.

[252] N. Menad, B. Bjõrkman, Polyvinyl chloride used as a chlorinating and a reducing agent, Res. Conserv. Recycl., 24 (1998) 257-274.

[253] G.-S. Lee, Y.J. Song, Recycling EAF dust by heat treatment with PVC, Min. Eng., 20 (2007) 739-746.

[254] T. Kosuda, T. Okada, S. Nozaka, Y. Matsuzawa, T. Shimizu, S. Hamanaka, S. Mishima, Characteristics and mechanism of low temperature dehydrochlorination of poly(vinyl chloride) in the presence of zinc(II) oxide, Polym. Degrad. Stabil., 97 (2012) 584-591.

[255] M. Blazsó, E. Jakab, Effect of metals, metal oxides, and carboxylates on the thermal decomposition processes of poly (vinyl chloride), J. Anal. Appl. Pyroly., 49 (1999) 125-143.

[256] M.A. Uddin, Y. Sakata, Y. Shiraga, A. Muto, K. Murata, Dechlorination of Chlorine Compounds in Poly(vinyl chloride) Mixed Plastics Derived Oil by Solid Sorbents, Indust. Eng. Chem. Res., 38 (1999) 1406-1410.

[257] J. Bozi, Z. Czégény, E. Mészáros, M. Blazsó, Thermal decomposition of flame retarded polycarbonates, J. Anal. Appl. Pyroly., 79 (2007) 337-345.

[258] G. Grause, M. Furusawa, A. Okuwaki, T. Yoshioka, Pyrolysis of tetrabromobisphenol-A containing paper laminated printed circuit boards, Chemosphere, 71 (2008) 872-878.

[259] M. Altarawneh, B.Z. Dlugogorski, Mechanism of thermal decomposition of tetrabromobisphenol A (TBBA), J. Phys. Chem. A, 118 (2014) 9338-9346.

[260] O. Terakado, R. Ohhashi, M. Hirasawa, Bromine fixation by metal oxide in pyrolysis of printed circuit board containing brominated flame retardant, J. Anal. Appl. Pyroly., 103 (2013) 216-221.

[261] M. Grabda, S. Oleszek-Kudlak, E. Shibata, T. Nakamura, Vaporization of zinc during thermal treatment of ZnO with tetrabromobisphenol A (TBBPA), J. Hazard. Mater., 187 (2011) 473-479.

[262] M. Grabda, S. Oleszek-Kudlak, E. Shibata, T. Nakamura, Influence of temperature and heating time on bromination of zinc oxide during thermal treatment with tetrabromobisphenol A, Environ. Sci. Technol., 43 (2009) 8936-8941.

[263] S. Oleszek, M. Grabda, E. Shibata, T. Nakamura, Study of the reactions between tetrabromobisphenol A and PbO and Fe_2O_3 in inert and oxidizing atmospheres by various thermal methods, Thermochim. Acta, 566 (2013) 218-225.

[264] S. Oleszek, M. Grabda, E. Shibata, T. Nakamura, TG and TG-MS methods for studies of the reaction between metal oxide and brominated flame retardant in various atmospheres, Thermochim. Acta, 527 (2012) 13-21.

[265] M. Rzyman, M. Grabda, S. Oleszek-Kudlak, E. Shibata, T. Nakamura, Studies on bromination and evaporation of antimony oxide during thermal treatment of tetrabromobisphenol A (TBBPA), J. Anal. Appl. Pyroly., 88 (2010) 14-21.

[266] M. Grabda, S. Oleszek-Kudlak, M. Rzyman, E. Shibata, T. Nakamura, Studies on Bromination and Evaporation of Zinc Oxide during Thermal Treatment with TBBPA, Environ. Sci. Technol., 43 (2009) 1205-1210.

[267] O. Terakado, S. Kuzuhara, H. Takagi, M. Hirasawa, Thermal Decomposition of Printed Circuit Board in the Presence of Zinc Oxide under Inert and Oxidative Atmosphere: Emission Behavior of Inorganic Brominated Compounds, Engineering 10 (2018) 606.

[268] J. Seader, J.J. Siirola, S.D. Barnicki, Perry's chemical engineer's handbook, Perry's Chemical Engineers' Handbook (1997).

[269] M.D. Hack, D.G. Truhlar, Nonadiabatic trajectories at an exhibition, J. Phys. Chem. A, 104 (2000) 7917-7926.

[270] C.D. Sherrill, The born-oppenheimer approximation, School of Chemistry and Biochemistry, Georgia Institute of Technology (2005).

[271] D. Young, Computational chemistry: a practical guide for applying techniques to real world problems, John Wiley & Sons (2004).

[272] E.G. Lewars, Computational chemistry: introduction to the theory and applications of molecular and quantum mechanics, Springer Science & Business Media (2010).

[273] M. Born, R. Oppenheimer, Zur quantentheorie der molekeln, Ann. Phys., 389 (1927) 457-484.

[274] E. Schrödinger, An undulatory theory of the mechanics of atoms and molecules, Phys. Rev., 28 (1926) 1049.

[275] A. Scherrer, F. Agostini, D. Sebastiani, E. Gross, R. Vuilleumier, On the mass of atoms in molecules: Beyond the Born-Oppenheimer approximation, Phys. Rev. X, 7 (2017) 031035.

[276] S. Ghosh, P. Verma, C.J. Cramer, L. Gagliardi, D.G. Truhlar, Combining Wave Function Methods with Density Functional Theory for Excited States, Chem. Rev., 118 (2018) 7249-7292.

[277] N.L. Doltsinis, Molecular dynamics beyond the Born-Oppenheimer approximation: mixed quantum–classical approaches, Computational nanoscience: Do it yourself (2006) 389-409.

[278] K. Ramachandran, G. Deepa, K. Namboori, Computational chemistry and molecular modeling: principles and applications, Springer Science & Business Media (2008).

[279] C.D. Sherrill, An introduction to Hartree-Fock molecular orbital theory, Georgia inst. of technology (2000).

[280] A.D. Becke, Density functional calculations of molecular bond energies, J. Chem. Phys., 84 (1986) 4524-4529.

[281] P. Elliott, M.H. Cohen, A. Wasserman, K. Burke, Density functional partition theory with fractional occupations, J. Chem. Theor. Comp., 5 (2009) 827-833.

[282] S.F. Sousa, P.A. Fernandes, M.J. Ramos, General Performance of Density Functionals, J. Phys. Chem. A, 111 (2007) 10439-10452.

[283] G. Sun, J. Kürti, P. Rajczy, M. Kertesz, J. Hafner, G. Kresse, Performance of the Vienna ab initio simulation package (VASP) in chemical applications, J. Mol. Struct.: Theochem, 624 (2003) 37-45.

[284] W. Kohn, L.J. Sham, Self-consistent equations including exchange and correlation effects, Phys. Rev., 140 (1965) A1133.

[285] A.J. Cohen, P. Mori-Sánchez, W. Yang, Challenges for density functional theory, Chem. Rev., 112 (2011) 289-320.

[286] C.J. Cramer, D.G. Truhlar, Density functional theory for transition metals and transition metal chemistry, Phys. Chem. Chem. Phys., 11 (2009) 10757-10816.

[287] W. Kohn, A.D. Becke, R.G. Parr, Density functional theory of electronic structure, J. Phys. Chem., 100 (1996) 12974-12980.

[288] R. Parr, W. Yang, Density functional theory of atoms and molecules New York: Oxford University Press, ISBN 0-19-509276-7, (1989).

[289] E.H. Lieb, A brief review of Thomas–Fermi theory, Citeseer, (2000).

[290] W. Koch, M.C. Holthausen, A chemist's guide to density functional theory, John Wiley & Sons (2015).

[291] P. Hohenberg, W. Kohn, Phys Rev 136: B864, Kohn W, Sham LJ (1965) Phys Rev 140 (1964) A1133.

[292] M. Levy, Universal variational functionals of electron densities, first-order density matrices, and natural spin-orbitals and solution of the v-representability problem, Proc. Natl. Acad. Sci., 76 (1979) 6062-6065.

[293] P.A.M. Dirac, Note on Exchange Phenomena in the Thomas Atom, Mathematical Proceedings of the Cambridge Philosophical Society 26 (2008) 376-385.

[294] L.H. Thomas, The calculation of atomic fields, Math. Proc. Cambridge Phil. Soc., 23 (2008) 542-548.

[295] J. Hafner, Ab-initio simulations of materials using VASP: Density-functional theory and beyond, J. Comp. Chem., 29 (2008) 2044-2078.

[296] T.C. Leung, X.W. Wang, B.N. Harmon, Band-theoretical study of magnetism in Sc_2CuO_4, Phys. Rev. B, 37 (1988) 384-388.

[297] A.D. Becke, Density-functional thermochemistry. II. The effect of the Perdew–Wang generalized-gradient correlation correction, J. Chem. Phys., 97 (1992) 9173-9177.

[298] J.P. Perdew, W. Yue, Accurate and simple density functional for the electronic exchange energy: Generalized gradient approximation, Phys. Rev. B, 33 (1986) 8800-8802.

[299] N.C. Handy, A.J. Cohen, Left-right correlation energy, Mol. Phys., 99 (2001) 403-412.

[300] C. Adamo, V. Barone, Exchange functionals with improved long-range behavior and adiabatic connection methods without adjustable parameters: The mPW and mPW1PW models, J. Chem. Phys., 108 (1998) 664-675.

[301] A.D. Becke, Density-functional exchange-energy approximation with correct asymptotic behavior, Phys. Rev. A, 38 (1988) 3098-3100.

[302] Y. Wang, J.P. Perdew, Spin scaling of the electron-gas correlation energy in the high-density limit, Phys. Rev. B, 43 (1991) 8911-8916.

[303] J.P. Perdew, Density-functional approximation for the correlation energy of the inhomogeneous electron gas, Phys. Rev. B, 33 (1986) 8822-8824.

[304] J.P. Perdew, Accurate Density Functional for the Energy: Real-Space Cutoff of the Gradient Expansion for the Exchange Hole, Phys. Rev. Lett., 55 (1985) 1665-1668.

[305] D.C. Langreth, J.P. Perdew, Theory of nonuniform electronic systems. I. Analysis of the gradient approximation and a generalization that works, Phys. Rev. B, 21 (1980) 5469-5493.

[306] J.P. Perdew, K. Burke, M. Ernzerhof, Generalized Gradient Approximation Made Simple [Phys. Rev. Lett. 77, 3865 (1996)], Phys. Rev. Lett., 78 (1997) 1396-1396.

[307] W.E. Pickett, S.C. Erwin, E.C. Ethridge, Reformulation of the $\mathrm{LDA}+U$ method for a local-orbital basis, Phys. Rev. B, 58 (1998) 1201-1209.

[308] A.G. Petukhov, I.I. Mazin, L. Chioncel, A.I. Lichtenstein, Correlated metals and the mathrm{LDA}+U method, Phys. Rev. B, 67 (2003) 153106.

[309] V.I. Anisimov, J. Zaanen, O.K. Andersen, Band theory and Mott insulators: Hubbard U instead of Stoner I, Phys. Rev. B, 44 (1991) 943-954.

[310] L. Hedin, New Method for Calculating the One-Particle Green's Function with Application to the Electron-Gas Problem, Phys. Rev., 139 (1965) A796-A823.

[311] S. Massidda, M. Posternak, A. Baldereschi, Hartree-Fock LAPW approach to the electronic properties of periodic systems, Phys. Rev. B, 48 (1993) 5058-5068.

[312] W. Schmidt, M. Schreiber, Exact and approximate solutions of the Peierls–Hubbard model, J. Chem. Phys., 86 (1987) 953-962.

[313] J. Hubbard, Electron correlations in narrow energy bands, Proc. Roy. Soc. (London), Ser. A, (1963) 238-257.

[314] H. Juro, On the Statistical Mechanical Treatment of the Absolute Rate of Chemical Reaction, Bulletin of the Chemical Society of Japan 13 (1938) 210-216.

[315] J.K. Nørskov, T. Bligaard, B. Hvolbæk, F. Abild-Pedersen, I. Chorkendorff, C.H. Christensen, The nature of the active site in heterogeneous metal catalysis, Chem. Soc. Rev., 37 (2008) 2163-2171.

[316] H. Eyring, The Activated Complex and the Absolute Rate of Chemical Reactions, Chem. Rev., 17 (1935) 65-77.

[317] G. Kresse, J. Hafner, Ab initio molecular dynamics for liquid metals, Phys. Rev. B, 47 (1993) 558-561.

[318] G. Kresse, J. Furthmüller, Efficient iterative schemes for ab initio total-energy calculations using a plane-wave basis set, Phys. Rev. B, 54 (1996) 11169-11186.

[319] G. Kresse, J. Furthmüller, Efficiency of ab-initio total energy calculations for metals and semiconductors using a plane-wave basis set, Comp. Mater. Sci., 6 (1996) 15-50.

[320] J. Kürti, G. Kresse, H. Kuzmany, First-principles calculations of the radial breathing mode of single-wall carbon nanotubes, Phys. Rev. B, 58 (1998) R8869-R8872.

[321] G. Kresse, D. Joubert, From ultrasoft pseudopotentials to the projector augmented-wave method, Phys. Rev. B, 59 (1999) 1758-1775.

[322] P.E. Blöchl, Projector augmented-wave method, Phys. Rev. B, 50 (1994) 17953-17979.

[323] B. Delley, Time dependent density functional theory with DMol3, J. Phys.: Condensed Matter, 22 (2010) 384208.

[324] B. Delley, From molecules to solids with the DMol3 approach, J. Chem. Phys., 113 (2000) 7756-7764.

[325] B. Delley, An all-electron numerical method for solving the local density functional for polyatomic molecules, J. Chem. Phys., 92 (1990) 508-517.

[326] S.H. Vosko, L. Wilk, M. Nusair, Accurate spin-dependent electron liquid correlation energies for local spin density calculations: a critical analysis, Can. J. Phys., 58 (1980) 1200-1211.

[327] J.P. Perdew, K. Burke, M. Ernzerhof, Generalized Gradient Approximation Made Simple, Phys. Rev. Lett., 77 (1996) 3865-3868.

[328] J.P. Perdew, K. Burke, Y. Wang, Generalized gradient approximation for the exchange-correlation hole of a many-electron system, Phys. Rev. B, 54 (1996) 16533-16539.

[329] A.D. Becke, A multicenter numerical integration scheme for polyatomic molecules, J. Chem. Phys., 88 (1988) 2547-2553.

[330] A.D. Boese, N.C. Handy, A new parametrization of exchange–correlation generalized gradient approximation functionals, J. Chem. Phys., 114 (2001) 5497-5503.

[331] B. Hammer, L.B. Hansen, J.K. Nørskov, Improved adsorption energetics within density-functional theory using revised Perdew-Burke-Ernzerhof functionals, Phys. Rev. B, 59 (1999) 7413-7421.

[332] A. Togo, F. Oba, I. Tanaka, First-principles calculations of the ferroelastic transition between rutile-type and $CaCl_2$ type SiO_2 at high pressures, Phys. Rev. B, 78 (2008) 134106.

[333] W.A. Adeagbo, P. Entel, Influence of dipole interactions on the lattice dynamics of crystalline ice, Phase Transitions, 78 (2005) 799-810.

[334] K. Parlinski, J. Łażewski, Y. Kawazoe, Ab initio studies of phonons in MgO by the direct method including LO mode, J. Phys. Chem. Solids, 61 (2000) 87-90.

[335] A. Togo, L. Chaput, I. Tanaka, Distributions of phonon lifetimes in Brillouin zones, Physical Review B 91 (2015) 094306.

[336] A. Togo, F. Oba, I. Tanaka, First-principles calculations of the ferroelastic transition between rutile-type and $CaCl_2$-type SiO_2 at high pressures, Phys. Rev. B, 78 (2008) 134106.

[337] K. Parlinski, Z. Li, Y. Kawazoe, First-principles determination of the soft mode in cubic ZrO_2, Phys. Rev. Lett., 78 (1997) 4063.

[338] N. Leclerc, E. Meux, J.-M. Lecuire, Hydrometallurgical extraction of zinc from zinc ferrites, Hydrometallurgy 70 (2003) 175-183.

[339] T. Suetens, B. Klaasen, K. Van Acker, B. Blanpain, Comparison of electric arc furnace dust treatment technologies using exergy efficiency, J. Clean. Prod., 65 (2014) 152-167.

[340] G. Assis, Emerging pyrometallurgical processes for zinc and lead recovery from zinc-bearing waste materials, Mintek, (1998).

[341] J. Antrekowitsch, H. Antrekowitsch, Hydrometallurgically recovering zinc from electric arc furnace dusts, JOM 53 (2001) 26-28.

[342] J. Korpas, V. Slovák, K. Wichterle, Waste poly (vinyl chloride) pyrolysis with hydrogen chloride abatement by steelmaking dust, Chem. Papers, 2016, pp. 926.

[343] G. Sivalingam, R. Karthik, G. Madras, Effect of Metal Oxides on Thermal Degradation of Poly(vinyl acetate) and Poly(vinyl chloride) and Their Blends, Ind. Eng. Chem. Res., 42 (2003) 3647-3653.

[344] G.V. Plotnikova, K.L. Kuznetsov, S.F. Malysheva, V.P. Udilov, V.Y. Seleznev, N.A. Belogorlova, V.A. Kuimov, Mechanical Properties of Polyvinyl Chloride Plastisols Containing New Flame Retardants, Int. Polym. Sci. Technol., 37 (2010) 29-32.

[345] H. Wang, H. Wang, Z. Guo, S. Qi, C. Tian, Flame Retardant Property of Sb_2O_3/SnO_2 and their Synergism in Flexible PVC, J. Fire Sci., 24 (2006) 195-210.

[346] T. Katami, A. Yasuhara, T. Okuda, T. Shibamoto, Formation of PCDDs, PCDFs, and Coplanar PCBs from Polyvinyl Chloride during Combustion in an Incinerator, Environ. Sci. Technol., 36 (2002) 1320-1324.

[347] C. Huggett, B.C. Levin, Toxicity of the pyrolysis and combustion products of poly(vinyl chlorides): A literature assessment, Fire Mater., 11 (1987) 131-142.

[348] P. Carty, E. Metcalfe, T.J. Saben, Thermal analysis of plasticised PVC containing flame retardant/smoke suppressant inorganic and organometallic iron compounds, Fire Safety J., 17 (1991) 45-56.

[349] T. Iida, K. Gotō, Investigations on poly(vinyl chloride). III. Effects of metal oxides upon thermal decomposition of poly(vinyl chloride), J. Polym. Sci.: Polym. Chem. Ed., 15 (1977) 2427-2433.

[350] M. Altarawneh, O.H. Ahmed, Z.-T. Jiang, B.Z. Dlugogorski, Thermal Recycling of Brominated Flame Retardants with Fe_2O_3, J. Phys. Chem. A, 120 (2016) 6039-6047.

[351] N. Ahubelem, M. Altarawneh, B. Dlugogorski, Kinetic and mechanistic study into emission of HCl in fires of PVC, (2013).

[352] R. Font, A. Gálvez, J. Moltó, A. Fullana, I. Aracil, Formation of polychlorinated compounds in the combustion of PVC with iron nanoparticles, Chemosphere, 78 (2010) 152-159.

[353] J.P. Perdew, Y. Wang, Erratum: Accurate and simple analytic representation of the electron-gas correlation energy, Phys. Rev. B, 45 (1992), 13244.

[354] A. Tkatchenko, M. Scheffler, Accurate Molecular Van Der Waals Interactions from Ground-State Electron Density and Free-Atom Reference Data, Phys. Rev. Lett., 102 (2009) 073005.

[355] K.J. Laidler, M.C. King, Development of transition-state theory, J. Phys. Chem., 87 (1983) 2657-2664.

[356] F.A. Carroll, Perspectives on structure and mechanism in organic chemistry, John Wiley & Sons2011.

[357] C.S. Lewis, L. Torres, J.T. Miyauchi, C. Rastegar, J.M. Patete, J.M. Smith, S.S. Wong, S.E. Tsirka, Absence of cytotoxicity towards microglia of iron oxide (α-Fe_2O_3) nanorhombohedra, Toxicol. Res., 5 (2016) 836-847.

[358] G. Tong, J. Guan, Q. Zhang, Goethite hierarchical nanostructures: Glucose-assisted synthesis, chemical conversion into hematite with excellent photocatalytic properties, Mater. Chem. Phys., 127 (2011) 371-378.

[359] A. Erlebach, H.-D. Kurland, J. Grabow, F.A. Müller, M. Sierka, Structure evolution of nanoparticulate Fe_2O_3, Nanoscale, 7 (2015) 2960-2969.

[360] S. Yang, X. Song, P. Zhang, L. Gao, Heating-Rate-Induced Porous α-Fe_2O_3 with Controllable Pore Size and Crystallinity Grown on Graphene for Supercapacitors, ACS Appl. Mater. Inter., 7 (2015) 75-79.

[361] B.E. Monsen, S.E. Olsen, L. Kolbeinsen, Kinetics of magnetite oxidation, Scandinavian J. Metall., 23 (1994) 74-80.

[362] E.R. Monazam, R.W. Breault, R. Siriwardane, Kinetics of Magnetite (Fe3O4) Oxidation to Hematite (Fe2O3) in Air for Chemical Looping Combustion, Ind. Eng. Chem. Res., 53 (2014) 13320-13328.

[363] L.X. Chen, T. Liu, M.C. Thurnauer, R. Csencsits, T. Rajh, Fe_2O_3 Nanoparticle Structures Investigated by X-ray Absorption Near-Edge Structure, Surface Modifications, and Model Calculations, J. Phys. Chem. B, 106 (2002) 8539-8546.

[364] M. Kurmoo, J.-L. Rehspringer, A. Hutlova, C. D'Orléans, S. Vilminot, C. Estournès, D. Niznansky, Formation of Nanoparticles of ε-Fe_2O_3 from Yttrium Iron Garnet in a Silica Matrix: An Unusually Hard Magnet with a Morin-Like Transition below 150 K, Chem. Mater., 17 (2005) 1106-1114.

[365] M. Altarawneh, A. Marashdeh, B.Z. Dlugogorski, Structures, electronic properties and stability phase diagrams for copper(i/ii) bromide surfaces, Phys. Chem. Chem. Phys., 17 (2015) 9341-9351.

[366] I.C. McNeill, L. Memetea, W.J. Cole, A study of the products of PVC thermal degradation, Polym. Degrad. Stabil., 49 (1995) 181-191.

[367] S.J. Blanksby, G.B. Ellison, Bond Dissociation Energies of Organic Molecules, Acc. Chem. Res., 36 (2003) 255-263.

[368] T. Liu, L. Xue, X. Guo, Y. Huang, C. Zheng, DFT and Experimental Study on the Mechanism of Elemental Mercury Capture in the Presence of HCl on α-Fe_2O_3(001), Environ. Sci. Technol., 50 (2016) 4863-4868.

[369] S. Yin, D.E. Ellis, H_2O adsorption and dissociation on defective hematite (0001) surfaces: A DFT study, Surf. Sci., 602 (2008) 2047-2054.

[370] M. Petrantoni, A. Hemeryck, J.M. Ducéré, A. Estève, C. Rossi, M. Djafari Rouhani, D. Estève, G. Landa, Periodic boundary versus quantum cluster approaches in the simulation of a nanoenergetic metallic model-system: Ni/Al(111) surface reactions, J. Phys. Chem. Solids, 71 (2010) 130-133.

[371] Y.-R. Luo, Handbook of bond dissociation energies in organic compounds, CRC press (2002).

[372] R. Wischert, C. Copéret, F. Delbecq, P. Sautet, Rücktitelbild: Optimal Water Coverage on Alumina: A Key to Generate Lewis Acid–Base Pairs that are Reactive Towards the CH Bond Activation of Methane (Angew. Chem. 14/2011), Angew. Chem., 123 (2011) 3382-3382.

[373] A. Comas-Vives, M. Schwarzwälder, C. Copéret, P. Sautet, Carbon–Carbon Bond Formation by Activation of CH3F on Alumina, J. Phys. Chem. C, 119 (2015) 7156-7163.

[374] N. Ahubelem, M. Altarawneh, B.Z. Dlugogorski, Dehydrohalogenation of ethyl halides, Tetrahedron Lett., 55 (2014) 4860-4868.

[375] S. Roy, G. Mpourmpakis, D.-Y. Hong, D.G. Vlachos, A. Bhan, R.J. Gorte, Mechanistic Study of Alcohol Dehydration on γ-Al_2O_3, ACS Catal., 2 (2012) 1846-1853.

[376] R.C.R. Neto, M. Schmal, Synthesis of CeO_2 and $CeZrO_2$ mixed oxide nanostructured catalysts for the iso-syntheses reaction, Appl. Catal. A,: 450 (2013) 131-142.

[377] Z. Wu, C. Li, Z. Wei, P. Ying, Q. Xin, FT-IR Spectroscopic Studies of Thiophene Adsorption and Reactions on Mo_2N/γ-Al_2O_3 Catalysts, J. Phys. Chem.B, 106 (2002) 979-987.

[378] W. Khaodee, N. Tangchupong, B. Jongsomjit, P. Praserthdam, S. Assabumrungrat, A study on isosynthesis via CO hydrogenation over ZrO_2–CeO_2 mixed oxide catalysts, Catal. Commun., 10 (2009) 494-501.

[379] P.M. Sommeling, P. Mulder, R. Louw, Formation of PCDFs during chlorination and oxidation of chlorobenzene in chlorine/oxygen mixtures around 340 °C, Chemosphere, 29 (1994) 2015-2018.

[380] Y. Zhang, D. Zhang, J. Gao, J. Zhan, C. Liu, New Understanding of the Formation of PCDD/Fs from Chlorophenol Precursors: A Mechanistic and Kinetic Study, J. Phys. Chem. A, 118 (2014) 449-456.

[381] M. Altarawneh, M.W. Radny, P.V. Smith, J.C. Mackie, E.M. Kennedy, B.Z. Dlugogorski, Adsorption of chlorophenol on the Cu(111) surface: A first-principles density functional theory study, Appl. Surf. Sci., 254 (2008) 4218-4224.

[382] M.C. Mantovani, C. Takano, P.M. Büchler, EAF and secondary dust characterisation, Ironmaking & Steelmaking 31 (2013) 325-332.

[383] T. Sofilic, A. Rastovcan-Mioc, S. Cerjan-Stefanovic, V. Novosel-Radovic, M. Jenko, Characterization of steel mill electric-arc furnace dust, J. Hazard. Mater., 109 (2004) 59-70.

[384] M. Al-Harahsheh, A. Al-Otoom, L. Al-Makhadmah, I.E. Hamilton, S. Kingman, S. Al-Asheh, M. Hararah, Pyrolysis of poly (vinyl chloride) and-electric arc furnacedust mixtures, J. Hazard. Mater., 299 (2015) 425-436.

[385] N.W. Assaf, M. Altarawneh, I. Oluwoye, M. Radny, S.M. Lomnicki, B.Z. Dlugogorski, Formation of Environmentally Persistent Free Radicals on alpha-Al$_2$O$_3$, EEnviron. Sci. Technol., 50 (2016) 11094-11102.

[386] N. Tsubouchi, H. Hashimoto, N. Ohtaka, Y. Ohtsuka, Chemical characterization of dust particles recovered from bag filters of electric arc furnaces for steelmaking: some factors influencing the formation of hexachlorobenzene, J. Hazard. Mater., 183 (2010) 116-124.

[387] P. Oustadakis, P.E. Tsakiridis, A. Katsiapi, S. Agatzini-Leonardou, Hydrometallurgical process for zinc recovery from electric arc furnace dust (EAFD): part I: Characterization and leaching by diluted sulphuric acid, J. Hazard. Mater. 179 (2010) 1-7.

[388] H. Matsuura, T. Hamano, F. Tsukihashi, Removal of Zn and Pb from Fe$_2$O$_3$–ZnFe$_2$O$_4$–ZnO–PbO mixture by selective chlorination and evaporation reactions, ISIJ Int. 46 (2006) 1113-1119.

[389] T. Havlik, B. Vidor e Souza, A.M. Bernardes, I.A. Schneider, A. Miskufova, Hydrometallurgical processing of carbon steel EAF dust, J. Hazard. Mater. 135 (2006) 311-318.

[390] R.Z. Al-Zaid, F.H. Al-Sugair, A.I. Al-Negheimish, Investigation of potential uses of electric-arc furnace dust (EAFD) in concrete, Cement Concrete Res., 27 (1997) 267-278.

[391] N. Menad, J.N. Ayala, F. Garcia-Carcedo, E. Ruiz-Ayucar, A. Hernandez, Study of the presence of fluorine in the recycled fractions during carbothermal treatment of EAF dust, Waste Manage., 23 (2003) 483-491.

[392] T. Sofilic, D. Barisic, U. Sofilic, J. Zivkovic, Monitoring of radionuclides in carbon steel blooms produced by EAF process, J. Min. Metall., Section B: Metall., 47 (2011) 125-136.

[393] M.K. Jha, V. Kumar, R. Singh, Review of hydrometallurgical recovery of zinc from industrial wastes, Res., Conserv. Recycl., 33 (2001) 1-22.

[394] A. Kekki, J. Aromaa, O. Forsen, Leaching characteristics of EAF and AOD stainless steel production dusts, Probl. Min. Process., 48 (2012) 599-606.

[395] M. Al-Harahsheh, A. Al-Otoom, L. Al-Makhadmah, I.E. Hamilton, S. Kingman, S. Al-Asheh, M. Hararah, Pyrolysis of poly(vinyl chloride) and-electric arc furnacedust mixtures, J. Hazard. Mater., 299 (2015) 425-436.

[396] A. Salamova, R.A. Hites, Brominated and chlorinated flame retardants in tree bark from around the globe, Environ. Sci. Technol., 47 (2012) 349-354.

[397] Y. Sakata, T. Bhaskar, M.A. Uddin, A. Muto, T. Matsui, Development of a catalytic dehalogenation (Cl, Br) process for municipal waste plastic-derived oil, JJ. Mater. Cycl. Waste Manage., 5 (2003) 113-124.

[398] G. Gourmelon, Global Plastic Production Rises, Recycling Lags, Worldwatch Institute, Washington (2015).

[399] L. Zhou, Z. Xu, Response to waste electrical and electronic equipments in China: legislation, recycling system, and advanced integrated process, Environ. Sci. Technol., 46 (2012) 4713-4724.

[400] Z. Tang, Q. Huang, J. Cheng, Y. Yang, J. Yang, W. Guo, Z. Nie, N. Zeng, L. Jin, Polybrominated diphenyl ethers in soils, sediments, and human hair in a plastic waste recycling area: a neglected heavily polluted area, Environ. Sci. Technol., 48 (2014) 1508-1516.

[401] F. Samara, B. Wyrzykowska, D. Tabor, D. Touati, B.K. Gullett, Toxicity comparison of chlorinated and brominated dibenzo-p-dioxins and dibenzofurans in industrial source samples by HRGC/HRMS and enzyme immunoassay, Environ. Int. 36 (2010) 247-253.

[402] P.W. O'Keefe, Formation of brominated dibenzofurans from pyrolysis of the polybrominated biphenyl fire retardant, firemaster FF-1, Environ. Health Perspect., 23 (1978) 347.

[403] N. Kollikkathara, H. Feng, D. Yu, A system dynamic modeling approach for evaluating municipal solid waste generation, landfill capacity and related cost management issues, Waste Manage., 30 (2010) 2194-2203.

[404] M. Altarawneh, M.W. Radny, P.V. Smith, J.C. Mackie, E.M. Kennedy, B.Z. Dlugogorski, A. Soon, C. Stampfl, A first-principles density functional study of chlorophenol adsorption on Cu_2O (110): CuO, J. Chem. Phys., 130 (2009) 184505.

[405] O.H. Ahmed, M. Altarawneh, Z.-T. Jiang, M. Al-Harahsheh, B.Z. Dlugogorski, Reactions of products from thermal degradation of PVC with nanoclusters of α-Fe_2O_3 (hematite), Chem. Eng. J., 323 (2017) 396-405.

[406] B. Zhang, X.-Y. Yan, K. Shibata, T. Uda, M. Tada, M. Hirasawa, Thermogravimetric-mass spectrometric analysis of the reactions between oxide (ZnO, Fe_2O_3 or $ZnFe_2O_4$) and polyvinyl chloride under inert atmosphere, Mater. Transact., JIM, 41 (2000) 1342-1350.

[407] G. Kresse, J. Hafner, Ab initio molecular dynamics for liquid metals, Phys. Rev. B, 47 (1993) 558.

[408] G. Kresse, J. Furthmüller, Efficient iterative schemes for ab initio total-energy calculations using a plane-wave basis set, Phys. Rev. B, 54 (1996) 11169.

[409] P.E. Blöchl, Projector augmented-wave method, Phys. Rev. B, 50 (1994) 17953.

[410] G. Kresse, D. Joubert, From ultrasoft pseudopotentials to the projector augmented-wave method, Phys. Rev. B, 59 (1999) 1758.

[411] K.A. Jackson, M.R. Pederson, D. Singh, C. Fiolhais, Atoms, molecules, solids, and surfaces: applications of the generalized gradient approximation for exchange and correlation, Phys. Rev. B, 46 (1992).

[412] K. Schwarz, P. Blaha, G.K. Madsen, Electronic structure calculations of solids using the WIEN2k package for material sciences, Comp. Phys. Commun., 147 (2002) 71-76.

[413] N. Troullier, J.L. Martins, Efficient pseudopotentials for plane-wave calculations. II. Operators for fast iterative diagonalization, Phys. Rev. B, 43 (1991) 8861.

[414] D. Sheppard, R. Terrell, G. Henkelman, Optimization methods for finding minimum energy paths, J. Chem. Phys., 128 (2008) 134106.

[415] G. Henkelman, B.P. Uberuaga, H. Jónsson, A climbing image nudged elastic band method for finding saddle points and minimum energy paths, J. Chem. Phys., 113 (2000) 9901-9904.

[416] H.S. Fogler, Essentials of chemical reaction engineering, Pearson Education (2010).

[417] A. Togo, I. Tanaka, First principles phonon calculations in materials science, Scripta Mater., 108 (2015) 1-5.

[418] C. Yan, D. Xue, Conversion of ZnO nanorod arrays into ZnO/ZnS nanocable and ZnS nanotube arrays via an in situ chemistry strategy, J. Phys. Chem. B, 110 (2006) 25850-25855.

[419] N. Marana, V. Longo, E. Longo, J. Martins, J. Sambrano, Electronic and structural properties of the (1010) and (1120) ZnO surfaces, J. Phys. Chem., 112 (2008) 8958-8963.

[420] F. Lopez, A. López-Delgado, J.M. de Vidales, E. Vila, Synthesis of nanocrystalline zinc ferrite powders from sulphuric pickling waste water, J. Alloy. Compd., 265 (1998) 291-296.

[421] V. Šepelák, U. Steinike, D.-C. Uecker, R. Trettin, S. Wißmann, K. Becker, High-temperature reactivity of mechanosynthesized zinc ferrite, Solid State Ionics 101 (1997) 1343-1349.

[422] J.M. De Vidales, A. López-Delgado, E. Vila, F. Lopez, The effect of the starting solution on the physico-chemical properties of zinc ferrite synthesized at low temperature, J. Alloy. Compd., 287 (1999) 276-283.

[423] O. Dulub, L.A. Boatner, U. Diebold, STM study of the geometric and electronic structure of ZnO (0001)-Zn,(0001)-O,(1010), and (1120) surfaces, Surf. Sci., 519 (2002) 201-217.

[424] H. Sawada, R. Wang, A.W. Sleight, An electron density residual study of zinc oxide, J. Solid State Chem., 122 (1996) 148-150.

[425] J. Jaffe, A. Hess, Hartree-Fock study of phase changes in ZnO at high pressure, Phys. Rev. B, 48 (1993) 7903.

[426] C. Noguera, Polar oxide surfaces, J. Phys., 12 (2000) R367.

[427] B. Meyer, D. Marx, Density-functional study of the structure and stability of ZnO surfaces, Phys. Rev. B, 67 (2003) 035403.

[428] C.B. Duke, R.J. Meyer, A. Paton, P. Mark, Calculation of low-energy-electron-diffraction intensities from ZnO (1010). II. Influence of calculational procedure, model potential, and second-layer structural distortions, Phys. Rev. B, 18 (1978) 4225.

[429] M.-R. He, R. Yu, J. Zhu, Subangstrom profile imaging of relaxed ZnO (1010) surfaces, Nano lett., 12 (2012) 704-708.

[430] E.I. Solomon, V. Henrich, Study of Four Single Crystal Faces of ZnO, by UPS, Surf. Sci. Spectra, 5 (1998) 186-188.

[431] S. Overbury, P. Radulovic, S. Thevuthasan, G. Herman, M. Henderson, C. Peden, Ion scattering study of the Zn and oxygen-terminated basal plane surfaces of ZnO, Surf. Sci., 410 (1998) 106-122.

[432] P. Tasker, The stability of ionic crystal surfaces, J. Phys. C, 12 (1979) 4977.

[433] S. Kenmoe, P.U. Biedermann, Water aggregation and dissociation on the ZnO (1010) surface, Phys. Chem. Chem. Phys., 19 (2017) 1466-1486.

[434] A. Wander, N. Harrison, An ab initio study of ZnO (1010), Surf. Sci., 457 (2000) L342-L346.

[435] S. Torbrügge, F. Ostendorf, M. Reichling, Stabilization of zinc-terminated ZnO (0001) by a modified surface stoichiometry, J. Phys. Chem. C, 113 (2009) 4909-4914.

[436] N. Jedrecy, S. Gallini, M. Sauvage-Simkin, R. Pinchaux, The ZnO non-polar (1010) surface: an X-ray structural investigation, Surf. Sci., 460 (2000) 136-143.

[437] O.G. Parchment, M.A. Vincent, I.H. Hillier, Speciation in aqueous zinc chloride. An ab initio hybrid microsolvation/continuum approach, J. Phys. Chem., 100 (1996) 9689-9693.

[438] P.L. Goggin, G. Johansson, M. Maeda, H. Wakita, The structures of zinc bromide complexes in aqueous solution, Acta Chem. Scand. A, 38 (1984).

[439] B. Li, H. Metiu, Does halogen adsorption activate the oxygen atom on an oxide surface? I. A study of Br_2 and HBr adsorption on La_2O_3 and La_2O_3 doped with Mg or Zr, J. Phys. Chem. C, 116 (2012) 4137-4148.

[440] Z. Hu, H. Metiu, Halogen Adsorption on CeO_2: The Role of Lewis Acid–Base Pairing, J. Phys. Chem. C, 116 (2012) 6664-6671.

[441] F. Keneshea, D. Cubicciotti, Vapor pressures of zinc chloride and zinc bromide and their gaseous dimerization, J. Chem. Phys., 40 (1964) 191-199.

[442] S. Batsanov, Dependence of the bond length in molecules and crystals on coordination numbers of atoms, J. Struct. Chem., 51 (2010) 281-287.

[443] D. Braun, PVC-origin, growth, and future, J. Vinyl and Addit. Technol., 7 (2001) 168-176.

[444] A. López, I. de Marco, B.M. Caballero, A. Adrados, M.F. Laresgoiti, Deactivation and regeneration of ZSM-5 zeolite in catalytic pyrolysis of plastic wastes, Waste Manage., 31 (2011) 1852-1858.

[445] L. Andrady Anthony, A. Neal Mike, Applications and societal benefits of plastics, Phil. Trans. R. Soc. B, 364 (2009) 1977-1984.

[446] B. Esckilsen, Global PVC markets: threats and opportunities, Plastics, Addit. Compd., 10 (2008) 28-30.

[447] P.J. Donaj, W. Kaminsky, F. Buzeto, W. Yang, Pyrolysis of polyolefins for increasing the yield of monomers' recovery, Waste Manage., 32 (2012) 840-846.

[448] N. Ahubelem, K. Shah, B. Moghtaderi, M. Altarawneh, B.Z. Dlugogorski, A.J. Page, Formation of chlorobenzenes by oxidative thermal decomposition of 1,3-dichloropropene, Combust. Flame, 162 (2015) 2414-2421.

[449] M. Sarker, M.M. Rashid, Waste plastics mixture of polystyrene and polypropylene into light grade fuel using Fe_2O_3 catalyst, Int. J. Renew. Energy Technol. Res., 2 (2013) 17-28.

[450] A. Demirbas, Pyrolysis of municipal plastic wastes for recovery of gasoline-range hydrocarbons, J. Anal. Appl. Pyroly., 72 (2004) 97-102.

[451] M. Al-Harahsheh, M. AlJarrah, M. Mayyas, M. Alrebaki, High-stability polyamine/amide-functionalized magnetic nanoparticles for enhanced extraction of uranium from aqueous solutions, J. Taiwan Instit. Chem. Eng., 86 (2018) 148-157.

[452] X. Ma, J. Shen, W. Pu, H. Sun, Q. Pang, J. Guo, T. Zhou, H. Cao, Water-resistant Fe–Ca–Ox/TiO_2 catalysts for low temperature 1,2-dichlorobenzene oxidation, Appl. Catal. A, 466 (2013) 68-76.

[453] X. Ma, Q. Sun, X. Feng, X. He, J. Guo, H. Sun, H. Cao, Catalytic oxidation of 1,2-dichlorobenzene over $CaCO_3$/α-Fe_2O_3 nanocomposite catalysts, Appl. Catal. A, 450 (2013) 143-151.

[454] S. Lomnicki, B. Dellinger, Development of Supported Iron Oxide Catalyst for Destruction of PCDD/F, Environ. Sci. Technol., 37 (2003) 4254-4260.

[455] I.E. Doronin, A.G. Svyazhin, Properties of steelmaking dust and the mechanism of its formation, Metallurgist 55 (2012) 879-886.

[456] M. Altarawneh, M.W. Radny, P.V. Smith, J.C. Mackie, E.M. Kennedy, B.Z. Dlugogorski, A. Soon, C. Stampfl, A first-principles density functional study of chlorophenol adsorption on $Cu_2O(110)$:CuO, J. Chem. Phys., 130 (2009) 184505.

[457] M. Altarawneh, B.Z. Dlugogorski, Formation of dibenzofuran, dibenzo-p-dioxin and their hydroxylated derivatives from catechol, Phys. Chem. Chem. Phys., 17 (2015) 1822-1830.

[458] M. Altarawneh, B.Z. Dlugogorski, E.M. Kennedy, J.C. Mackie, Quantum Chemical Study of Low Temperature Oxidation Mechanism of Dibenzofuran, J. Phys. Chem. A, 110 (2006) 13560-13567.

[459] M. Altarawneh, B.Z. Dlugogorski, Formation of polybrominated dibenzofurans from polybrominated biphenyls, Chemosphere, 119 (2015) 1048-1053.

[460] O.H. Ahmed, M. Altarawneh, Z.-T. Jiang, M. Al-Harahsheh, B.Z. Dlugogorski, Reactions of products from thermal degradation of PVC with nanoclusters of α-Fe$_2$O$_3$ (hematite), Chem. Eng. J., 323 (2017) 396-405.

[461] O.H. Ahmed, M. Altarawneh, M. Al-Harahsheh, Z.-T. Jiang, B.Z. Dlugogorski, Recycling of zincite (ZnO) via uptake of hydrogen halides, Phys. Chem. Chem. Phys. 20 (2018) 1221-1230.

[462] O.H. Ahmed, M. Altarawneh, M. Al-Harahsheh, Z.-T. Jiang, B.Z. Dlugogorski, Catalytic de-halogenation of alkyl halides by copper surfaces, J. Environ. Chem. Engi, 6 (2018) 7214-7224.

[463] L.-S. Zhong, J.-S. Hu, H.-P. Liang, A.-M. Cao, W.-G. Song, L.-J. Wan, Self-Assembled 3D Flowerlike Iron Oxide Nanostructures and Their Application in Water Treatment, Adv. Mater., 18 (2006) 2426-2431.

[464] G. Su, H. Lu, L. Zhang, A. Zhang, L. Huang, S. Liu, L. Li, M. Zheng, Thermal Degradation of Octachloronaphthalene over As-Prepared Fe$_3$O$_4$ Micro/Nanomaterial and Its Hypothesized Mechanism, Environ. Sci. Technol., 48 (2014) 6899-6908.

[465] J.P. Perdew, Y. Wang, Pair-distribution function and its coupling-constant average for the spin-polarized electron gas, Phys. Rev. B, 46 (1992) 12947-12954.

[466] R.F. Bader, A quantum theory of molecular structure and its applications, Chem. Rev., 91 (1991) 893-928.

[467] S. Grimme, J. Antony, S. Ehrlich, H. Krieg, A consistent and accurate ab initio parametrization of density functional dispersion correction (DFT-D) for the 94 elements H-Pu, J. Chem. Phys., 132 (2010) 154104.

[468] S.L. Dudarev, G.A. Botton, S.Y. Savrasov, C.J. Humphreys, A.P. Sutton, Electron-energy-loss spectra and the structural stability of nickel oxide: An LSDA+U study, Phys. Rev. B, 57 (1998) 1505-1509.

[469] S.L. Dudarev, A.I. Liechtenstein, M.R. Castell, G.A.D. Briggs, A.P. Sutton, Surface states on NiO (100) and the origin of the contrast reversal in atomically resolved scanning tunneling microscope images, Phys. Rev. B, 56 (1997) 4900-4908.

[470] G. Henkelman, H. Jónsson, A dimer method for finding saddle points on high dimensional potential surfaces using only first derivatives, J. Chem. Phys., 111 (1999) 7010-7022.

[471] B.J. Berne, G. Cicootti, D.F. Coker, Classical and Quantum Dynamics in condensed Phase Simulations, in: W. Scientific (Ed.) (1998), 385-404.

[472] K.J. Laidler, Chemical kinetics, 1987.

[473] A. Togo, L. Chaput, I. Tanaka, G. Hug, First-principles phonon calculations of thermal expansion in Ti_3SiC_2, Ti_3AlC_2, and Ti_3GeC_2, Phys. Rev. B, 81 (2010) 174301.

[474] K. Parlinski, Z.Q. Li, Y. Kawazoe, First-Principles Determination of the Soft Mode in Cubic ZrO2, Phys. Rev. Lett., 78 (1997) 4063-4066.

[475] G.-D. Fang, D.D. Dionysiou, S.R. Al-Abed, D.-M. Zhou, Superoxide radical driving the activation of persulfate by magnetite nanoparticles: Implications for the degradation of PCBs, Appl. Catal. B, 129 (2013) 325-332.

[476] P. Hu, S. Zhang, H. Wang, D.a. Pan, J. Tian, Z. Tang, A.A. Volinsky, Heat treatment effects on Fe_3O_4 nanoparticles structure and magnetic properties prepared by carbothermal reduction, J. Alloy. Compd., 509 (2011) 2316-2319.

[477] Y. Zhao, Z. Qiu, J. Huang, Preparation and Analysis of Fe3O4 Magnetic Nanoparticles Used as Targeted-drug Carriers**Supported by the Technology Project of Jiangxi Provincial Education Department and Jiangxi Provincial Science Department, Chin. J. Chem. Eng., 16 (2008) 451-455.

[478] L. Blaney, Magnetite (Fe_3O_4): Properties, synthesis, and applications, Lehigh Rev., 15 (2007) 32-81.

[479] R.J. Hill, J.R. Craig, G.V. Gibbs, Systematics of the spinel structure type, Phys. Chem. Min., 4 (1979) 317-339.

[480] S. Sasaki, Radial Distribution of Electron Density in Magnetite, Fe_3O_4, Acta Crystallogr. B, 53 (1997) 762-766.

[481] R.M. Cornell, U. Schwertmann, The iron oxides: structure, properties, reactions, occurrences and uses, John Wiley & Sons (2003).

[482] C. Zhou, Q. Zhang, L. Chen, B. Han, G. Ni, J. Wu, D. Garg, H. Cheng, Density functional theory study of water dissociative chemisorption on the Fe_3O_4 (111) surface, J. Phys. Chem., 114 (2010) 21405-21410.

[483] A.R. Lennie, N.G. Condon, F.M. Leibsle, P.W. Murray, G. Thornton, D.J. Vaughan, Structures of Fe_3O_4 (111) surfaces observed by scanning tunneling microscopy, Phys. Rev.B, 53 (1996) 10244-10253.

[484] T. Yang, X.-D. Wen, C.-F. Huo, Y.-W. Li, J. Wang, H. Jiao, Carburization of the Fe_3O_4(111) Surface, J. Phys. Chem. C, 112 (2008) 6372-6379.

[485] R.M. Van Natter, J.S. Coleman, C.R.F. Lund, DFT models for active sites on high temperature water-gas shift catalysts, J. Mol. Catal. A, 292 (2008) 76-82.

[486] J. Ahdjoudj, C. Martinsky, C. Minot, M.A. Van Hove, G.A. Somorjai, Theoretical study of the termination of the Fe_3O_4 (111) surface, Surf. Sci., 443 (1999) 133-153.

[487] M.E. Grillo, M.W. Finnis, W. Ranke, Surface structure and water adsorption on Fe_3O_4(111): Spin-density functional theory and on-site Coulomb interactions, Phys. Rev. B, 77 (2008) 075407.

[488] M. Ritter, W. Weiss, Fe_3O_4(111) surface structure determined by LEED crystallography, Surf. Sci., 432 (1999) 81-94.

[489] W. Weiss, W. Ranke, Surface chemistry and catalysis on well-defined epitaxial iron-oxide layers, Prog. Surf. Sci., 70 (2002) 1-151.

[490] L. Zhu, K.L. Yao, Z.L. Liu, First-principles study of the polar (111) surface of Fe_3O_4, Phys. Rev. B, 74 (2006) 035409.

[491] C. Zhou, Q. Zhang, L. Chen, B. Han, G. Ni, J. Wu, D. Garg, H. Cheng, Density Functional Theory Study of Water Dissociative Chemisorption on the Fe_3O_4(111) Surface, J. Phys. Chem. C, 114 (2010) 21405-21410.

[492] L. Huang, B. Han, Q. Zhang, M. Fan, H. Cheng, Mechanistic Study on Water Gas Shift Reaction on the Fe_3O_4 (111) Reconstructed Surface, J. Phys. Chem. C, 119 (2015) 28934-28945.

[493] J. Drga, J. Chovanec, J. Kudelcik, Density of State of Fe_3O_4, University Rev., 9 (2015) 48-50.

[494] X. Yu, Y. Li, Y.-W. Li, J. Wang, H. Jiao, DFT+U Study of Molecular and Dissociative Water Adsorptions on the Fe_3O_4(110) Surface, J. Phys. Chem. C, 117 (2013) 7648-7655.

[495] D.-H. Lim, C.M. Lastoskie, Density Functional Theory Studies on the Relative Reactivity of Chloroethenes on Zerovalent Iron, Environ. Sci. Technol., 43 (2009) 5443-5448.

[496] D.-M. Huang, D.-B. Cao, Y.-W. Li, H. Jiao, Density Function Theory Study of CO Adsorption on Fe3O4(111) Surface, J. Phys. Chem. B, 110 (2006) 13920-13925.

[497] S. Yin, D. Ellis, H_2O adsorption and dissociation on defective hematite (0 0 0 1) surfaces: A DFT study, Surf. Sci., 602 (2008) 2047-2054.

[498] M.M. Bhasin, J.H. McCain, B.V. Vora, T. Imai, P.R. Pujadó, Dehydrogenation and oxydehydrogenation of paraffins to olefins, Appl. Catal. A, 221 (2001) 397-419.

[499] H. Metiu, S. Chrétien, Z. Hu, B. Li, X. Sun, Chemistry of Lewis acid–base pairs on oxide surfaces, J. Phys. Chem. C, 116 (2012) 10439-10450.

[500] Z. Fang, Y. Wang, D.A. Dixon, Computational Study of Ethanol Conversion on Al_8O_{12} as a Model for γ-Al_2O_3, J. Phys. Chem. C, 119 (2015) 23413-23421.

[501] S. Biswas, A. Pramanik, P. Sarkar, Computational studies on the reactivity of alkyl halides over (Al_2O_3) n nanoclusters: an approach towards room temperature dehydrohalogenation, Nanoscale, 8 (2016) 10205-10218.

[502] A. Covaci, S. Harrad, M.A.-E. Abdallah, N. Ali, R.J. Law, D. Herzke, C.A. de Wit, Novel brominated flame retardants: a review of their analysis, environmental fate and behaviour, Environ. Int., 37 (2011) 532-556.

[503] M. Altarawneh, B.Z. Dlugogorski, Thermal decomposition of 1, 2-Bis (2, 4, 6-tribromophenoxy) ethane (BTBPE), a novel brominated flame retardant, Environ. Sci. Technol., 48 (2014) 14335-14343.

[504] L.S. Birnbaum, D.F. Staskal, Brominated flame retardants: cause for concern?, Environ. Health Perspect., 112 (2004) 9.

[505] L. Fang, M. Zheng, K. Xiao, Y. Yang, Tissue-dependent distribution and bioaccumulation of polychlorinated dibenzo-p-dioxins and dibenzofurans in vegetation samples collected from Dongting Lake, China, Environ. Toxicol. Chem., 27 (2008) 49-56.

[506] J. Paasivirta, New types of persistent halogenated compounds, Springer (2008).

[507] M.R. Moore, W. Vetter, C. Gaus, G.R. Shaw, J.F. Müller, Trace organic compounds in the marine environment, Marine Pollut. Bulletin, 45 (2002) 62-68.

[508] S. Kumagai, G. Grause, T. Kameda, T. Yoshioka, Simultaneous recovery of benzene-rich oil and metals by steam pyrolysis of metal-poly (ethylene terephthalate) composite waste, Environ. Sci. Technol., 48 (2014) 3430-3437.

[509] M. Altarawneh, M.W. Radny, P.V. Smith, J.C. Mackie, E.M. Kennedy, B.Z. Dlugogorski, Adsorption of chlorophenol on the Cu (1 1 1) surface: A first-principles density functional theory study, Appl. Surf. Sci., 254 (2008) 4218-4224.

[510] K. Akubo, M.A. Nahil, P.T. Williams, Aromatic fuel oils produced from the pyrolysis-catalysis of polyethylene plastic with metal-impregnated zeolite catalysts, J. Energy Instit., (2017).

[511] F. Zaera, An organometallic guide to the chemistry of hydrocarbon moieties on transition metal surfaces, Chem. Rev., 95 (1995) 2651-2693.

[512] M.T. Buelow, G. Zhou, A.J. Gellman, B. Immaraporn, The transition state for metal-catalyzed dehalogenation, Catal. Lett., 59 (1999) 9-13.

[513] H. Yu, E.M. Kennedy, A.A. Adesina, B.Z. Dlugogorski, A review of CFC and halon treatment technologies–The nature and role of catalysts, Catal. Surveys Asia, 10 (2006) 40-54.

[514] M.T. Buelow, B. Immaraporn, A.J. Gellman, The transition state for surface-catalyzed dehalogenation: C–I cleavage on Pd (111), J. Catal., 203 (2001) 41-50.

[515] J.-L. Lin, A.V. Teplyakov, B.E. Bent, Effects of Alkyl Chain Structure on Carbon−Halogen Bond Dissociation and β-Hydride Elimination by Alkyl Halides on a Cu (100) Surface, J. Phys. Chem., 100 (1996) 10721-10731.

[516] J.L. Lin, B.E. Bent, Carbon-halogen bond dissociation on copper surfaces: effect of alkyl chain length, J. Phys. Chem., 96 (1992) 8529-8538.

[517] T. Fujimori, T. Itai, A. Goto, K.A. Asante, M. Otsuka, S. Takahashi, S. Tanabe, Interplay of metals and bromine with dioxin-related compounds concentrated in e-waste open burning soil from Agbogbloshie in Accra, Ghana, Environ. Pollut., 209 (2016) 155-163.

[518] S. Gur, T. Danielson, Q. Xiong, C. Hin, S. Pannala, G. Frantziskonis, A. Savara, C.S. Daw, Wavelet-based surrogate time series for multiscale simulation of heterogeneous catalysis, Chem. Eng. Sci., 144 (2016) 165-175.

[519] J.E. Sutton, J.M. Lorenzi, J.T. Krogel, Q. Xiong, S. Pannala, S. Matera, A. Savara, Electrons to Reactors Multiscale Modeling: Catalytic CO Oxidation over RuO_2, ACS Catal., 8 (2018) 5002-5016.

[520] C.J. Jenks, B.E. Bent, N. Bernstein, F. Zaera, The chemistry of alkyl iodides on copper surfaces. 1. Adsorption geometry, J. Phys. Chem. B, 104 (2000) 3008-3016.

[521] L. Barbosa, D. Loffreda, P. Sautet, Chemisorption of trichloroethene on the PdCu alloy (110) surface: A periodical density functional study, Langmuir, 18 (2002) 2625-2635.

[522] C. Sambiagio, S.P. Marsden, A.J. Blacker, P.C. McGowan, Copper catalysed Ullmann type chemistry: from mechanistic aspects to modern development, Chem. Soc. Rev., 43 (2014) 3525-3550.

[523] G. Evano, N. Blanchard, M. Toumi, Copper-mediated coupling reactions and their applications in natural products and designed biomolecules synthesis, Chem. Rev., 108 (2008) 3054-3131.

[524] G. Evano, M. Toumi, A. Coste, Copper-catalyzed cyclization reactions for the synthesis of alkaloids, Chem. Commun., (2009) 4166-4175.

[525] M.-T. Nguyen, C.A. Pignedoli, D. Passerone, An ab initio insight into the Cu (111)-mediated Ullmann reaction, Phys. Chem. Chem. Phys., 13 (2011) 154-160.

[526] M.X. Yang, S. Sarkar, B.E. Bent, S.R. Bare, M.T. Holbrook, Degradation of multiply-chlorinated hydrocarbons on Cu (100), Langmuir, 13 (1997) 229-242.

[527] J.P. Perdew, J.A. Chevary, S.H. Vosko, K.A. Jackson, M.R. Pederson, D.J. Singh, C. Fiolhais, Atoms, molecules, solids, and surfaces: Applications of the generalized gradient approximation for exchange and correlation, Phys. Rev. B, 46 (1992) 6671.

[528] Q. Jiang, P. Fenter, T. Gustafsson, Geometric structure and surface vibrations of Cu (001) determined by medium-energy ion scattering, Phys. Rev. B, 44 (1991) 5773.

[529] M. Altarawneh, M.W. Radny, P.V. Smith, J.C. Mackie, E.M. Kennedy, B.Z. Dlugogorski, 2-Chlorophenol adsorption on Cu(1 0 0): first-principles density functional study, Surf. Sci., 602 (2008) 1554-1562.

[530] S. Wang, Y. Cao, P. Rikvold, First-principles calculations for the adsorption of water molecules on the Cu (100) surface, Phys. Rev. B, 70 (2004) 205410.

[531] P. Singnurkar, I. Bako, H.P. Koch, E. Demirci, A. Winkler, R. Schennach, DFT and RAIRS investigations of methanol on Cu (110) and on oxygen-modified Cu (110), J. Phys. Chem. C, 112 (2008) 14034-14040.

[532] L. Ma, J. Sun, X. Lu, S. Zhang, H. Qi, L. Liu, Y. Shao, X. Shao, Copper ion salts of arylthiotetrathiafulvalenes: synthesis, structure diversity and magnetic properties, Beils. J. Org. Chem. 11 (2015) 850.

[533] I.A. Suleiman, M.W. Radny, M.J. Gladys, P.V. Smith, J.C. Mackie, E.M. Kennedy, B.Z. Dlugogorski, Thermodynamic stability and structure of cuprous chloride surfaces: a DFT investigation, Phys. Chem. Chem. Phys., 17 (2015) 7038-7045.

[534] G.C. Bond, R. Burch, Specialist Periodical Reports: Catalysis, Royal Society of Chemistry, 6 (1983) 27.

[535] M. Altarawneh, A. Marashdeh, B.Z. Dlugogorski, Structures, electronic properties and stability phase diagrams for copper (i/ii) bromide surfaces, Phys. Chem. Chem. Phys., 17 (2015) 9341-9351.

[536] X.-L. Zhou, F. Solymosi, P. Blass, K. Cannon, J. White, Interactions of methyl halides (Cl, Br and I) with Ag (111), Surf. Sci., 219 (1989) 294-316.

[537] J. Björk, F. Hanke, S. Stafström, Mechanisms of halogen-based covalent self-assembly on metal surfaces, J. Amer. Chem. Soc., 135 (2013) 5768-5775.

[538] K.J. Laidler, M.C. King, Development of transition-state theory, J. phys. chem., 87 (1983) 2657-2664.

[539] A. Togo, L. Chaput, I. Tanaka, G. Hug, First-principles phonon calculations of thermal expansion in Ti_3SiC_2, Ti_3AlC_2, and Ti_3GeC_2, Phys. Rev. B, 81 (2010) 174301.

[540] T. Makino, S. Zulaehah, J.S. Gueriba, W.A. Diño, M. Okada, CH_3Cl/Cu (410): Interaction and Adsorption Geometry, J. Phys.Chem. C, (2018).

[541] T. Livneh, Y. Lilach, M. Asscher, Dipole–dipole interactions among CH_3Cl molecules on Ru (001): Correlation between work function change and thermal desorption studies, J. Chem. Phys., 111 (1999) 11138-11146.

[542] F. Solymosi, A. Berkó, K. Révész, Adsorption of CH3Cl on clean and Cl-dosed Pd (100) surfaces, Surf. Sci., 240 (1990) 50-58.

[543] T. Livneh, M. Asscher, Surface chemistry of CH_3Br and methyl modified by copper deposition on Ru (001), J. Phys. Chem. B, 103 (1999) 5665-5674.

[544] M. Altarawneh, B.Z. Dlugogorski, E.M. Kennedy, J.C. Mackie, Quantum Chemical and Kinetic Study of Formation of 2-Chlorophenoxy Radical from 2-Chlorophenol: Unimolecular Decomposition and Bimolecular Reactions with H, OH, Cl, and O_2, J. Phys. Chem. A, 112 (2008) 3680-3692.

[545] A. Peters, D.W. Dockery, J.E. Muller, M.A. Mittleman, Increased particulate air pollution and the triggering of myocardial infarction, Circulation 103 (2001) 2810-2815.

[546] A. Nel, Air Pollution-Related Illness: Effects of Particles, Science 308 (2005) 804-806.

[547] I.M. Kennedy, The health effects of combustion-generated aerosols, Proc. Comb. Instit., 31 (2007) 2757-2770.

[548] A. Valavanidis, K. Fiotakis, E. Bakeas, T. Vlahogianni, Electron paramagnetic resonance study of the generation of reactive oxygen species catalysed by transition metals and quinoid redox cycling by inhalable ambient particulate matter, Redox Report 10 (2005) 37-51.

[549] L. Yang, G. Liu, M. Zheng, R. Jin, Q. Zhu, Y. Zhao, X. Wu, Y. Xu, Highly Elevated Levels and Particle-Size Distributions of Environmentally Persistent Free Radicals in Haze-Associated Atmosphere, Environ. Sci. Technol., 51 (2017) 7936-7944.

[550] P.E. Rasmussen, A.J. Wheeler, N.M. Hassan, A. Filiatreault, M. Lanouette, Monitoring personal, indoor, and outdoor exposures to metals in airborne particulate matter: Risk of contamination during sampling, handling and analysis, Atmo. Environ., 41 (2007) 5897-5907.

[551] S.C. Bondy, S.X. Guo-Ross, A.T. Truong, Promotion of transition metal-induced reactive oxygen species formation by β-amyloid, Brain Res., 799 (1998) 91-96.

[552] E. Vejerano, S. Lomnicki, B. Dellinger, Formation and Stabilization of Combustion-Generated Environmentally Persistent Free Radicals on an Fe(III)$_2$O$_3$/Silica Surface, Environ. Sci. Technol., 45 (2011) 589-594.

[553] S. Lomnicki, H. Truong, E. Vejerano, B. Dellinger, Copper Oxide-Based Model of Persistent Free Radical Formation on Combustion-Derived Particulate Matter, Environ. Sci. Technol., 42 (2008) 4982-4988.

[554] S. Mosallanejad, B.Z. Dlugogorski, E.M. Kennedy, M. Stockenhuber, S.M. Lomnicki, N.W. Assaf, M. Altarawneh, Formation of PCDD/Fs in Oxidation of 2-Chlorophenol on Neat Silica Surface, Environ. Sci. Technol., 50 (2016) 1412-1418.

[555] U.G. Nwosu, A. Roy, A.L.N. dela Cruz, B. Dellinger, R. Cook, Formation of environmentally persistent free radical (EPFR) in iron(iii) cation-exchanged smectite clay, Environ. Sci., 18 (2016) 42-50.

[556] X. Ruan, Y. Sun, W. Du, Y. Tang, Q. Liu, Z. Zhang, W. Doherty, R.L. Frost, G. Qian, D.C.W. Tsang, Formation, characteristics, and applications of environmentally persistent free radicals in biochars: A review, Biores. Technol., 281 (2019) 457-468.

[557] F. Lu, G.N. Salaita, L. Laguren-Davidson, D.A. Stern, E. Wellner, D.G. Frank, N. Batina, D.C. Zapien, N. Walton, A.T. Hubbard, Characterization of hydroquinone and related compounds adsorbed at Pt (111) from aqueous solutions: electron energy-loss spectroscopy, Auger spectroscopy, LEED, and cyclic voltammetry, Langmuir, 4 (1988) 637-646.

[558] N.V. Richardson, P. Hofmann, A spectroscopic investigation of the adsorption of phenol on Cu{110}, Vacuum, 33 (1983) 793-796.

[559] A.J.R. Hensley, Y. Wang, J.-S. McEwen, Adsorption of phenol on Fe (110) and Pd (111) from first principles, Surf. Sci., 630 (2014) 244-253.

[560] M. Altarawneh, M.W. Radny, P.V. Smith, J.C. Mackie, E.M. Kennedy, B.Z. Dlugogorski, 2-Chlorophenol adsorption on Cu(100): First-principles density functional study, Surf. Sci., 602 (2008) 1554-1562.

[561] J. Ye, C. Liu, D. Mei, Q. Ge, Active Oxygen Vacancy Site for Methanol Synthesis from CO2 Hydrogenation on In2O3(110): A DFT Study, ACS Catal., 3 (2013) 1296-1306.

[562] P. Singnurkar, I. Bako, H.P. Koch, E. Demirci, A. Winkler, R. Schennach, DFT and RAIRS Investigations of Methanol on Cu(110) and on Oxygen-Modified Cu(110), J. Phys. Chem. C, 112 (2008) 14034-14040.

[563] M.S. Rayson, M. Altarawneh, J.C. Mackie, E.M. Kennedy, B.Z. Dlugogorski, Theoretical Study of the Ammonia−Hypochlorous Acid Reaction Mechanism, J. Phys. Chem. A, 114 (2010) 2597-2606.

[564] M. Altarawneh, A.A.H. Al-Muhtaseb, B.Z. Dlugogorski, E.M. Kennedy, J.C. Mackie, Rate constants for hydrogen abstraction reactions by the hydroperoxyl radical from methanol, ethenol, acetaldehyde, toluene, and phenol, J. Comp. Chem., 32 (2011) 1725-1733.

[565] V.A. Lubarda, On the effective lattice parameter of binary alloys, Mech. Mater., 35 (2003) 53-68.

[566] W. Zhong, G. Overney, D. Toma´nek, Structural properties of Fe crystals, Phys. Rev. B, 47 (1993) 95-99.

[567] S. Wang, Y. Cao, P.A. Rikvold, First-principles calculations for the adsorption of water molecules on the Cu (100) surface, Phys. Rev. B, 70 (2004) 205410.

[568] H.W. Hugosson, W. Cao, S. Seetharaman, A. Delin, Sulfur- and Oxygen-Induced Alterations of the Iron (001) Surface Magnetism and Work Function: A Theoretical Study, The J. Phys. Chem., C, 117 (2013) 6161-6171.

[569] P. Błoński, A. Kiejna, Structural, electronic, and magnetic properties of bcc iron surfaces, Surf. Sci., 601 (2007) 123-133.

[570] J. Jeon, B. Yu, First-principles Study of the Physical Properties of Ultrathin MgO Films on Fe (001) Surfaces, J. Kor. Phys. Soc., 59 (2011) 2291-2296.

[571] K.O. Legg, F. Jona, D.W. Jepsen, P.M. Marcus, Low-energy electron diffraction analysis of clean Fe (001), J. Phys. C, 10 (1977) 937-946.

[572] N.W. Larsen, Microwave spectra of the six mono-13C-substituted phenols and of some monodeuterated species of phenol. Complete substitution structure and absolute dipole moment, J. Mol. Stru., 51 (1979) 175-190.

[573] X. Jia, W. An, Adsorption of Monocyclic Aromatics on Transition Metal Surfaces: Insight into Variation of Binding Strength from First-Principles, J. Phys. Chem. C, 122 (2018) 21897-21909.

[574] G. Li, J. Han, H. Wang, X. Zhu, Q. Ge, Role of Dissociation of Phenol in Its Selective Hydrogenation on Pt(111) and Pd(111), ACS Catal., 5 (2015) 2009-2016.

[575] D. Wiśnios, A. Kiejna, J. Korecki, First-principles study of the adsorption of MgO molecules on a clean Fe(001) surface, Phys. Rev. B, 92 (2015) 155425.

[576] O.H. Ahmed, M. Altarawneh, M. Al-Harahsheh, Z.-T. Jiang, B.Z. Dlugogorski, Catalytic de-chlorination of products from PVC degradation by magnetite (Fe_3O_4), Appl. Surf. Sci., 480 (2019) 792-801.

[577] J. Wang, D. Domin, B. Austin, D.Y. Zubarev, J. McClean, M. Frenklach, T. Cui, W.A. Lester, A Diffusion Monte Carlo Study of the O−H Bond Dissociation of Phenol, J. Phys. Chem. A, 114 (2010) 9832-9835.

[578] E.P. Vejerano, G. Rao, L. Khachatryan, S.A. Cormier, S. Lomnicki, Environmentally Persistent Free Radicals: Insights on a New Class of Pollutants, Environ. Sci. Technol., 52 (2018) 2468-2481.

[579] C.D. Okeson, M.R. Riley, A. Fernandez, J.O.L. Wendt, Impact of the composition of combustion generated fine particles on epithelial cell toxicity: influences of metals on metabolism, Chemosphere, 51 (2003) 1121-1128.

[580] H. He, Y. Wang, Q. Ma, J. Ma, B. Chu, D. Ji, G. Tang, C. Liu, H. Zhang, J. Hao, Mineral dust and NOx promote the conversion of SO2 to sulfate in heavy pollution days, Scientific Reports, 4 (2014) 4172.

[581] Y. Fu, C. Kuppe, V.K. Valev, H. Fu, L. Zhang, J. Chen, Surface-Enhanced Raman Spectroscopy: A Facile and Rapid Method for the Chemical Component Study of Individual Atmospheric Aerosol, Environ. Sci. Technol., 51 (2017) 6260-6267.

[582] A. Soon, M. Todorova, B. Delley, C. Stampfl, Oxygen adsorption and stability of surface oxides on Cu (111): A first-principles investigation, Phys. Rev. B, 73 (2006) 165424.

[583] A. Soon, M. Todorova, B. Delley, C. Stampfl, Thermodynamic stability and structure of copper oxide surfaces: A first-principles investigation, Phys. Rev. B, 75 (2007) 125420.

[584] I.A. Suleiman, M.W. Radny, M.J. Gladys, P.V. Smith, J.C. Mackie, E.M. Kennedy, B.Z. Dlugogorski, Interaction of Chlorine and Oxygen with the Cu(100) Surface, J. Phys. Chem. C, 114 (2010) 19048-19054.

[585] P. Błoński, A. Kiejna, J. Hafner, Theoretical study of oxygen adsorption at the Fe(110) and (100) surfaces, Surf. Sci., 590 (2005) 88-100.

[586] X. Yu, X. Zhang, High coverage water adsorption on CuO(011) surface, hys. Chem. Chem. Phys., 19 (2017) 18652-18659.

[587] A.F. Slater, W.J. Swiggard, B.R. Orton, W.D. Flitter, D.E. Goldberg, A. Cerami, G.B. Henderson, An iron-carboxylate bond links the heme units of malaria pigment, Proc. Natn Acad. Sci., 88 (1991) 325-329.

[588] H. Li, B. Pan, S. Liao, D. Zhang, B. Xing, Formation of environmentally persistent free radicals as the mechanism for reduced catechol degradation on hematite-silica surface under UV irradiation, Environ. Pollut., 188 (2014) 153-158.

[589] W. Pan, J. Chang, X. Liu, Q. Xue, J. Fu, A. Zhang, Interfacial formation of environmentally persistent free radicals—A theoretical investigation on pentachlorophenol activation on montmorillonite in PM2.5, Ecotoxico. Environ. Safety, 169 (2019) 623-630.

[590] M.L. Honkela, J. Björk, M. Persson, Computational study of the adsorption and dissociation of phenol on Pt and Rh surfaces, Phys. Chem. Chem. Phys., 14 (2012) 5849-5854.

[591] N.W. Assaf, M. Altarawneh, M.W. Radny, J. Al-Nu'airat, B.Z. Dlugogorski, Formation of environmentally-persistent free radicals (EPFR) on α-Al_2O_3 clusters, RSC Advances 7 (2017) 52672-52683.

[592] Q. Sun, M. Altarawneh, B.Z. Dlugogorski, E.M. Kennedy, J.C. Mackie, Catalytic Effect of CuO and Other Transition Metal Oxides in Formation of Dioxins: Theoretical Investigation of Reaction Between 2,4,5-Trichlorophenol and CuO, Environ. Sci. Technol., 41 (2007) 5708-5715.

[593] M. Pelucchi, C. Cavallotti, A. Cuoci, T. Faravelli, A. Frassoldati, E. Ranzi, Detailed kinetics of substituted phenolic species in pyrolysis bio-oils, Reac. Chem. Eng., 4 (2019) 490-506.

[594] E. Vejerano, S. Lomnicki, B. Dellinger, Lifetime of combustion-generated environmentally persistent free radicals on Zn(ii)O and other transition metal oxides, J. Environ. Monit., 14 (2012) 2803-2806.

[595] T. Makino, S. Zulaehah, J.S. Gueriba, W.A. Diño, M. Okada, CH3Cl/Cu(410): Interaction and Adsorption Geometry, J. Phys. Chem. C, 122 (2018) 11825-11831.

[596] T. Livneh, Y. Lilach, M. Asscher, Dipole–dipole interactions among CH3Cl molecules on Ru(001): Correlation between work function change and thermal desorption studies, J. Chem. Phys., 111 (1999) 11138-11146.

[597] F. Solymosi, A. Berkó, K. Révész, Adsorption of CH3Cl on clean and Cl-dosed Pd(100) surfaces, Surf. Sci., 240 (1990) 50-58.

[598] T. Livneh, M. Asscher, Surface Chemistry of CH3Br and Methyl Modified by Copper Deposition on Ru(001), J. Phys. Chem. B, 103 (1999) 5665-5674.

[599] J. Björk, F. Hanke, S. Stafström, Mechanisms of Halogen-Based Covalent Self-Assembly on Metal Surfaces, J. Ame. Chem. Soc., 135 (2013) 5768-5775.